High Harmonic Generation for Coherent Diffractive Imaging

A thesis submitted for the degree of

Doctor of Philosophy

by

Sven Teichmann

SWIN BUR NE
CENTRE FOR ATOM OPTICS AND ULTRAFAST SPECTROSCOPY

CXS
ARC Centre of Excellence for
COHERENT X-RAY SCIENCE

Centre for Atom Optics and Ultrafast Spectroscopy and
ARC Centre of Excellence for Coherent X-Ray Science

Faculty of Engineering and Industrial Sciences
Swinburne University of Technology
Melbourne, Australia

November 25, 2009

Declaration

I, Sven Teichmann, declare that this thesis entitled:

"High Harmonic Generation for Coherent Diffractive Imaging"

is my own work and has not been submitted previously, in whole or in part, in respect of any other academic award.

Sven Teichmann

Centre for Atom Optics and Ultrafast Spectroscopy and
ARC Centre of Excellence for Coherent X-Ray Science
Faculty of Engineering and Industrial Sciences
Swinburne University of Technology
Melbourne, Australia

Dated this day, November 25, 2009

Abstract

This dissertation presents experimental work on a high-harmonic generation source and coherent diffractive imaging. A novel and successful approach of employing harmonic emission that consists of multiple harmonic orders and its utilization for coherent diffractive imaging is presented, and associated results are discussed. This work may prove valuable particularly for time-resolved spectroscopy, sources of soft x-ray and extreme-ultraviolet radiation, and imaging based on harmonic emission.

A high-harmonic generation apparatus has been built featuring a highly flexible high-harmonic interaction geometry, optical elements for tailoring of the harmonic emission and a flexible stage that serves experimental purposes, in particular for coherent diffractive imaging. Based on a semi-infinite argon or helium gas cell design, the harmonic emission can be phase-matched and tailored according to the experimental requirements for high flux and so that the spectral width of the harmonic beam is confined to only a few intense harmonic orders. This beam can be directly used for experimental purposes without any narrow-bandwidth optics in the beam path that might affect the harmonic emission in its spatial, spectral or temporal domain. Also any loss in harmonic flux due to intrinsic inefficiencies can be avoided. A technique for in-situ spectral characterization has been developed, which is based on an application of the maximum entropy method to the interference pattern from a Young double-slit pair illuminated by the harmonic emission. This approach is more flexible than and avoids serious problems associated with a different approach based on the use of a fast

Fourier transform to extract the spectral information.

The multiple-order high harmonic emission is utilized for coherent diffractive imaging. Due to its nature, this source provides a high degree of spatial coherence, but the temporal coherence is poor. Thus, we have developed a new algorithm for phase-retrieval that can process the diffraction pattern which is a superposition of the diffraction patterns of each individual harmonic order of the high-harmonic beam. This algorithm is a modified version of the conventional algorithm (Gerchberg-Saxton-Fienup) for coherent diffractive imaging and includes the spectrum optimization iterative procedure (gradient descent method) within the main reconstruction iterative process. Also, an application of the maximum entropy method is employed for improvement of the quality of the reconstructed image. The formalism can readily be adapted to any short-wavelength polychromatic source in which there is a high degree of spatial coherence at each sampled wavelength but poor temporal coherence across the sampled spectrum. Diffraction patterns of wide dynamic range can be acquired by means of a new design involving a beam stop and image stitching. Binary and non-binary periodic and non-periodic samples have been successfully reconstructed. It is noted that the employment of multiple-wavelength coherent diffractive imaging is a necessity when operating the high-harmonic source in the water-window (~ 4.4 to 2.3 nm). In this spectral region the spectral spacing $\Delta\lambda$ of adjacent harmonic orders is $0.05 \text{ nm} > \Delta\lambda > 0.01 \text{ nm}$, which may be comparable to or even smaller than the spectral resolution $\Delta\delta$ of a diffraction grating that is used for selecting a single harmonic order for coherent diffractive imaging (e.g., $\Delta\delta = 0.05$ nm for the 1200 grooves/mm-grating of the monochromator Setpoint GIMS#4, spectral range from 4.4 nm to 10.6 nm). Thus, the diffracted harmonic beam may consist of several harmonic orders instead of one single harmonic order.

This high-harmonic source is a potential source of extreme-ultraviolet and soft x-ray radiation and for time-resolved spectroscopy, such as femtosecond photoelectron spectroscopy and for polychromatic diffractive imaging with high spatial resolution, where only a few harmonic orders of short wavelength or a dominant photon energy are required and any optics in the harmonic beam path, such as reflection gratings, is undesirable. The novel and flexible approach of spectral extraction based on the application of the maximum entropy method to the interference pattern of this source can be employed for efficient in-situ spectral characterization and thus allows us to effectively tailor the harmonic source for the experimental requirements. The formalism of lensless polychromatic diffractive imaging may be adapted and applied to the multimode x-ray free-electron laser sources that are under current development and thus provides a powerful tool for imaging in the extreme-ultraviolet and soft x-ray region. The current activity in the development of this novel kind of source suggests that this approach may find direct application in proposals for imaging of single molecules with atomic resolution using short pulse coherent diffractive imaging. The relaxation of the requirement that the illuminating source be strictly monochromatic in diffractive imaging may well prove to be valuable in the future design and analysis of materials and biomolecules.

Curriculum Vitae

Sven Teichmann was born in Germany on October 5, 1978. He studied Physics at the Technische Universität München, Germany, 1999 to 2005, and specialised in Quantum Optics while conducting research work at the Max-Planck-Institut für Quantenoptik, Germany, 2004 to 2005. He started his doctorate in September 2005 at the Centre for Atom-Optics and Ultrafast Spectroscopy. His research work was performed in the Short Wavelength Laser Source Program of the Australian Research Council Centre of Excellence for Coherent X-Ray Science (CXS) and, partly, in collaboration with coworkers from the Experimental Methods Program and the Theory and Modeling Program at CXS. The research work was supervised under the direction of Professor Lap Van Dao and Professor Peter Hannaford.

Publications

The work presented in this dissertation is based on the following publications and has been carried out partly in collaboration with coworkers within the Australian Research Council Centre of Excellence for Coherent X-Ray Science:

L. Van Dao, S. Teichmann, and P. Hannaford. Phase-matching for generation of few high order harmonics in a semi-infinite gas cell. *Phys. Lett. A*, **372**:5254 (2008).

L. Van Dao, S. Teichmann, J. A. Davis, and P. Hannaford. Generation of high flux, highly coherent extreme ultraviolet radiation in a gas cell. *J. Appl. Phys.*, **104**:023105 (2008).

R. A. Dilanian, B. Chen, S. Teichmann, L. Van Dao, H. M. Quiney, and K. A. Nugent. High-harmonic-generation spectrum reconstruction from Young's double-slits interference pattern using the maximum entropy method. *Opt. Lett.*, **33**:2341 (2008).

B. Chen, R. A. Dilanian, S. Teichmann, B. Abbey, A. G. Peele, G. J. Williams, P. Hannaford, L. Van Dao, H. M. Quiney, and K. A. Nugent. Multiple wavelength diffractive imaging. *Phys. Rev. A*, **79**:023809 (2009).

S. Teichmann, P. Hannaford, and L. Van Dao. Phase-matched emission of few high-harmonic orders from a helium gas cell. *Appl. Phys. Lett.*, **94**:171111 (2009) and *Virtual Journal of Ultrafast Science (Ultrafast Methods and Measurement Techniques)*, **8(6)**:June 2009 (2009).

S. Teichmann, B. Chen, R. A. Dilanian, P. Hannaford, and L. Van Dao. Spectral characteristics across the spatial profile of a high-harmonic beam. *J. Phys. D: Appl. Phys.*, **42**:135108 (2009).

R. A. Dilanian, B. Chen, G. J. Williams, H. M. Quiney, and K. A. Nugent; S. Teichmann, P. Hannaford, and L. Van Dao; A. G. Peele. Diffractive imaging using a polychromatic high-harmonic generation soft-x-ray source. *J. Appl. Phys.*, **106**:023110 (2009).

B. Chen, R. A. Dilanian, S. Teichmann, L. Van Dao, H. M. Quiney, G. Williams, A. Peele, E. Balaur, C. Tran, and K. A. Nugent. *Manuscript under revision.*

S. Teichmann, B. Chen, J. A. Davis, L. Van Dao, and P. Hannaford. Efficient and highly coherent extreme ultraviolet high-harmonic source. *Ultrafast Phenomena XVI, Proceedings of the 16th International Conference*, Stresa, Italy. Springer, Berlin Heidelberg, Springer Series in Chemical Physics, Vol. 92, 2009.

Contents

Chapter 1

Introduction

1.1 This project

The experimental and theoretical work presented in this dissertation was performed in the Short Wavelength Laser Source Program of the Australian Research Council Centre of Excellence for Coherent X-Ray Science (CXS) and conducted at the Centre for Atom Optics and Ultrafast Spectroscopy (CAOUS) at Swinburne University of Technology. One of the main tasks was the design and development of a high-flux tabletop coherent extreme-ultraviolet and soft x-ray source and its constant improvement depending on the experimental requirements. Another main task was the application of this source for coherent diffractive imaging, with this task including the design and development of the experimental setup for coherent diffractive imaging and its constant improvement depending on the quality requirements of the diffraction images acquired by our group. This is when we developed the idea of multiple-harmonic-order coherent diffractive imaging and of the spectral characterization of the harmonic beam by means of a Young double-slit. The computational algorithms were developed by the CXS Theory and Modeling Group at the University of Melbourne, and their successful implementation into and adaption to our high-harmonic generation apparatus was performed by our group at Swinburne University of Technology. In collaboration with the CXS Experimental Methods Group and the CXS Theory and Modeling Group this work provides the foundation for future research using highly-coherent x-ray free-electron laser sources [1] currently under international development. Another main part of the author's work was the idea and the design of a new kind of corrugated waveguide for quasi-phase-matching to improve the flux and the maximum achievable energy of the harmonic photons which is presented in section A.4.2.

In March 2007 the Femtosecond High Power Laser Facility and ancillary equipment were installed at CAOUS. The femtosecond laser system combines a femtosecond oscillator and a two-stage multi-pass amplifier and is the first system of its kind with this energy range in Australia. Based on a semi-infinite gas cell configuration, harmonic emission in the extreme-ultraviolet region with a high photon flux, high spatial coherence and good spatial beam profile can now be generated routinely in argon, neon and helium as the nonlinear medium. By properly adjusting the macroscopic phase-matching conditions, the harmonic emission can be spectrally tailored and adjusted to the experimental requirements. Harmonic emission can be confined to 1 to 4 intense harmonic orders around 30 nm in argon, and to 4 to 6 intense harmonic orders around 9.5 nm in helium [2, 3, 4, 5]. Our studies in collaboration with the CXS Theory and Modeling Program and the CXS Experimental Methods Program have demonstrated that it is possible to employ this harmonic source for multiple wavelength coherent diffraction imaging [6, 7]. In collaboration with the CXS Theory and Modeling Program a new method for extraction of the high-harmonic generation power spectrum from Young double-slit interference fringes has been developed [8]. This spectral information is fed into a modified Gerchberg-Saxton-Fienup algorithm [9] that recovers images using diffraction data obtained on the multiple harmonic order output of this source, thus eliminating the large losses incurred through selecting a single wavelength for conventional coherent diffractive imaging by means of wavelength-selective optical elements [6, 7].

Not only does the harmonic beam consist of a few phase-matched harmonic orders as a potential source for multiple-wavelength coherent diffractive imaging of homogeneous, binary and non-binary, periodic and non-periodic samples [6, 9, 7], but also it is a possible source for time-resolved spectroscopy, such as femtosecond photoelectron spectroscopy, in the extreme-ultraviolet and soft x-ray region [10]. In both cases few harmonic orders of short wavelength or a dominant photon energy are required and any optics in the harmonic beam path, such as a reflection gratings, are undesirable. The multiple-order harmonic emission can also be employed to develop imaging schemes for non-homogeneous objects by slightly varying the laser frequency in order to obtain overlapping diffraction images, and by using various exotic polymers, such as polyacetylene polymers (pure carbon), fluoro-polymers and polymers with sulphonate side groups and polymers doped with very heavy elements. Furthermore, the multiple-order harmonic emission can facilitate studies of birefringence/dichroism by analyzing the polarization properties of the polymers in the presence of stress/strain and external electric fields.

Extending the harmonic emission of this source into the water-window [11, 12, 13] may allow the non-crystallographic structural determination of membrane proteins. The short-pulse, short-wavelength bright and coherent light may allow the direct observation of the structures and reaction dynamics of isolated molecules, and thus a study of biological systems such as membrane proteins. These proteins mediate the activity of pharmaceuticals in human medical therapies. Their structures, however, are still mostly unknown as they are largely inaccessible to conventional crystallographical techniques due to their reluctance to form crystalline specimens. A breakthrough in this area could revolutionize rational drug design through the insight gained into the function of membrane proteins. Furthermore, fundamental issues in the use of this type of light source, including the nature of the interaction between intense coherent x-rays and electronic matter and the management of radiation damage throughout the interaction, the efficiency of diffraction processes in these highly coupled light-matter systems and the detection of the scattered light, the preparation and handling of suitable biological systems, and the design of algorithms to extract structural information from diffraction data are also under exploration. We note that the employment of multiple-wavelength coherent diffractive imaging is a necessity when operating the high-harmonic source in the water-window ($\sim$ 4.4 to 2.3 nm, see figure 2.1.1). Here, the spectral spacing $\Delta\lambda$ of adjacent harmonic orders is 0.05 nm $> \Delta\lambda >$ 0.01 nm. When using a monochromator with a diffraction grating appropriate for this spectral range, the spectral resolution $\Delta\delta$ of this grating might not satisfy the condition $\Delta\delta < \Delta\lambda$ (e.g., $\Delta\delta = 0.05$ nm for a 1200 grooves/mm-grating of the monochromator Setpoint GIMS#4, see table A.2). Thus, the harmonic beam diffracted from this grating consists of several harmonic orders. Yet, by employing our multiple-wavelength coherent diffractive imaging approach, this high-harmonic emission can be employed for coherent diffractive imaging in the water-window.

1.2 The associated field of research

Femtosecond-laser-driven high-harmonic generation sources provide spatially coherent ultrashort pulses of extreme-ultraviolet radiation and soft x rays [14]. By their nature, these table-top and highly versatile sources produce a laser-like beam that consists of multiple longitudinal coherent modes. The harmonic emission can be tailored according to the experimental requirements for applications in atomic and molecular spectroscopy, condensed matter physics, imaging on the sub-nanoscale, and plasma physics [15, 12, 16, 10, 17]. In principle, the characteristics of the laser beam are imprinted onto the harmonic beam. Nevertheless, the chosen interaction geometry and the intrinsic process of plasma formation lead to a complex spatially and temporally dependent induced nonlinear polarization in the medium and strongly determine the conversion efficiency, the spatial, spectral, and temporal properties, and the coherence of the harmonic emission.

Since the first experimental work on high-harmonic generation in 1987 [18] considerable progress has been achieved and femtosecond laser-driven high-harmonic generation sources have become an increasingly important supply of coherent extreme-ultraviolet radiation and soft x-rays up to the water window (~ 4.4 to 2.3 nm), which in particular is important for biological applications, [19, 11] and even the keV regime [20]. Despite reports of phase-matched and quasi phase-matched harmonic emission [14, 21, 22, 23, 24, 25] and reaching the absorption limit [23, 21, 25], appropriate control over the characteristics of the output and in particular increasing the brightness or flux of the high-harmonic generation sources still remains one of the major challenges. In fact, due to the highly nonlinear nature of high-harmonic generation, the conversion efficiency depends strongly on the experimental setup, even within the absorption limit, and the ultimate optimization conditions are still far from being fully characterized.

Soft x-ray microscopy is an important imaging technique that currently relies on the routine availability of access to synchrotron sources. However, the possibility of sources that enable small-scale x-ray microscopes [26] is helping to drive the development of alternative x-ray sources such as x-ray lasers [1], compact synchrotron sources [27], and high-harmonic generation sources [28]. The imaging requires a high degree of spatial and temporal coherence, driven by the inherent chromaticity of diffractive optics [29] or the need for spatial [30, 31] and temporal [32] coherence in diffraction based methods. If the light is not completely coherent, a coherent component is selected [33, 34, 35]. Due to its coherent nature, high-harmonic generation emission is beginning to be used for coherent diffractive imaging [33, 6]. High-harmonic generation sources exhibit a high degree of spatial coherence but produce an output of poor temporal coherence due to the multiple longitudinal modes. The need for selecting a single wavelength leads to an inherently wasteful usage of the harmonic flux which further drives the need for increasing the brightness of the harmonic sources. The underlying problem is that the phase-space acceptances of imaging systems using diffractive optics [26] or coherent diffraction [33, 34] are not well matched to the phase space of the light delivered by this type of tabletop source. A better match between the phase space of the incident light and the image formation method will provide a corresponding improvement in efficiency in the utilization of the source. The technique of coherent diffractive imaging only dates back 10 years: the first experimental work on coherent diffractive imaging was performed in 1999 [36]. Since then, coherent diffractive imaging has become a well-established technique that enables the structure, shape and size of finite, non-periodic objects to be deduced from x-ray diffraction intensity measurements [34, 37, 30, 38, 35, 39, 36, 40, 41, 42] and resolutions as low as 5 nm have been achieved [43]. Usually an error reduction or a hybrid input-output algorithm are employed to reconstruct the sample from the diffraction pattern [44, 45]. In both cases the diffraction pattern is considered as the Fourier transform of the sample which is only true when $\Delta\lambda/\lambda \ll 1$, where λ is the wavelength of the illuminating radiation and $\Delta\lambda$ is the associated spectral width. As high-harmonic sources allow the upconversion of the frequency of the driving laser system such that coherent water-window radiation can be produced [11, 12, 13], the possibility of a table-top high-contrast setup for imaging thick biophysical systems, such as membrane proteins, is very appealing. However, employing narrow-bandwidth optical elements, such as a monochromator or wavelength-selective multilayer mirrors, to select a single wavelength to satisfy the aforementioned spectral requirement is accompanied by a high loss of the harmonic flux due to intrinsic inefficiencies of the optical elements. Furthermore, the temporal as well as the spatial characteristics can be altered depending on the requirements of the desired experimental application. Thus, the opportunity of employing high-harmonic generation sources as imaging systems in the water-window spectral range is significantly diminished when focusing on thick biological samples.

A more efficient matching between the phase space of the incident light and the image formation may allow us to provide corresponding efficiencies in the utilization of the high-harmonic generation sources for coherent diffractive imaging and thus alleviate the problem of employing high-harmonic generation sources as imaging systems in the extreme-ultraviolet and soft x-ray spectral range, and in particular in the water-window range. Rather than discriminating against all coherent modes but one of this source, we spectrally tailor the harmonic source in such a way that the harmonic beam is confined to only a few phase-matched harmonic orders. This is achieved by properly setting the macroscopic phase-matching conditions, in particular the effective interaction length between the nonlinear medium and the focused femtosecond laser beam, the intensity and diameter of the focused laser beam, and the species of the nonlinear medium and its pressure. Thus, harmonic emission can be confined to ~ 1 to 4 intense harmonic orders at wavelengths of ~ 30 nm in argon, and to ~ 4 to 6 intense harmonic orders at wavelengths of ~ 9.5 nm in helium [2, 3, 4, 5]. The harmonic beam is then employed for multiple-wavelength coherent diffractive imaging.

In order to efficiently tailor the harmonic source in the spectral domain, high-harmonic-generation spectrum reconstruction from a Young double-slit interference pattern using the maximum entropy method is performed. The in-situ capacity to monitor the spectral characteristics of the harmonic beam is explained in detail in [8]. The method is based on maximum entropy analysis of a Young double-slit interference pattern. Recovery of the spectrum of a high-harmonic-generation light source has been performed before by means of fast Fourier transform [46]. However, whereas the maximum entropy method gives (an estimate of) the harmonic spectrum, the fast Fourier transform approach yields the convolution of the high-harmonic generation spectrum with the Fourier transform of the diffraction pattern from the Young double-slit. The more flexible maximum entropy method does not require any prior information about the number of harmonics as well as their positions or shapes and has yielded reliable spectra under conditions where the simpler fast Fourier transform approach cannot. The conventional coherent diffractive imaging reconstruction technique is based on Fienup's extensions of the algorithm first proposed by Gerchberg and Saxton [47, 44]. The most critical limitations of this approach is that the incident beam that illuminates the object must be fully spatially coherent and quasi-monochromatic. Thus, we have developed a reconstruction method that is not critically reliant on the assumption that the illumination possesses essentially perfect spatial and temporal coherence.

Two distinct approaches can overcome these difficulties. The first approach extends the conventional coherent diffractive imaging algorithm to enable diffractive imaging to be achieved using polychromatic diffraction data, and the second approach first extracts a single monochromatic component from polychromatic diffraction data, enabling the conventional coherent diffractive imaging approach to be applied without modification [9]. In fact, our demonstration of coherent diffractive imaging that simultaneously uses multiple wavelengths [6, 9, 7] is the spectral analogue of a recent development in x-ray holographic imaging that uses multiple [48] or complex [49] reference waves. Both methods are well-suited to the low temporal coherence, high spatial coherence optical field produced by an high-harmonic generation source. In particular, the first approach involves a modified Gerchberg-Saxton iterative reconstruction algorithm and a maximum entropy method refinement step that enables high quality diffractive imaging using all of the effectively available harmonic orders from an high-harmonic generation source, and yields at least an order of magnitude improvement in the efficiency of the use of photons in an high-harmonic generation based tabletop x-ray microscope.

The possibility of using non-monochromatic sources will evidently extend the applicability of coherent diffractive imaging experiments to better enable the exploitation of high-harmonic generation sources for diffractive imaging. In general, the approach of coherent diffractive imaging based on multiple coherent modes and the associated formalism can be applied equally well to any polychromatic short-wavelength source. The current activity in the development of multimode x-ray free-electron laser sources [1] with high spatial resolution suggests that our approaches may find direct application in proposals to image single molecules with atomic resolution using short pulse coherent diffractive imaging. The relaxation of the requirement that the illuminating source be strictly monochromatic in diffractive imaging technologies may well prove to be valuable in the future design and analysis of materials and biomolecules.

Chapter 2

High-harmonic generation and coherent diffractive imaging

2.1 Introduction

Since the first generation of high-harmonic orders in 1987 [18], (femtosecond) laser-driven high-harmonic generation sources have become an increasingly important supply of coherent extreme-ultraviolet radiation and soft x-rays down to the water window ($\sim$ 4.4 to 2.3 nm) [19, 11] and the keV-regime [20]. Compared to synchrotrons and x-ray free electron lasers, these sources are small-scale and highly versatile, and their resulting unique characteristic output can be tailored according to the experimental requirements. The ultrashort pulses of reasonable brightness and high coherence are used in various experimental works and applications ranging from atomic [50, 51] and molecular [52, 53, 54] spectroscopy, to solid-state [55, 56, 57] and plasma [58, 59, 60] physics. In particular, due to its coherent nature, harmonic emission is increasingly being used for coherent-diffractive imaging based on a single wavelength [33] and even multiple harmonic orders [6].

By their nature, high-harmonic generation sources produce a laser-like beam that consists of multiple longitudinal coherent modes. Harmonic emission ranges from wavelengths in the vacuum-ultraviolet, extreme-ultraviolet to the soft x-ray region, as shown in figure 2.1.1 and nowadays can be routinely generated by means of high-power ultrafast laser systems. In principle, the characteristics of the laser beam are imprinted onto the harmonic beam. Nevertheless, the chosen interaction geometry for the harmonic generation process and the intrinsic process of plasma formation in particular lead to a complex spatially and temporally dependent induced nonlinear polarization in the nonlinear medium and thus strongly determine the conversion efficiency, the spatial, spectral and temporal properties, and the coherence of the harmonic emission. In particular, it has been shown that the large and time-varying refractive index due to the plasma produced when focussing the driver pulse into the nonlinear medium is the major reason why high-harmonic generation experiments only exhibit partial coherence [28]. Therefore, and because of the highly nonlinear nature of high-harmonic generation, each of the harmonic sources that are currently in operation is unique in its experimental setup and the characteristics of the resulting harmonic output.

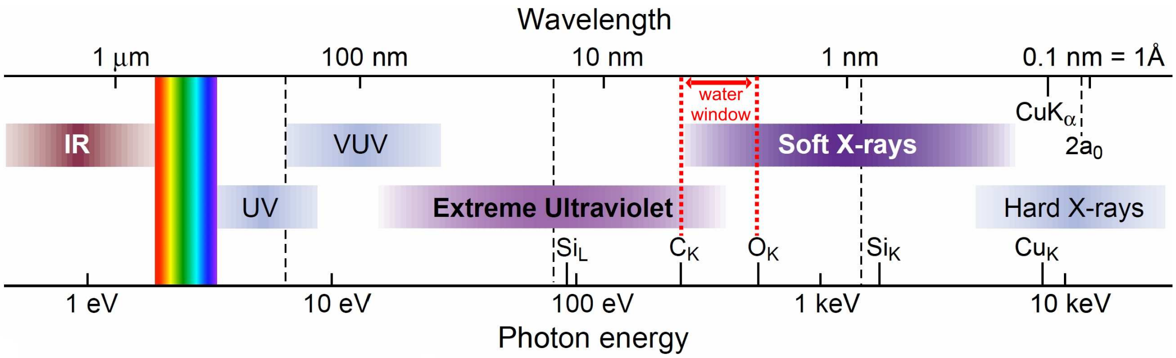

Figure 2.1.1: The electromagnetic spectrum as it extends from the infrared (IR) to the x-ray regions. High-harmonic generation sources cover the range from vacuum-ultraviolet (VUV) to soft x-ray radiation and thus allow one to address the water window (∼ 4.4 to 2.3 nm), which is particularly important for coherent diffractive imaging of biological samples (from [61]).

2.2 Historical background

The first observation of harmonic generation was made in 1961 by P.A. Franken et al. at the University of Michigan [62]. The experimental work was based on employing a ruby laser (pulsed ruby optical maser) that delivered 1 ms pulses of ~ 3 J at 694.3 nm. These pulses were focused inside a crystalline quartz sample. Analyzing the emergent beam by a quartz prism spectrometer revealed frequency up-conversion to the second harmonic order of the fundamental beam at 347.2 nm. For many years only low-order harmonics could be observed by focusing intense laser radiation into nonlinear solid media or pulsed gas jets. Experimental work on harmonic generation sped up considerably in the late 1980s. Rapid technological progress led to high peak-power and ultrashort pulse laser systems; in particular, this refers to the development of titanium:sapphire (Ti:Sa) as a new high-gain optical amplification medium and the technique of chirped-pulse amplification. In combination with the technique of self-mode-locked Ti:Sa laser oscillators this technical progress allowed the development of ultrahigh peak-power and ultrashort pulse amplifiers which are a prerequisite to generating nonlinear processes in the strong field regime. In 1987 McPherson et al. at the University of Illinois in Chicago generated harmonic emission up to the 17th order in neon gas [18]. The source used for irradiation of the target gas was a krypton fluoride laser system radiating at 248 nm and producing pulses of energies up to ~ 20 mJ of duration ~ 350 fs. The intensity in the focal region was estimated to be in the range $\sim 10^{15}$ to 10^{16} W/cm^2. The harmonic output was analyzed by means of a grazing-incidence spectrometer equipped with a gold-coated, spherical, 600 lines/mm-grating blazed at 120 nm and a single-stage microchannel plate with a phosphored fiber-optic anode serving as detector. The highest harmonics produced were the 17th in neon and the 13th in helium. Harmonics up to the 9th order could be produced in xenon and harmonics up to the 5th order in argon and krypton. An excerpt of the milestones of the research on high harmonic generation can be found in [63].

2.3 Principles of high-harmonic generation

2.3.1 Nonlinear optics and laser-matter interactions

High-harmonic generation is a highly nonlinear optical process occurring in the so-called strong field regime. Three highly nonlinear processes can occur in this regime when a nonlinear medium is exposed to an intense electromagnetic field [64]. A necessary requirement to generate these processes is that the electric field is of the order of the Coulomb field binding the outer electron to the nonlinear target medium, that is, focused intensities usually need to be $> 10^{13}$ W/cm^2 and can be achieved by focusing a femtosecond laser beam. However, the necessary focused intensity depends strongly on the desired process and the chosen nonlinear medium, such as a gas of atoms, molecules or clusters, or a solid material.

2.3.1.1 Nonlinear processes in the strong field regime

Above-threshold ionization: electrons that are initially in the ground state can absorb a number of photons whose total energy is larger than required for ionization. Thus, the ejected electrons can have a high kinetic energy. A typical above-threshold ionization spectrum shows a number of peaks separated by the energy of a photon of the driver pulse.

Multiple ionization: after ionization, the electrons can be injected into the vacuum one at a time, that is, in a sequential stripping process, or simultaneously, that is, in a non-sequential stripping process. The first mechanism of multiple ionization can be understood in terms of ionization of the atom, then of the singly-charged ion, then of the doubly-charged ion, and so on. A considerable amount of effort has been and is still being devoted to the second stripping process of multiple ionization which is less well understood. In particular, the proposal of electron scattering from a parent ion leading to the ejection of a second electron is a widely accepted idea that might explain the non-sequential stripping process.

High-harmonic generation: frequency up-conversion can occur when electrons produced by ionization are accelerated in the electric field of the laser beam and recombine with parent ions. This can lead to the emission of coherent radiation with frequencies that are multiple integers of the frequency of the driving laser field. In an atomic gas only odd orders are expected to be observed due to inversion symmetry. Nevertheless, recent experiments have shown symmetry breaking under particular experimental conditions. A typical high-harmonic generation spectrum shows the following characteristic behaviour: a fast decrease in intensity for the first few harmonic orders, followed by a long plateau of harmonics with approximately constant intensity, and finally a sharp cut-off. Note that the characteristics of an experimental high-harmonic generation power spectrum depend strongly on the characteristics of the pump pulse.

2.3.2 The ‘Simple Man’s Theory’ or the ‘Three-Step-Model’

An accurate description of high-harmonic generation involves the integration of the time-dependent Schrödinger equation in order to calculate the single-atom response, and incorporation of propagation effects. However, the so-called ‘Simple Man’s Theory’ or the ‘Three-Step-Model’ can provide many qualitative insights into the physical understanding of the interaction between atoms and strong laser fields and accurately predicts the general features of high-harmonic generation. Both classical [65, 66] and quantum [67, 68] calculations have confirmed this model.

2.3.2.1 Historical background

The theoretical problem of describing nonlinear phenomena occurring in the strong field regime involves solving the time-dependent Schrödinger equation that describes the interaction of a many-electron nonlinear medium with an electromagnetic field. Theoreticians have concentrated on solving the problem of a hydrogen atom, or more generally, a single-active electron atom in a strong laser field. Currently considerable effort is being invested to extend and to go beyond the single-active electron atom approximation. Kulander et al. pioneered the numerical solution of the time-dependent Schrödinger equation in the early 1990s [69, 70, 71]. In the mid-1990s, the semi-classical strong field approximation was developed by Lewenstein and coworkers [67]. The time-dependent Schrödinger equation and strong field approximation (see section A.1) are both highly successful models providing deep insights into the physics underlying the nonlinear processes that occur in the strong field regime and allowing detailed predictions of the output of these processes. Realistic modeling has to take into account both the calculation of the single-atom response and the solution of propagation equations in the generating nonlinear medium for the emitted radiation. Nevertheless, it is the so-called 'Simple Man's Theory' or 'Three-Step-Model' that provides many qualitative insights in the physical understanding of the interaction between atoms and strong laser fields. The 'Three-Step-Model' was first proposed in 1987 by Van Linden van den Heuvell and Muller [72] in the context of above-threshold ionization. Later, this model was extended by Corkum and others to understand multiple ionization and high-harmonic generation. A milestone in the understanding of high-harmonic generation was the work of Kulander et al. and coworkers in 1992 [66, 65]: the cutoff of the high-harmonic generation spectrum is given by the sum of the ionization potential of the nonlinear medium and x times the ponderomotive potential, where x is a constant factor. This result was interpreted in terms of the 'Simple Man's Theory' and led to the formulation of the semi-classical strong-field approximation developed by Lewenstein and others [67].

2.3.2.2 The 'Three-step model'

For driver pulses much longer than the period of the carrier frequency, high-harmonic generation can be understood and described by the so-called semi-classical picture or the 'Three-step model'. The quasi-classical or semi-classical approach was pioneered by Kulander et al. and Corkum [66, 65], and is based on the so-called quasi-static model [73]. The quasi-static model, or the 'Two-step model', itself consists of two steps. First, the ionization probability or rate $W \propto exp(-1/E)$ as a function of the laser electric field E is calculated using tunneling-ionization models [74]. The tunnel ionization models describe the formation of a sequence of electron wavepackets, one near each peak of the laser electric field. Second, classical mechanics is used to consider the trajectory of the electron when it propagates freely in the laser electric field. Thus, the 'Two-step model' is a quasi- or semi-classical picture. The ionization process of the nonlinear medium, and in particular the tunneling ionization and its rate, are described by quantum mechanics. After ionization, the electron wavepacket is described as a free classical particle which is not affected by the Coulomb field of the remaining ionic parent. In order to explain nonlinear phenomena such as multiple ionization, above-threshold ionization and high-harmonic generation, the quasi-static model needs to be extended in order to incorporate interaction processes between the electron injected into the vacuum and the parent ionic complex. There are three possible electron-ion interactions [65]. First, inelastic scattering: depending on the energy of the ejected electron, collisional ionization can occur and lead to the correlated ejection of two electrons. Thus, due to the highly intense laser field, inelastic scattering can lead to excited states, which will contribute to the experimental results. Second, elastic scattering: elastic scattering of an electron leads to dephasing from its harmonic motion in the laser electric field and therefore to absorption of energy from the electric field. Third, radiative relaxation: the interaction between an electron and the parent ion can lead to the emission of electromagnetic radiation. If the ground state is negligibly depleted, then the electron will pass the ionic parent in the same way during each laser cycle to a good approximation. Thus, any electromagnetic radiation is emitted at a harmonic of the laser frequency. In fact, the nonlinear medium is not instantly separated into an ionic complex and a free electron particle after illumination with a highly-intense laser driver pulse, giving rise to the term quasi-plasma. There is a significant probability that the electron is in the close vicinity of the parent quasi-ion for several optical periods.

The quasi-classical, semi-classical or the so-called ‘Three-step model’ allows high-harmonic generation to be described quantitatively and to be understood qualitatively to a certain extent. In fact, this model allows the main characteristics of high-harmonic generation to be explained. Quantum-mechanical models [67, 68] extend this model and provide corrections in both the qualitative and quantitative description. In the first step, the electric field of a high-power ultrashort laser pulse perturbs the Coulomb barrier binding the outer electron to the nonlinear medium. The electric field can be so strong that the Coulomb barrier is suppressed and the electron can undergo tunneling through the Coulomb barrier, which is described in the quantum-mechanical picture. This is the reason for the term semi- or quasi-classical. Second, after the tunneling process, the trajectory of the electron is described on the basis of a free particle in the laser electric field. The electron exhibits harmonic motion in the laser electric field and gains momentum. In the third step, when the electric field changes its sign, the electron traverses its trajectory and can return and interact with the ionic parent. If recombination occurs, the emission of a photon with higher energy than the incident photon can occur. The polarization of the laser electric field is a crucial parameter. Only if the laser electric field is linearly polarized can the electron return to the ionic parent. For elliptic polarization there are no classical electron trajectories. However, for a slightly elliptical field, high-harmonic generation is not suppressed, but rather significantly reduced, that is, due to the finite extent of the electronic wave packet and quantum diffusion effects [67, 75]. The probability for the electron to stay near the nonlinear medium for several optical periods without recombination cannot be neglected. In fact, rescattering and recollision processes [76] play a crucial role in shaping the spectrum of high-harmonic generation.

To estimate the maximum harmonic order that can be generated by an intense laser beam, the intensity at which the laser field becomes comparable to the Coulomb field of an atomic nonlinear medium needs to be estimated. The barrier suppression ionization model [77, 78] predicts that the electron may freely escape under the assumption that ionization occurs when the combination of the Coulomb potential $U_{Coulomb}$ and the potential of the laser field U_{laser} corresponds to the ionization potential I_p of the atom. Hereafter, effects such as quantum tunneling, diffusion and quantum wave packet reflections are neglected [67, 75]. The following calculation is based on the assumption that the nonlinear medium is an atomic species.

$$U_{combined}(r) = U_{Coulomb} + U_{laser} = -\frac{e^2}{4\pi\epsilon_0 r} - erE_{laser}, \tag{2.3.1}$$

where e is the electron charge, ϵ_0 is the dielectric constant, E_{laser} is the amplitude of the laser electric field and r is the radial coordinate of the electron with respect to the centre of the atom. Calculation of $dU_{combined}/dr = 0$ leads to

$$|r_{extremum}| = \sqrt{\frac{e}{(4\pi\epsilon_0 E_{laser})}}, \tag{2.3.2}$$

which, when substituting r with $r_{extremum}$ in equation (2.3.1), under the assumption of $U_{combined} = I_p$ allows the determination of the amplitude of the laser electric field required to ionize the nonlinear medium

$$E_{laser} = \frac{(\pi\epsilon_0 I_p)^2}{e^3}. \tag{2.3.3}$$

The associated intensity of the time-averaged harmonic laser electric field is

$$I_{laser} = \frac{\epsilon_0 c E_{laser}^2}{2} = \frac{\pi^2\epsilon_0^3 c I_p^4}{2e^6}. \tag{2.3.4}$$

Thus, only the ionization energy of the chosen nonlinear medium determines the required intensity of the fundamental laser beam. The ionization energy of common noble gases in their neutral and ionic state is given in table 2.1. Figure 2.3.1 shows the required intensity of the laser electric field versus the ionization potential of the

Element	$I_{p,1}$	$I_{p,2}$	$I_{p,3}$	$I_{p,4}$	$I_{p,5}$	$I_{p,6}$
He	24.6	54.4				
Ne	21.6	41.0	63.4	97.1	126.2	157.9
Ar	15.8	27.6	40.7	59.8	75.0	91.0
Kr	14.0	24.4	37.0	52.5	64.7	78.5
Xe	12.0	21.2	32.1	47.6	59.0	72.0

Table 2.1: Ionization energies $I_{p,q}$ in eV of the noble gases. The subscript q refers to the order of the ionization process.

nonlinear medium according to equation (2.3.4). It has to be noted that the barrier suppression ionization model [77, 78] appears to be insufficient to adequately describe the intensity at which ionization occurs when the generating medium is exposed to few-cycle laser pulses [79, 11, 80, 81]. In that case the nonlinear medium can survive to higher laser intensities before being ionized and thus is able to emit harmonics of higher brightness and higher order.

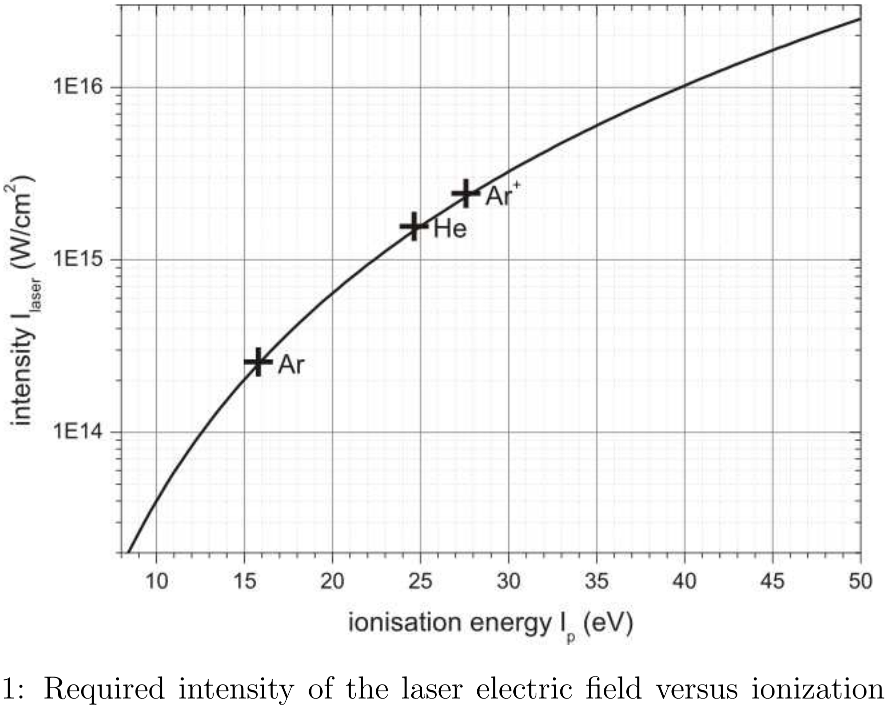

Figure 2.3.1: Required intensity of the laser electric field versus ionization energy of the nonlinear medium according to the barrier suppression ionization model.

Kulander et al. and Corkum suggested that the harmonic cut-off is given by [66, 65, 67]

$$E_{cut-off} = I_p + 3.17U_{pond}, \tag{2.3.5}$$

where I_p is the ionization potential of the generating medium and $U_{pond} \propto I\lambda^2$ is the ponderomotive potential which scales linearly with the laser field intensity I and quadratically with the wavelength of the fundamental laser beam. The ponderomotive potential is the mean kinetic energy of an electron oscillating in a harmonic laser electric field. As a free particle in the laser electric field, the electron experiences the force

$$F = m_e\ddot{x} = -eE_0cos(\omega_0t + \varphi), \tag{2.3.6}$$

where m_e is the electron mass, x is the location of the electron with respect to the centre of the atom, e is the electron charge, ω_0 is the frequency of the driving laser field and t and φ are the time and the phase when the electron is injected into the vacuum. Here $t = 0$ is the time when the electron leaves the atom. Integration of equation (2.3.6) leads to

$$\dot{x} = -\frac{eE_0}{m_e}\left(sin\left(\omega_0t + \varphi\right) - sin\left(\varphi\right)\right). \tag{2.3.7}$$

Assuming there is no net drift to the motion of the electron, that is, $\varphi = 0$, the mean kinetic energy is given by

$$U_p = \frac{m_e\langle\dot{x}^2\rangle}{2} = \frac{e^2I}{2\omega^2m_e\epsilon_0c}. \tag{2.3.8}$$

The maximum kinetic energy that the electron can accumulate in the laser electric field is the sum of the ionization energy I_p of the nonlinear generating medium and a term that is proportional to the laser intensity I. This implies that harmonic photons of high energy can routinely be generated by means of high peak-power ultrashort pulse laser systems. For example, if $I \approx 1.67 \times 10^{14}$ W/cm^2 and the wavelength of the driving laser pulse is 800 nm, then $U_p \approx 10$ eV. Thus the ponderomotive potential is of the same order of magnitude as the ionization energies of the neutral noble gases. If the laser intensity is one order of magnitude larger, then $U_p \approx 100$ eV, and a further order of magnitude results in $U_p \approx 1000$ eV. The generation of these high-energy photons requires one to enter the regime of high-field optical science via high peak-power ultrashort laser pulses. Nowadays pulses with a peak power $> 10^{12}$ W can be delivered routinely from a table-top laser and pulse amplification systems, and pulses with a peak power $> 10^{15}$ W from even larger systems. By focusing these pulses, light intensities of $> 10^{20}$ W/cm^2 can be achieved. However, the brightness of the harmonic radiation and in particular the cutoff energy are determined by a complex interplay of several mechanisms and are not determined by the laser electric field intensity alone. Integration of equation (2.3.7) allows one to determine the trajectory of the electron in the laser electric field. The recombination time is the time after the electron recombines with the ionic medium, that is, the time when the electron wavepacket returns to the origin of location. This is determined by the following transcendental equation

$$\cos(\omega_0 t + \varphi) - \cos(\varphi) = -\omega_0 t \sin(\varphi) \, . \tag{2.3.9}$$

The maximum kinetic energy of the electron in the laser electric field is given by

$$E_{max} = \frac{m_e \langle \dot{x} \rangle^2}{2} = 2 V_{pond} \left(\sin(\omega t + \varphi) - \sin(\varphi) \right)^2 . \tag{2.3.10}$$

The electron acquires the maximum kinetic energy when it is released at a phase $\varphi \approx 17°$. The scaling factor $2(sin(\omega t + \varphi) - \sin(\varphi))^2$ versus the phase φ at the time of release is shown in figure 2.3.2. The maximum photon energy after recombination with the ionic parent medium to the former ground state is therefore given by [66, 65, 67]

$$E_{cutoff} = I_p + E_{kin,max} \approx I_p + 3.17 U_p . \tag{2.3.11}$$

Based on equation (2.3.11), the maximum or cutoff harmonic order that can be achieved is given by

$$q_{max} = \frac{I_p + 3.17 U_p}{\hbar \omega_0} , \tag{2.3.12}$$

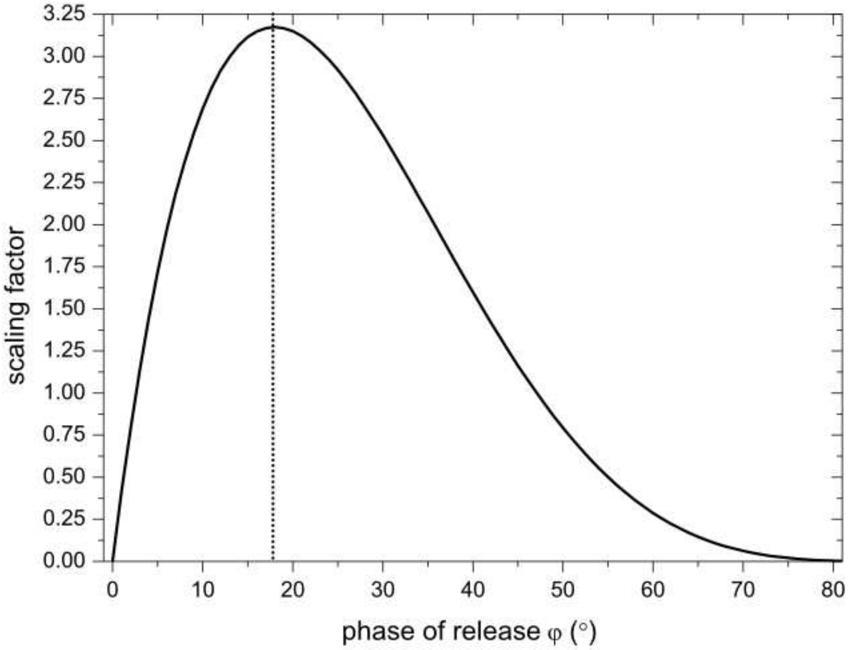

Figure 2.3.2: Scaling factor of the kinetic energy of the electron as a function of the phase of the laser electric field at the time of release based on equation (2.3.10).

where $\hbar = h/(2\pi)$ is Planck's constant. However, different values for the scaling factor of the ponderomotive potential have been reported: based on [82] the scaling factor is calculated to be 3, while propagation effects for very high laser intensities can possibly lead to a scaling factor of ~ 2 [83], and the harmonic spectrum can be extended to $I_p + 8U_p$ when phase-locked high-order-harmonic and sub-100-as pulses are generated from stretched molecules [84]. Based on equation (2.3.12) the maximum order that can be generated in the noble gases in their neutral and ionic state is displayed in table 2.2. Here the maximum harmonic order is determined by the ionization potential I_p and the laser intensity at which the noble gases and their ions ionize. The wavelength of the driving laser pulse is assumed to be 800 nm and effects such as quantum tunneling and quantum wave packet reflections are neglected [67, 75]. It is the ionization potential that determines the upper limit of the intensity at which the nonlinear medium ionizes. Note that the equation for the cutoff energy depends on the assumption that the laser intensity is a constant. This assumption does not hold when dealing with ultrashort pulses. Since the laser intensity can change during a single period the cutoff energy

element	$q_{max,1}$	$q_{max,2}$
He	199	4311
Ne	119	1369
Ar	39	297
Kr	27	185
Xe	17	111

Table 2.2: Maximum harmonic orders based on the laser intensity at which noble gases in their atomic and ionic state are ionized. The subscripts 1 and 2 refer to the associated first and second ionization energy according to table 2.1.

rule might not be applicable any longer. Indeed, higher harmonics than expected could be observed in many experiments dealing with few-cycle laser pulses. It is interesting to note that the noble gases (e.g., helium) that produce very high-order harmonics generate less bright radiation than the gases that are ionized at lower intensities due to a smaller cross-section and associated nonlinear susceptibility; that is, in atoms of large diameter the electron wavepacket is less tightly bound to the Coulomb potential and thus undergoes a smaller spread before returning and recombining with the parent ion compared to the tightly bound electron wavepacket of smaller atoms.

2.4 Characteristics of high-harmonic radiation

2.4.1 Generation of coherent extreme-ultraviolet radiation

The generation of coherent vacuum- or extreme-ultraviolet radiation is hampered due to unavailability of optical resonators such as the ones used for lasers. This is due to the finite lifetime of the gain medium, the low reflectivity of available optics and possible damage to any optical element in the optical path due to the radiation itself. In particular, the higher the frequency of the generated harmonic radiation, the higher the possibility that it ionizes any kind of material. Short-wavelength sources such as synchrotrons, free-electron and x-ray lasers only offer partially coherent radiation.

Spatial coherence of incoherent light sources such as an undulator can be achieved by means of pinhole filtering but this involves a high loss of the created radiation.

2.4.2 Coherence and phase

The underlying physical process of high-harmonic generation is regarded as fully coherent and deterministic. Thus, high-harmonic generation is expected to create fully spatially coherent radiation in the vacuum- and extreme-ultraviolet and soft x-ray region. However, experimental work has demonstrated that the generated radiation is only partially coherent and does not reflect the full coherence of the driving laser pulse [28].

2.4.2.1 Coherence degradation mechanisms

Several coherence degradation mechanisms have been identified that spoil the mapping of the characteristics of the fundamental beam onto the high-harmonic beam [28]: first, the large and time-varying refractive index associated with the intrinsic generation of a (quasi-) plasma has been identified as the major reason why high-harmonic generation experiments only exhibit partial coherence. Second, harmonic emission at any particular wavelength can result from multiple electron trajectories. These trajectories are characterized by injection of the electron into the vacuum at different phases. Thus a complex and spatially varying multimode wavefront of the harmonic radiation can be created and can be the reason why the harmonic beam lacks the characteristics of the fundamental laser beam. Third, ionization of the nonlinear medium occurs twice during an optical cycle of the laser electric field. Thus, for each particular harmonic order two separate electron trajectories generate the same photon energy. However, these electron trajectories involve slightly different ionization and recollision times. Fourth, in many-cycle driver pulses many optical cycles can contribute to the signal of a particular harmonic order, and thus potentially lead to a degradation of the coherence properties. Spatial coherence can easily be measured by means of Fresnel bi-mirror interferometry, and a double-pinhole or a double-slit experiment [63]. The correlation between the phase of the radiation emerging from both sources determines the visibility of the interference fringes observed. If the phase difference is constant and deterministic, and thus correlated, the visibily will be unity, whereas any coherence degradation or variation in the phase difference will result in a visibility smaller than unity.

2.4.2.2 Phase-locked harmonic emission

Time-dependent single-atom response calculations reveal that harmonics are in general not locked in phase [85]. In fact the phase difference between adjacent harmonics appears to be completely random in the plateau region and the Fourier components of the atomic dipole moment are not locked in phase. In this context phase-locked does not mean that the harmonic components exhibit the same phase but that the phase difference between two consecutive harmonic orders is constant. Nevertheless, the time-dependent single-atom emission consists of a train of ultrashort pulses with two dominant pulses and several smaller pulses all of different amplitude per laser half-cycle. The two main pulses (with different amplitude) correspond to two dominant electron wavepacket trajectories that essentially determine the atomic dipole moment. The probability amplitudes for these two emission processes are actually comparable and interfere very efficiently, leading to apparently random phases as mentioned previously.

2.4.2.3 Dynamical phase and frequency shifts

The dynamical phase $\theta(t_q)$ is obtained from the wavelet transform of the induced dipole (or dipole acceleration), corresponding to each instant (t_q) of electron-ion core recollision [86]

$$d_\omega(t_q) = |d_\omega(t_q)|e^{-iS(t_q)}, \tag{2.4.1}$$

where $S(t_q) = \omega t_q + \theta(t_q)$. The dynamical phases of the cutoff harmonics exhibit a time profile that mimics the laser pulse shape. For harmonics below the cutoff the phase of the long trajectories exhibits a stronger intensity dependence than that of the short trajectories. For intermediate or plateau harmonics both short and long returning electronic wave packets show a sensitive dependence on laser intensity with the long trajectory still showing a stronger intensity dependence. The instantaneous frequency $\omega(t)$ is given by $dS(t)/dt = \omega + d\theta(t)/dt$ [86]. A blue shift is given by $d\omega(t)/dt > 0$ and corresponds to the rising part of the driver pulse. A red shift is given by $d\omega(t)/dt < 0$ and corresponds to the falling part of the driver pulse. The overall frequency chirp depends on the relative contributions of the rising and falling part of the laser pulse. For low to intermediate laser intensities, the two contributions cancel and there is no net frequency shift. For intense laser pulses, when the atom is ionized before the peak intensity is reached, the rising part of the pulse dominates the process and a net blue shift can be observed.

2.4.3 Spectral characteristics

In general, the high-harmonic generation power spectrum exhibits a typical behaviour [70]. The intensity of the first few harmonic orders drops by several orders of magnitude. The power spectrum then levels off into a harmonic plateau where the intensity of adjacent harmonics varies only slightly, by a factor of ~ 2. Finally, the power spectrum drops sharply in intensity over the last few orders and thus virtually comes to an end. The power spectrum depends strongly on whether the high-harmonic generation is produced by excitation pulses consisting of a few optical cycles or many optical cycles [79, 11, 80, 81]. Characteristics, such as conversion efficiency, spectral resolution and noise, spectral cutoff, observation of even and odd orders, and observation of harmonic sub-bands representing attosecond pulses, are all related to the length of the pump pulses with respect to the length of the carrier frequency.

2.4.3.1 Explanation of the typical spectral shape

The recollision model of Kulander et al. and Corkum et al. is a quasi- or semi-classical picture [66, 65, 67]. The ionization process and in particular the tunneling ionization and its rate are described in a quantum-mechanical picture [74]. After ionization the electron wavepacket is described as a free classical particle which is not affected by the Coulomb field of the remaining ionic parent. Extension of this recollision picture by quantum-mechanical effects [67, 75] allows us to explain the main features of a typical high-harmonic generation spectrum by means of bremsstrahlung with an appropriate cutoff [76]. Quantum interference between different parts of the same electron wavepacket (e.g., the part entering and the part leaving the Coulomb field of the parent ion) leads to very high order harmonics and is the reason for significant differences between the classical and quantum results. When recolliding or rescattering of the free electron with the parent ion occurs, the electron wavepacket emits broadband bremsstrahlung with no harmonic sub-structure at all. The harmonic orders only emerge from this broadband radiation through the interference in time of the emission associated with different optical cycles of the laser pulse. The spectrum is given as the Fourier transform of the bremsstrahlung radiation. For odd harmonics there are maxima in the intensity which are proportional to the squared-number of encounters, $(2N/2)^2$, multiplied by the squared-magnitude of the Fourier amplitude of the bremsstrahlung acceleration. However, for even harmonics, the intensity of the output is linear with the number of encounters, $2N/2$, multiplied by the squared-magnitude of the Fourier amplitude of the bremsstrahlung acceleration. The higher the number of encounters, or the longer the temporal width of the pump pulse with respect to the temporal width of the carrier frequency, the better resolved the high-harmonic generation spectrum. This is related to what is believed to be the so-called fundamental trade-off: the use of very short driving pulses increases the conversion efficiency, but results in a broader spectrum for the individual harmonic peaks. Note that an electron wavepacket can be modeled in such a way that it is an ensemble of individual classical electron trajectories. The results have to be averaged. Then, this approach allows us to explain wavepacket spreading, but does not allow quantum interference which is an important feature in explaining the higher harmonics in a typical high-harmonic generation spectrum. However, if quantum interference is included, then a fast amplitude decay of the electron wavepacket can be observed due to wavepacket spreading. This leads to a bremsstrahlung supercontinuum with an envelope comparable to the envelope of a typical high-harmonic generation spectrum. If the wavepacket spreads further, subtle beginnings of a high-harmonic generation spectrum are observed. Nevertheless, the more the wavepacket spreads the more complex the spectral structure becomes. But only when these fast frequency components (due to interference) of the dipole acceleration are included can the typical shape of a high-harmonic generation spectrum be seen. Wavepacket interference leads to a complex spatial structure and thus after Fourier transformation to high frequencies or oscillations of the dipole acceleration. This is the reason for the increased spectral weight around the harmonic cutoff.

2.4.3.2 Many-cycle and few-cycle pump pulses

For many-cycle driver pulses, that is, pump pulses that are much longer than the period of the carrier frequency ($\gtrapprox$ 25 fs corresponding to $\gtrapprox$ 8 optical cycles at 800 nm), the harmonic power spectrum is dominated by the periodic motion of the electron in the laser electric field and exhibits the following characteristic shape: the intensity of the first few harmonics drops quickly, levels off into a harmonic plateau with slowly decreasing intensity and is followed by a sharp cutoff. All harmonics show a discrete structure and are thus well separated and resolved. The established harmonic cutoff rule is in excellent agreement with experiments. Its validity results from the fact that the amplitude of the pump pulse does not change significantly during the generation of each of the individual harmonics. Thus the intensity of the driver pulse that determines the ponderomotive potential is well-known. The existence of the harmonic plateau is in contradiction with perturbation theory, which suggests that the strength of the qth harmonic order should scale as the input field to the qth power. The plateau occurs because each harmonic order depends on both the previous and next order. Thus, all harmonic orders are virtually coupled to each other and are finally coupled back to the fundamental order which represents the frequency of the fundamental laser beam. The plateau of harmonic orders decreases in intensity by typically a factor of 2 or less between each order whilst perturbation theory predicts a decrease of several hundred times between each consecutive order.

For many-cycle driver pulses ($\gtrapprox$ 25 fs for a centre wavelength of 800 nm) the spectrum is well-resolved. Harmonic peaks in the spectrum are well-separated and there is a sharp cutoff according to the cutoff rule. However, for few-cycle driver pulses ($\lessapprox$ 25 fs for a centre wavelength of 800 nm) the spectral characteristics of high-harmonic generation change as follows [79, 11, 80, 81]: for $\sim$ 25 fs driving pulses the electron motion in the laser field is mainly periodic, but has aperiodic contributions. The harmonic peaks in the power spectrum are still separated, but broadening and inter-peak noise is expected. Also, there is no sharp cutoff of the spectrum any more as in the case of a 100 fs driving pulse. For driver pulses of duration between 10 and 20 fs the electron motion in the laser field becomes strongly aperiodic. Smearing of the discrete nature of the single harmonic orders is observed and becomes stronger with increasing order. This effect can be attributed to the broad bandwidth of the driving pulse which is mixed by the nonlinear atomic response. Moreover there are regions in the spectrum that are separated by sharp drops. The dipole response in the time domain explains this feature as these sub-bands are generated during different cycles of the laser pulse. Thus, few-cycle pulses ensure good correspondence between the time and frequency history of the harmonic spectrum. For $\sim$ 5 fs driving pulses the effects mentioned for the case of the 10 fs pump pulses become more pronounced. In fact, fewer sub-bands can be observed in the spectral domain and the last sub-band that corresponds to the highest orders generated in the high-harmonic generation process hardly displays any spectral separation of the smeared-out harmonic orders. This implies that these harmonics are generated during very few re-encounters of the electron with the parent ion. As in the case of the 10 fs pump pulse correspondence between the frequency and temporal domain can be observed but which is far more exact than in the previous case. Note that in the so-called single-cycle regime ($\lessapprox$ 5 fs) non-adiabatic effects cause the atomic response to lag behind the pump field. Thus, ionization is suppressed and the generation of even higher harmonic orders can be observed.

The established cutoff rule is given by $E_{cutoff} = I_p + 3.17U_p$ [66, 65, 67] and has been confirmed in many experiments using driving pulses longer than 100 fs. For pulses shorter than 100 fs, the cutoff rule no longer applies as the amplitude of the pump pulse changes significantly during the generation of each individual harmonic. Thus, the intensity of the driver pulse that determines the ponderomotive potential is not precisely known. In fact, when the pump pulse consists of a few optical cycles [79, 11, 80, 81] and the intensity of the laser beam is such that it corresponds to the threshold between the tunneling and the multiphoton ionization regime, $U_p \approx I_p/2$, the atomic dipole response no longer responds instantaneously to the exciting field, but shows a nonadiabatically delayed response and thus reduces the ionization rate. The cutoff rule is only valid when the instantaneous intensity at which the harmonics are generated is known. In that case the cutoff rule can be understood as a rough estimate for the width of the harmonic plateau.

2.4.4 Time frequency characteristics

The Keldysh parameter is defined as

$$\gamma = \sqrt{I_p/(2U_p)}, \tag{2.4.2}$$

where I_p is the ionization potential of the nonlinear medium and U_p is the ponderomotive potential that the freed electron experiences in the laser electric field [86].
Weak field: $\gamma > \sqrt{2}$ corresponding to $I_p > U_p$. For lowest-order harmonics the

multiphoton mechanism dominates the low-energy regime and the time profile (at a given frequency) is smooth and continuous.

Intermediate field: $\gamma = \sqrt{2}$ corresponding to $I_p = U_p$. For low-order to intermediate harmonics the time profiles develop extended structures which may be attributed to the near resonant effect of the excited states (particularly the $2p$ state).

Strong field: $\gamma < \sqrt{2}$ corresponding to $I_p < U_p$. For intermediate to high-order harmonics well above the ionization threshold fast burst time profiles develop which can be attributed to the tunneling mechanism and the time-frequency profile shows a net-like structure. For each burst the electron emits a continuous frequency profile which is clear evidence of the existence of the bremsstrahlung radiation emitted by each recollision of the electron wave packet with the parent ion.

In the limit of the tunneling regime of cutoff harmonics, two bursts per optical cycle are observed which occur at the return time of maximum kinetic energy electrons (emitted at a phase of 17 degrees, see figure 2.3.2 and equation (2.3.10)). The agreement of the full (ab initio) quantum-mechanical and quasi-classical models in the tunneling limit is rather striking. Below the cut-off there exist two trajectories for the electron according to the semi-classical model and stationary phase analysis of the dipole acceleration. The first or short trajectory exists at $17 - \alpha$ degrees and the second or long trajectory at $17 + \alpha$ degrees. In this case the burst shows a sub-structure that reflects these trajectories.

2.4.5 Harmonic conversion efficiency

Three requirements need to be turned into reality in order to achieve high brightness of the harmonic emission: first, the phases of the fundamental beam and the desired harmonic order need to be matched, or the phase-mismatch needs to be minimized. This can be achieved using established phase-matching or quasi-phase-matching techniques. Second, a short pulse with a short rise time is needed. In the special case of few-cycle driver pulses, the nonlinear medium can survive to higher laser intensities before being ionized and thus is able to emit harmonics of higher brightness and higher order. Third, a nonlinear medium of large effective susceptibility needs to be chosen for high power output of the harmonic emission. Usually heavier noble gas atoms, such as argon, are used as their cross-section and nonlinear susceptibility is large compared to light noble gas atoms, such as helium.

2.4.5.1 Adiabatic phase contribution and the coherence length

For long driver pulses the adiabatic approximation holds in which it is assumed that the free electron density does not change significantly during one optical cycle [87]. Under this assumption the harmonic phase grows linearly with propagation distance [22, 88]. Once the electron has tunneled out of the generating target, its evolution between the time of birth τ_b and recombination τ_r is determined by the quasi-classical action according to Lewenstein's quasi-classical model [83, 67, 67]. The phase of the Nth harmonic can be obtained from a Fourier transformation of the atomic dipole moment [87]

$$\Phi_N = S(\tau_b(\xi) - \tau_r(\xi)) - N\omega_0\tau_r(\xi), \tag{2.4.3}$$

where ξ is a parameter characterizing the propagation distance. Note that the primary change in phase is given by varying recombination times τ_r. Due to free electrons the laser field experiences a blue shift of its frequency. The associated phase shift grows linearly with propagation distance

$$\Phi_l(\xi) = \omega_p^2(\tau)\xi/(2c\omega_0), \tag{2.4.4}$$

where the plasma frequency is $\omega_p^2 = 4\pi n(\tau)e^2/m$ and n is the time-dependent electronic density. In a frame that propagates with the harmonic wave, this phase change shifts the recombination time

$$\tau_r(\xi_2) = \tau_r(\xi_1) + \Phi_l(\Delta\xi)/\omega_0, \tag{2.4.5}$$

where the propagation distance is given by $\Delta\xi = \xi_2 - \xi_1$. Therefore a shift of τ_r is associated with a change of the phase of the Nth harmonic. The adiabatic assumption is given by $\Delta n = n(\tau_r) - n(\tau_b) \approx 0$. Thus, the times of birth and recombination are shifted by the same amount with increasing propagation distance and the laser field experienced by the electron remains unchanged. Therefore, the quasi-classical action remains unchanged. As a consequence, the resulting phase change is given by $N\Phi_l$. The coherence or de-phasing length translates into

$$l_c = \frac{2\pi c\omega_0}{N\omega_p^2(\tau)} = \frac{mc\omega_0}{N2n(\tau)e^2} \propto \frac{1}{Nn(\tau)}. \tag{2.4.6}$$

In the adiabatic regime oscillations of the harmonic yield on the de-phasing length-scale are therefore observed.

2.4.5.2 Phase of the laser-induced atomic polarization

Theoretical studies of the laser-induced phase of the atomic dipole moment suggest a universal piecewise-quasi-linear dependence on the laser intensity [88]. The phase develops according to the quasi-classical action when the electron wavepacket develops in the laser field. With regard to harmonic orders in the cutoff region, for electrons with maximum kinetic energy there is only one relevant trajectory. For harmonics in the plateau region, contributions of two relevant trajectories (corresponding to short and long return times) have to be taken into account. The value of the phase is also influenced by quantum effects such as tunneling, diffusion and interference. The phase itself plays a crucial role in the conversion efficiency and the coherence properties of the harmonic radiation generated in the nonlinear medium. For low-intensity driven harmonics the phase is a linear function of intensity that has the slope $-3.2U_p$, where U_p is the ponderomotive potential. In this region the intensity of the induced dipole increases steeply but smoothly. For harmonics in the plateau region, the phase is a linear function of intensity that has the slope $-5.8U_p$. The harmonic dipole response shows a complex, almost oscillatory behaviour that increases slowly with intensity. This finally leads to quantum interference. The atomic dipole response or dipole moment is a sum of contributions from complex trajectories of the electron. Only particular trajectories of the electron wavepacket contribute significantly. The phase is related to the action of the electron along the dominant trajectory. The quasi-classical action is the time integral over the sum of the kinetic energy and the ionization potential. The electronic wavepacket picks up the phase $exp(-i \cdot \text{quasiclassical action})$ (see [88]) while traversing in the electromagnetic laser field. The Fourier components of the induced atomic dipoles are given as sums of contributions of the relevant electron trajectories. With regard to the cutoff one trajectory has to be considered and with regard to the plateau two trajectories have to be taken into account. If the laser focus is in front of the nonlinear medium, on-axis phase-matching can be achieved and the spatial and spectral profile of the harmonics generated are regular and Gaussian shape. If the laser is focused after the nonlinear medium, off-axis phase-matching can be achieved and on-axis phase-matching can be prevented resulting in an annular harmonic spatial profile. Nevertheless, the harmonic efficiency is larger than in the first case. These results are based on the following assumptions: the laser driver pulse is Gaussian in space and square in the temporal domain, and the nonlinear medium is a truncated Lorentzian in space with a full-width at half-maximum of 0.8 mm.

2.4.6 The aperture effect

When truncating a Gaussian laser beam, several factors can affect the harmonic yield [89]: the transmitted energy and focussed intensity, the ionization rates and therefore the refractive index of the plasma, the amplitude and phase of the generated harmonics, the focal and interaction volume in both the longitudinal and transverse direction, the Gouy phase shift gradient, diffraction of the laser beam, and modifications of the Strehl ratio. Aperturing the laser beam yields the same qualitative behaviour for plateau harmonics regardless of the particular harmonic order or the chosen generating nonlinear medium [89]. First, a sharp rise for a narrow diaphragm, which can be explained by the fact that the focussed intensity scales as the fourth power of the diameter of the iris for small apertures. Second, a peak, and third, a slow fall up to the full diaphragm diameter. The fall can be understood in terms of a decreased focal volume both transversely and longitudinally which can be seen when using a diffraction integral. Note that the Strehl ratio is the ratio of the focussed intensity of an aberrated (experimental) laser beam and a perfectly diffraction limited (theoretical) laser beam. To determine the Strehl ratio, a Shack-Hartmann wavefront sensor [89] can be used to measure the wavefront of the laser beam. The measured far field data are used as initial conditions in a numerical beam propagation software. Numerical studies reveal that the harmonics are generated earlier in the pulse when the diaphragm is opened but with variable harmonic yields. This effect can be explained by considering the coherence length and the harmonic dipole. For large diaphragms, the harmonic flux peaks early on the rising edge of the pulse envelope. This is due to a higher level of ionization which spoils phase matching and depletes the neutral medium. The time profile shows multiple short ripples that appear when the cell length corresponds to an odd number of the rapidly decreasing coherence length. When going from lighter to heavier elements the first phase matching regime is replaced by the second regime (see section 2.5). In heavy gases the optimum diaphragm diameter is larger corresponding to high intensities for which there is a balance between electronic and atomic dispersion. The atomic dispersion is small for light gases. Therefore the optimum diameter is smaller.

2.4.7 Femtosecond laser-driven high-harmonic generation

Experimentally it turned out that few-cycle excitation pulses are beneficial for high-harmonic generation compared to many-cycle pump pulses [79, 11, 80, 81]. Atoms can survive higher laser intensities before being ionized and thus are able to emit harmonics of higher brightness and higher order. Therefore the barrier suppression model appears to be insufficient to adequately describe the intensity at which ionization occurs when the generating medium is exposed to ultrashort laser pulses. Numerical investigation of the dependence of the level of ionization on the pulse duration for pulses of fixed peak intensities by integrating the time-dependent Schrödinger equation in one dimension supports this assumption. Even in the tunneling regime neutral atoms are able to experience higher ponderomotive potentials under ultrashort-pulse illumination than is possible using longer excitation pulses.

In the case of a 5 fs driving pulse the high-harmonic generation spectrum consists of several smeared sub-bands. These sub-bands correspond to sub-femtosecond pulses in the temporal domain and can experimentally be achieved by employing spectral filters such as metal foils or broadband x-ray mirrors. Theoretically it can be demonstrated that the phase relationship between different harmonics or harmonic sub-bands is not strongly perturbed despite the significant atomic ionization. Therefore, the harmonic field generated during each re-encounter only weakly depends on the history of the interaction (e.g., previous re-encounters). Thus, a single re-encounter regime is not a requirement for attosecond pulses as widely thought several years before. When the pump pulse consists of a few optical cycles, and the Keldysh parameter is close to unity (the threshold between the tunneling and the multiphoton ionization regime), the atomic dipole response no longer responds instantaneously to the exciting field, but shows a nonadiabatically delayed response and thus reduces the ionization rate. The ionization rate saturates at higher values of the electric field. Thus, harmonic emission with higher harmonic order is expected compared to many-cycle pump pulses. For shorter driver pulses a redistribution of energy between the different harmonic orders within the harmonic power spectrum can be observed, where lower harmonics are weaker and higher harmonics are stronger in intensity. There is believed to be the so-called fundamental trade-off; the use of very short driving pulses increases the conversion efficiency, but results in a broader spectrum for the individual harmonic peaks. However, the technique of intra-atom phase-matching by means of pulse-shaping appears to alleviate this fundamental tradeoff by providing single harmonic peaks (e.g., the 27th in argon gas) of reasonable width (0.24 eV which corresponds to 0.81 % of the harmonic energy).

2.5 Phase-matching

In the following, a brief description of phase-matching is presented. Quasi-phase-matching is explained in section A.3. A comprehensive description of phase-matching and quasi-phase-matching can be found in the literature, such as [61, 63].

For coherent buildup of harmonic radiation, the laser-induced nonlinear polarization wavefront (which is in phase with the laser wavefront) and the harmonic wavefront need to propagate in phase. Nevertheless, the speed of the incident and the harmonic waves depend on the index of refraction and thus depend on the wavelength. The propagated distance over which the polarization and the harmonic wavefronts slip out of phase by π, the so-called coherence length

$$L_{coh} = \pi/\Delta k \tag{2.5.1}$$

(where Δk is the phase-mismatch in the propagation vectors), can be significantly shorter than the Rayleigh parameter of the focused laser beam. Therefore the coherence length is

$$L_{coh} = \frac{\lambda_0}{2q\left(n\left(\lambda_0\right) - n\left(\lambda_0/q\right)\right)}, \tag{2.5.2}$$

where λ_0 is the wavelength of the fundamental radiation and n is the wavelength-dependent refractive index of the generating medium. After traveling a distance of one coherence length, the fundamental driving laser pulse and the generated harmonic radiation of a particular harmonic order q are out of phase. Since L_{coh} scales linearly with $1/q$, phase matching becomes more difficult with increasing harmonic order q. This means that higher-order harmonics go in and out of phase with the fundamental radiation more often than lower-order harmonics. Note that the high-harmonic generation process is limited to the coherence length L_{coh} and not to the laser confocal parameter $2z_R$ in the case of $2z_R > L_{coh}$. Two phase-matching regimes exist [89]: in the first regime phase matching is achieved early in the driver pulse. The atomic dispersion counterbalances the Gouy phase shift dispersion. This regime applies to lighter elements, such as helium. In the second regime, phase-matching is achieved when the electronic dispersion counterbalances the atomic dispersion. When going from lighter to heavier elements, such as argon, the first phase-matching regime is replaced by the second regime.

2.5.1 Phase-mismatches

The phase-mismatch is a separate issue from the reabsorption of harmonic emission from the generating medium. Reabsorption [23, 21, 25] plays a role when the harmonic radiation is already phase-matched. Nevertheless, the harmonic yield is limited by several phase-mismatch phenomena, such as different diffraction rates for the driving and generated radiation, the dependence of the refractive index on the wavelength of the fundamental and harmonic radiation, and the dependence of the intrinsic phase of the harmonic emission on the intensity in both the radial and longitudinal direction.

2.5.1.1 Plasma phase-mismatch

When generating harmonic radiation at intensities that are high enough to ionize the generating medium, refraction due to the plasma has to be taken into account as it can severely limit the coherence length and thus the harmonic yield. The index of refraction of a plasma is given by

$$n_p(\omega) = \sqrt{1 - \left(\frac{\omega_p}{\omega}\right)^2} \approx 1 - \frac{1}{2}\left(\frac{\omega_p}{\omega}\right)^2 \tag{2.5.3}$$

and is usually much smaller than 1. The plasma frequency is given by

$$\omega_p = e\sqrt{\frac{N_e}{\epsilon_0 m_e}}, \tag{2.5.4}$$

where ϵ_0 is the electric constant, m_e the electron mass and N_e the density of the free electrons. Substituting n in equation (2.5.2) with n_p from equation (2.5.3) results in

$$L_{coh,p} = \frac{4\pi^2 m_e}{N_e e^2 \lambda_0 \mu_0 \left(q - 1/q\right)}, \tag{2.5.5}$$

where $\mu_0 = 1/(c^2\epsilon_0)$ is the magnetic constant. Equation (2.5.5) implies that the coherence length decreases with increasing electron density. Assuming a linear dependence between the density of the nonlinear generating medium and the electron density suggests that increasing the gas pressure does not necessarily lead to higher brightness of the harmonic yield [90, 24, 23]. In particular the higher-order harmonics are affected as $L_{coh,p} \propto 1/q$ and a higher intensity of the driving laser field is required, thus increasing the ionization rate.

2.5.1.2 Geometrical phase-mismatch

Geometrical phase mismatch is primarily due to the Gouy phase shift when focusing a laser beam as described in detail in [91]. The Gouy phase contributes to the phase evolution of the radiation along the axis of propagation as can be seen when considering a Gaussian principal mode

$$E\left(\rho, z\right) = A_0 \frac{\omega_0}{\omega\left(z\right)} e^{-(\rho/\omega(z))^2} e^{ik\rho^2/(2R(z))} e^{i(kz-\eta(z))}. \tag{2.5.6}$$

The first factor describes the transverse amplitude distribution, the second factor the spherical curvature of the wavefronts and the third factor the phase evolution along the z axis which is collinear with the wavevector of propagation. Here $\omega_0 = \sqrt{\lambda z_R/\pi}$ is half the beam waist with respect to the centre of focus, $\omega\left(z\right) = \omega_0\sqrt{1 + \left(z/z_R\right)^2}$ the beam radius, ρ the transverse coordinate, $k = 2\pi/\lambda$ the amplitude of the wavevector, $R(z) = z\left(1 + (z_R/z)^2\right)$ the radius of curvature of the wavefronts, and $\eta(z) = \tan^{-1}(z/z_R)$ is the Gouy phase. The Rayleigh length z_R is related to the confocal parameter via $b = 2z_R$. The phase for the qth harmonic at each point where it is produced along z is $\varphi_q = q\eta(z)$. Thus the Gouy phase shift for the harmonics as they propagate is negligible. Taking the derivative $d\varphi/dz$ and setting it to π leads to the coherence length associated with the Gouy shift

$$|L_{coh,G}| = \frac{\pi z_R}{q\left(\tan(z/z_R)^{-2} + 1\right)}. \tag{2.5.7}$$

The coherence length becomes longer when evaluated away from the focus. Thus the focus of the driving laser beam can be increased relative to the gas jet to confine the interaction region to a single geometrical coherence length thereby avoiding destructive phase cancelations. Equation (2.5.7) can be approximated to

$$|L_{coh,G}| \approx \frac{\pi}{q}\left(z_R + \left(\frac{z}{z_R}\right)^2\right). \tag{2.5.8}$$

For a typical $f/50$ geometry with 800 nm wavelength, the Rayleigh range is given by $z_R = \pi w_0^2/\lambda \approx 2.5$ mm, where $w_0 = 4/\pi f\lambda/d_p$ and d_p is the diameter of the incident laser beam.

2.5.1.3 Intensity-dependent phase-mismatches

The intensity of the driving laser field varies in the longitudinal and transverse directions. As the dipole phase of the generating medium is intensity-dependent, it also varies in the longitudinal and transverse directions. This can lead to on- and off-axis phase-mismatch and deterioration of the desired spatial harmonic profile and the harmonic yield. Experimental results and theoretical predictions can be found in [22, 92, 93].

2.5.2 Experimental phase-matching

For efficient frequency-conversion in a nonlinear medium the driving and the generated signals must be phase-matched when traveling through the medium. A variety of techniques have been developed that rely on crystalline solids as the generating medium. Phase-matching is usually achieved by combining an anisotropic material and differing source and signal polarizations. Using lanthanum boron oxide and beta barium borate, radiation with wavelengths as short as 200 nm can be generated [94]. Conventional implementation of phase-matching relies on anisotropic materials and is usually achieved by means of nonlinear solids involving crystal-poling techniques, developed in the mid-1990s. Only a few solids provide reasonable transmission in the vacuum-ultraviolet region and virtually no nonlinear solid provides reasonable transmission in the extreme-ultraviolet region (see figure 2.1.1). Therefore, using nonlinear solids for frequency-conversion is limited to wavelengths usually longer than 150 to 200 nm [95]. Gases can offer reasonable transmission in both the vacuum-ultraviolet and extreme-ultraviolet range. Since gases are isotropic, the conventional and established techniques of phase-matching cannot be applied. New methods need to be developed. New phase-matching techniques have already been proposed or even developed. Indeed, recent work such as employment of modulated waveguides demonstrates that the highly nonlinear nature of high-harmonic generation should not be understood as a limitation but as an opportunity that allows the application of new control mechanisms to tailor coherent vacuum-ultraviolet and extreme-ultraviolet radiation that would not be possible in conventional nonlinear optics. The perturbative approach allows calculation of the electric field of a harmonic of order q after having passed the generating medium of length L by means of [95]

$$E_{q,\omega}(L) \approx \int_0^L e_w^q(z) d(z) e^{i\Delta k z} dz, \tag{2.5.9}$$

where ω is the angular frequency of the driver pulse, $d(z)$ is the nonlinear coefficient depending on the position z in the generating medium and $\Delta k = qk_\omega - k_{q,\omega}$ is the phase-mismatch between the pump and the signal radiation. Here k_ω is the k-vector of the driver pulse and $k_{q,\omega}$ is the k-vector of a particular harmonic. Three cases are possible now: first, if $\Delta k \neq 0$ then the rapid oscillating term $e^{ik\Delta z}$ will average $E_{q,\omega}(L)$ to zero. Second, traditional phase-matching aims to achieve a zero phase mismatch between the driver pulse and the harmonic radiation, that is, $\Delta k = 0$. Phase-matching can be achieved to a certain degree by means of a straight waveguide to balance the phase contributions of the material, the laser-induced plasma and the waveguide itself. Phase-matching fails in the case of large ionization but can lead to extended coherence lengths. Third, quasi-phase-matching modulates either the driver electric field or the nonlinear coefficient to suppress harmonic radiation in out-of-phase zones and to initiate harmonic radiation in in-phase zones.

2.5.2.1 Phase-matching in a gas jet

As explained in [22], a local maximum of the harmonic signal can be achieved when the laser is focussed in front of the medium. The harmonic radiation is created on-axis in a regular way corresponding to optimal phase matching, that is, when the total phase of the harmonic, that is, the sum of the Gouy phase and the dipole phase, is varying slowly and regularly. The spatial, spectral and temporal profiles therefore map the characteristics of the laser beam and are of Gaussian shape. Note that the spatial pattern is of “super-Gaussian” shape [22] since its full-width at half-maximum is smaller than the full-width at half-maximum of the driver pulse. When the laser is focused behind the medium, but closer to the medium compared to the first maximum, another local maximum of the harmonic signal can be achieved. The harmonic radiation exhibits a complex spatial pattern. This is due to the rapidly varying phase and amplitude of the dipole in both the longitudinal and transverse directions. Efficient harmonic generation on-axis is prevented, whereas there are particular directions where the harmonic generation is phase-matched in a better way. The spatial pattern is annular and broader than the laser beam. Nevertheless the temporal profile is comparable to the first case(the first maximum, when the laser is focussed in front of the medium), whereas the spectral profile is also Gaussian but much broader than in the first case . Note that when the laser is focused into the medium, the spectral and temporal profiles are no longer Gaussian, but exhibit a complex ring structure that is much broader than when the laser is focussed in front of or behind the medium. These results are based on the following assumptions: the laser driver pulse is Gaussian in space, the laser driver pulse is square in the temporal domain, and the nonlinear medium is a truncated Lorentzian with a full-width at half-maximum of 0.8 mm [22]. High-harmonic generation by focusing a driver pulse into a gas jet is limited due to the small interaction length given by a multiple of the laser confocal parameter. Another severe limitation is the Gouy shift reducing the coherence length: the tighter the focusing, the larger the effect. Usually the conversion efficiency achieved by this technique per harmonic is of the order 10^{-7} (argon). This technique is also disadvantageous with regard to the harmonic beam quality, the degree of coherence and the maximum harmonic achievable (the higher the harmonic, the higher the required intensity, the shorter the coherence length, the smaller the conversion efficiency).

2.5.2.2 Phase-matching in a hollow waveguide

When traveling through a fully ionized gas the phase between the generating pulse and the signal slips by π after $\sim 50\ \mu$m. Matching the phase velocities of the driver pulse and the signal would enhance the harmonic output due to a larger interaction volume. To date most high-harmonic generation experiments have been performed in a free space configuration by tightly focussing a laser beam into the generating medium. Here, the laser focus leads to dominating phase shifts and limits phase-matching considerably. A waveguide circumvents this problem by allowing careful tuning of the phase velocity of the generating pulse and eliminating beam divergence effects. Thus phase-matching is achieved by counterbalancing the dispersion contributions of the plasma and the waveguide with the dispersion contributions of the neutral medium. This technique has been applied successfully to enhance the output of mid-plateau harmonics by a factor of $\sim$ 100 to 1000 [14, 96, 24]. This can be done by adjusting the guide diameter or the gas pressure inside the waveguide. Previous work has proposed the use of a transient waveguide created by a laser-induced plasma for phase-matched frequency conversion using high-order frequency mixing. A waveguide confines the beam by repeated glancing-incidence reflections on the inside walls [97]. Here the phase velocity is extended by an additional, geometric component. The k-vector of light passing a waveguide is given by

$$k \approx \frac{2\pi}{\lambda} + \frac{2\pi N_a \delta(\lambda)}{\lambda} - N_e r_e \lambda - \frac{u_{nm}^2 \lambda}{4\pi a^2}, \tag{2.5.10}$$

where the fist term corresponds to simple vacuum propagation (λ is the wavelength of the driving laser pulse), the second results from dispersion of the gas (N_a is the atom density, δ depends on the dispersive characteristics of the generating medium), the third term results from dispersion of the plasma (N_e is the electron density due to ionization), and the last term corresponds to the waveguide (u_{nm} is a constant corresponding to the propagation mode in the waveguide and a is the diameter of the waveguide). The phase-matching condition

$$\delta k = q k_{laser} - k_{x-ray}, \tag{2.5.11}$$

where q is the harmonic order, can be optimized by adjusting several experimental parameters such as the wavelength of the driving pulse, the gas pressure and the species and the size of the waveguide and its spatial mode. The conversion efficiency is between 10^{-4} and 10^{-6} for harmonic conversion at photon energies in the 20 to 50 eV range, and decreases rapidly at higher photon energies [98]. The following equation is an estimate of the enhancement in efficiency of a particular harmonic due to waveguide phase-matching [99]

$$\eta = 1 + \left(\frac{\Delta k}{\kappa_q}\right)^2, \tag{2.5.12}$$

where Δk is the phase-mismatch between the induced polarization and the generated harmonic radiation due to different refractive indices under the condition that the length of the hollow fibre is much larger than the absorption length of the qth harmonic, that is, when $\kappa_q z \gg 1$. Soft x-ray light hardly interacts with the waveguide. Its phase velocity is thus slightly greater than the speed of light in vacuum. The phase velocity of the driving laser pulse is modified due to material dispersion, plasma dispersion and waveguide dispersion. These contributions are of opposite sign thus allowing the phase velocity to be matched to the phase velocity of a particular harmonic by simply varying the gas pressure. Nevertheless, this technique fails for higher harmonics as the higher intensities lead to significant ionization of the medium and thus to significant creation of plasma. At a particular intensity or harmonic the plasma contributions spoil phase-matching. Note that a tapered waveguide can counterbalance the loss of energy of the driver pulse due to waveguide leakage or ionization of and interaction with the nonlinear medium.

The spatial coherence of the harmonics is directly related to the spatial quality of the laser beam when it travels through the ionized medium. Both phase-matching and spatial coherence are optimized when the laser mode in the waveguide establishes a steady-state mode [100]. This steady-state mode is not a geometric eigenmode of the hollow waveguide. The ionized medium leads to a strong negative lens that has a big impact on the central part of the laser beam and leads to additional phase shifts. Full spatial coherence is achieved when a steady-state mode can be established in the waveguide, depending on its length. This mode enables a flat spatial phase of the harmonic radiation and ensures optimal phase-matching conditions at a fixed pressure. Moreover, a large generating volume around the waveguide axis is ensured and more atoms can contribute to coherent build-up of the harmonics thus leading to higher harmonic output power. A gas jet is faced with the problem of a combination of strong radial dependence of intensity and Gouy phase. This leads to spatially and temporally varying phase matching conditions. The phase front of the harmonics is expected to be complex and erratic. The degree of coherence is expected to be lower and the harmonic output power is smaller.

We now consider the nonlinear propagation dynamics of an ultrashort pulse in a hollow waveguide [101, 102]. Theoretically it can be shown that transverse effects play an important role in the self-focusing dynamics, even for pulse powers below the critical power for self-focusing in free space. The excitation of higher-order modes of the waveguide results in temporal broadening of the pulse and depends on the initial peak power. Novel spatio-temporal dynamics due to self-focusing in a waveguide is expected that does not occur for self-focusing in bulk material. In particular for femtosecond laser pulses space-time focusing and self-steepening [101, 102] play important roles in the spectral and temporal dynamics of the pulse. Steady-state analysis indicates that self-focusing is due to the transfer of radiation energy from the fundamental mode to higher-order modes of the waveguide. When increasing the input power, higher-order modes are excited leading to temporal broadening of the pulse due to group velocity mismatch between the excited modes. This effect becomes more pronounced as the input power approaches the critical power $P_{crit} \approx 1.9\,(\lambda^2/\,(4\pi n_0 n_2))$ for self-focusing in free space, where n_0 is the real part and n_2 the imaginary part of the nonlinear refractive index. For a very weak cw-beam oscillating behaviour of the peak intensity with the propagation distance of the waveguide is observed due to a mismatch between the propagation constants of the fundamental and the next higher order excited mode. For a pulsed many-cycle driver pulse similar behaviour is observed. The group velocity decreases as the order of the mode increases and the pulsed field transferred to the higher modes lags behind the pulse in the fundamental mode and experiences a nonlinear frequency chirp that is not equal to that of the fundamental field. As a result, oscillations in the temporal profile form at the back edge of the pulse. As the pulse is shorted to a few optical cycles, no oscillations occur at the back edge of the pulse any more and oscillations completely cease after a particular distance. Pulse broadening is attributed to the mismatch in the group delay between the fundamental and excited modes provided the pulses are of peak power of the order of the critical power for self-focusing [101, 102]. The resultant spectra are asymmetric, with the red side having more energy but with the blue side having a longer tail. Note that the peak intensity and the temporal profile continually fluctuate, but that the spectrum steadily broadens and shows no sign of fluctuation.

2.6 Coherent diffractive imaging with a high harmonic source

The first experiment on coherent diffractive imaging was performed in 1999 [36], and since then has attracted much research. Nowadays, coherent diffractive imaging is a well-established technique that enables the structure, shape and size of finite, non-periodic objects to be determined from x-ray diffraction intensity measurements [36, 40, 41, 42, 43, 44, 45]. Indeed, resolutions down to 5 nm [43] have been achieved by employing this technique. In particular, coherent x-ray diffractive imaging is the only technique currently available to perform three-dimensional imaging at nanometer resolution of the interior of micrometer-sized particles. In recent years the technique of coherent diffractive imaging has been applied successfully to a range of objects, including both inorganic and biological samples [43, 44, 45] with the only limitation being radiation damage to the sample.

2.6.1 Imaging with extreme-ultraviolet and soft-x-ray radiation

In contrast to coherent diffractive imaging, scanning probe techniques such as atomic force microscopy are limited to surface structures and do not allow the morphological analysis of the interior of a complex object. Electron microscopy allows the resolution of crystalline structures on an atomic scale provided the thickness of the sample is < 500 nm [103], whereas tomography of macromolecular ensembles and inorganics with a thickness of ≥ 500 nm can be performed only at lower resolution. Nevertheless, many biological specimens and samples of interest for materials science are too thick to be analyzed by electron microscopy. Due to advances in imaging and labeling techniques, far-field light microscopy of living cells can be performed with a resolution as low as 200 nm [104]. However, the resolution is ultimately limited by the wavelength of the visible or near-ultraviolet light. Compared to the aforementioned techniques, employing extreme-ultraviolet or soft x-ray radiation from synchrotrons for high-resolution imaging of thick samples has proven to be a promising and successful approach, and imaging in the so-called water-window of micrometer-thick samples and three-dimensional tomography of a cell at a resolution of ~ 60 nm has been achieved [61, 105, 106, 107, 108].

2.6.2 Techniques for imaging in the extreme-ultraviolet and soft-x-ray spectral range

Imaging with extreme-ultraviolet or soft-x-ray radiation is usually performed with diffractive optical elements such as Fresnel zone plates. Spatial resolutions of $\leq$ 15 nm have been achieved with state-of-the-art zone plates [109]. However, high magnifications are characterized by a short working distance and a small depth of the focus, and they potentially exhibit large chromatic aberrations. Furthermore, the efficiency of zones plates for first-order diffracted light is only ~ 10 % [61]. Another technique for imaging in the extreme-ultraviolet or soft x-ray region is holography, such as Gabor holography [110]. Based on radiation from a synchrotron, Fourier transform x-ray holography of gold test objects has been performed and demonstrated with a resolution ≤ 60 nm [111]. However, the employment of holographical techniques for imaging in the extreme-ultraviolet and the soft-x-ray regime is limited by the requirement that the sample to be analyzed needs to be surrounded by a large highly transmissive region [112].

First demonstrated in 1999 [36], coherent diffractive imaging is a new technique for imaging where no optical elements are needed. Instead, the sample is illuminated with coherent radiation and the object is reconstructed from the diffraction pattern by means of computer algorithms. In general, the nature of this lensless imaging technique allows aberration-free imaging, and offers a very large depth of focus. Non-periodic isolated objects can be imaged at a resolution that is only limited, in principle, by the wavelength of the radiation used for illumination and by the largest angle of scattering where diffraction speckles are recorded. In principle, it offers the possibility to achieve diffraction-limited resolution of the reconstructed object. Based on synchrotron radiation, this technique allowed the reconstruction of a cell and its internal components with a resolution $\leq$ 30 nm [35]. The potential of this approach has led to rapid developments, such as the imaging of a nanostructured non-periodic object using a soft-x-ray free-electron laser with a resolution of $\sim$ 60 nm [113] and high-resolution ab initio three-dimensional x-ray diffraction microscopy [114].

2.6.3 Coherent diffractive imaging

In the case that the sample to be analyzed, described by the function $t(\mathbf{r})$, is illuminated with a coherent and plane wave light field, the diffracted image in the far field is the Fourier transform of the sample [115]

$$F(\mathbf{R}) = |F(\mathbf{R})|\, exp\left(i\psi(\mathbf{R})\right) = \tilde{F}\left(t\left(\mathbf{r}\right)\right) = \int_{-\infty}^{\infty} t\left(\mathbf{r}\right) exp\left(2\pi i\mathbf{R}\mathbf{r}\right) d\mathbf{r}. \tag{2.6.1}$$

Here, $\mathbf{r}$ refers to real space and $\mathbf{R}$ to the reciprocal space. As

$$t(\mathbf{r}) = \tilde{F}^{-1}\left(\tilde{F}\left(t\left(\mathbf{r}\right)\right)\right) = \tilde{F}^{-1}\left(|F(\mathbf{R})|\, exp\left(i\psi(\mathbf{R})\right)\right), \tag{2.6.2}$$

the sample, $t(\mathbf{r})$, can be reconstructed from the intensity distribution $|F(\mathbf{R})|^2$ of the diffraction pattern when the phase information $\psi(\mathbf{R})$ is known. Retrieving the phase information from a diffraction pattern is a well-known problem in the field of x-ray crystallography and can be dealt with by the technique of oversampling [116, 117]. In order to do so, the so-called degree of oversampling σ needs to meet the following requirement [118]

$$\sigma = \frac{\mathrm{ROI}_{\mathrm{electron}} + \mathrm{ROI}_{\overline{\mathrm{electron}}}}{\mathrm{ROI}_{\mathrm{electron}}} > 2, \tag{2.6.3}$$

where $\mathrm{ROI}_{\mathrm{electron}}$ is the region of interest of the sample that is characterized by an electron density > 0, and $\mathrm{ROI}_{\overline{\mathrm{electron}}}$ is characterized by an electron density $= 0$, that is, it is the complement of $\mathrm{ROI}_{\mathrm{electron}}$ [117]. In that case, if $\sigma > 2$, the phase can be retrieved from the diffraction pattern by computer algorithms. A comparison of different phase retrieval algorithms is given in [44].

The well-established technique of coherent diffractive imaging is based on Fienup's extensions of the algorithm first proposed by Gerchberg and Saxton [14, 34]. This algorithm propagates a numerical representation of a scalar wavefield between the planes of the object and the detector using instances of the fast-Fourier transformation. The wavefield in these fixed planes is constrained by the application of a priori information, and the iteration between planes is continued until self-consistency is achieved [34]. The reliance on Fourier representations of a single scalar wavefield to carry all of the information about the target system leads to one of the most critical limitations of the Gerchberg-Saxton-Fienup approach: the incident beam that illuminates the object must be fully spatially coherent and quasi-monochromatic [40]. Thus, a typical experimental scheme for coherent diffractive imaging is determined by the three following steps: first, the sample to be analyzed is illuminated by monochromatic, coherent radiation of appropriate wavelength, flux/fluence and dose. The resulting diffraction pattern is recorded for two-dimensional imaging, or a tilt series is recorded for three-dimensional imaging. Second, the phases of the diffraction pattern are recovered by means of appropriate phase-retrieval algorithms. In the Gerchberg-Saxton-Fienup scheme the phases are set randomly at the beginning with regard to the definition of the initial conditions. Third, Fourier-transformation from reciprocal to real space recovers the object from the diffraction pattern. Due to the randomly set phases, noise emerges. A finite support constraint is imposed before transforming back into reciprocal space. The phases generated are then combined with the measured diffraction amplitudes to start the next iteration. Usually after a number of iterations the object emerges from the noise.

2.6.3.1 Experimental scheme and requirements

In order to obtain a high-quality reconstruction from the diffraction pattern of the illuminated object, some experimental parameters, such as the distance between the sample and the detector, the sample size, the quality of the harmonic emission and the nature of the wavefield leaving the sample, need to be considered.

In general, coherent diffractive imaging experiments and successful object recovery depend on certain requirements which can be separated into radiation requirements and phase retrieval requirements. Regarding radiation requirements, coherent diffractive imaging relies on monochromatic and coherent radiation of appropriate wavelength. The coherence length is crucial and needs to be larger than the product of the maximum diffraction angle and the sample width. Flux/fluence (number of photons per unit area and per second) and dose (energy per unit mass) need to meet minimum values required to make a three-dimensional coherent diffractive image at a given resolution. Usually, the performance of a coherent diffractive imaging experiment is limited by radiation damage. Nevertheless, compared to biological samples the radiation tolerance (and thus the resolution) of material-science samples can be relatively high. Regarding phase retrieval requirements, an object support must be given for the object to emerge from the noise when transforming from reciprocal to real space. This can be done by imposing a blank frame around the object to be analyzed before transforming from real to reciprocal space. In particular, the experimental conditions need to be designed such that the following requirements are met. In order to record a far-field diffraction pattern and thus satisfy the Fraunhofer criterion for plane wave illumination, the sample needs to be placed at a sufficiently long distance z from the detector. The lower border of z is determined by

$$z \gg \frac{d^2}{\lambda_c}, \tag{2.6.4}$$

where d is the diameter of the sample and λ_c is the wavelength of the illuminating radiation. The so-called oversampling ratio OR and its value for the lower border is given by

$$OR = \sqrt{\sigma} > \sqrt{2}. \tag{2.6.5}$$

Only in that case can the phase be successfully retrieved from the recorded diffraction pattern [117, 118]. For a successfully reconstructed sample, the size of each pixel within that reconstructed image is determined by [9]

$$r_{recon} = \alpha \frac{z\lambda_c}{pN} =\propto \frac{ORd}{N}, \tag{2.6.6}$$

where p is the size of the pixel and N is the number of pixels of the detector, and $\alpha = 0.94$ (Sparrow criterion) or $\alpha = 1.22$ (Rayleigh criterion). However, the achieved resolution will be larger than the above value. Considering the requirements for the ratio z/d according to equations (2.6.4) and (2.6.5)

$$\frac{z}{d} \gg \sqrt{2}\frac{p}{\lambda_c} \Leftrightarrow OR > \sqrt{(}2), \tag{2.6.7}$$

and taking into account that $r_{recon} \propto z$ for given values of the wavelength of the illuminating radiation, λ, and for the parameters of the detector, p and N, a balance between z and d has to be found. Thus, in order to improve the resolution of the image the distance between the detector and the sample can only be made smaller when simultaneously decreasing the diameter of the sample.

2.6.3.2 Ultrashort-pulse coherent diffractive imaging

Coherent diffractive imaging relies on elastic scattering of the illuminating light with the sample in order to produce the diffraction pattern. However, another dominant photon-matter interaction process is K-shell photoionization. This process is responsible for radiation damage of the sample. Within 10 fs of x-ray absorption K-shell holes decay by emitting Auger electrons with energies between 250 and 500 eV. When photo and Auger electrons escape a sample with increasing charge a growing population of secondary electrons is left behind. The ensemble of secondary electrons is trapped and grows still further by collisional ionization. The trapped electrons quickly relax in energy and form a neutralizing cloud around the positively charged ions. After several tens of femtoseconds a macroscopic motion of the sample takes place and leads to an outward radial motion of the ions, called Coulomb explosion, leading to destruction of the sample. Employing coherent diffractive imaging based on ultrashort pulses can thus minimize damage to the sample by the illuminating radiation. In particular, femtosecond coherent diffractive imaging allows the recording of the diffraction pattern of the object before radiation damage can destroy the sample. Pulsed radiation of an x-ray free-electron laser or a high-harmonic generation source is used that is shorter in duration than the timescale of the damaging process itself. The general concept of femtosecond coherent diffractive imaging of non-periodic samples is to illuminate one particle per pulse and record the diffraction pattern. The particle orientation will be random and thus the individual diffraction pattern will be noisy. In particular, this applies to the largest diffraction angles where the highest-resolution orientation information resides. Moreover, the small scattering cross-sections of single macromolecules require high pulse fluences ($\sim 10^{12}$ photons per $(100\,\mathrm{nm})^2$). General ideas and concepts developed for single-particle reconstructions in cryo-electron microscopy for extracting tomographic information from a large ensemble of randomly oriented noise images can be applied here. The dose can be reduced significantly when orienting the particle in at least one dimension or when forming symmetric nanoclusters.

2.6.4 Multiple-harmonic-order coherent diffractive imaging

By their nature, high-harmonic generation sources produce a laser-like beam consisting of multiple longitudinal coherent modes. However, iterative methods [45] for image reconstruction inherently assume a fully coherent wave field. Thus, a single wavelength needs to be selected, for example, by means of a monochromator or a narrow-bandwidth system of multilayer mirrors. The selection of a segment of the spectrum and inefficiencies of the optical elements involved lead to a significant decrease of the flux of the beam incident on the sample. Despite the use of quasi-phase-matched and absorption-limited harmonic generation, increasing the brightness of harmonic emission still remains one of the major challenges. Thus, such long exposure times may be required that the approach of high-harmonic generation based coherent diffractive imaging is rendered impractical. Therefore, it is desirable to utilize as much of the generated harmonic emission as possible in order to keep the acquisition time short and avoid sample damage or detrimental effects due to possible poor long-term stability of the harmonic source. This can be achieved by employing a multiple-harmonic order beam for illumination of the sample to be analyzed.

Short-time acquisition of high-quality diffraction patterns can be achieved by optimization of the harmonic emission with respect to its spatial and spectral domain considering the absorptive characteristics of the sample. The effective spectral range and the relative weight of the single harmonic orders strongly depend on the focusing geometry and the control over the phase-matching parameters: by appropriate choice of the species of gas and its pressure, the interaction geometry, the position of the laser focus and the intensity and diameter of the laser beam, harmonic emission can be phase-matched and confined to just a few orders [3, 2, 4, 5]. In particular, a high-harmonic generation source that features only a few multiple harmonic orders without any optics in the beam path not only allows multiple-wavelength coherent diffractive imaging with high spatial resolution [6], but also it is a potential source for time-resolved spectroscopy, such as femtosecond photoelectron spectroscopy, in the extreme-ultraviolet and soft x-ray region [10]. When using harmonic emission consisting of a few harmonic orders to illuminate a sample for coherent diffractive imaging, it is desirable that reconstruction methods can be employed that are not critically reliant on the assumption that the harmonic emission possesses essentially perfect spatial and temporal coherence. Therefore, a novel approach has been developed that extends the conventional coherent diffractive imaging algorithm to enable diffractive imaging to be achieved using polychromatic diffraction data. This novel approach is the fundamental experimental method for reconstruction of the sample from coherent diffractive images presented in this work which are in fact an incoherent superposition of the diffraction patterns from each of the multiple harmonic orders in the harmonic emission beam. The experimental procedure, implications and the algorithm are discussed in detail in section 4.3 and in [9, 6, 7].

In general, the approach of multiple-harmonic-order coherent diffractive imaging eliminates the need for an illuminating wavefield that exhibits perfect spatial and temporal coherence and allows the processing of diffraction images that are a superposition of different diffraction images associated with each harmonic order of the multiple-harmonic order high-harmonic generation source. Thus, the possibility of using non-monochromatic sources will extend the applicability of coherent diffractive imaging experiments to better enable the usage of high-harmonic generation sources for diffractive imaging. In general, the formalism involved can be readily adapted to any short-wavelength polychromatic source in which there is a high degree of spatial coherence at each sampled wavelength, but poor temporal coherence across the sampled spectrum. Our novel approach may also, consequentially, be adapted and applied to the multi-mode x-ray free-electron laser sources that are under current development. The current activity in the development of multi-mode x-ray free-electron laser sources with high spatial resolution suggests that this approach may find direct application in proposals to image single molecules with atomic resolution using short pulse coherent diffractive imaging. The relaxation of the requirement that the illuminating source be strictly monochromatic in diffractive imaging may well prove to be valuable in the future design and analysis of materials and biomolecules.

Chapter 3

Experimental setup

3.1 Femtosecond laser system

The high-power femtosecond laser system used for high-harmonic generation and the work presented in this dissertation consists of a $\sim$ 10 nJ/pulse femtosecond titanium:sapphire oscillator that serves as a seed laser for two amplification stages. The first stage amplifies the laser pulses up to an energy of $\sim$ 2.6 mJ per pulse. The second stage is cryogenically cooled and allows achievement of pulse energies up to $\sim$ 6.5 mJ. The laser system is displayed in figure 3.1.1. However, for the experimental work described in this thesis only the first stage amplifier is employed.

3.1.1 Seed laser

High-harmonic generation is of a highly nonlinear nature. Thus, experimental instabilities, particularly when associated with the fundamental laser beam, can result in an unstable and unreliable harmonic output. Therefore, a highly stable seed laser needs to be chosen. A mirror-dispersion-controlled titanium:sapphire (Ti:Sa) oscillator has been chosen as the seed laser (Femtolasers Femtosource Synergy-20).

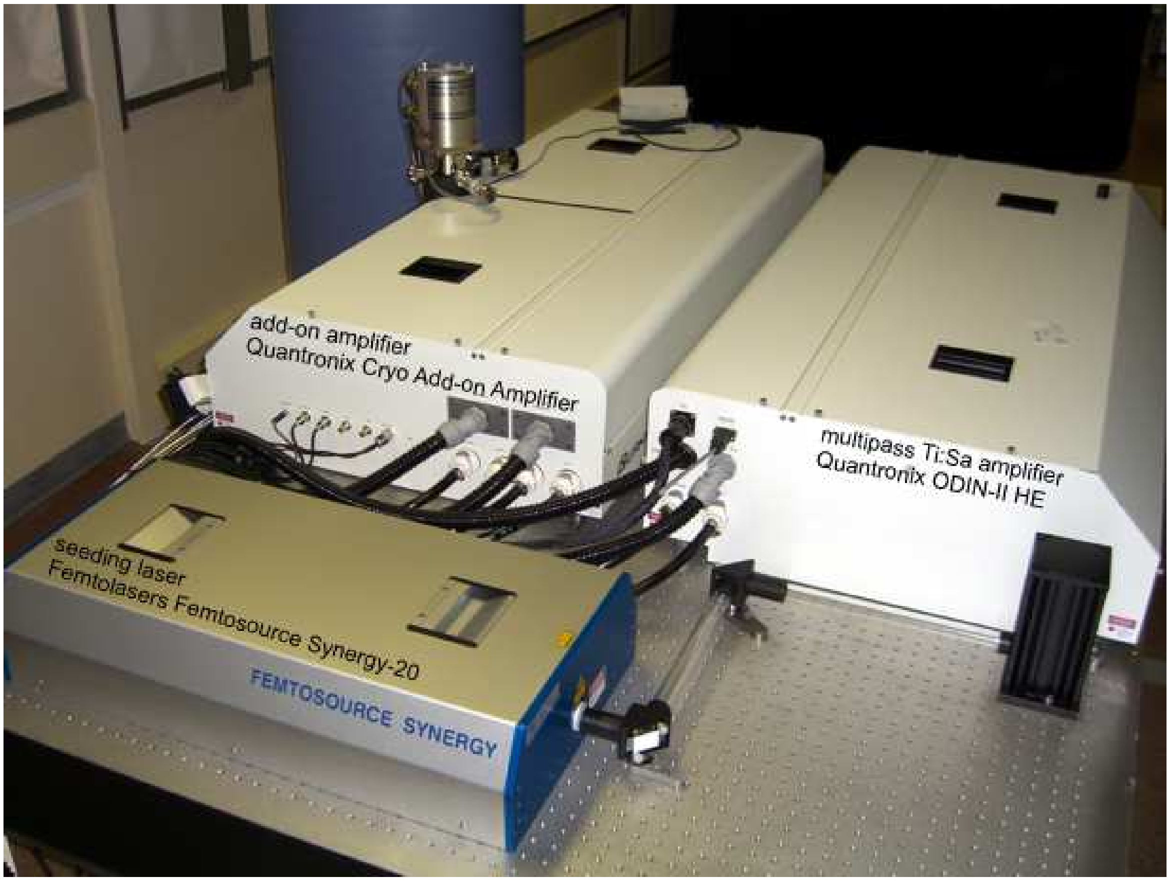

Figure 3.1.1: The high-power femtosecond laser system consisting of a highly stable femtosecond titanium:sapphire oscillator and two amplification stages.

The specifications of the laser output are displayed in table 3.1.

The chosen seed laser system allows the generation of ultrashort optical pulses of high quality, high stability and high repeatability due to a mirror-dispersion-control set. This set consists of chirped-multi-layer dielectric mirrors [119] for broadband intracavity group-delay dispersion in the oscillator over bandwidths as broad as 80 THz and low-dispersion quarter-wave mirrors for coupling the laser beam into the resonator and the mode-locked pulse out of the resonator. The water-cooled Ti:Sa crystal is pumped by a pump laser (Coherent Verdi V-5) that provides a TEM_{00} mode (e^{-2}-diameter of 2 mm) of pump power 3.4 W (up to 5 W) at 532 nm. The output of this laser is vertically polarized (σ-polarization, SP) and needs to be rotated horizontally for the seed laser by means of a periscope. The generation of mode-locked pulses is achieved

pulse duration	< 20 fs
spectral width @ 798 nm	~ 76 nm
output power (average)	~ 630 mW
output energy @ 75 MHz	~ 8.4 nJ

Table 3.1: Specifications of the laser emission from the Femtosource Synergy-20 as measured from the manufacturer after the installation.

by means of self-mode-locking [120], which is usually initiated by a small perturbation of the length of the laser cavity.

3.1.2 Amplification system

The output from the mirror-dispersion-controlled Ti:Sa oscillator has an energy of 8.4 nJ per pulse. These pulses are amplified to an energy of 2.6 mJ by means of a multipass Ti:Sa amplifier system (Quantronix Odin-II HE) through the technique of chirped-pulse amplification [121]. The specifications of the output from the multipass Ti:Sa amplifier system are displayed in table 3.2. For the work presented in this thesis only the output of this multipass Ti:Sa oscillator is used.

centre wavelength	805 nm
pulse energy (maximum)	2.6 mJ
pulse width (FWHM, sech^2)	28 fs
contrast ratio (pre/post pulse)	$> 4000 : 1$
shot-to-shot instability (rms)	1 %
M^2 (x/y)	1.30/1.34
beam size (e^{-2})	12 mm
repetition rate	1 kHz
output polarization	horizontal
beam pointing (x/y)	6.34/13.20 mrad

Table 3.2: Specifications of the laser emission from the ODIN-II HE as measured from the manufacturer after the installation.

The technique of chirped-pulse amplification is based on stretching the short pulse in time by a factor of 10^3 to 10^4, amplification of the pulse, and compression of the pulse. In this laser system the technique of chirped-pulse amplification is realized as follows: first, stretching of the pulse is achieved by multi-pass propagation of the pulse onto a single grating, which exhibits negative dispersion [122, 123]. The stretcher is arranged in an off-Littrow geometry. Second, amplification of the pulse is performed by multiple passes through the gain medium without the use of a cavity. Compared to a regenerative amplifier amplified spontaneous emission can be suppressed to a greater degree as the optical path is not a resonator, and typically a higher gain per pass can be achieved. An eight-pass amplifier is used as the first stage amplifier. A Pockels cell is used to select a single pulse from the oscillator pulse train with a 1 kHz repetition rate after the first 4 passes. An additional two-pass amplifier is used as a power amplifier. Both Ti:Sa amplification stages are pumped by the same pump laser (Quantronix Darwin-527) by dividing energy between the two stages with a beam splitter. The pump laser is a diode-pumped, Q-switched frequency-doubled neodymium:yttrium lithium fluoride laser. Third, compression of the amplified pulse is achieved by a grating pair which exhibits positive dispersion [122, 123]. The compressor is arranged in an off-Littrow geometry.

3.2 Optics and mechanics

Optical and mechanical elements are used to direct the output of the multipass Ti:Sa oscillator or the Cryo Add-on Amplifier to the interaction section of the high-harmonic generation apparatus. These elements are mirrors, apertures and lenses and are described in the following sub-sections. Additionally, a quarter-waveplate is used for experimental work that is only marginally important for the work presented in this thesis. This element is described in section A.7. Furthermore this section discusses in detail the harmonic intensity as a function of ellipticity and the reliability and repeatability of the harmonic emission when employing the quarter-waveplate.

3.2.1 Mirrors

A vertical and an horizontal periscope arrangement are used to direct the laser beam from the output of the multipass Ti:Sa oscillator to the high-harmonic interaction section. All mirrors are driven by micrometer screws to allow the laser beam to overlap with the optical axis of the high-harmonic generation axis. Here, the optical axis is defined as the centre of the interaction geometry in the transverse direction and the centre of the charge-coupled device detector chip. All mirrors have a protected dielectrical silver coating and are of diameter 2 inches. Silver is used because it avoids the small dip in reflectance exhibited by aluminum near 805 nm. In the near ultraviolet, silver has very low reflectance, and aluminum is the prefered choice. However, from the visible to the mid-infrared, silver offers the highest internal reflectance (average > 95 % from 400 nm to 20 μm) available from a metallic coating. Also, silver has a smaller effect than aluminum on the polarization state in these regions of the spectrum and the protected silver coating has shown no broadening effect on a pulse of duration 52 fs [124].

3.2.2 Aperture

The unapertured and unfocused laser beam has a e^{-2}-diameter of 12 mm. A calibrated aperture is applied to the beam, thus allowing it to be radially truncated from 1 to 12 mm with a reliable stepsize of 250 μm. The diameter of the aperture can be > 12 mm, in which case no calibration is possible. This simulates the case of an unapertured laser beam. So, the aperture does not need to be removed when a reference measurement of the unapertured laser beam is needed. The aperture is mounted on a precision x/y-stage so that it can be aligned properly with respect to the centre of the laser beam.

Radially truncating, or aperturing, the laser beam before focusing allows the harmonic yield to be maximized. This is due to a compromise between considerations of the focal geometry and the amount of generated plasma, and the amplitude and phase of the harmonic dipole [89]. The effects of radially truncating the laser beam on the high-harmonic generation process are multiple, coupled and non-trivial. The improvement in harmonic fluence is reported to span up to two orders of magnitude. When focusing a radially truncated laser beam, the three-dimensional field distribution of truncated non-telecentric focusing systems can be very complex and depends strongly on the experimental conditions. Depending on the Fresnel number and the aperture-lens separation, focal shifts and asymmetric field distributions around the focus may have to be taken into account [125, 126, 127, 128]. For our experimental parameters, these effects are usually small and can be neglected (see figures 5.1.1 and 5.1.2).

3.2.3 Lens

After the laser beam passes the aperture of variable diameter, it propagates through a lens and is focussed into the high-harmonic interaction geometry. For the experimental work presented in this thesis two fused silica 1-inch-diameter lenses of focal lengths 400 and 500 mm are mainly used. The lens is mounted on precision $x/y/z$-stages that can be driven manually as well as by means of a precision stepper motor that is computer-controlled as explained in sections A.6.1 and A.6.2. The lens is carefully aligned in an iterative process. The x- and y-stage are used to carefully centre the lens with respect to the centre of the fundamental laser beam. The reflections from the front and back surface of the lens and their propagation back to the laser system are used as an indicator of proper alignment. Alignment of the x- and y-stage and scanning the range of the z-stage also ensure that the z-stage is installed in such a way that the harmonic emission does not move away or only negligible moves away from the centre of the charge-coupled device detector chip.

The need for focusing is due to the high intensities needed for high-harmonic generation. Nowadays table-top laser systems can provide ultrashort laser pulses of peak intensity $\sim 10^{12}$ W/cm^2. Larger systems can even provide pulses of peak intensity $\sim 10^{15}$ W/cm^2. However, in order to address the strong field regime and study highly nonlinear phenomena such as above-threshold ionization, multiple ionization and, in particular, high-harmonic generation, the intensity of the laser pulses needs to be of order 10^{13} to 10^{15} W/cm^2 or larger when employing noble gases as the nonlinear medium. Therefore, focusing of these pulses is a necessary prerequisite to achieve light intensities larger than 10^{13} W/cm^2. Focusing an ultrashort laser pulse delivered from a table-top laser system can be performed by means of a lens or a curved mirror.

It has to be taken into account that focusing of a broadband laser pulse reshapes the pulse and introduces spatio-temporal distortions. In particular, depending on the pulse parameters and the focusing geometry, significant lengthening of the pulse can occur and lead to decreased peak pulse power. As high-harmonic generation is very sensitive to the spatio-temporal characteristics of the pump pulse, it is necessary to consider spatio-temporal effects and ensure that the pulse remains short at the focus. Chromatic aberrations of the fundamental laser beam as it passes the lens are considered in section A.2. More precise calculations of the focal volume can be achieved when taking into account truncation of the laser beam that is Gaussian in its spatial domain [129]. Furthermore, the three-dimensional field distribution of truncated non-telecentric focusing systems can be very complex and depends strongly on the experimental conditions. Depending on the Fresnel number and the aperture-lens separation, focal shifts and asymmetric field distributions around the focus may have to be taken into account [125, 126, 127, 128]. Also, propagation effects in the nonlinear medium, such as self-focusing and filamentation [130, 131], need to be taken into account. However, for our experimental parameters, these effects are usually small and can be neglected as 63 GW$< P < P_{crit}$, where P is the laser power and $P_{crit} \approx 100$ GW is the critical power for argon gas at a pressure of 15 Torr [132]. Thus, the mechanism dominating high-intensity pulse propagation in our experiment is ionization-induced defocusing and plasma dispersion.

3.3 High-harmonic generation apparatus

The output of the high-power femtosecond laser system is directed to the high-harmonic generation vacuum apparatus. The generation of harmonic emission takes place in the high-harmonic interaction section. The harmonic beam then propagates into the next section where spatial and spectral filters can be inserted - the harmonic beam tailoring section. Experimental work, such as coherent diffractive imaging, is performed in the experiment chamber. The high-harmonic generation apparatus is completed by appropriate detection and characterization hardware. The high-harmonic generation apparatus is displayed schematically in figure 3.3.1 and shown in figure 3.3.2. As one of the main parts of the work presented in this dissertation was the design, manufacturing, assembly and continuous improvement of the high-harmonic generation apparatus, elements of this apparatus of particular interest are shown in figure 3.3.3. All of these elements are made in-house.

3.3.1 High-harmonic interaction section

The high-harmonic interaction section is the first part of the high-harmonic generation apparatus. It consists of a highly flexible sub-section that is compatible with the most important interaction geometries. Here, the harmonic process is initiated. Two further sub-sections act as differential pumping stages. The high-harmonic interaction section is displayed schematically in figure 3.3.1 and shown in figure 3.3.2.

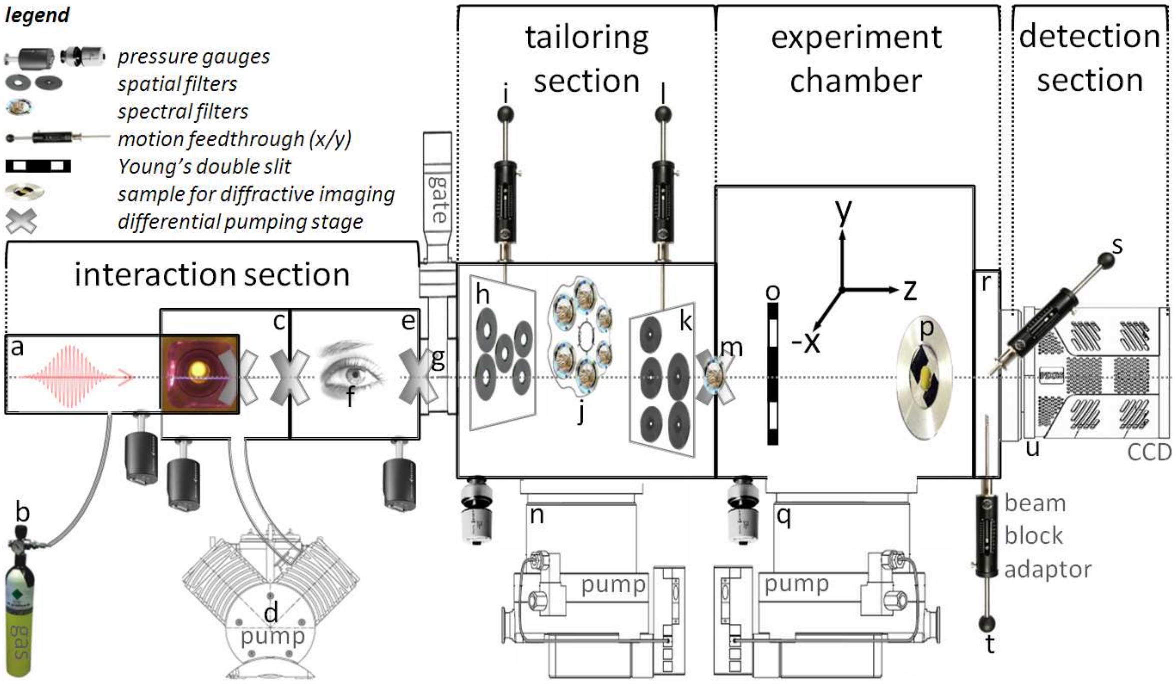

Figure 3.3.1: Scheme of the high-harmonic generation apparatus.

3.3.1.1 Semi-infinite gas cell

The semi-infinite gas cell is shown schematically as item a) in figure 3.3.1. It is defined by the entry point for the laser pulses, an ~ 2 mm thick fused silica glass window, and the exit point for out-coupling of the harmonic emission, an ~ 1 mm thick aluminium foil with a ~ 100 μm-diameter pinhole. Depending on the chosen focal length of the focusing lens, the semi-infinite gas cell is usually of order ~ 10 cm; in particular its length is 43 cm (26 cm) for the lens of focal length 50 cm (40 cm). The end-part of the semi-infinite gas cell, with the laser focus placed in the exit plane of the gas cell, is shown in picture b) of figure 3.3.3. The term semi-infinite is based on the fact that the length of the gas cell is much larger than the effective interaction length between the laser electric field and the nonlinear medium, which is usually < 1 cm in the experimental work in this dissertation. It is noted that different definitions of the term semi-infinite gas cell exist, such as that in the semi-infinite geometry, in which the gas occupies the region from the focusing lens to a thin exit foil near the laser focus [133]. The gas cell is continuously supplied with gas from a gas reservoir, marked

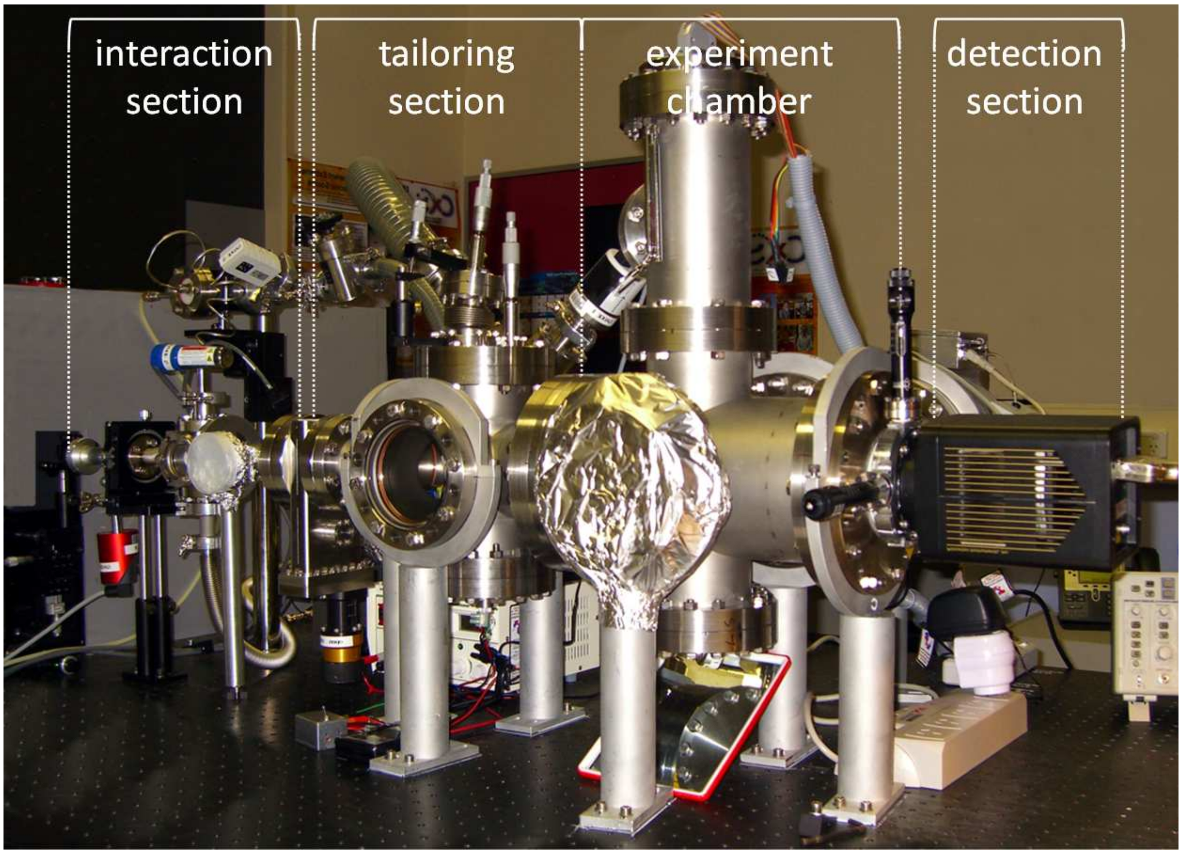

Figure 3.3.2: Photo of the high-harmonic generation apparatus.

as item b) in figure 3.3.1. The pressure inside the gas cell is precisely controlled by means of a combination of a mass flow controller (McMillan Mass Flow Controller Model 80D) and micrometer-screw-handled pressure valves. The pressure is monitored with pressure gauges.

In general, interaction geometries that allow the realization of high density and a long interaction length of the nonlinear medium aim to produce a high fluence of harmonic emission where either a guiding material or a self-guided beam is employed to avoid self-defocusing of the driver laser beams [134, 135, 14, 23, 24, 21]. In particular, the semi-infinite gas cell geometry allows the production of brighter harmonics than do sub-centimeter cells [133]. Two more important advantages of using a semi-infinite gas cell geometry are of a technical nature. The gas jet (see picture a) of figure A.4.1)

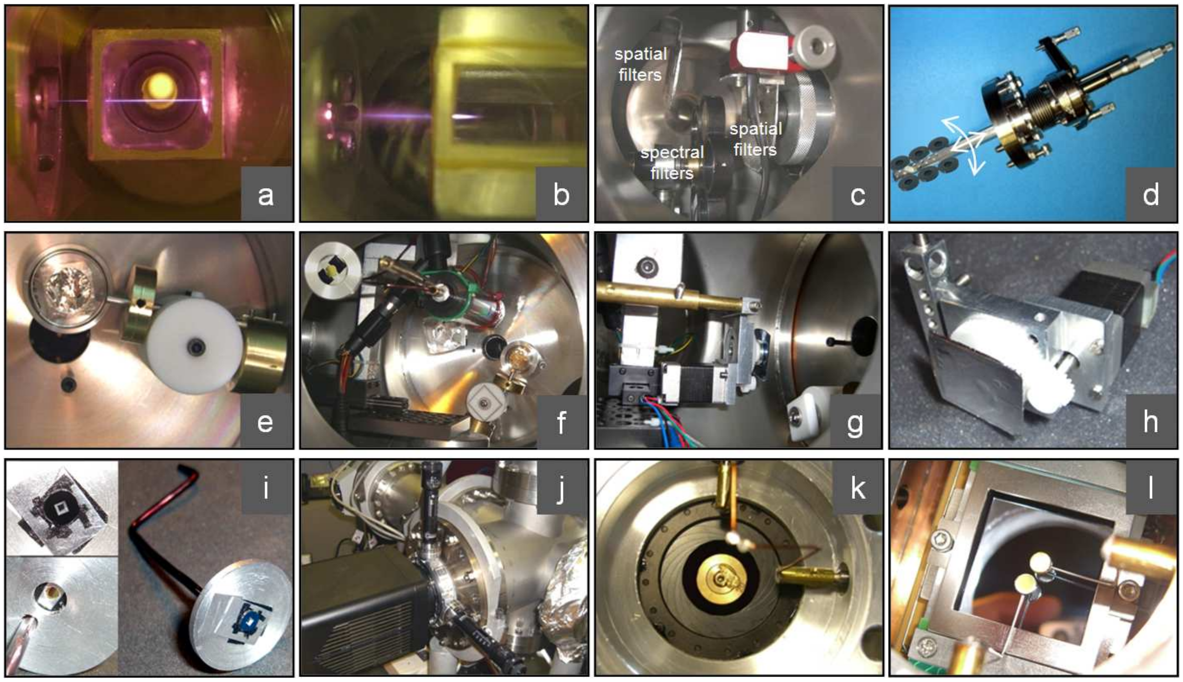

Figure 3.3.3: Photos of elements of the high-harmonic generation apparatus that are of particular interest: a) infinite and b) semi-infinite gas cell, c) spatial and spectral filters and d) the wobble stick of the tailoring section, e) spectral filter, f) to g) mounts for the h) silicon wafer with the Young double-slits and i) the sample for coherent diffractive imaging of the experiment section, j) detection section, k) sample holder and sample for coherent diffractive imaging with the beam blocks in the foreground, l) beam blocks in front of the charge-coupled device camera.

or the finite gas cell design (as shown in picture a) of figure 3.3.3) will lead to twice the gas ballast (gas leaving the gas cell through the entry and exit pinholes) compared to the semi-infinite gas cell. Also, a greater stability is achieved when the laser beam can freely propagate through the nonlinear medium instead of being confined between an entry and an exit gas nozzle. However, when opting for such a long interaction geometry, the pulse likely undergoes nonlinear effects such as self-focusing as well as wave-front distortions from ionizing electrons. These may influence the phase matching conditions, especially over an extended propagation distance as in the semi-infinite cell configuration. Therefore, the phase mismatches induced by the neutral atoms [134, 135], free electrons, and geometrical dispersions [14, 23] have to be taken into account. Defocusing effects can lead to severe distortions of the harmonic emission in the spatial domain [136]. Furthermore, distortions in the spectral domain, such as frequency shifts and spectral broadening can occur [137, 138, 139]. Finally, when the interaction length between the laser electric field and the nonlinear medium becomes comparable to the absorption length of the medium, it becomes important to consider absorption due to the neutral medium [23].

It is noted that the high-harmonic interaction section is employed in different experimental work to host alternative geometries, such as a gas get, a finite gas cell, or even a guided-beam geometry, as shown in figure A.4.1 and explained in section A.4. In particular, in section A.4.2 a new kind of modulated waveguide for corrugation-induced, first-order quasi-phase-matching is presented.

3.3.1.2 Differential pumping stages

The exit pinhole of the gas cell allows out-coupling of the harmonic emission. The harmonic emission propagates through several differential pumping stages that allow the high-pressure gas cell (up to > 1 atm) to be isolated from the experiment chamber (10^{-6} to 10^{-5} mbar). The immediate space around the exit of the gas cell is the first differential pumping stage as denoted by part c) in figure 3.3.1. It is pumped by a piston pump (part d), Pfeiffer Vacuum XtraDry 150-2) at a pressure between 10^{-2} and 10^{-1} mbar. This differential pumping stage (part e)) is separated from the second stage by a ~ 500 μm-diameter pinhole. This stage is connected to the tailoring section by a vacuum gate (part g)). This gate allows the interaction section to be isolated from the rest of the high-harmonic generation apparatus. If needed, work at atmospheric pressure can be performed in either the interaction section or the other parts of the high-harmonic generation apparatus without disturbing the part that is still under vacuum. When this gate is open, the second stage is pumped by a turbo-molecular drag pump (part n), Pfeiffer Vacuum TMU 262) at a pressure between 10^{-3} and 10^{-2} mbar. The pressure of each differential stage is monitored by pressure gauges. The second differential pumping stage allows a protected silver mirror to be inserted into the beam path in order to out-couple the fundamental laser beam via a viewport for further spatial and spectral analysis, as indicated as part f). The protected silver mirror can be moved in and out of the beam path via a mechanical system that is magnetically coupled to the outside of the high-harmonic generation apparatus.

3.3.2 Harmonic beam tailoring section

The harmonic beam tailoring section follows after the high-harmonic interaction section. Here, the harmonic emission is tailored by means of spatial or spectral filtering. The harmonic beam tailoring section is schematically displayed in figure 3.3.1 and shown in figure 3.3.2. The inside of this section is shown in picture c) of figure 3.3.3. The harmonic beam tailoring section and the experiment section are separated from the interaction section by a vacuum gate, marked as part f) in figure 3.3.1. This gate allows the interaction section to be isolated from the rest of the high-harmonic generation apparatus or vice versa. If needed, work at atmospheric pressure can be performed in either the interaction section or the other parts of the high-harmonic generation apparatus without disturbing the part that is still in operation under vacuum conditions. The harmonic beam tailoring section is pumped by a turbo-molecular drag pump (part n), Pfeiffer Vacuum TMU 262) at a pressure between 10^{-4} and 10^{-3} mbar, which is monitored by a pressure gauge.

3.3.2.1 Spectral filters

The harmonic beam copropagates with the fundamental laser beam through the differential pumping stages of the interaction section. In order to isolate the harmonic emission, the fundamental laser beam passes through spectral filters (Lebow Company, U.S.A.) that have a high transmission for the harmonic emission but are opaque for $\sim$ 800 nm radiation. For the argon (helium) gas cell an aluminium metal foil (a combination of silver and zirconium metal foils) is used. These ultra-thin foils are usually 100 to 300 nm thick and mounted on a metal ring. A filter wheel serves as host for the metal rings as indicated by part j) in figure 3.3.1. The filter wheel is driven by an electric motor and thus can be controlled from outside the high-harmonic generation apparatus. Moreover, this filter wheel also hosts neutral density filters used for alignment of the laser beam with respect to the optical axis of the apparatus, and in particular the centre of the charge-coupled device detector chip. It is axiomatic that the ultra-thin metal filters exhibit pinholes. According to the manufacturer the maximum single pinhole allowed is 1 μm in diameter. However, rather than one large pinhole, most spectral filters have several very small pinholes. The allowed light leakage through the pinholes is 1 part in 10^5 measured by visible light transmission for foils of a thickness $>$ 200 nm. Thus, a second spectral filter (part m)) is used to block the fundamental light that passes these pinholes. This filter is mounted on a rotation mount that is magnetically coupled to the outside of the high-harmonic generation apparatus. A picture of the rotation mount and the spectral filter is shown in picture c) of figure 3.3.3.

3.3.2.2 Spatial filters

The spectral filters absorb the fundamental radiation. In order to reduce the thermal impact on the ultra-thin spectral filters, spatial filtering of the divergent laser beam is performed before the harmonic and the laser beam reach the spectral filters. Several pinhole spatial filters of diameters 100 μm to 5 mm can be employed as indicated in part h) in figure 3.3.1. These spatial filters are mounted on a hand-made so-called wobble stick as shown in picture d) of figure 3.3.3. A linear motion feed-through (part i)) is mounted on a flexible bellow on top of the harmonic beam tailoring section. Under vacuum conditions the flexible bellow is in a compressed state. In combination with spring-loaded micrometer screws, excellent control over the x-, y- and z-direction is achieved and the several pinholes can be easily dialled and inserted into the beampath of the copropagating fundamental and harmonic beam. After passing the first set of spatial filters, the harmonic beam is isolated from the fundamental laser beam by spectral filters. Then a second set of spatial filters of diameter 500 μm to 50 μm can be used for precision spatial filtering of the harmonic beam as indicated by part k) in figure 3.3.1. This set of precision spatial filters is mounted on a linear motion feedthrough (part l)) for the y-direction and a piezoelectrically driven motor (New Focus Picomotor Actuator Model 8302) for the x-direction. Thus, excellent control in the x- and y-directions is achieved and the precision pinholes can be precisely placed at any point across the spatial profile of the harmonic beam.

3.3.3 Experiment chamber

Once the harmonic beam has passed the tailoring section after appropriate treatment with spatial and spectral filters, the harmonic emission can be employed for experimental work in the experiment section. The experiment section is schematically displayed in figure 3.3.1 and shown in figure 3.3.2. The inside of this section is shown in pictures f) and g) of figure 3.3.3. Picture f) also shows a 2 cm-diameter hole by which the experiment section is connected to the tailoring section. The experiment section is pumped by a turbo-molecular drag pump (part q), Pfeiffer Vacuum TMU 521) at a pressure between 10^{-5} and 10^{-4} mbar, which is monitored by a pressure gauge. When the rotation mount with the spectral filter, as shown in picture e), is placed in front of the 2 cm-diameter hole, the foil acts as differential stage and the experimental section is at a pressure between 10^{-6} and 10^{-5} mbar.

3.3.3.1 Young double-slits

Several pairs of Young double-slits (part o) in figure 3.3.1) can be employed for a variety of experimental purposes. The geometrical data of these slits is summarized in table 4.1 in section 4.2.2. The pairs are used to characterize the degree of spatial coherence as explained in section 4.2.2 and to extract the spectral characteristics of the multiple-order harmonic beam by the application of the maximum entropy method as explained in section 4.2.3. The Young double-slits are etched into a silicon wafer. This wafer is mounted on a hand-made rotation stage that is driven by a precision stepper motor as shown in the pictures g) and h) of figure 3.3.3. The motor can be controlled from the outside of the high-harmonic generation apparatus. Thus, the silicon wafer can be precisely rotated such that the interference pattern emerging from the Young double-slits after illumination with the multiple-harmonic orders is aligned with respect to the x- or y-direction of the charge-coupled device detector chip (see figure 4.2.3). The rotation mount is mounted on a set of x/y-translation stages. Thus, the Young double-slits can be precisely positioned at any point across the spatial profile of the harmonic beam. The Young double-slits are located very close to each other with a spatial separation of ~ 5 mm. Furthermore, the silicon wafer also features different pinholes for diffractive imaging purposes. At the longitudinal coordinate z for the position of the silicon wafer the harmonic beam exhibits a diameter > 5 mm. Thus, the charge-coupled device detector chip acquires images that are a superposition of different interference and diffraction patterns. Therefore, the harmonic beam can be spatially filtered by precision pinholes of diameter ≥ 50 μm as explained in section 3.3.2.2 so that the harmonic emission is spatially restricted to only one of the structures on the silicon wafer.

3.3.3.2 Sample holder for coherent diffractive imaging

Employing the harmonic beam for coherent diffractive imaging is one of the main goals of the experimental work of this dissertation. The sample to be investigated (part p) in figure 3.3.1) is mounted on a sample holder that allows precision alignment of the sample with a particular region of the spatial profile of the harmonic beam, preferably with the intense centre of the harmonic beam. A photo of the sample holder is shown in the picture f) and photos of samples are shown in the pictures i) and k) of figure 3.3.3. The sample is mounted on a linear stepper motor that controls the sample's position in the z-direction. The stepper motor is mounted on a set of x/y-translation stages. All motors can be controlled from the outside of the high-harmonic generation apparatus. A LabView-based software module allows the motors to be individually addressed with respect to their speed and acceleration and relative and absolute movement. Thus, by monitoring the diffraction pattern on the charge-coupled device detector chip, the sample can be placed exactly at the x/y-position where the maximum intensity of the spatial profile of the harmonic beam was measured and at a z-position as close as the beam blocks that are mounted directly above the surface of the detector chip.

3.3.3.3 Beam block adaptor

The hand-made beam block adaptor allows the acquisition of diffraction patterns over a dynamic range that exceeds the dynamical range of the charge-coupled device detector chip. Three different diffraction patterns of the same sample are taken with special emphasis on the diffractive features in the centre (first pattern) and in the wings of the diffraction pattern. For the latter a very long exposure time is needed in order to resolve the features with a reasonable signal-to-noise ratio. Saturation of the centre features in the acquired image is avoided by placing a beam stop over the centre of the charge-coupled device detector chip. This is done for the x- (second pattern) and y-direction (third pattern). The three diffraction images are then combined. This technique allows the acquisition of high-dynamic range diffraction patterns that are free from any diffraction from supportive elements of the beam block, such as very thin wires that the beam block is mounted on. A photo of the beam block adaptor is shown in the picture j) of figure 3.3.3 and photos of the beam blocks are shown in the pictures k) and l). The beam block adaptor (part r) in figure 3.3.1) is mounted between the end flange of the vacuum chamber of the experimental section and the charge-coupled device detector chip (part u)). The adaptor has one linear motion feed-through for the x-direction (part s)) as well as for the y-direction (part t)). These beam blocks are mounted directly above the surface of the detector chip as shown in picture l) of figure

3.3.3 at a distance of < 1 mm and are placed at the centre of the diffraction pattern as shown in picture k). The adaptor also features an aperture of variable diameter that is magnetically coupled to the outside of the high-harmonic generation apparatus. The sample can be placed before or after the aperture. In either case the aperture reduces any stray harmonic light that might be scattered in the tailoring section or experiment chamber and thus improves the quality of the acquired diffraction images. The beam blocks (picture l) of figure 3.3.3) themselves are of circular shape and made from a material that is opaque to the harmonic emission. They are attached to the linear motion feed-throughs by thin wires. The surfaces of the beam blocks are polished. Beam blocks of different diameter are used depending on the chosen sample and its diffraction pattern and depending on the chosen nonlinear medium in the gas cell. The medium determines the spectral range of the harmonic emission and thus affects the diffraction pattern in its spatial domain, in particular the spatial extent of the high-intensity centre features of the diffraction pattern that tend to quickly saturate.

3.3.4 Detection and characterization hardware

3.3.4.1 Detector

A charged-coupled device camera system (Princeton Instruments PI-SX:1300, $N = 1300$ pixels in the x-direction and 1340 pixels in the y-direction) serves as detecting device for the high-harmonic emission. The camera system is schematically displayed as item u) in figure 3.3.1 and shown in figure 3.3.2. The charge-coupled device detector chip is displayed in the pictures i) of figure 3.3.3. This camera system features a back-illuminated charge-coupled device chip with an 1300×1340 imaging array of 20 μm $\times$ 20 μm pixels. The camera housing has a vacuum-open-nose flange which is directly mounted onto the beam block adaptor. A conflat flange adaptor allows the camera to be mounted on standard conflat equipment. When in operation, the camera is thermoelectrically cooled to a temperature of -30^oC to allow for low dark current and long exposure times. Depending on the experimental requirements, a high speed readout of 1 MHz (16 bit) for rapid image acquisition or a low speed readout of 1 kHz (16-bit) for high sensitivity with wide dynamic range, high signal-to-noise ratio and excellent energy resolution can be chosen. The camera system features a USB 2.0 interface and is controlled by means of commercial software (Princeton Instruments WinView). The commercial software is only used for acquisition purposes as explained in section A.6.1 and A.6.2, and data processing is performed by software modules written in the programming suite LabView (National Instruments). According to the manufacturer, the relation between the number of detected photons $N_{photons}$ and the signal counts c is given by

$$N_{photons} = \frac{3.65cg}{E\ QE}, \tag{3.3.1}$$

where $E\ [eV]$ is the photon energy, g is the gain depending on the setting of the software for the controller of the camera system as displayed in table A.1 of section A.5.1, and QE is the quantum efficiency as given in figure A.5.1.

3.3.4.2 Spectrometer

A spectrometer (Setpoint GIMS#4) with a grazing-incidence diffraction grating can be inserted into the beam path in order to acquire a reference spectrum for the maximum entropy method-based reconstructed harmonic power spectrum as explained in section 4.2. The far-field profile of the diffraction pattern is then detected along the height of the exit slit of the spectrometer and the harmonic spectrum is scanned by precision rotation of an appropriate grating covering the necessary spectral range. The spectrometer is inserted into the beam path between the experiment section and the data acquisition system as shown in figure 3.3.4. This spectrometer features a constant angle of deviation using rotatable spherical gratings covering a wide spectral range of 4.4 to 85.0 nm as shown in table A.2 of section A.5.2. Based on an off-Rowland scheme, the spectra are recorded in a plane perpendicular to the diffracted rays. Thus, exact focusing of the entrance slits takes place only for the wavelength λ_{focus}, which corresponds to the intersection of the plane of registration with the Rowland circle. The alignment to a different wavelength is produced by precision rotation of the grating.

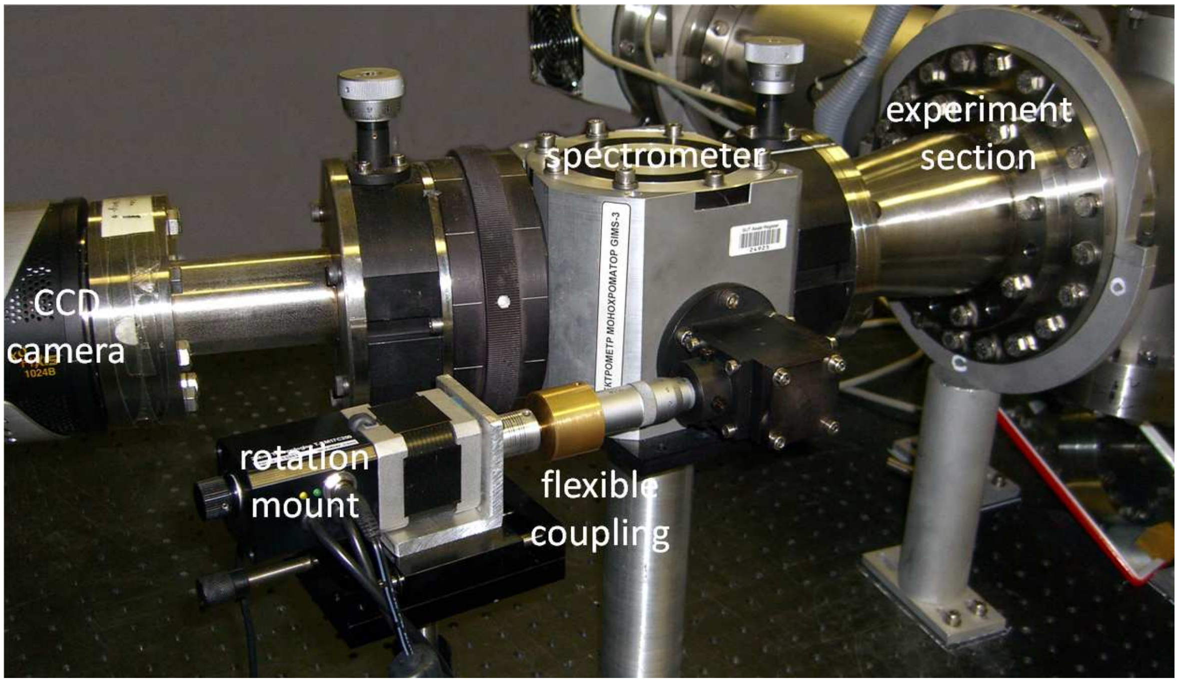

Figure 3.3.4: A spectrometer with a grazing-incidence diffraction grating can be inserted into the beam path in order to acquire a reference spectrum for the maximum entropy method-based reconstructed harmonic power spectrum.

A set of four gratings with different dispersion characteristics, as shown in table A.2 of section A.5.2, is used to provide an extended range of spectral coverage. Each grating is mounted in its individual pre-aligned holder. The spectral range covered by the four gratings is 4.4 to 85.0 nm, but can be extended on both sides with some losses in spectral resolution or realignment of the exit slit (focal plane) position. The spectrometer has micrometer driven entrance and exit slit assemblies. The slit width can be varied from 0.5 μm to 200 μm with an accuracy of ~ 0.5 μm. The slit height is 20 mm. The harmonic power spectrum is recorded by precision rotation of the grating. The rotation of the grating is controlled manually by means of a micrometer screw. Thus, the spectrometer system only offers manual means for recording of the spectrum. Therefore, a hardware-software system was designed for automated acquisition of the spectrum. The linear micrometer screw of the spectrometer is flexibly coupled to a rotation mount as shown in figure 3.3.4. The rotation mount is mounted on a linear translation stage to allow the propulsive movement of the linear micrometer screw when rotated. The rotation mount can be controlled by software and synchronized with the data acquisition software as explained in section A.6.1. The software is calibrated with respect to the position of the linear micrometer screw. A spectrum can thus be easily acquired by programming the spectral range, the step size and the parameters for acquiring statistical data as explained in section A.6.2.

3.3.4.3 Young double-slits

As explained in section 3.3.3.1 Young double-slits are used to characterize the degree of spatial coherence as explained in section 4.2.2 and to extract the spectral characteristics of the multiple-order harmonic beam by the application of the maximum entropy method as explained in section 4.2.3.

3.3.4.4 Alternative hardware

For early experimental work a hand-made ion detector and a soft x-ray, deep ultraviolet silicon photodiode were used. The purpose of the ion detector is to detect ions generated in the process of high-harmonic emission where a particular amount of plasma is intrinsic to the generation process. The ion detector is a combination of a simple parallel-plate capacitor and appropriate hand-made electronic circuitry for signal isolation and amplification and a lock-in amplifier (Stanford Research Systems SR830). The purpose of the photodiode (OSI Optoelectronics inversion layer silicon photodiode - soft x-ray and deep ultraviolet enhanced series) is to detect the harmonic photons directly and provide a signal that scales linearly with the number of detected photons. The photodiode is connected to appropriate electronic circuitry for signal isolation and amplification and a lock-in amplifier (Stanford Research Systems SR830).

Chapter 4

Experimental methods

In this chapter the experimental methods for characterization of the harmonic emission in the spatial and spectral domain are discussed. Here, the experimental methods refer to software-based procedures as well as experiment-based procedures that were implemented in the course of designing and revising the experimental setup.

4.1 Analysis of the spatial domain

Analysis of the harmonic emission in the spatial domain is performed by data acquisition based on a charged-coupled device detector chip. For experimental flexibility, efficiency and automation it is necessary to customize the method of data extraction via commercial software and extend it by means of hand-written software. For extraction of the harmonic intensity from the data images, the resulting data files are processed by software written in LabView (National Instruments). This allows customized data read-out and processing on-the-fly while WinView is in data acquisition mode. A detailed description of the ActiveX-based software interface can be found in section A.6.1. The need for automation of the experimental setup requires appropriate synchronization of any hardware, which needs to be controlled, with the data acquisition software WinView. In combination with the previously described ActiveX-based software interface to WinView for automated extraction of information from acquired images, a very flexible and efficient scheme has been established and changes to or extensions of the existing experimental hardware can be quickly incorporated in order to conduct computer-based automated measurements of the experimental setup. A detailed description of this software can be found in section A.6.2.

4.2 Analysis of the spectral domain and coherence properties

The coherence properties of the harmonic emission are analyzed by means of Young double-slits. Characterization in the spectral domain is performed by an application of the maximum entropy method to the interference pattern of the Young double-slits. Optionally a grazing-incidence spectrometer (Setpoint GIMS#4) can be used.

4.2.1 Spectrometer

A spectrometer with grazing-incidence diffraction grating can be inserted into the beam path in order to acquire a reference spectrum for the reconstructed harmonic power spectrum that is based on the maximum entropy method. The far-field profile of the diffraction pattern is then detected along the height of the exit slit of the spectrometer and the harmonic spectrum is scanned by precision rotation of an appropriate grating covering the necessary spectral range.

4.2.1.1 Calibration of spectrometer

In order to accurately measure the spectrum with the grazing incidence spectrometer, a calibration procedure needs to be performed that involves the precise measurement of the position of the zeroth diffraction order. Calibration of the spectrometer is only performed when the grating has been changed or when the spectrometer has been removed and reinserted into the beam path. The grating is installed on a grating holder that is fixed to a rotation table inside the spectrometer housing. The rotation mount is driven by a micrometer screw, so that any particular angle of the grating is mapped to the setting of the driving micrometer screw z_{screw}. The position of the zeroth order is determined from the peak curve that is measured when the grating is rotated as demonstrated in figure 4.2.1. The position of the peak (black dotted curve) is determined manually and by fitting an appropriate peak function (red dashed curve). Both are usually found to be in good agreement and to lead to the value $z_{screw,0}$. It is

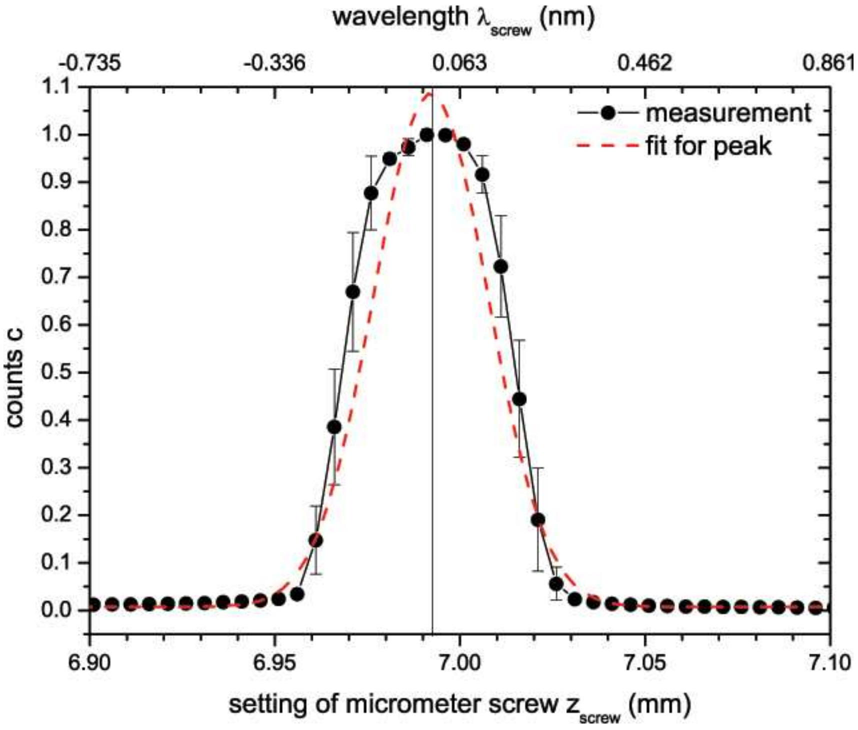

Figure 4.2.1: Calibration of the spectrometer by determining the zeroth order from the grating.

noted that the shape of the peak curve can vary significantly depending on the settings of the entry and exit slit and the region of interest on the charge-coupled device detector chip for extraction of the intensity information.

4.2.1.2 Rotation of grating

The harmonic power spectrum is recorded by dialing the micrometer screw that drives the rotation mount. The harmonic spectrum can thus be mapped to values $z_{screw,\lambda}$. The difference of the position of the zeroth order $z_{screw,0}$ and $z_{screw,\lambda}$ when multiplied by the linear dispersion D_a determines the accurate position of the harmonic orders. Thus the wavelength is given by

$$\lambda = \left(z_{screw,0} - z_{screw,\lambda}\right) D_a. \tag{4.2.1}$$

It is noted that the spectrometer is operated with a constant angle of deviation $\alpha_{dev} = \alpha_{inc} + \alpha_{diff} = 166\ ^\circ$ and that the dependance of the wavelength from the angles of incidence $\alpha_{inc} = \alpha/2 \pm \Delta$ and diffraction $\alpha_{diff} = \alpha/2 \mp \Delta$ is linear to a very good approximation as $\Delta \leq 1\ ^\circ$. D_a depends on the chosen grating and can vary slightly with the angle of incidence and diffraction, e.g., < 0.1 % for the 300 grooves/mm grating. The micrometer screw can be driven manually. However, it is coupled to a precision rotation stepper motor that is synchronized with the aforementioned data acquisition software WinView. Through LabView-based software this stepper motor can be controlled and synchronized with the controller for the charge-coupled device detector chip. Thus, the start position $z_{screw,begin}$ and the end position $z_{screw,end}$, the step size Δz_{screw}, and multiple measurements for each position z_{screw} for statistical purposes can be easily programmed.

4.2.1.3 Spectrum extraction

The intensity of the harmonic spectrum is mapped to the values $z_{screw,\lambda}$ and determined by the region of interest of the charge-coupled device detector chip chosen for extraction of the harmonic intensity as shown in figure 4.2.2. The relative weighting of the harmonic orders is the same for orders with wavelength $\geq 32.2\ nm$. But for harmonic orders with wavelength $\leq 29.8\ nm$ the relative weighting depends strongly on the selected region of interest. The regions of interest only differ in their length relative to the entry or exit slits of the spectrometer. For a larger region of interest (ROI), e.g., ROI 1 in the inset of figure 4.2.2, the relative weighting for harmonic orders with wavelength $\leq 29.8\ nm$ is larger when compared to a smaller region of interest, e.g., ROI 4. As the spectrally resolved far-field profile of the harmonics is detected along the height of the exit slit, this effect can be associated with the profile of the harmonic emission in its spatial domain as the profile is not necessarily symmetric with respect to the entry slit of the spectrometer. Furthermore, it can also be shown that the relative weighting of the harmonic orders can vary significantly across the spatial domain. In particular, for certain phase-matching parameters the harmonic beam can exhibit higher orders far off the centre.

4.2.2 Young double-slits

In order to measure the degree of spatial coherence on different length-scales, three different Young double-slits are used. The geometrical parameters of the Young double-slits are displayed in table 4.1. Here, d is the slit spacing, w is the slit width, and h is the slit height. Using Young double-slits instead of a pinhole pair, and in particular choosing an appropriate value for h ensures that the interferogram covers a reasonable number of pixels on the charge-coupled device detector chip in a direction perpendicular to the spread of the interference pattern. Thus, when extracting the cross-section of the interference pattern, a reasonable number of rows can be chosen, which is beneficial

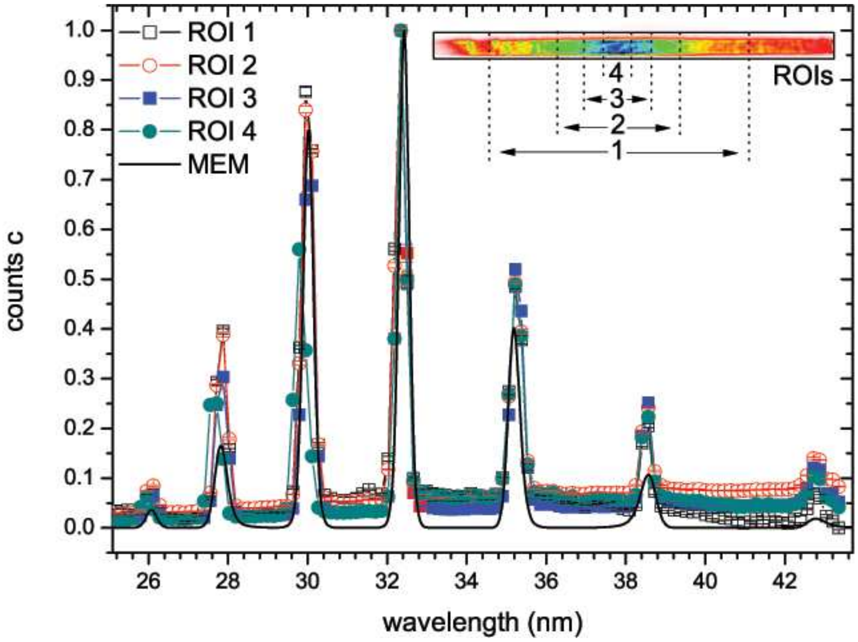

Figure 4.2.2: The relative weighting of the harmonic orders in the power spectrum can vary depending on the selected region of interest of the charge-coupled device detector chip. The inset shows the harmonic beam diffracted by the grating.

for the stability of the extraction process as described below.

pair	d / μm	w / μm	h / μm
S1	20.0(1)	5.0(5)	50.0(5)
S2	50.0(1)	10.0(5)	50.0(5)
S3	100.0(1)	20.0(5)	50.0(5)

Table 4.1: Geometrical data of the Young double-slits.

The Young double-slits are used to extract information about the degree of spatial coherence as well as the power spectrum of the multiple-harmonic order emission as shown in [140, 46, 141] and in our work [8, 5] and as discussed in the following. For a typical measurement of the coherence properties of a (quasi-) monochromatic electric field by means of illuminating a double-slit (or a double-pinhole), the fringe visibility is given by

$$\upsilon = \frac{I_{max} - I_{min}}{I_{max} + I_{min}}, \tag{4.2.2}$$

where I_{max} is the intensity of the centre and I_{min} is the intensity of the first minimum of the interferogram. The degree of spatial coherence γ_{12} is related to the fringe visibility by

$$|\gamma_{12}| = \upsilon \frac{I_1 + I_2}{2\sqrt{I_1 I_2}}, \tag{4.2.3}$$

where I_1 and I_2 are the intensities of the electric field at the two individual slits of the Young double-slit. Therefore γ_{12} depends on the fringe visibility as well as on whether the individual slits are equally illuminated. The degree of spatial coherence can thus be described as

$$|\gamma_{12}| > \upsilon. \tag{4.2.4}$$

Generally, the measured fringe visibility underestimates the degree of spatial coherence. However, great care is taken to illuminate both individual slits equally so that the spatial coherence is given directly by the fringe visibility $|\gamma_{12}| \approx \upsilon$. In the case of a harmonic beam consisting of several orders q centred at wavelengths λ_q, the measured intensity distribution of the interferogram on the charge-coupled device detector chip is given by

$$I_T(x) = \sum_q F(q) I(x, \lambda_q), \tag{4.2.5}$$

where x is the spatial coordinate and $F(q)$ is the relative weighting of the qth harmonic order in the power spectrum. As the interference pattern of a monochromatically illuminated Young double-slit for each spatial coordinate x and each wavelength λ within the power spectrum is given by

$$I(x|\lambda) \propto |\gamma_{12}|\, cos\left(2\pi \frac{xD}{Z\lambda}\right) sinc^2\left(\pi \frac{W}{Z\lambda}\right), \tag{4.2.6}$$

where c is the speed of light, and D, Z and W are the experimental parameters as defined in figure 4.2.3 of section 4.2.3.1, the individual degree of spatial coherence of each harmonic order $\gamma_{12} = \gamma_{12}(q)$ contributes to the measured intensity distribution of the interference pattern. Thus

$$\langle|\gamma_{12}|\rangle = |\gamma_{12}| > \upsilon = \frac{I_{T,max} - I_{T,min}}{I_{T,max} + I_{T,min}} \tag{4.2.7}$$

and the extracted degree of spatial coherence is in fact an average value of all of the effective orders in the harmonic beam. However, in the case of only a few generated phase-matched harmonic orders, the harmonic orders can be assumed to have the same, or at least a very similar, degree of spatial coherence [2, 3, 4]. In fact, this assumption is a very good approximation, as the measured average degree of spatial coherence varies only negligibly when adjusting the macroscopic phase-matching parameters which strongly influence the number of effective harmonic orders and their relative weighting in the power spectrum.

4.2.3 Maximum entropy method for spectrum extraction

In the following, the application of the maximum entropy method is discussed. Rather than using a spectrometer for spectral characterization of the harmonic emission, the maximum entropy method is applied to the interferogram from the Young double-slits. This approach is highly advantageous for the experimental work discussed in this thesis. No alignment issues of the spectrometer with respect to the centre of the harmonic beam arise and the harmonic beam can be used directly for experimental purposes without any optics in the beam path that might affect the harmonic emission in its spatial, spectral or temporal domain. But, in particular, no harmonic flux is lost due to intrinsic inefficiencies of the diffraction grating, and spectral characterization by means of the maximum entropy method is essential for real-time or in-situ spectral characterization of the centre and, especially, across the profile of the harmonic beam.

4.2.3.1 Algorithm

In a standard measurement of coherence the incident electric field is assumed to be quasi-monochromatic. Then the temporal coherence effects are isolated from the measurement of the degree of the spatial coherence [142]. If a Young double-slit or double-pinhole is illuminated with polychromatic light, the resulting interference pattern will exhibit a degree of temporal as well as spatial coherence and contain information about the power spectrum of the incident light [143]. Recovery of the power spectrum of the harmonic emission from a fringe pattern created by a Young double-pinhole experiment has been reported previously [46]. This approach used a fast Fourier transform to extract the spectral information. Although this work showed very good quality of reconstruction of the high-harmonic generation spectrum, the use of a fast Fourier transform can lead to some artifacts due to its discrete nature. Moreover, one of the serious problems of Fourier transform based methods is the appearance of ripples due to the termination effect even where Fourier coefficients with higher orders are regarded as negligible [144]. It should also be noted that the method presented in [46] can only be applied to a measurement of the intensity distribution in the far-field produced by a slit or pinhole pair and requires that the separation of the slit or pinhole pair be very much larger than the width of the slits or diameter of the pinholes.

In the following, a more flexible approach to this problem based on an application of the maximum-entropy method is introduced. Spectral analysis is performed by applying the maximum entropy method to the interference pattern of the Young double-slit pair illuminated with the emission of the harmonic source. A detailed description of the maximum entropy method formalism can be found in [145], and its adaption for high-harmonic generation spectrum reconstruction from a Young double-slit interference pattern is discussed in detail in [8]. This method allows in-situ precision spectral characterization of the harmonic source and, in particular, allows one to probe the spectrum at any part across the harmonic beam. Also, the application of the maximum entropy method for the extraction of spectral information from the Young double-slit interference pattern is a more flexible approach compared to [46]. The method presented in the following does not require any prior information about the number of harmonic orders, their position or shape. Also, it has yielded reliable spectra in conditions where simpler Fourier based methods cannot [8].

The experimentally measured total intensity distribution $I_T(x)$ is given by the incoherent superposition of the fringe patterns from each part of the spectrum

$$I_T(x) = \int_0^\infty S(\lambda)\, I(x|\lambda)\, d\lambda \tag{4.2.8}$$

where $I(x|\lambda)$ is the interference pattern of a monochromatically illuminated Young double-slit for each spatial coordinate x and each wavelength λ of the harmonic spectrum. The interference pattern is defined by

$$I(x|\lambda) = 2\left(1 + |\gamma_{12}|\, cos\left(2\pi\frac{xD}{Z\lambda}\right)\right) sinc^2\left(\pi\frac{W}{Z\lambda}\right), \tag{4.2.9}$$

where γ_{12} is the complex degree of coherence, c is the speed of light, and D, Z and W are the experimental parameters as defined in figure 4.2.3. The most probable high-harmonic generation power spectrum distribution is given by the distribution with the maximum value of the entropy functional

$$S(\lambda)^{n+1} = S(\lambda)^n\, exp\left(-\eta\frac{\partial C}{\partial S}\right), \tag{4.2.10}$$

where η is the Lagrange multiplier, and is reached through iterations $n = 0, 1, 2, ...$ while the following condition needs to be satisfied

$$C = \frac{1}{M}\Sigma_{j=1}^{M}\left(\frac{\left|{I_T}^{MEM}(x_j) - I_T(x_j)\right|^2}{\sigma^2(I_T)}\right). \tag{4.2.11}$$

M is the number of experimental points, $I_T^{MEM}(x)$ is the maximum entropy method estimate of $I_T(x)$, and $\sigma(I_T)$ is the estimated uncertainty in the measurement of $I_T(x)$.

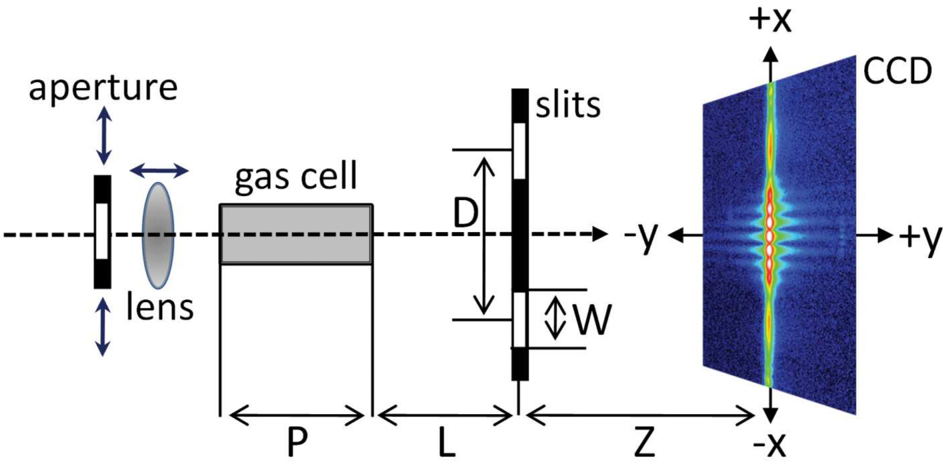

Figure 4.2.3: Schematic representation of the Young double-slit experimental setup.

The reliability of reconstruction is measured using

$$R_F(\%) = 100\left(1 - \frac{\sum_{j=1}^{M}\left|I_T^{MEM}(x_j) - I_T(x_j)\right|}{\sum_{j=1}^{M} I_T(x_j)}\right). \tag{4.2.12}$$

The iterative process of the maximum entropy method is not stopped unless $R_F > 95\,\%$. The stability of the generated spectrum is tested with respect to small changes of the geometrical parameters of the experimental setup and the parameters that are significant for extracting the cross-section of the acquired interference pattern. A set of parameters is chosen that allows efficient, stable and reliable application of the maximum entropy method algorithm to the acquired interference pattern for extraction of the spectral characteristics.

4.2.3.2 Reliability of the maximum entropy method output towards experimental instabilities and variations

For reliable extraction of the spectral characteristics from the interference pattern, the parameters of the maximum entropy method algorithm are ideally adjusted in such a way that $R_F = 100\ \%$. This corresponds to a perfect match of the experimental cross-section of the acquired interference pattern and the reconstructed cross-section associated with the maximum entropy method generated spectrum. In practice, maximum entropy method reconstruction is regarded as successful when $R_F > 95\ \%$. This corresponds to a very good overlap of the experimental and reconstructed cross-section as demonstrated in figure 4.2.4.

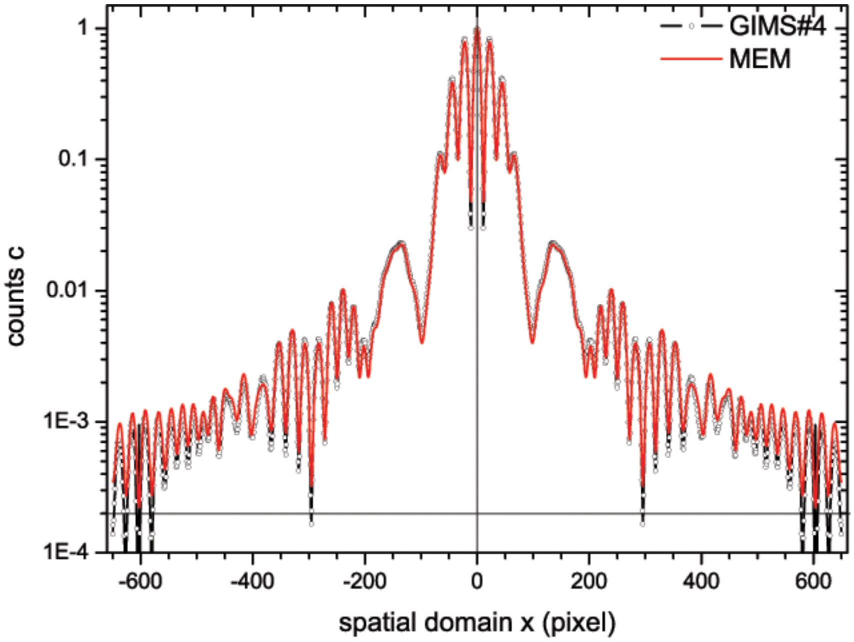

Figure 4.2.4: Experimental (black dotted curve, GIMS#4) and reconstructed (red solid curve, MEM) interference pattern.

In order to guarantee the validity of the maximum entropy method reconstructed spectrum, the parameters of the maximum entropy method algorithm and for the extraction of the cross-section of the experimental interference pattern from the charge-coupled device detector chip are varied slightly to understand how experimental instabilities or systematic errors, such as inaccurate settings of the parameters related to the geometrical configuration of the maximum entropy method Young double-slit experimental setup, affect the generated harmonic spectrum as displayed in figure 4.2.5. The top sub-figure of figure 4.2.5 serves as a reference and displays the experimental (black dotted curve, GIMS#4) and reconstructed (red solid curve, MEM) spectrum based on the optimized parameters:

Width of the Young double-slits (second sub-figure from the top of figure 4.2.5): $w = 5\ \mu m \pm \Delta w$. For proper spectrum extraction the accurate width of the Young double-slits is essential. Small variations in the 1 to 2 % range lead to inaccurate weighting and a shifting of the less-intense harmonic orders. Larger variations in the ~ 1 % range create artefacts such as non-existing harmonic orders.

Angle of the interference pattern with respect to the charge-coupled device pixel array (third sub-figure from the top): $\alpha = 0 \pm \Delta\alpha$. Ideally the angle between the interference pattern and the charge-coupled device pixel array is obsolete, that is, 0°. Extracting the experimental cross-section at an angle with respect to the pixel array creates inaccurate weighting and shifting of the less intense harmonic orders and can also lead to the generation of non-existing higher harmonic orders.

Number of rows chosen for extraction of the cross-section of the interference pattern (fourth sub-figure from the top): $\#\ rows$. The spectral power distribution is invariant with the number of rows ≤ 21 to a very good approximation.

Distance of the Young double-slits: $d = 20\ \mu m \pm \Delta d$. The validity of the maximum entropy method based spectrum depends strongly on this parameter. Even a small mismatch (< 1 %) can lead to an improper spectral power distribution and significant shifting of the harmonic orders.

Resolution of the charge-coupled device detector chip (fifth sub-figure from the top): $res = 13\ \mu m \pm \Delta res$. A mismatch as small as < 1 % can lead to significant shifting of the harmonic orders. However, the spectral power distribution is insignificantly affected.

Distance between the charge-coupled device chip and the Young double-slit (sixth sub-figure from the top): $z = 23.7\ mm \pm \Delta z$. An improperly set value of z of error ~ 1 % will lead to shifted harmonic orders. However, the spectral power distribution is not affected to a good approximation.

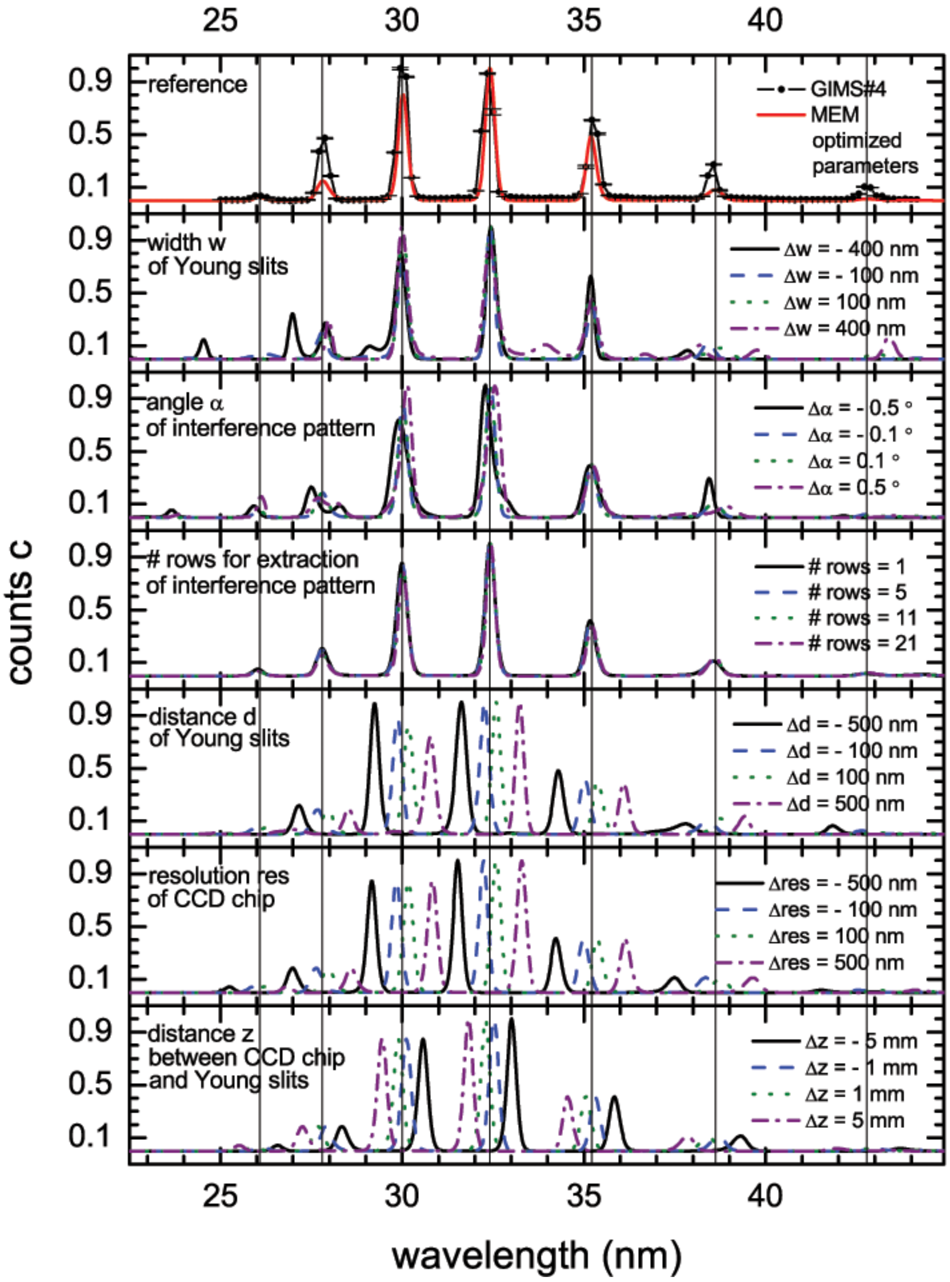

Figure 4.2.5: Effect on the reconstructed spectrum when parameters related to the geometrical configuration and extraction of the experimental cross-section of the interference pattern are varied (coloured lines according to legends in sub-figures).

In all cases of non-optimized or mismatched parameters, a severe mismatch of the experimental and reconstructed cross-section of the interference pattern can be observed and the value of the repeatability decreases rapidly $R_F \ll 95$ %. Thus, the generated harmonic spectrum can be inaccurate and even exhibit non-existing harmonic orders. Therefore, the maximum entropy method based spectrum extraction is only regarded as successful and sufficient when $R_F > 95$ % and a good overlap between the experimental and reconstructed cross-section of the interference pattern is achieved. This is performed by employing a spectrometer for a reference measurement and iterative optimization of the experimental parameters and is tested for any maximum entropy method based extraction of the spectral characteristics from the experimental cross-section.

4.2.3.3 Calibration and tuning with spectrometer

In order to fine-tune the maximum entropy method parameters a reference measurement is performed by means of a grazing-incidence spectrometer (Setpoint GIMS#4). This allows the parameters to be adjusted in such a way that $R_F \approx 100$ % and that an almost perfect overlap of the experimental and reconstructed cross-section of the interference pattern is achieved as demonstrated in figure 4.2.4. The chosen set of parameters then allows efficient, stable and reliable application of the maximum entropy method algorithm to the acquired interference pattern for extraction of the spectral characteristics.

The following procedure is followed to achieve fine-tuning of the maximum entropy method parameters:
Depending on the setting of the phase-matching parameters the centre of the spatial profile of the harmonic beam might not overlap with the optical axis of the high-harmonic generation apparatus, in particular with the centre of the charge-coupled device detector chip. Thus, the entrance slits of the grazing incidence spectrometer might not sample the centre of the spatial profile of the harmonic beam. Therefore, the phase-matching parameters are set in such a way that the harmonic beam is perfectly centred with respect to the charge-coupled device detector chip. For this procedure the harmonic beam is detected directly by the charge-coupled device detector chip without

any optics, in particular without the grazing incidence spectrometer, in the beam path. The Young double-slits are mounted on a precision $x/y/z$-translation stage and precisely moved at any point of the spatial domain of the harmonic beam. An interference pattern of high dynamic range is taken to cover both the intensity information in the centre as well as in the wings. Additionally, a background image is taken by transforming the linear polarization of the fundamental laser beam into circular polarization by means of a quarter-waveplate. The quarter-waveplate is mounted on a precision $x/y/z$-translation stage which is adjusted in such a way that the rotation of the quarter-waveplate does not or at least negligibly affects the spatial domain of the harmonic beam and, in particular, its position on the charge-coupled device detector chip.

The gas cell is now separated from the rest of the high-harmonic generation apparatus by means of a vacuum gate. The gas ballast of the gas cell is still being removed constantly by the piston pump of the first pressure gradient section and by the turbomolecular drag pump of the second pressure gradient section which ends at the vacuum gate. Also, harmonic generation inside the gas cell is still in operation while the experimental chamber is repressurized to atmospheric pressure. Thus, the gas cell setup virtually does not experience any change of the phase-matching parameters, in particular the pressure inside the gas cell and the intensity of the laser beam. The grazing incidence spectrometer is installed between the experimental chamber and the charge-coupled device detector chip. The experimental chamber is then depressurized to a pressure comparable to the pressure in the second pressure gradient section. Thus, when opening the vacuum gate, any unnecessary gas flow and destabilization of the pressure inside the gas cell can be avoided. All sections are monitored by means of pressure gauges. In particular, the pressure inside the gas cell is monitored closely. If the pressure inside the gas cell varies by more than ±1 Torr, the procedure is started from the beginning.

A reference spectrum is taken by means of the grazing incidence spectrometer. As we ensure that the entrance slits are aligned with respect to the optical axis of the high-harmonic generation apparatus, the spectrum extraction refers to the centre of the spatial domain of the harmonic beam. The far-field profile of the interference pattern is detected along the height of the exit slit of the spectrometer and the harmonic spectrum is scanned by precision rotation of an appropriate grating covering the necessary spectral range. Additionally the spectrometer is calibrated by precision scanning of the zeroth order of the harmonic beam diffracted by the grating.

The maximum entropy method based spectrum reconstruction is compared with the spectrum acquired by the grazing incidence spectrometer. A fine-tuning of the maximum entropy method related parameters can now be performed in an iterative process in order to improve the overlap between the experimentally measured spectrum and the reconstructed spectrum as demonstrated in figure 4.2.6. Depending on the quality of this procedure and the number of iterations, $95\ \% \leq R_F \leq 100\ \%$ and an almost perfect overlap of the experimental and reconstructed cross-section of the interference pattern is achieved as shown in figure 4.2.4.

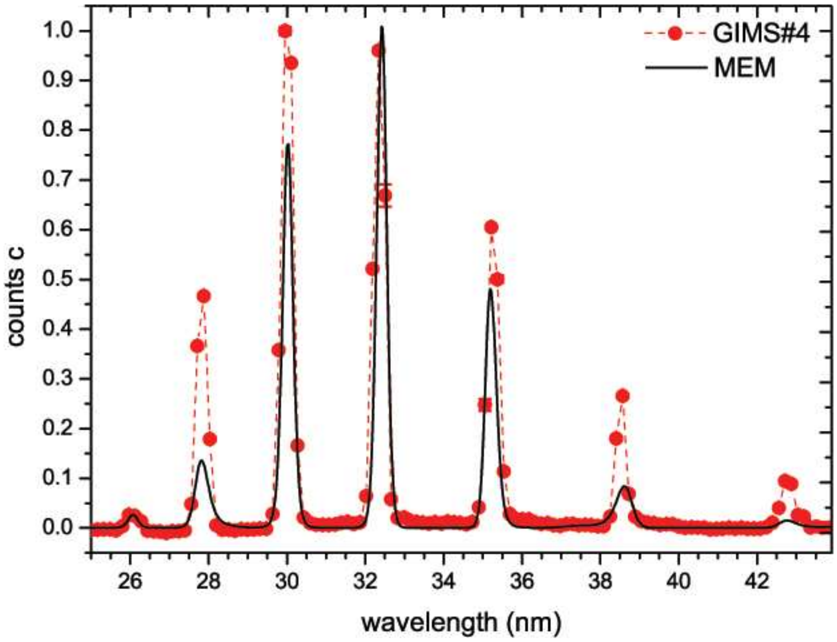

Figure 4.2.6: Experimental (red dots, dashed curve, GIMS#4) and reconstructed (black solid curve, MEM) power spectrum.

The reason for the difference in the intensity distribution of the maximum entropy method based reconstruction and the measured spectrum is the varying efficiency of the spectrometer grating and the charge-coupled device detector chip. Furthermore, the selection of the region of interest on the charge-coupled device detector chip for spectrum extraction can affect the relative weighting of the harmonic orders in the power spectrum as discussed before.

4.3 Multiple-harmonic-order coherent diffractive imaging

Femtosecond-laser-based high-harmonic generation sources are increasingly being used for coherent diffractive imaging [14] in order to satisfy the increased demand for high-resolution morphological and dynamical studies of weakly-scattering, nanometer-scale objects. Compared to synchrotrons and x-ray free electron lasers, these sources provide an output that exhibits a high degree of spatial coherence, but they are small-scale and highly versatile, and their unique characteristic output can be tailored to the experimental requirements. However, by their nature, high-harmonic generation sources produce a laser-like beam that consists of multiple longitudinal coherent modes. Iterative methods [45] for image reconstruction inherently assume a fully coherent wave field. Thus, a single wavelength needs to be selected which leads to a significantly decreased flux of the harmonic beam.

In the following, a novel approach for coherent diffractive imaging is presented that relies on illumination of the sample with a multiple-order harmonic beam. The effective spectral range and the relative weight of the single harmonic orders of the harmonic beam depend strongly on the focusing geometry and the control over the phase-matching parameters: by appropriate choice of the species of gas and its pressure, the interaction geometry, the position of the laser focus and the intensity and diameter of the laser beam, harmonic emission can be phase-matched and confined to just a few orders [3, 2, 4, 5]. Thus, the harmonic orders of the harmonic beam can be tailored according to the experimental requirements and all effectively available harmonic orders can be employed to keep the acquisition time for the coherent diffractive imaging short and to avoid sample damage or detrimental effects due to possible poor long-term stability of the harmonic source. However, employing a harmonic beam consisting of multiple harmonic orders for coherent diffractive imaging requires a reconstruction method that is not critically reliant on the assumption that the harmonic emission possesses essentially perfect spatial and temporal coherence. This approach extends the conventional coherent diffraction imaging algorithm to enable diffractive imaging to be achieved using polychromatic diffraction data. A detailed description of this work can be found in [9].

4.3.1 Methodology

The procedure of acquiring diffraction information from the sample after illumination with a multiple-order harmonic beam consists of several steps. First, one image of low-angle and two images of high-angle diffractive information are acquired. Second, the three diffractive images are stitched together. Third, the stitched diffractive image is the data set that the modified Gerchberg-Saxton iteration and the maximum entropy method refinement procedure are applied to in order to recover the image of the sample. A schematic representation of the methodology is displayed in figure 4.3.1.

4.3.2 Acquisition

In order to achieve a high resolution of the reconstructed object from the coherent diffractive images, images of high dynamic range need to be taken. Only then can diffractive features at high angles be captured, where the high-resolution information resides. The natural dynamic range of the charged-coupled detector is not sufficient to

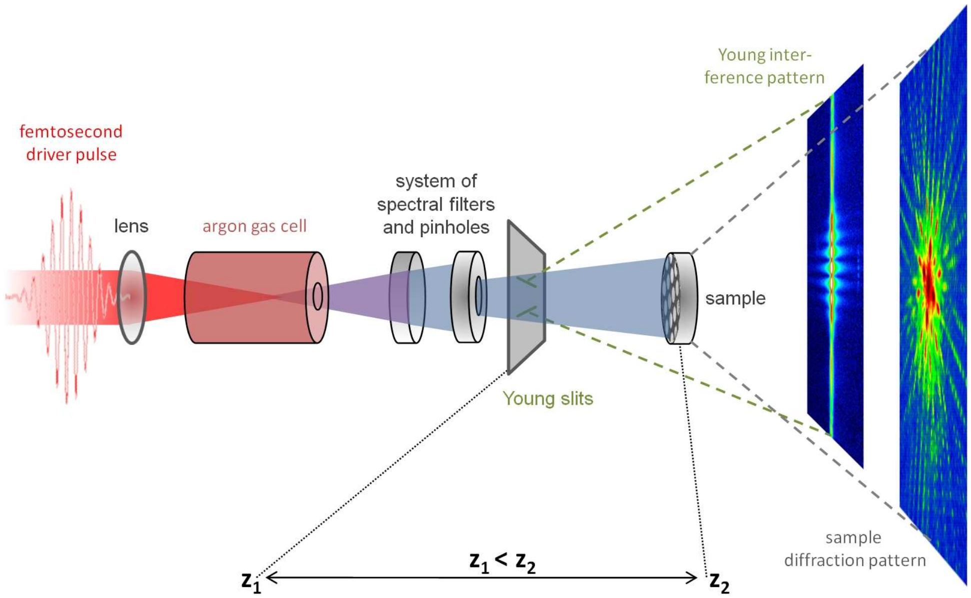

Figure 4.3.1: Schematic of the high-harmonic generation gas cell setup and setup for spectral analysis of the harmonic emission and for coherent diffractive imaging.

acquire these features, that is, the diffractive features in the centre of the image saturate rapidly, but the diffractive features at the high angles require a longer exposure time. As explained in section 3.3.3.3, a beam block adaptor is used to allow the acquisition of a diffraction pattern with a dynamic range that significantly exceeds the dynamical range of the charge-coupled device detector chip. Here, three different diffraction patterns of the same sample are taken with special emphasis on the diffractive features in the centre (first pattern) and in the wings of the diffraction pattern. For the latter the beam block adaptor is placed over the centre of the charge-coupled device detector chip. This is done for the x- (second pattern) and y-direction (third pattern). The three diffraction images are then combined as explained in section 4.3.4 and shown in figure 4.3.4. A photo of the beam block adaptor is shown in the picture j) and photos of the beam blocks are shown in the pictures k) and l) of figure 3.3.3. A schematic representation of the methodology is displayed in figure 4.3.1.

In the following, the acquisition of these three coherent diffractive images and images of the interference pattern for analysis of the spectral composition of the harmonic beam is discussed:

The harmonic source is optimized with respect to the harmonic intensity by adjusting the macroscopic phase-matching parameters. Here, the centre of the harmonic beam coincides with the centre of the detector chip.

Now the harmonic beam is analyzed in its spectral domain. The Young double-slit is moved into the beam path. An interference pattern of high dynamic range from the Young double-slits is taken in order to extract the spectral information by the application of the maximum entropy method as explained in section 4.2.3. In-situ spectral characterization allows the spectral power distribution to be matched with respect to the transmissive characteristics of the sample by adjusting the macroscopic phase-matching parameters. The background picture is taken by venting the gas cell. Then the Young double-slit is moved out of the beam path. The stability and repeatability of the characteristics of the harmonic emission and in particular the spectral composition of the harmonic beam are discussed in section 4.3.3.

The sample is now positioned at the appropriate transverse and longitudinal coordinates, so that the centre of the diffraction pattern coincides with the centre of the detector chip. The appropriate exposure time is determined.

It has to be noted that the charge-coupled device exhibits a peculiarity that requires special care. Charge from the previous image can remain on the detector chip despite a so-called cleaning procedure after each acquisition. These ghost images have the potential to lead to deteriorated reconstruction results. Thus, the charge-coupled device has to be powered down and restarted. In that case the background information of the new and the previous image are different and the procedure of subtraction of the background information, such as harmonic and fundamental stray light as well as noise from the detector chip and its controller, is rendered useless. Therefore, the detector system is restarted, a background image is taken, and then the signal image is taken. The inverse order of this procedure cannot be applied, as the background image needs to be taken with the horizontal or vertical beam stop in position. However, repositioning of the micrometer screw-driven beam block would not result in exactly the same position and thus rendered the procedure of subtraction of the background useless.

Now the features of the centre of the diffractive image are acquired. The detector system is powered down and restarted to eliminate any information from previously taken images. Special care is taken that the detector chip, which is cooled down to $-30°C$, has equilibrated thermally. The background picture is taken with the gas cell still empty. The gas cell is now repressurized. The image with the diffractive features in its centre is taken.

After acquisition of the low-angle diffraction information, the high-angle diffraction information is captured. The horizontal beam block is moved into the beam path and placed in the centre of the detector chip. The appropriate exposure time is determined. The gas cell is now vented in order to take the background information. The detector system is powered down and restarted to eliminate any ghost images. The background image is taken with the gas cell still empty and with the horizontal beam block in position. The gas cell is now repressurized. The image with the high-angle diffractive features is taken. The horizontal beam block is moved out of the harmonic beam path.

After acquisition of the high-angle diffraction information with the horizontal beam block, the high-angle diffraction information with the vertical beam block is captured. The vertical beam block is moved into the beam path and placed in the centre of the detector chip. The appropriate exposure time is determined. The gas cell is now vented in order to take the background information. The detector system is powered down and restarted to eliminate any ghost images. The background image is taken with the gas cell still empty and with the vertical beam block in its position. The gas cell is now repressurized. The image with the high-angle diffractive features is taken. The vertical beam block is moved out of the harmonic beam path.

The characteristics of the harmonic source and in particular the composition of the power spectrum are analyzed again. First, the harmonic source is analyzed in its spatial domain. This applies in particular to the position of the centre of the harmonic beam on the detector chip and to the harmonic intensity. Second, now the harmonic beam is analyzed in its spectral domain by the aforementioned procedure.

4.3.3 Reliability of the experimental procedure

The acquisition of diffraction data and the object reconstruction in the context of the aforementioned methodology is a delicate process that requires stability, repeatability and reliability of the characteristics of the harmonic emission. In particular, the process of venting the gas cell and repressurizing in order to take background and signal images has the potential to render this methodology impractical. Therefore, the stability, repeatability and reliability of the harmonic source are analyzed for each acquisition of diffraction data as explained in section 4.3.2.

Figure 4.3.2 displays the harmonic beam in its spatial domain. The gas cell is vented and repressurized numerous times and each time a data set is taken. In all cases the spatial profile of the harmonic beam is recorded over ~ 10 to 100 laser shots, i.e., each measurement incorporates shot-to-shot instabilities of the fundamental laser beam. These single measurements are normalized and the data sets are compared with each other, leading to a mean value (left picture of figure 4.3.2) of the spatial profile of the harmonic beam and its standard deviation (right picture). The experimental settings for the harmonic beam are as described in section 5.2. The standard deviation across the averaged spatial profile of the harmonic beam for several measurements is very small < 3.4 %. This indicates a very good realiability and repeatability of the harmonic beam across the spatial profile although the process of venting and repressurizating is a fundamental limitation in the operation of the harmonic source.

Figure 4.3.3 displays the harmonic beam in its spectral domain. The spectrum is extracted by applying the maximum entropy method to the interference pattern emerging from a Young double-slit illuminated with the harmonic emission as explained

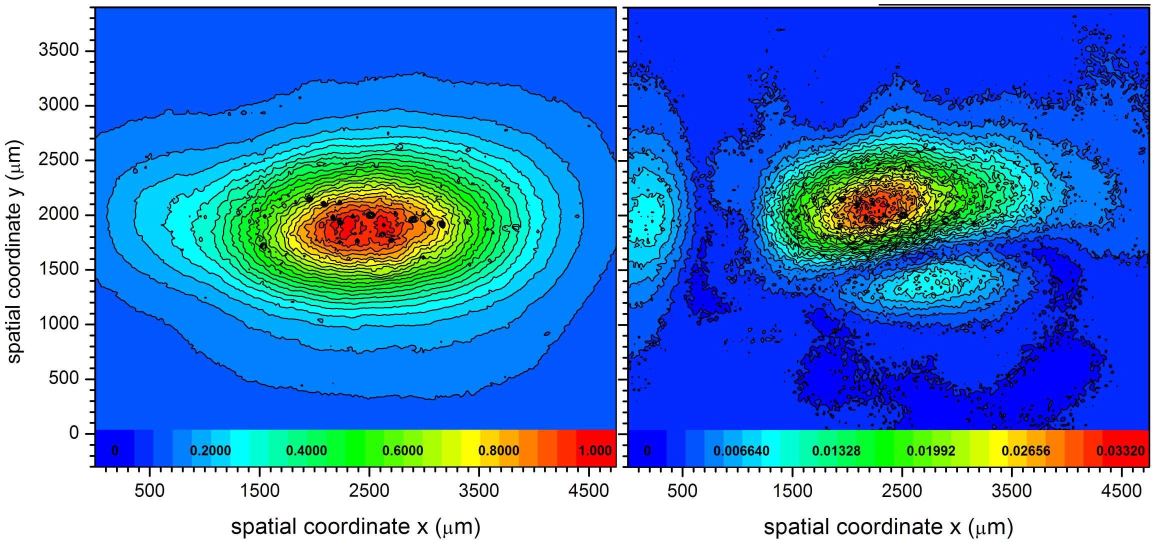

Figure 4.3.2: Averaged profile (left picture) of the harmonic beam and associated standard deviation (right picture) for the gas cell after several procedures of venting and repressurizing.

in section 4.2.3. The very good reliability and repeatability of the harmonic emission in the spatial domain implies that the same applies to the interference pattern and thus to the spectral composition of the harmonic emission. Several measurements are taken after repressurizating the gas cell, and in all cases the spectral composition of the harmonic beam is recorded over $\sim$ 10 to 100 laser shots, i.e, each measurement incorporates shot-to-shot instabilities of the fundamental laser beam. These single data sets are then normalized and compared with each other, leading to a mean value (left picture of figure 4.3.3) of the spectral profile of the harmonic beam and its standard deviation (right picture). The experimental settings for the harmonic beam are as described in the experimental conditions of section 5.2. The standard deviation across the averaged spectrum is reasonably small. For the peak of the dominant harmonic orders - 23rd to 27th - it ranges from $\sim$ 2 to 6 %. The averaged intensity of the spectral range between the harmonic orders is characterized by a standard deviation $<$ 0.2 %. This indicates a reasonably good realiability and repeatability of the spectral characteristics of the harmonic beam although the process of venting and repressurizating is a fundamental limitation in the operation of the harmonic source.

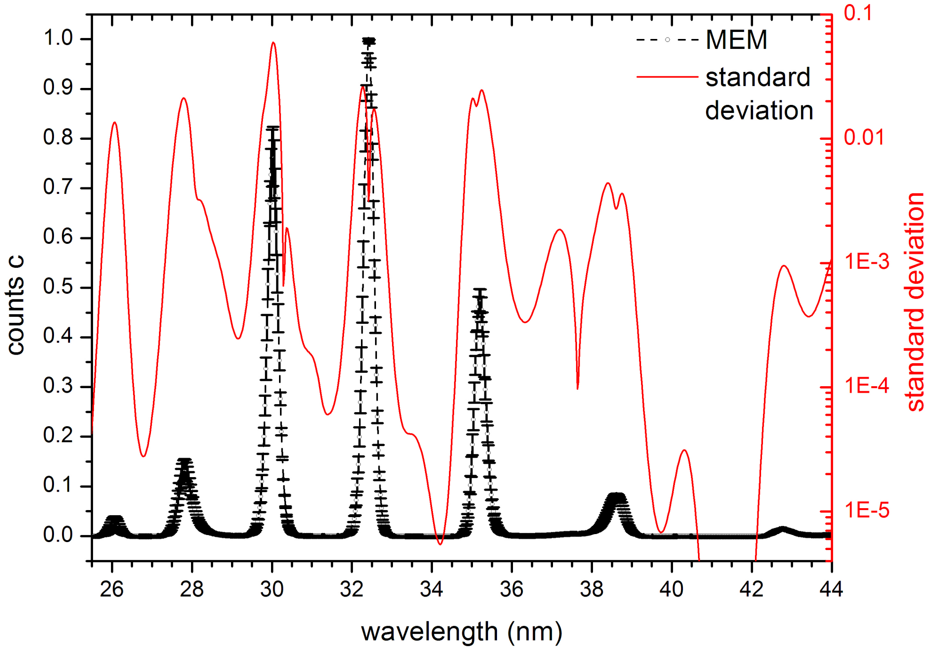

Figure 4.3.3: Averaged spectrum (black dashed curve) of the harmonic beam obtained by the maximum entropy method and associated standard deviation (red solid curve) for the gas cell after several procedures of venting and repressurizing.

4.3.4 Image stitching

The methodology of our approach to acquire diffraction information over a dynamic range that significantly exceeds the natural dynamic range of the charge-coupled detector chip involves the acquisition of one image of low-angle and two images of high-angle diffraction information. A detailed description of this work can be found in [7]. The first image features a region of interest (ROI) of low-angle diffraction data in its centre as shown in picture a) of figure 4.3.4 and denoted by ROI c. The second image (b) features high-angle diffraction data with the horizontal beam block placed in the centre of the detector chip thus avoiding saturation in ROI c. This beam block has a horizontal support that leads to missing diffraction data in the image as denoted by ROI h. The third image (c) features high-angle diffraction data with the vertical beam block placed in the centre of the detector chip thus avoiding saturation in ROI c. This beam block has a vertical support that leads to missing diffraction data in the image as denoted by ROI v. Because of their complementary information, images a), b), and

c) can be combined and stitched together. This results in the diffraction image d) that contains both low- and high-angle diffraction data without any saturation and without any diffraction information from supporting material, such as a wire that holds the object that serves as a beam block.

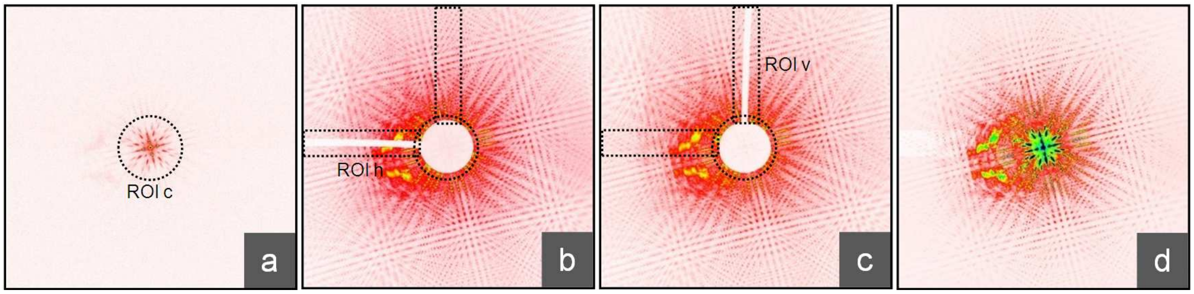

Figure 4.3.4: One image (a) of low-angle and two images (b and c) of high-angle diffraction information are acquired and stitched together to form one single image (d).

In order to smoothly stitch the information from the three images together, a region somewhat larger than ROI c/ROI h/ROI v is chosen and a coefficient function F is used to weight the data sets. This can be written as

$$I = (1 - G)\, I_{ROI\ c} + G_c \left((1 - F)\, I_{\overline{ROI\ h}} + F I_{\overline{ROI\ v}} \right), \tag{4.3.1}$$

where F and G are the coefficient functions as defined below, $I_{ROI\ c}$ is the data from ROI c as denoted in picture a) and $I_{\overline{ROI\ h(v)}}$ is the data from the pictures b) and c) with the missing data from ROI h(v). The coefficient functions F and G are Gaussian functions

$$F = exp\left(-\frac{r_F^2}{2\sigma_F^2} \right), \tag{4.3.2}$$

where

$$r_F = \begin{cases} |y - y_0|, & \text{if } r \geq R_F \\ 0, & \text{otherwise} \end{cases} \tag{4.3.3}$$

and

$$G = exp\left(-\frac{r_G^2}{2\sigma_G^2}\right), \tag{4.3.4}$$

where

$$r_G = \begin{cases} \left|x^2 + y^2\right|, & \text{if } r \geq R_G \\ 0, & \text{otherwise} \end{cases} \tag{4.3.5}$$

and x, y, y_0, r, R_G and R_F are spatial coordinates referring to the x- and y-direction and the spatial dimensions of ROI c, ROI h and ROI v.

4.3.5 Reconstruction algorithm

The conventional coherent diffraction imaging reconstruction technique is based on Fienups extensions of the algorithm first proposed by Gerchberg and Saxton [47, 44], the so-called Gerchberg-Saxton-Fienup algorithm. In the Gerchberg-Saxton-Fienup algorithm a numerical representation of a scalar wavefield is propagated between the object and detector planes using instances of the fast Fourier transformation. The wavefield in these fixed planes is constrained by the application of a priori information, and the iteration between planes is continued until self-consistency is achieved. The reliance on Fourier representations of a single scalar wavefield to carry all of the information about the target system leads to one of the most critical limitations of the Gerchberg-Saxton-Fienup approach: the incident beam that illuminates the object must be fully spatially coherent and quasi-monochromatic.

In the following, a novel approach, the so-called multiple-harmonic-order coherent diffraction imaging reconstruction algorithm, is discussed. This approach eliminates the need for an illuminating wavefield that exhibits perfect spatial and temporal coherence and allows diffraction images to be processed that are a superposition of different diffraction images associated with each harmonic order of the multiple-harmonic order high-harmonic generation source. A detailed description of this work can be found in [9]. While diffraction data produced using a high-harmonic generation source is considered explicitly here, the formalism can be readily adapted to any short-wavelength polychromatic source in which there is a high degree of spatial coherence at each sampled wavelength, but poor temporal coherence across the sampled spectrum. The novel approach may also, consequentially, be adapted and applied to the multi-mode x-ray free-electron laser sources [1] currrently are under development. The scheme of this approach is displayed in figure 4.3.5.

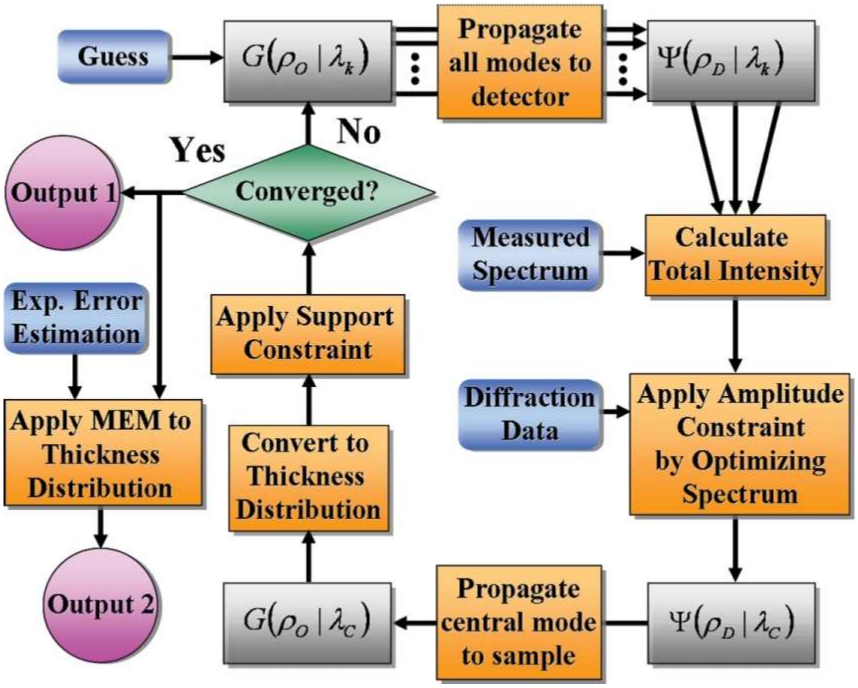

Figure 4.3.5: Scheme of the image reconstruction algorithm: the reconstruction takes place in two sections; the first, denoted output 1, is the image from the modified Gerchberg-Saxton iteration; the second, denoted output 2, is a maximum entropy method (MEM) refinement step.

4.3.5.1 Modified Gerchberg-Saxton iteration

The multiple-harmonic-order coherent diffraction imaging reconstruction approach assumes that the incident polychromatic illumination has been characterized such that the spectral power distribution, $F(\lambda)$, is known. Extraction of the spectral power distribution of the harmonic emission can be achieved by application of the maximum-entropy-method to the interference pattern of a Young double-slit illuminated with the harmonic emission. A detailed description of the formalism can be found in [8]. The total observed intensity distribution at the position (x, y) on the detector plane $I_T(x, y)$ is then the superposition of the intensity distributions $I(x, y|\lambda)$ from each part of the spectrum. Thus, the discrete form is given by

$$I_T(x, y) = \sum_{k=1}^{M} F(\lambda_k) I(x, y|\lambda_k), \tag{4.3.6}$$

where the spectrum is considered over the interval $\lambda_c - \Delta\lambda M/2 \leq \lambda_k \leq \lambda_c + \Delta\lambda M/2$, M is the total number of sample points in the spectrum, and λ_c is the central wavelength of the spectral power distribution. The scheme for the first part of the image reconstruction, the application of the modified Gerchberg-Saxton iteration, is displayed in figure 4.3.5 and discussed in the following. The wavefield from an object illuminated with a coherent plane wave of wavelength λ_k can be written in terms of the thickness function $T(\mathbf{r})$ [146]

$$G\left(\mathbf{r}|\lambda_k\right) = exp\left(i\frac{2\pi}{\lambda_k} n\left(\lambda_k\right) T\left(r\right)\right), \tag{4.3.7}$$

where the object consists of a single known material of complex refractive index $n(\lambda_k)$ and $\mathbf{r} = (x, y)$ is the spatial coordinate in the object plane. The field of the exiting wavefield $G(\mathbf{r}\lambda_k)$ after propagation from the object plane to the detector plane is described by the paraxial Fresnel free-space approximation [112]

$$\Psi\left(\mathbf{R}|\lambda_k\right) = -\frac{i}{Z\lambda_k} exp\left(i2\pi\frac{Z}{\lambda_k}\right) exp\left(i\pi\frac{R^2}{Z\lambda_k}\right) \tilde{F}\left[exp\left(i\pi\frac{r^2}{Z\lambda_k}\right) G\left(\mathbf{r}|\lambda_k\right)\right], \tag{4.3.8}$$

where $\mathbf{R} = (X, Y)$ is the spatial coordinate in the detector plane. $\tilde{F}$ denotes the Fourier transform operator and Z is the distance between the object and the detector. The total observed intensity distribution of the diffraction pattern in the detector plane is given by the superposition of the intensity distributions from each part of the harmonic power spectrum $F(\lambda_k)$. Considering the absorptive and transmissive characteristics of the sample, which depend on the wavelength via the complex refractive index $n(\lambda_k)$, the spectral power distribution of the illuminating and the exiting wavefield are not necessarily the same. Thus, the characteristics of the object need to be considered during the course of the reconstruction process. Therefore, equation (4.3.6) can be written as

$$I_T\left(\mathbf{R}\right) = \sum_{k=1}^{M} \tilde{F}\left(\lambda_k\right) \left|\Psi\left(\mathbf{R}\right)|\lambda_k\right|^2, \tag{4.3.9}$$

where $\tilde{F}\left(\lambda_k\right)$ is a function of $F\left(\lambda_k\right)$ and $n(\lambda_k)$. Reconstruction of the thickness function $T(\mathbf{r})$, and thus reconstruction of the object itself, is achieved by employing a modified algorithm from the method used in coherent quasi-monochromatic diffractive imaging. In order to initialize the algorithm, estimates of the starting conditions need to be given: estimation of the initial form of the thickness function $T(\mathbf{r})$ and calculation of the exiting wavefield $G(\mathbf{r}|\lambda_k)$ for all individual harmonic orders centred at the wavelengths λ_k of the spectral power distribution of the harmonic beam. The reconstruction is then obtained by iteratively applying the following steps until the iteration is self-consistent:

Estimation of the initial form of the thickness function $T(\mathbf{r})$ and calculation of the exiting wavefield $G(\mathbf{r}|\lambda_k)$ for all individual harmonic orders centred at the wavelengths λ_k of the spectral power distribution of the harmonic beam.

Propagation of the exiting wavefield for the detector plane, $\Psi(\mathbf{R}\lambda_k)$, for all harmonic orders.

Superposition of the propagated wavefields and thus calculation of the total intensity distribution $I_T(\mathbf{R})$.

Consideration of the effect of the characteristics of the sample on the spectral power distribution of the exiting wavefield, thus optimizing $\tilde{F}(\lambda)$ and imposing the amplitude constraint.

Propagation of the central mode at the wavelength λ_k back to the object plane and extraction of the thickness function $T(\mathbf{r})$.

Application of a support constraint and calculation of the exiting wavefield $G(\mathbf{r}|\lambda_k)$ for all harmonic orders centred at the wavelengths λ_k of the harmonic beam.

The key extension in this algorithm compared to the Gerchberg-Saxton-Fienup formalism is a combination of employing multiple forward-propagation modes, $G\left(\mathbf{r}|\lambda_{1\ldots M}\right) \xrightarrow{FFT} \Psi\left(\mathbf{R}|\lambda_{1\ldots M}\right)$, and a single back-propagation mode, $\Psi\left(\mathbf{R}|\lambda_c\right) \xrightarrow{FFT} G\left(\mathbf{r}|\lambda_c\right)$, during the process of reconstruction, where M is the total number of sampled points of the spectral power distribution $F(\lambda)$, c refers to the central wavelength λ_c of that spectrum and FFT stands for fast Fourier transform. The spectral power distribution $F(\lambda_k)$ can change to $\tilde{F}(\lambda_k)$ during the propagation of the illuminating wavefield through the object. The initial spectral power distribution is extracted from the interference pattern of a Young double-slit that is illuminated with the harmonic emission by application of the maximum-entropy-method. A detailed description can be found in [8]. Using this initial spectrum as a starting point, the predicted intensity distribution, $I_T\left(R\right)$, is fitted to the measured intensity distribution, $I_{exp}\left(R\right)$, via the distribution of spectral weights. The spectrum optimization procedure is based on the gradient descent rule, which can be deduced from the error cost function

$$E^2 = \frac{1}{2N}\sum_{j=1}^{N}\left(\sqrt{I_T\left(R_j\right)} - \sqrt{I_{exp}\left(R_j\right)}\right)^2. \tag{4.3.10}$$

Here $I_T(\mathbf{R})$ is as defined by equation (4.3.9). The gradient descent based spectral optimization is reached through iterations n = 0,1,2, ... defined by

$$\tilde{F}^{n+1}(\lambda_k) = \tilde{F}^{n}(\lambda_k) - \eta\frac{\partial E^2}{\partial F(\lambda_k)}, \tag{4.3.11}$$

where η is a positive step-size parameter. The amplitude constraint is defined by

$$\Psi\left(\mathbf{R}|\lambda_k\right) = \Psi\left(\mathbf{R}|\lambda_k\right)\frac{\sqrt{\tilde{I}\left(\mathbf{R}|\lambda_k\right)}}{\left|\Psi\left(\mathbf{R}|\lambda_k\right)\right|}, \tag{4.3.12}$$

where

$$\tilde{I}\left(\mathbf{R}|\lambda_k\right) = \tilde{F}\left(\lambda_k\right)\left|\Psi\left(\mathbf{R}|\lambda_k\right)\right|^2 \frac{\sum_{j=1}^{N} I_{exp}\left(R_j\right)}{\sum_{j=1}^{N} I_T\left(R_j\right)}. \tag{4.3.13}$$

4.3.5.2 Maximum entropy method based reconstruction refinement

The output of the modified Gerchberg-Saxton iteration, the thickness function $T(\mathbf{r})$, can contain some noise artefacts due to the reconstruction algorithm fitting noise within the original data set. The quality of this output can be improved by application of the maximum entropy method. The procedure of the application of the maximum entropy method based refinement of the reconstruction from the modified Gerchberg-Saxton iteration is the second part of the image reconstruction. The scheme of this approach is displayed in figure 4.3.5. Similar to the application of the maximum entropy method to the interference pattern of a Young double-slit illuminated with the multiple-order harmonic emission, where the most probable spectral power distribution is determined by the distribution and the maximum value of the entropy functional is achieved, the most probable thickness function $T(\mathbf{r})$ is given by the thickness distribution where the entropy functional reaches its maximum as explained in section 4.2.3. A detailed description can be found in [147]. As further explained in section 5.4.3.1, the maximum entropy method refinement produces a much smoother image. However, some of the details of the reconstruction from the modified Gerchberg-Saxton iteration are lost. This indicates that the algorithm is probably under-fitting the data due to an over-estimate of the noise level in the data.

4.3.6 Sample preparation

The work on coherent diffractive imaging presented in this dissertation is based on different samples and presented in sections 5.4.3 and 5.4.4. Binary periodic and aperiodic samples are used, where binary refers to either transmissive or absorptive, and periodic and aperiodic refer to a two-dimensional array with pinholes of the same or different size and shape. These samples are prepared by etching techniques and could be mounted on the sample host without any further work. However, a non-binary periodic sample with a wavelength-dependent refractive index has been chosen as well, consisting of a thin perforated carbon film mounted in a sandwich. A precision pinhole in the sandwich defines the sample and the area is illuminated with the multiple-order harmonic beam. In the following, the carbon film sample, its preparation and effects of the quality of the sandwiched precision pinhole are discussed.

4.3.6.1 Holey carbon film samples

The non-binary periodic sample is a perforated carbon film mounted on a copper grid (2SPI Quantifoil). The carbon film has to be sandwiched so that it can be mounted on the sample host. As shown in picture a) of figure 4.3.6, the carbon film is mounted on a precision pinhole by means of a fixation ring. The pinhole is necessary to define the size of the illuminated area. This sandwich is then mounted on a metal ring that is part of the sample host. The sample holder is discussed in section 3.3.3.2. The carbon film is of thickness $\sim$ 40 nm and is mounted on a copper grid as shown in picture b). A zoom into this picture shows a small part of the sample lying on the copper grid as shown in picture c). Here, a specific sample (2SPI Quantifoil R2/1) is shown. The carbon film exhibits an array of pinholes with diameter 2 μm and a spacing of 3 μm between the pinholes. However, different samples are available, where the pinholes have a different size and spacing or are irregular. Due to the manufacturing process, there is a possibility that parts of the carbon film are covered with a polymer layer of thickness $\leq$ 20 nm. Picture d) shows the 20 μm-diameter precision, high-quality pinhole (Melles Griot mounted standard precision pinholes and mounted pinholes for high-energy laser applications) used to define the area of the carbon film that is illuminated with the emission of the multiple-order harmonic beam. The pinholes are made up of either stainless steel or gold-coated copper substrates, and are thus opaque to the harmonic beam, and have been processed by femtosecond-laser ablation. For the 20 μm-diameter precision standard pinhole the manufacturer states an uncertainty of 2 μm for the diameter and a thickness of 13 μm. However, the diameter of the pinhole is less important than the actual quality of the edges of the pinhole. The quality can very drastically affect the diffraction images as discussed below in section 4.3.6.3.

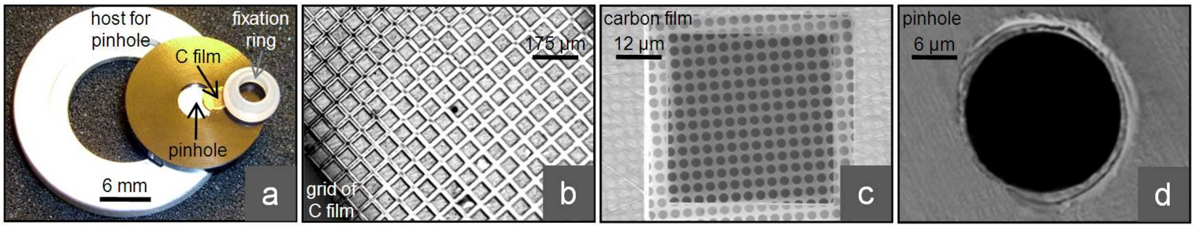

Figure 4.3.6: Preparation of the carbon film sample: the carbon film is mounted in a sandwich structure (a); support grid of the carbon film (b); carbon film on grid (c); 20 μm-diameter pinhole to define the area of the carbon film for diffractive imaging (d).

4.3.6.2 Alignment of the holey carbon film samples

As shown in picture c) of figure 4.3.6, the thickness of the support grid is the same size as the length of the free area between the grids. The diameter of the sandwich pinhole is half of that length. Thus, although one-quarter of the supported carbon film is actual carbon film that can be illuminated with the harmonic beam, the alignment of the free standing carbon film with the pinhole needs to be verified before the sample is installed inside the experiment section of the high-harmonic generation apparatus on the sample host. Verification of the alignment is performed by optical microscopy as shown in figure 4.3.7. After mounting the sandwich the condition of the carbon film (picture a)) and its position with respect to the pinhole (picture b)) is examined. A transmission image (picture c)) then confirms that the beam path for the harmonic beam through the pinhole and the carbon film is clear.

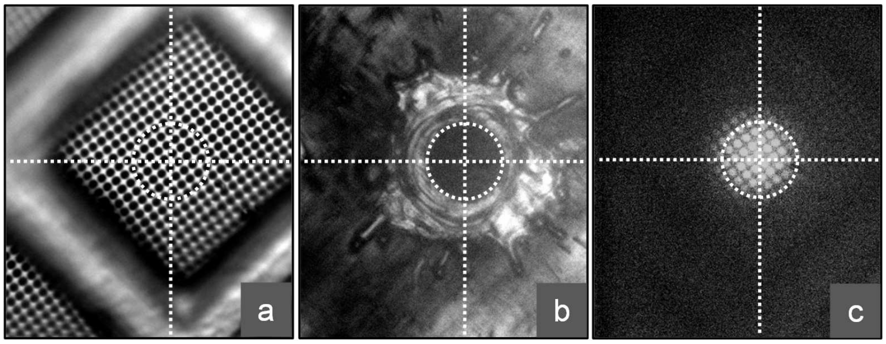

Figure 4.3.7: Alignment of the sandwiched carbon film sample by optical microscopy: intact surface of the carbon film (a) mounted on the pinhole (b); transmission image of the sandwich (c).

4.3.6.3 Effect of the pinholes on the diffractive images

The carbon film is mounted on a precision pinhole by means of a fixation ring as shown in picture a) of figure 4.3.6. The pinhole, as shown in picture d), serves to define the region of interest of the carbon film sample that is illuminated with the harmonic emission. In all experiments and in all fabricated sandwiches so-called precision pinholes are used. The pinholes are fabricated by femtosecond-laser fabrication, and the term precision refers to the diameter of the pinholes. However, it strongly depends on the quality of the edges of the particular pinhole used in the sandwich whether the diffraction images are free of distortions and can be used for coherent diffractive imaging.

Ideally the pinhole is a two-dimensional plane that serves to restrict the area of illumination of the carbon film sample. Light traversing such a circular pinhole produces a diffraction pattern of concentric rings of decreasing width with increasing radius. To a good approximation this applies to the pinhole in the picture d) of figure 4.3.6, and, in fact, successful coherent diffractive imaging can be performed with that pinhole as discussed in section 5.4.3.1. Picture a) in figure 4.3.8 shows another 20 μm-diameter pinhole used for coherent diffractive imaging of the aforementioned carbon film sample. The thickness of this pinhole is 13 μm and it exhibits a distinct structure of the surface throughout its thickness. The diffraction pattern of the pinhole is displayed in picture b) and, in particular, exhibits three regions of high-intensity features (dotted ellipses). The diffracted intensity of the concentric rings is small compared to diffractive features that result from the dominant three-dimensional structure of the pinhole. Using the pinhole for coherent diffractive imaging of the carbon film sample leads to the diffraction pattern shown in the pictures c) and d). In picture c) the harmonic beam first passes the pinhole and then the carbon film. The diffractive features of the pinhole dominate the diffractive features of the carbon film and, in particular, three regions of high-intensity features (dotted ellipses) can be seen that spatially coincide with the regions marked by dotted ellipses in picture b). In picture d) the harmonic beam first passes the carbon film and then the pinhole. Here, the diffractive features of the carbon film dominate and, in particular, a radial ray structure can be seen. The intensity of these rays is small compared to the intensity of the centred diffractive features of the carbon film, but large compared with the large-angle diffractive features.

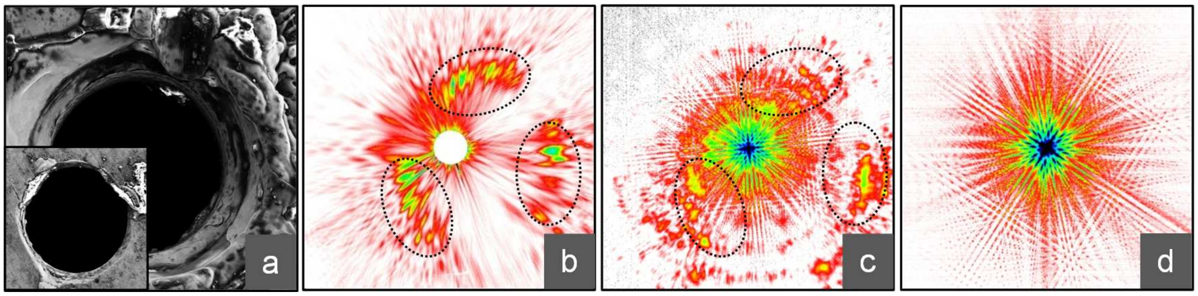

Figure 4.3.8: Distortions in the diffractive images: complex structure of the mounted pinhole on both sides (a); diffraction pattern of the pinhole (b); harmonic beam illuminates the pinhole first, then the carbon film (c); harmonic beam illuminates the carbon film first, then the pinhole (d).

In both cases, pictures c) and d) in figure 4.3.8, the modified Gerchberg-Saxton iteration, as discussed in section 4.3.5, is not able to recover the illuminated carbon film sample. In the case of the aforementioned carbon film, whose structure can be verified by means of scanning electron microscopy, the diffraction pattern can be simulated to a very good approximation. Thus the effect of the pinhole with dominant three-dimensional structural elements can be identified. However, employment of a pinhole can hamper or even spoil the reconstruction of the coherent diffractive images of samples that cannot be analyzed by means of other experimental methods. In fact, this is the case for objects of interest such as clusters of biomolecules and in particular membrane proteins. If the illuminated area of such a sample needs to be restricted by such a pinhole, then it has to be guaranteed that the pinhole does not affect the diffraction pattern as discussed above. Experimentally it turned out that even pinholes with smooth edges and of apparently high quality can significantly contribute to the diffraction pattern. In order to avoid dominant contributions from the pinhole due to its three-dimensional structure to the diffraction pattern of the sample of interest, e.g., the carbon film, the pinholes are first mounted on the sample holder without any mounted sample. The diffraction pattern of the pinhole is recorded. Only if the diffraction pattern is dominated by concentric rings of decreasing width with increasing radius is such a pinhole used for coherent diffractive imaging.

Chapter 5

Results and discussion

In the following chapter the experimental results for the argon and helium gas cell are presented. The sections of this chapter are self-consistent and presented in the style of a publication. Thus, this chapter can be read on its own without the need for any other chapter. By varying the diameter of the aperture applied to the fundamental laser beam and the position of the laser focus inside the argon gas cell, the harmonic beam is studied in the spatial and spectral domain and the flux of the multiple-order harmonic emission is studied. In particular, spectral characterization is performed across the spatial profile of the harmonic beam. Moreover, phase-matched high-order harmonic generation in a helium and an argon semi-infinite gas cell are analyzed and compared by variation of the effective interaction length between the laser field and the nonlinear medium. The coherence lengths related to plasma formation and the Gouy phase shift on the output are observed, and the atomic scattering factors for photoabsorption, the effective propagation lengths and the energy conversion efficiencies are deduced. Furthermore, the degree of spatial coherence is measured for various experimental conditions in the centre of the beam as well as across the profile of the harmonic emission.

5.1 Applying an aperture to the fundamental laser beam (argon)

Studies of the spatial mode and its intensity and in-situ spectral characterization of the high-harmonic emission from a semi-infinite argon-filled gas cell driven by a femtosecond laser are performed. The harmonic output is tailored by positioning the laser focus with respect to the exit plane of the gas cell and by applying an aperture of variable diameter to the laser beam. Analysis of the spectral characteristics is performed in-situ by applying the maximum entropy method to the interference pattern emerging from a Young double-slit pair illuminated by the harmonic emission. This method allows the high-harmonic generation emission to be precisely and simultaneously scanned in its spatial and spectral domain and in particular the spectrum to be probed across the harmonic beam.

5.1.1 Introduction

In the following, the high-harmonic emission from a semi-infinite argon gas cell in its spatial and spectral domain is discussed. Efficient generation of two to seven highly coherent harmonic orders in a tunable band from 26 to 43 nm is achieved. Changes of the spatial mode and its intensity are discussed and in-situ spectral characterization of the harmonic output is performed while scanning the position of the laser focus with respect to the exit plane of the gas cell and while varying the diameter of an aperture applied to the laser beam. In-situ spectral characterization is performed by applying the maximum entropy method to the interference pattern emerging from a Young double-slit pair illuminated with the output of this source [8]. The Young double-slit pair can be precisely positioned between the detector and the harmonic source and, in particular, at any point across the harmonic beam. This method allows the spectrum to be precisely and simultaneously scanned in the centre and across the harmonic beam and the harmonic modes to be characterized in both their spatial and spectral domain.

Relinquishing the use of a monochromator has several important advantages and is a necessity for precise spatial scanning of the harmonic spectrum across the whole beam. Any inefficiencies or imperfections of the monochromator are avoided and all available harmonics can be utilized for experimental usage leading to a high effective photon flux.

5.1.2 Experimental conditions

The pump laser for the harmonic source is a 1-kHz multi-pass chirped-pulse amplifier system that produces 30-fs pulses centred at 805 nm. The unapertured and unfocused laser beam has a e^{-2}-diameter of 12 mm and an energy of 2 mJ per pulse. The spatial profile of the laser beam is of elliptical shape and characterized by $M_x^2/M_y^2 \approx 1.30/1.34$ and a beam pointing of $x/y \approx 6.3/13.2$ mrad (see section 3.1). The spatial profile of the laser beam exhibits distortions in the wings ($\sim$ 4 to 5 mm from the beam centre) that carry significant power. A calibrated aperture of diameter $w = 1$ to 12 mm mounted on a precision x/y-translation stage is inserted in the beam before it is focused into an argon gas cell by a lens of focal length 500 mm and diameter 2.54 cm. The lens is mounted on a precision $x/y/z$-translation stage to allow proper alignment with respect to the centre of the laser beam and to move the laser focus longitudinally with respect to the exit plane of the gas cell. The argon gas cell is operated at 15 Torr and has a glass window for entry of the laser pulses and a 100 to 200 μm-wide exit pinhole at its end to out-couple the harmonic emission. In vacuum, the theoretical e^{-2}-radius of the focused intensity distribution of the apertured femtosecond laser beam varies from $r_{focus}(w) = 57$ to 31 μm (figure 5.1.1) and the theoretical Rayleigh range varies from $\langle R_{focus}(w) \rangle = 20$ to 5 mm (figure 5.1.2) for an aperture with diameter ranging from $w = 3$ to 6 mm [129]. Because of the chosen focal geometry and defocusing due to the intrinsic plasma generation, the effective focused intensity is $< 3 \times 10^{14}$ W/cm^2. The harmonic beam which is separated from the fundamental laser beam by means of aluminium spectral filters propagates into an experimental vacuum chamber operated at a pressure of $< 10^{-5}$ Torr. A translation stage holds three pairs of Young double-slits separated by a distance of 1 mm. The one used for the experimental work presented here has a slit-to-slit spacing of 20 μm and a slit width of 5 μm. All the Young double-slits can be precisely moved at any point in the harmonic beam. A 50 μm-wide precision pinhole, that is placed at a distance of 20 cm in front of the three different Young double-slits, is used to spatially restrict the harmonic beam to only one Young double-slit in order to avoid simultaneous illumination of all three pairs with the harmonic beam. In this experiment diffraction due to the spatial filter and the exit pinhole of the gas cell can be neglected. The beam and the interference pattern are detected with a 26.8 mm×26.8 mm charge-coupled device chip of pixel size 20 μm×20 μm (see section 3.3.4.1). The geometry for all experiments is: $D = 20$ μm, $W = 5$ μm, $Z = 0.26$ m, $L = 0.68$ m and $P = 0.43$ m (see figure 4.2.3). Optionally, a grazing incidence spectrometer (Setpoint GIMS#4) can be inserted into the beam path. The harmonic spectrum is recorded by precision rotation of a 300 grooves/mm-grating that covers a spectral range from $\sim$ 18 to 42 nm. The maximum entropy method is

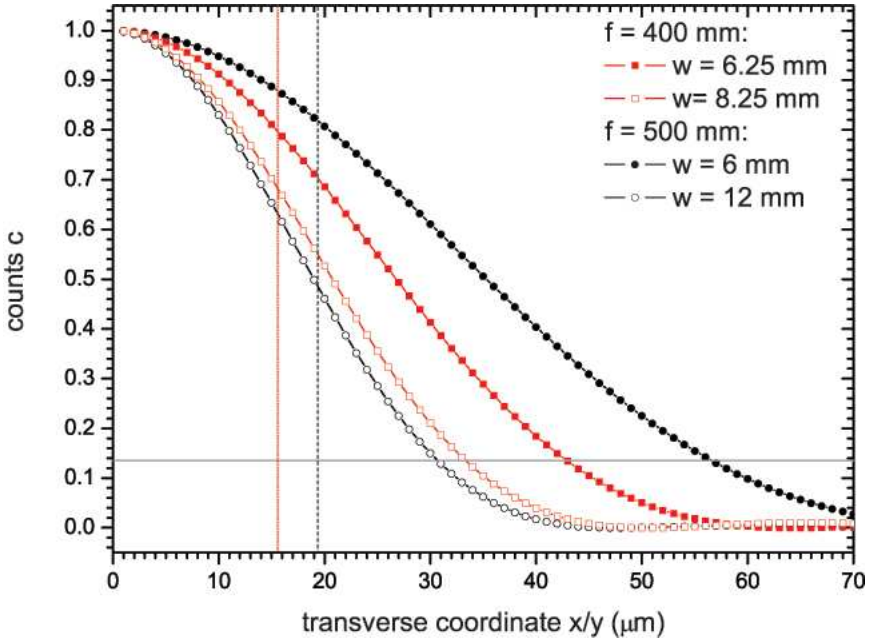

Figure 5.1.1: Radial intensity distribution of the fundamental laser beam for different aperture diameters and for the 400 and 500 mm-focal length lenses. The black short dash (red dot) solid vertical line indicates the diffraction limit of the lens of focal length 500 (400) mm.

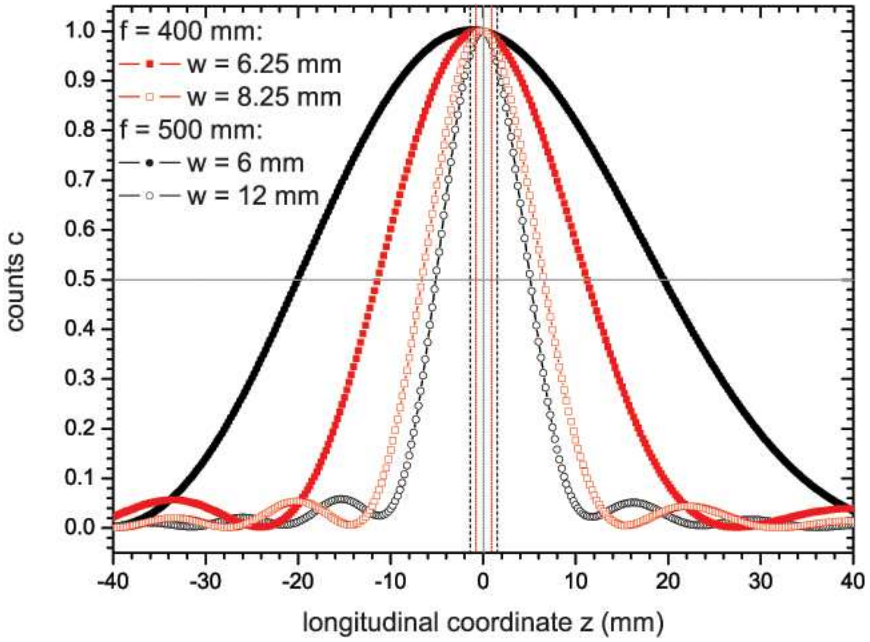

Figure 5.1.2: Rayleigh range of the fundamental laser beam for different aperture diameters and for the 400 and 500 mm-focal length lenses. The black short dash (red dot) solid vertical line indicates the diffraction limit of the lens of focal length 500 (400) mm.

applied to the recorded interference pattern from the Young double-slit pair in order to reconstruct the power spectrum of the harmonic emission [8]. This method allows in-situ precision spectral characterization of the harmonic source and, in particular, allows the spectrum to be probed in any region across the spatial profile of the harmonic beam. The validity of the generated spectrum is tested with respect to small changes of the geometrical parameters of the experimental setup and the parameters that are significant for extracting the cross-section of the recorded interference pattern. The chosen parameters allow efficient, stable and reliable application of the maximum entropy method algorithm to the recorded interference pattern for extraction of the spectral characteristics (see figures 4.2.4 and 4.2.6).

5.1.3 Spatial and spectral characteristics and harmonic flux

5.1.3.1 Introduction

We assume a laser beam that is Gaussian in its spatial domain and incorporate a Strehl ratio of 0.4. Easy estimations of the focal volume are presented in section A.2. The three-dimensional field distribution of truncated non-telecentric focusing systems can be very complex and depends strongly on the experimental conditions. Depending on the Fresnel number and the aperture-lens separation, focal shifts and asymmetric field distributions around the focus may have to be taken into account [125, 126, 127, 128]. For our experimental parameters, these effects are usually small and can be neglected. The truncation coefficient is defined as

$$\alpha = \left(\frac{a}{w}\right)^2, \tag{5.1.1}$$

where a is the diameter of the aperture and w is the spot size of the Gaussian beam at the plane of the aperture. For $0.25 \leq \alpha \leq 1$, the confocal parameter of the truncated focused Gaussian laser beam ranges from 39.6 to 10.2 mm as shown in figure 5.1.2 [129]. For $\alpha \approx 1$ the confocal parameter can be of the size of the displacement of the focal point with respect to the exit from the gas cell. However, in that case a significant fraction of plasma would be formed which would dominate the propagation of the laser pulse in argon gas at 15 Torr and lead to Rayleigh ranges that are up to a factor of 1.66 larger compared to diffraction-limited Gaussian laser beams [148]. Moreover, the spatial quality of the laser beam and imperfections of any optics in the beam can lead to a longer longitudinal focal volume. We neglect self-focusing and filamentation [130, 131] as 63 GW$< P < P_{crit}$, where P is the laser power and $P_{crit} \approx 100$ GW is the critical power for argon gas at a pressure of 15 Torr [132]. Thus, the mechanism dominating high-intensity pulse propagation and tight focusing in our experiment, corresponding to $\alpha > 0.5$, is ionization-induced defocusing.

5.1.3.2 Spatial characteristics

In figures 5.1.3 and 5.1.4 we present the results of studies of the harmonic beam in the spatial domain with the in-vacuo laser focus placed in the exit plane of the gas cell and 10 mm inside the gas cell for $0.25 \leq \alpha \leq 1$. The outer and inner white perimeters of the beam cross-section indicate normalized intensities of 19 % and 41 %, respectively. In both cases of the focus position and for small α, in particular $\alpha < 0.39$, the beam cross-section has a circular-like shape and does not vary much. The diffraction-induced decrease in radial focal volume for larger aperture diameters is compensated by a higher transmission of energy, $T = 1 - exp(-2\alpha)$, of the Gaussian TEM_{00} laser mode by the aperture for larger values of α. Thus, the effective transverse interaction volume does not change significantly. The high spatial quality is achieved because distorted parts of the beam are discarded by the aperturing of the laser beam and, in particular, any asymmetry of the beam with respect to different values of the beam diameter, divergence, M^2 and pointing for the x- and y-direction can be neglected. For $0.39 \leq \alpha \leq 0.5$, when the flux or intensity is highest, the beam mimics the characteristics of the laser beam and is of elliptical shape. Severe distortions develop for larger α when distorted parts of the laser beam can pass the aperture. The cross-section grows quickly along the major ellipse axis and slower along the minor ellipse axis and turns into a rhombus-like shape. The spatial distortions are much more severe when the laser focus is placed at the exit of the gas cell, in particular for $0.69 \leq \alpha \leq 1$. The harmonic beam splits into two local centres along the former minor axis of the ellipse which move away from each other for larger α. It is well known that defocusing effects can lead to oscillating intensity at specific points in time and space of the laser beam and form two packets that move away from each other [136]. However, the formation of the centres only occurs along the former minor ellipse axis and not in a ring structure. Also, this phenomenon should be more prominent in the case when the laser focus is placed inside the gas cell rather than at the exit due to the longer propagation length. We therefore attribute this complex spatial pattern to peculiarities of the gas flow around the exit plane of the gas cell and possibly off-axis phase-matching [22].

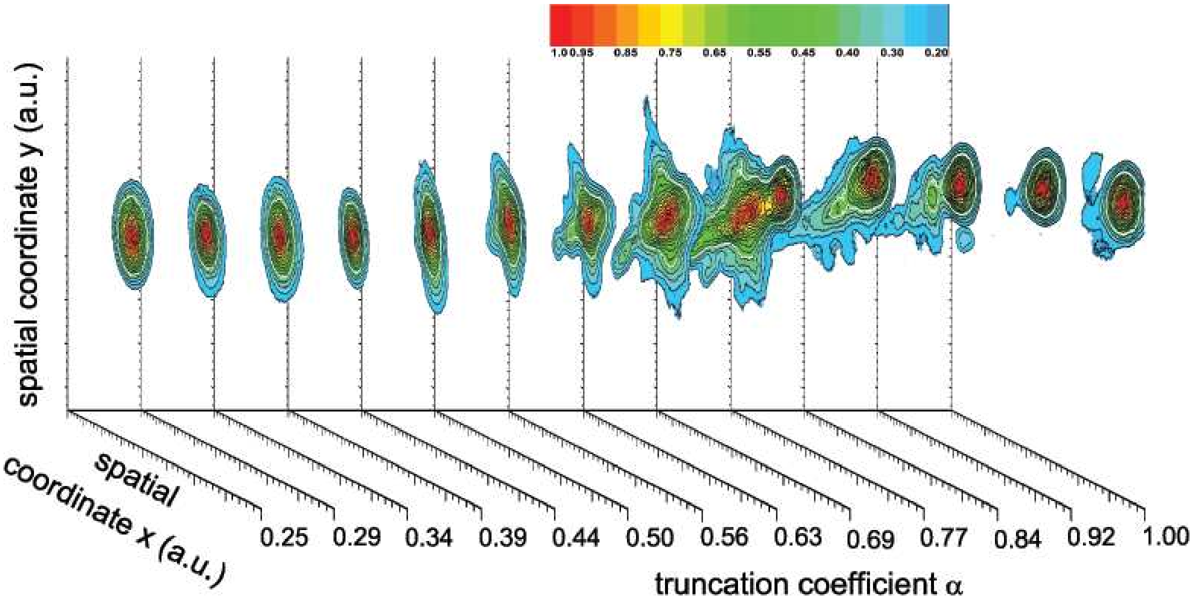

Figure 5.1.3: Contour plots of the harmonic beam with the laser focus placed in the exit plane of the gas cell for $0.25 \leq \alpha \leq 1$. The outer (inner and white) perimeter indicates an intensity of 19 % (41 %).

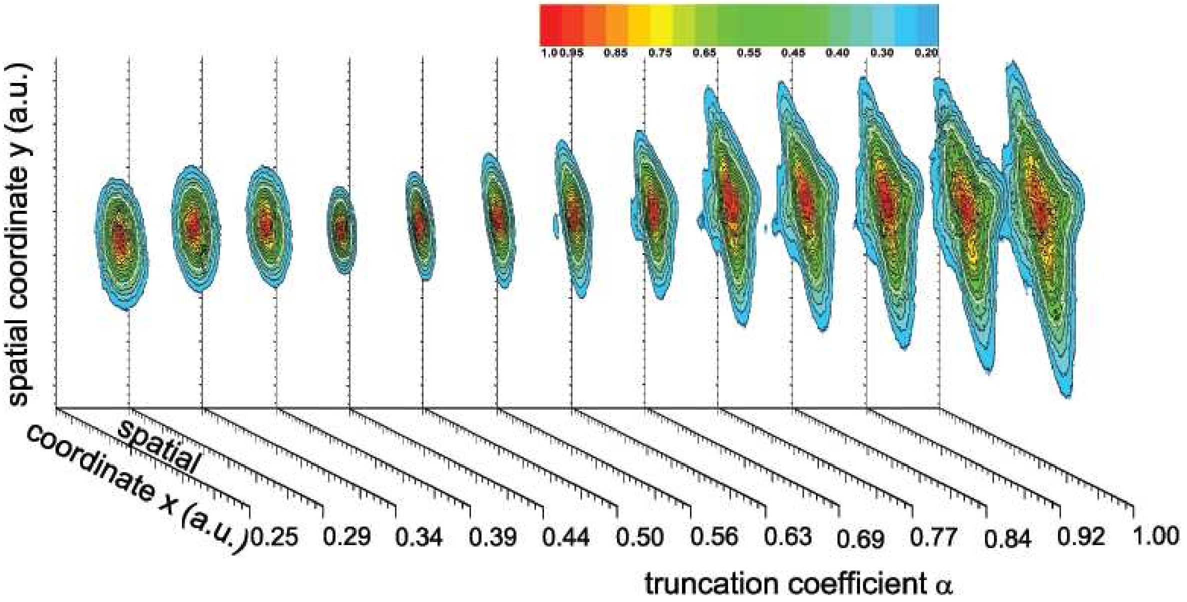

Figure 5.1.4: Contour plots of the harmonic beam with the laser focus placed 10 mm inside the gas cell for $0.25 \leq \alpha \leq 1$. The outer (inner and white) perimeter indicates an intensity of 19 % (41 %).

5.1.3.3 Harmonic intensity

Figure 5.1.5 displays the relative intensity of the harmonic beam for the two focus positions. When the laser focus is placed at the exit of the gas cell, the intensity curve exhibits a characteristic sharp rise for smaller values of α before falling off. This behaviour is the same for all harmonic orders within the plateau and is qualitatively the same for different gases [89]. In fact, when the laser focus is placed in the exit plane of the gas cell, the difference between the maximum intensity and the intensity when the laser beam is unapertured spans three orders of magnitude. However, when the laser focus is placed inside the gas cell there is no characteristic peak structure and the maximum achievable intensity corresponds to the intensity achieved for the unapertured laser beam. This effect cannot be explained by absorption due to the long propagation length of $\sim$ 10 mm after the focus in argon gas. Rather, it is attributed to different phase-matching conditions that favour higher-order harmonic orders close to the cutoff that are of low intensity (see also figure 5.1.6).

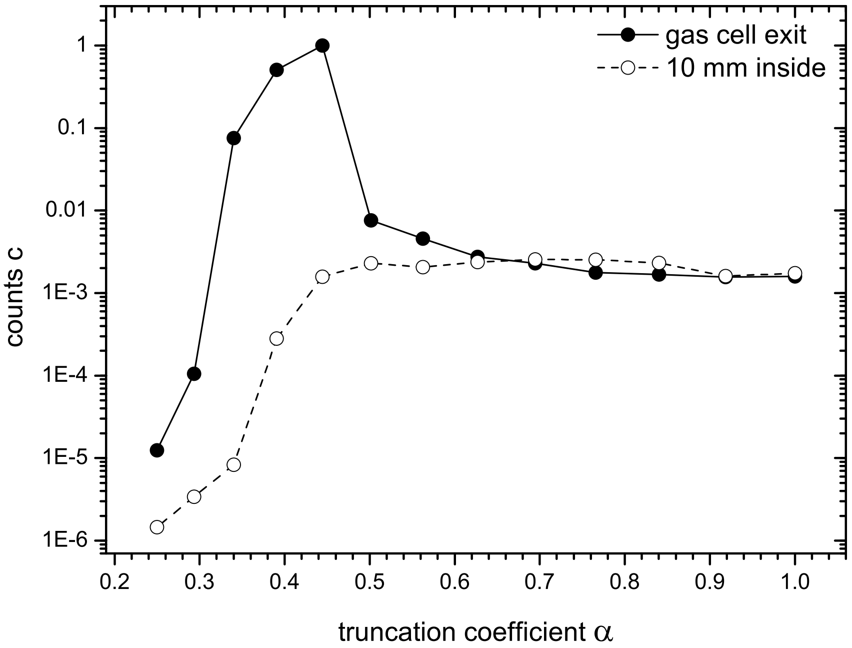

Figure 5.1.5: Relative intensities of the harmonic beams for the laser focal point placed at the exit of (black solid dots) and 10 mm inside the gas cell (black hollow dots).

5.1.3.4 Spectral characteristics

In figure 5.1.6 we present studies of the harmonic beam in the spectral domain with the in-vacuo laser focus placed at the exit plane of the gas cell and 10 mm inside the gas cell for $0.39 \leq \alpha \leq 0.92$. For relative comparison the power spectra have been normalized. The harmonic cutoff,

$$q_{max} = \frac{I_p + 3.17U_p}{\hbar\omega}, \tag{5.1.2}$$

increases steadily with increasing α. I_p is the ionization potential and $U_p = e^2E^2/(4m\omega^2) = 9.33 \times 10^{-14} I\lambda^2$ $[eV]$ is the ponderomotive potential; e, E, m, ω, I [W/cm^2], and λ [μm] are the electron charge, electric field amplitude, electron mass, laser angular frequency and intensity, respectively. Depending on whether the laser focus is at the exit or inside the gas cell, the most intense highest harmonic order, as well as highest flux, is observed for $\alpha = 0.39$ or $\alpha = 0.44$ when the focused intensity approaches the threshold intensity $I_{thr} \approx 2.5 \times 10^{14}$ W/cm^2; i.e., when an electron is stripped off the atom. For larger α the focused intensity will still increase until it converges towards its ultimate limit of $I_{max} = 3.0 \times 10^{14}$ W/cm^2 due to defocusing. This value is determined by the maximum achievable ionic charge state

$$\eta_{max} = C^2 N_c/N \approx 0.36 \tag{5.1.3}$$

and only depends on the half-angle of convergence $C \approx r/f$, where $f = 500$ mm is the focal length of the lens, $r = w/2$, N is the gas number density of the generating medium and N_c is the critical electron number density of the plasma [148]. I_{max} is associated with the generation of the 47th harmonic order. According to the Ammosov-Delone-Krainov ionization rate model [74], I_{max} is the effective intensity that generates a plasma fraction of 0.36, which is reached approximately 8 fs after the peak of the electric field when the neutral medium is depleted by 20 % (see figure 5.1.7). So, for any α the gas can be exposed to the peak of the electric field envelope and thus can generate harmonic orders for intensities up to I_{max}. Although the focused intensity can be larger than I_{thr}, the power spectra shift to higher wavelengths for $\alpha > 0.44$ due to significant plasma generation. Relatively, but not absolutely, the power spectra exhibit stronger higher harmonic orders when the laser is focused inside the gas. However, relatively as well as absolutely, the power spectra exhibit more intense low harmonic orders when the laser focus is placed at the gas cell exit indicating absorption characteristics for argon gas as well as phase-matching conditions that favour lower harmonic orders. For $\alpha > 0.44$ significant plasma formation takes place and manifests itself in an increased spectral width as well as spectral blue-shifting [137, 138, 139]. These effects are more prominent for a longer interaction length, when the laser focus is placed inside the gas cell, and for increasing focal energy densities, when α is larger. When the laser focus is at the exit of the gas cell, and for $0.6 \leq \alpha \leq 1$, the harmonic beam splits into two parts. The spectrum is determined for the more intense part and appears significantly red-shifted. Propagational frequency shifting is neglected since the laser focus is placed in the exit plane.

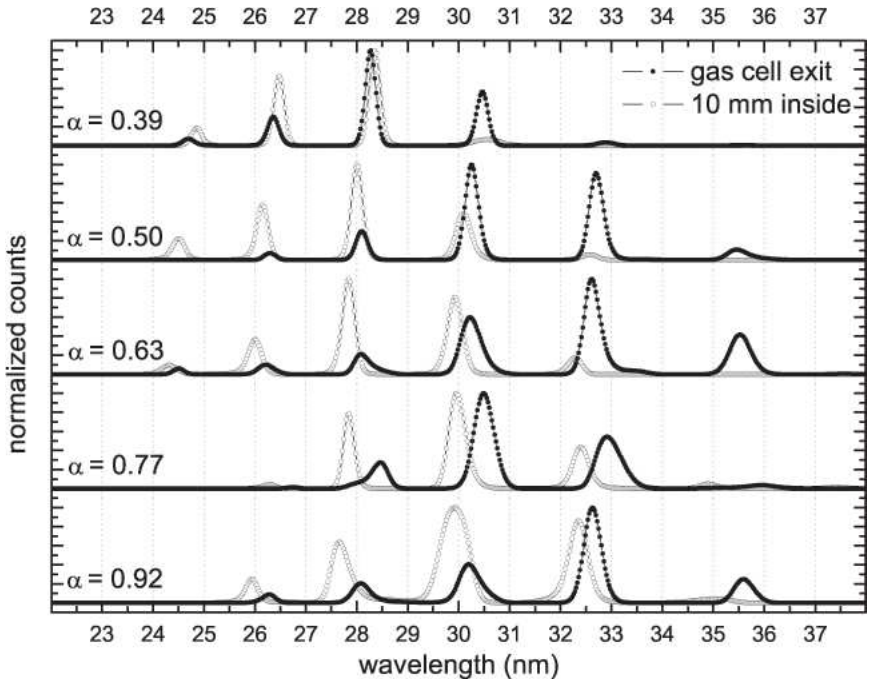

Figure 5.1.6: Harmonic beam in the spectral domain when the laser focus is placed at the exit of the gas cell (black solid dots) and 10 mm inside the gas cell (black hollow dots) for $0.39 \leq \alpha \leq 0.92$.

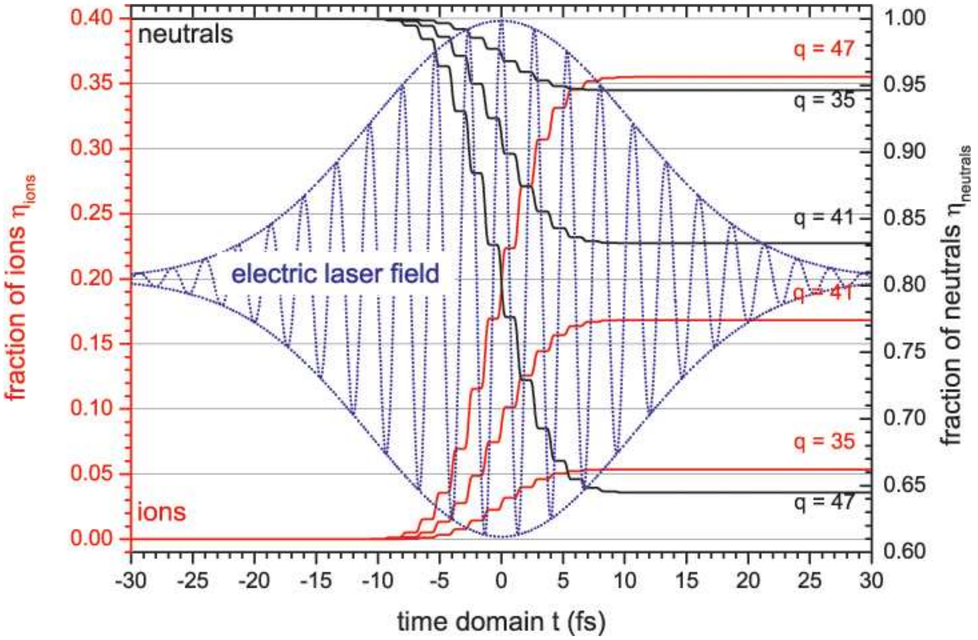

Figure 5.1.7: Calculation of the fraction of ions η_{ions} and neutrals $\eta_{neutrals}$ for the detected maximum harmonic order 47th (corresponding to I_{max}) and the orders 41 (corresponding to I_{thr}) and 35 in argon.

5.1.3.5 Conclusion

Studies of the spatial mode of a multiple-order harmonic beam and its intensity are presented and in-situ spectral characterization of femtosecond laser-driven high-harmonic emission from a semi-infinite argon gas cell is performed. The harmonic output can be efficiently tailored by positioning the laser focus and applying an aperture to the laser beam. High spatial quality and high intensity of the harmonic beam are achieved for small aperture diameters and when the laser focus is placed close to the exit plane of the gas cell. Spectral characterization is performed by the application of the maximum entropy method. It is found that spectral analysis by interpretation of the interference pattern is much more precise than a spectrometer regarding the relative weighting of the harmonic orders [6, 8]. Furthermore, relinquishing the use of a spectrometer allows any inefficiences or imperfections of the optical elements to be avoided. Thus, all available harmonic orders can be utilized for experimental usage leading to a very high effective photon flux. Therefore this source is a potential source for time-resolved spectroscopy, such as femtosecond photoelectron spectroscopy, in the extreme-ultraviolet and soft x-ray region [10], and for multiple wavelength coherent diffractive imaging with high spatial resolution [6], where few harmonic orders of short wavelength or a dominant photon energy are required and any optics in the harmonic beam path, such as reflection gratings, is undesirable.

5.1.4 Spectral characteristics across the spatial profile of a high-harmonic beam

The spectral characteristics and degree of spatial coherence of a few-order high-harmonic beam generated by femtosecond laser pulses in an argon gas cell are studied in-situ by applying the maximum entropy method to the interference pattern from a Young double-slit pair. Power spectra of the harmonics taken across the beam profile are presented for different effective interaction lengths and different diameters of an aperture applied to the fundamental laser beam. The role of the effective focused intensity and the associated fraction of generated plasma on the high-harmonic generation process is discussed. This work is presented in [5].

5.1.4.1 Introduction

Spectral characterization of high-harmonic generation is usually performed by means of a spectrometer. Due to its intrinsic inefficiencies, grating-based spectral discrimination leads to a greatly reduced harmonic flux and may introduce distortions to the harmonic emission. Moreover, the use of a spectrometer only allows the spectral characteristics to be sampled over a small area of the harmonic beam, which for a properly aligned beam is usually restricted to the centre of the beam.

In the following, precision in-situ spectral characterization across the spatial profile of a harmonic beam by the application of the maximum entropy method to the interference pattern from a Young double-slit pair is presented [8]. The characteristics of the harmonic emission depend strongly on aperturing of the fundamental laser beam [89] and on the position of the laser focus with respect to the nonlinear medium [22]. By properly adjusting these macroscopic phase-matching parameters harmonic emission can be achieved that is confined to effectively one to four intense harmonic orders around 30 nm in a semi-infinite argon gas cell. Depending on the parameters the harmonic emission can exhibit both a uniform and non-uniform composition of the power spectrum across the beam. It is noted that section 3.2.3 provides a detailed discussion about spatio-temporal distortions, chromatic aberrations, the three-dimensional of the laser focus and potential effects such as self-focusing and filamentation. Due to the given experimental conditions, the mechanism dominating high-intensity pulse propagation is ionization-induced defocusing and plasma dispersion.

The spatially dependent spectral composition of a beam of multiple harmonic orders in the far field is very complex and depends strongly on the experimental parameters. If the laser focus is placed in a medium of length much smaller than the Rayleigh length of the laser beam, the generated harmonic orders depend mainly on the transverse distribution of the effective intensity. If the length of the medium is significantly long relative to the Rayleigh length of the laser beam, then harmonic emission before and after the focus will contribute to the harmonic beam. This depends on both the longitudinal and transverse coordinates and will incorporate harmonic orders with different cones of divergence and different phase fronts. Thus, complex spatial patterns and spectral compositions can arise. The focused intensity will increase steadily with the truncation coefficient α (see equation (5.1.1)), but it is ultimately limited to $I_{max} = 3 \times 10^{14}$ W/cm^2 due to the chosen focal geometry. This value is determined by the maximum achievable ionic charge state η_{max} (see equation (5.1.3)). I_{max} is associated with the generation of the 47th harmonic order and, according to the Ammosov-Delone-Krainov ionization rate model [74], is the effective intensity that generates a plasma fraction of 0.36. This amount of plasma is reached approximately 8 fs after the peak of the electric field. Here, the neutral medium is depleted by 20 % (see figure 5.1.7). Therefore, for any α the gas can be exposed to the peak of the electric field envelope and thus, in principle, harmonics up to the 47th order can be generated for intensities up to I_{max}. However, the highest emitted harmonic order is ultimately limited by the phase-matching conditions and may be significantly smaller than expected.

5.1.4.2 Validity of the maximum entropy method for spectral characterization across the spatial profile

Spectral characterization is performed across the spatial profile of the multiple-order harmonic beam as depicted in figures 5.1.12 and 5.1.13. Here, spectra are sampled for the centre (point 1) of the profile and for perimeters that are associated with 41 % (point 2) and 19 % (point 3) of the harmonic intensity from the centre. The spectra for the points 2 and 3 represent the spectra for any points on that perimeter. In order to verify the validity of these points representing any points on that perimeter, spectral characterization is performed for three more points on that particular perimeter for any measurement presented in the following.

The validity of the maximum entropy method for spectral characterization across the spatial profile is tested for an harmonic beam of good, reasonably good and poor quality of the spatial profile as demonstrated in figure 5.1.8. The sample point 1 represents the centre and the points 2, 4, 6 and 8 (3, 5, 7 and 9) represent the perimeter of 41 % (19 %) of the harmonic intensity in the centre. The spectral characteristics across the spatial profile as shown in the left sub-figure of figure 5.1.8 are presented in figure 5.1.9. It can be seen that the spectra sampled at the points 2, 4, 6 and 8 (3, 5, 7 and 9) and thus representing the perimeter of 41 % of the harmonic intensity in the centre match very well. Slight mismatch of the precise position of the particular harmonic orders and their spectral width can be seen, but can be neglected in the context of this work. However, these spectral abnormalities can be attributed to a slight asymmetry of the spatial profile of the harmonic beam, where the contour lines of the right (left) part appear to be slightly compressed (stretched). It is important to note that in that case one particular point on a perimeter can represent the spectral characteristics for any other point on that perimeter. The fact that the spectra from the centre and the perimeters match is due to the relatively small aperture diameter ($w = 6.85$ mm) and will be explained later.

The spectra across the spatial profile do not have to match, as can be seen in the following. The spectral characteristics across the spatial profile as shown in the middle sub-figure of figure 5.1.8 are presented in figure 5.1.10. Here, the spectra of the centre and the points 2, 4, 6, and 8, corresponding to the perimeter of 41 % of the intensity of the centre, match reasonably well. However, the spectra of the points 3, 5, 7, and 9, corresponding to the perimeter of 19 % of the intensity of the centre, exhibits a considerably different weighting of the harmonic orders in the

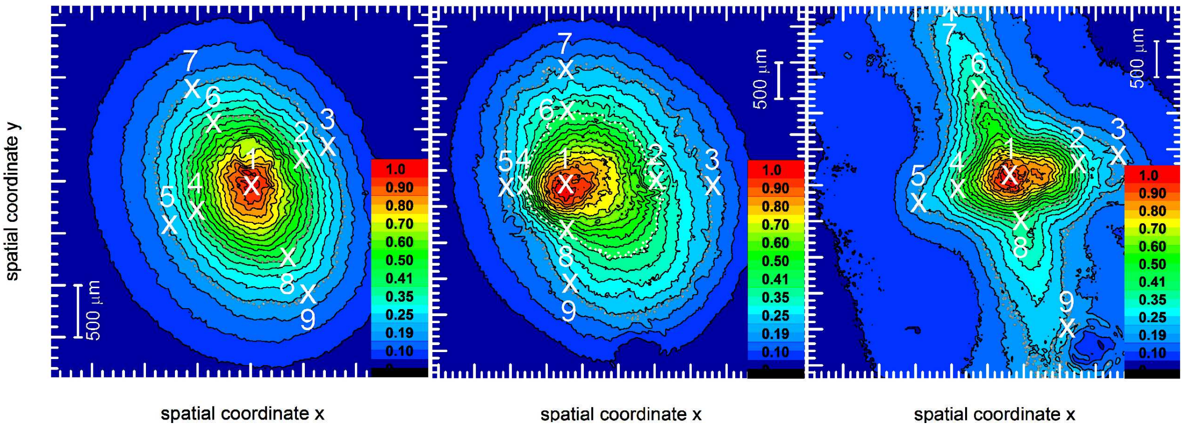

Figure 5.1.8: Good (left sub-figure), reasonably good (middle sub-figure) and poor (right sub-figure) quality of the spatial profile of the harmonic beam. Spectral characterization is sampled at the point 1 (centre), points 2, 4, 6 and 8 (41 % of the harmonic intensity in the centre), and 3, 5, 7 and 9 (19 %).

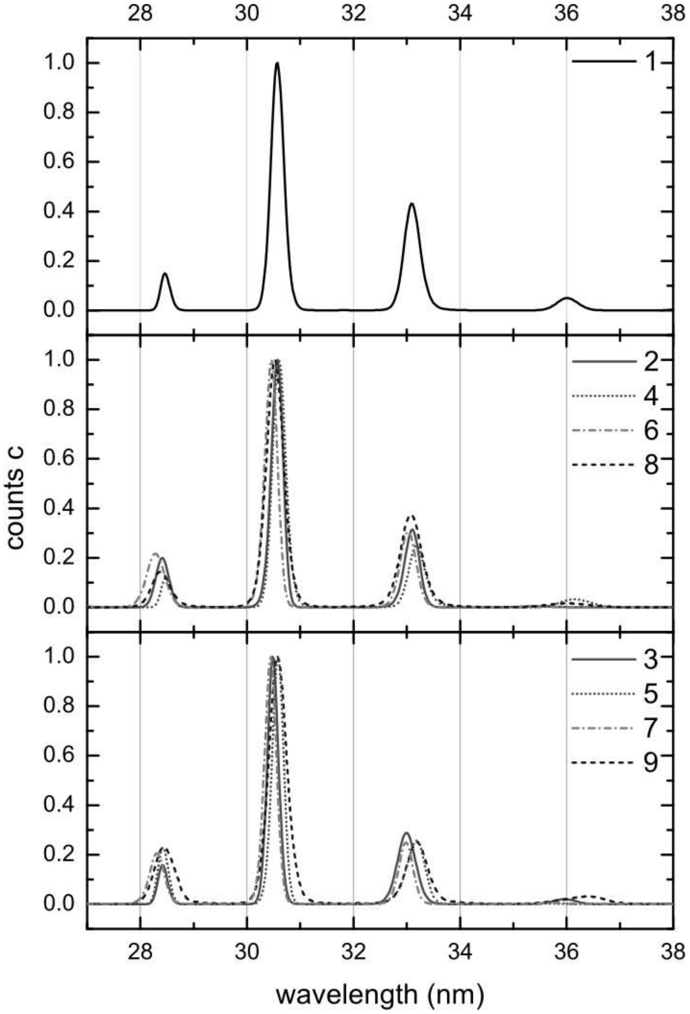

Figure 5.1.9: Spectral characteristics across the good spatial profile for the points 1 to 9 as described in the left sub-figure of figure 5.1.8.

power spectrum. However, it can be seen that the spectra sampled at the points corresponding to one particular perimeter match reasonably well with respect to the dominant harmonic orders within the spectral power distribution.

The mismatch of the precise position of the particular harmonic orders and their spectral width is more pronounced than in figure 5.1.9 and can be attributed to a more distinct asymmetrical shape of the spatial profile of the harmonic beam due to a larger aperture diameter ($w = 7.5$ mm). For an even larger diameter ($w = 9$ mm) the spatial profile is of poor quality (right sub-figure of figure 5.1.8) and the spectral characteristics

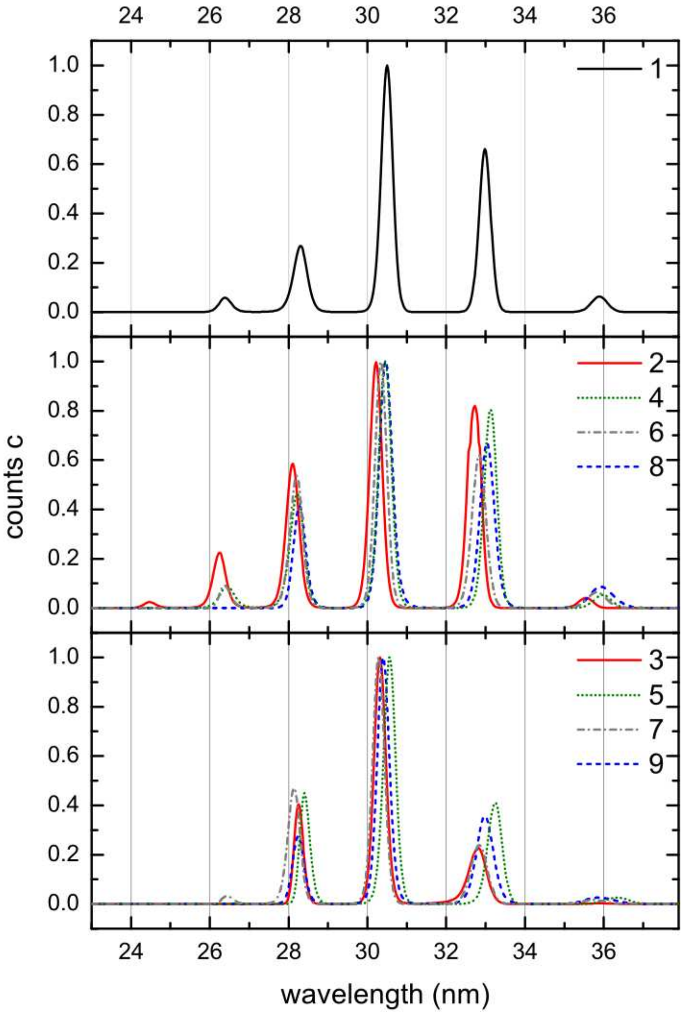

Figure 5.1.10: Spectral characteristics across the reasonably good spatial profile for the points 1 to 9 as described in the middle sub-figure of figure 5.1.8.

across the spatial profile and within one particular perimeter differ significantly as shown in figure 5.1.11. Here, the precise position of the particular harmonic orders and their spectral width is very poor compared to figure 5.1.10 and figure 5.1.9. This can be attributed to the very poor quality of the spatial domain of the harmonic beam and to a probably differing degree of spatial coherence of the harmonic orders across the beam. In that case one particular point on a perimeter cannot represent the spectral characteristics for any other point on that perimeter.

5.1.4.3 Spectra across the spatial profile for different effective interaction lengths and aperture diameters

The spectra are sampled across the profile of the harmonic beam at different points 1 (centre), 2 (perimeter of 41 % intensity) and 3 (perimeter of 19 % intensity) as shown in figure 5.1.12. In figure 5.1.13 the spectral characteristics across the spatial profile of the harmonic beam with the in-vacuo laser focus placed in the exit plane of the gas cell, as well as 5 mm and 10 mm inside the gas cell, for $\alpha = 0.44$, 0.56 and 1.00 are presented. For $\alpha = 0.44$ (0.56) one particular point on a perimeter can (reasonably well) represent the spectral characteristics for any other point on that perimeter. However,

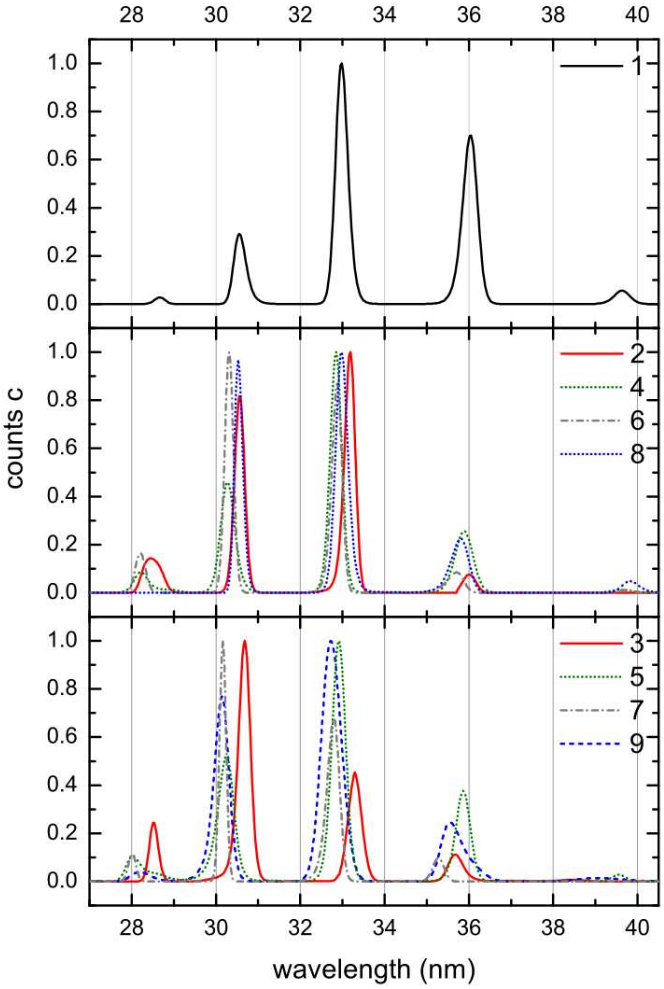

Figure 5.1.11: Spectral characteristics across the poor spatial profile for the points 1 to 9 as described in the right sub-figure of figure 5.1.8.

for $\alpha = 1.00$ the spectra sampled at the points 2 and 3 do not necessarily represent the spectra of any other sample point of the associated perimeter.

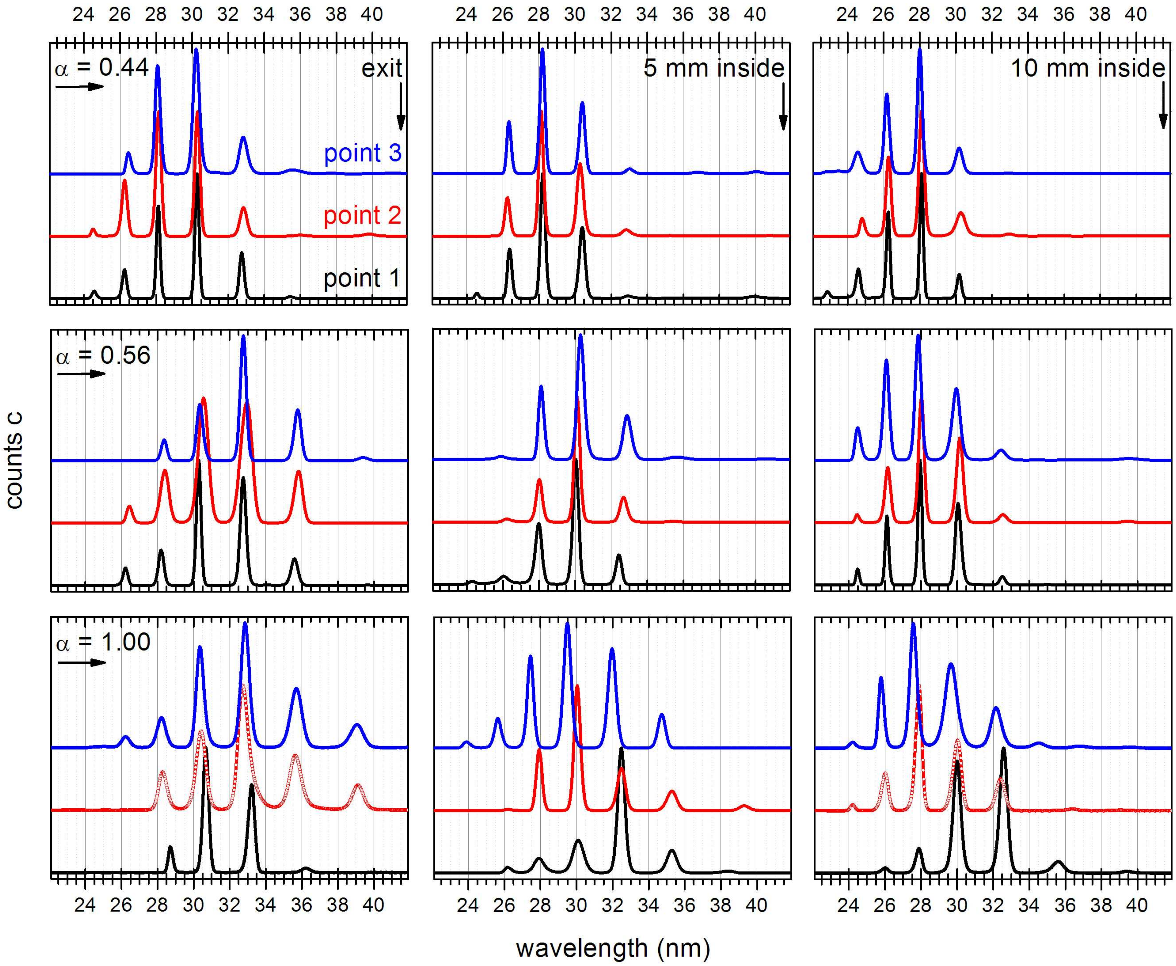

Figure 5.1.12: Spectral characteristics across the harmonic beam with the laser focus in the exit plane (left), 5 mm (middle) and 10 mm (right) inside the gas cell for $\alpha = 0.44$ (top), 0.56 (middle) and 1.00 (bottom) sampled for point 1 (black line, bottom), 2 (red line, middle) and 3 (blue line, top) as shown in figure 5.1.13.

For $\alpha = 0.44$ the harmonic beam mimics the characteristics of the laser beam and a good spatial beam profile of elliptical shape is obtained; i.e., distorted parts in the wings of the fundamental laser beam are discarded due to the small aperture diameter, and the effects of plasma dispersion and defocusing are very small due to the low ionization level. However, the asymmetric characteristics of the spatial profile of the

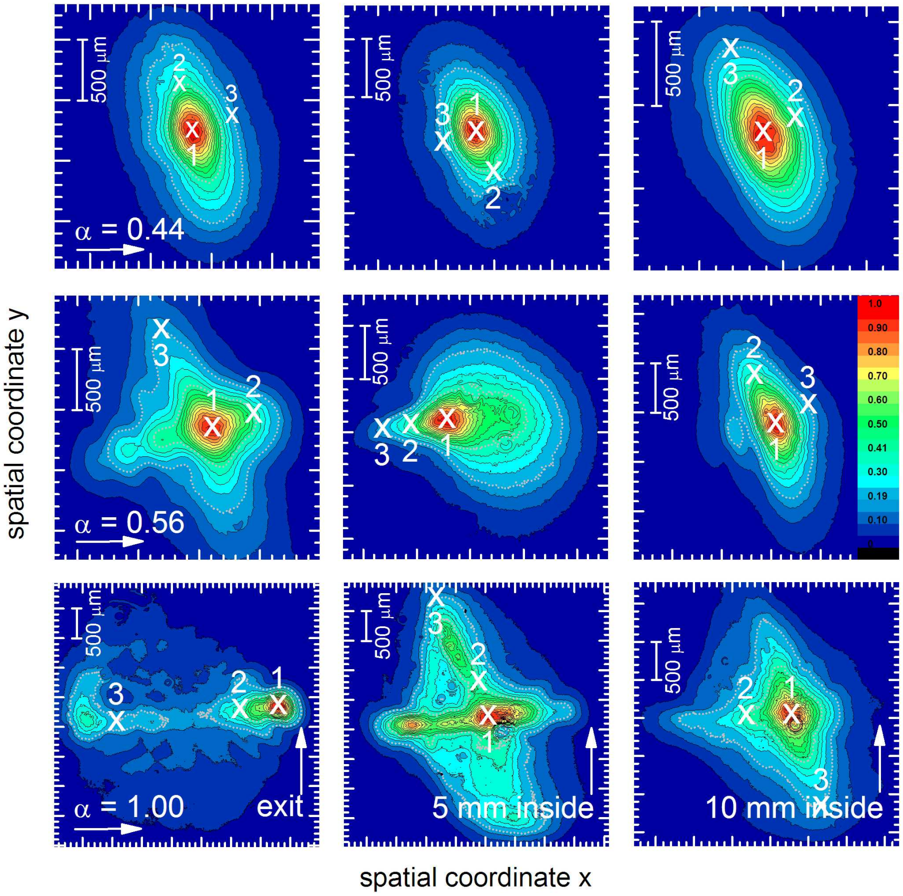

Figure 5.1.13: Spatial modes of the harmonic beam with the laser focus in the exit plane (left), 5 mm (middle) and 10 mm (right) inside the gas cell for $\alpha = 0.44$ (top), 0.56 (middle) and 1.00 (bottom). The points 1, 2 and 3 indicate where the spectral characteristics have been sampled across the harmonic beam: in the centre and on a perimeter corresponding to 41 % and 19 % of the maximum intensity of the harmonic beam, respectively.

laser beam with respect to different values of the beam diameter, divergence, M^2 and pointing for the x- and y-direction are imprinted onto the spatial profile of the harmonic beam. For $\alpha = 0.44$ the highest harmonic intensity is measured when the laser focus is placed at the exit of the gas cell as shown in figure 5.1.5. The energy conversion efficiency is then $\sim 3 \times 10^{-7}$. However, when the laser focus is placed 10 mm inside the gas cell, the flux is considerably lower ($\sim 1/650$). For this value of α the highest harmonic order - the 35th - is detected when the laser focus is placed 10 mm inside the gas cell. The intensity of the focused laser beam for this particular harmonic order is associated with the ion state $\eta \approx 0.05$ (see figure 5.1.7), which is still very small. Spectral characterization across the harmonic beam for all three interaction lengths reveals that the spectral range and the relative weighting of the harmonic orders are homogeneously distributed across the harmonic beam to a good approximation. For all three cases and for all spatial sample points a fringe visibility of

$$\nu = \frac{I_{\Delta q,max} - I_{\Delta q,min}}{I_{\Delta q,max} + I_{\Delta q,max}} \approx 0.95(1) \tag{5.1.4}$$

is measured, where $I_{\Delta q,max(min)}$ is the intensity of the centre (the first minimum) of the interference pattern for the harmonic beam consisting of orders Δq. As demonstrated in [149, 150, 151] several mechanisms exist that can lead to deteriorated coherence properties. Depending on the experimental parameters and their variation, the degree of spatial coherence can vary significantly across the spatial profile of the harmonic beam. When employing Young double-slits of spacing 20 μm, we cannot observe this behaviour. This indicates that the harmonic phase does not vary significantly on a length-scale of 20 μm, which is much smaller than the e^{-2}-diameter of the harmonic beam ($\sim$ 1 mm) at the position of the Young double-slits. However, we note that in an independent measurement we could determine a fringe visibility of $\nu_{50(100)\ \mu m} \approx 0.73(1)$ (0.71(1)) when using Young double-slits with a spacing of 50(100) μm. This indicates that the degree of spatial coherence varies significantly on a length-scale of ≥ 50 μm across the spatial profile of the harmonic beam. Nevertheless, in this work the focus is on the slit spacing of 20 μm as the size of the samples that are employed for coherent diffractive imaging with this source is ≤ 20 μm [6, 9, 7]. For $\alpha > 0.44$ significant plasma formation, up to $\eta \approx 0.36$, takes place and manifests itself as an increased spectral width as well as spectral blue-shifting [138, 139]. These effects are more prominent for a longer interaction length - when the laser focus is placed inside the gas cell - and for increasing focal energy densities - when α is larger.

For $\alpha = 0.56$, when distorted parts of the laser beam can pass the aperture, distortions of the harmonic beam in the spatial profile are observed and become more severe when the laser focus is placed at the exit of the gas cell. Now, the relative weighting of the power spectra exhibits larger variations and small spectral shifting of harmonic orders is seen. The relative weighting of the power spectra depends strongly on the interaction length whether the maximum order is detected in the centre or off-centre. When the laser focus is placed in the exit plane of the gas cell, the centre exhibits the highest order - 31st. However, when the focus is 10 mm inside the gas cell, the highest harmonic order - 33rd - is measured off-centre. Higher orders are not generated efficiently due to the increasing amount of plasma and associated phase-mismatch. For $\alpha = 0.56$ the highest harmonic intensity for the laser focus placed 10 mm inside the gas cell is measured as shown in figure 5.1.5. However, the harmonic intensity is only $\sim 1/500$ of the maximum flux achieved for the case when the laser focus is placed at the exit of the gas cell for $\alpha = 0.44$. For all three cases and for all spatial sample points, a fringe visibility of $\nu = 0.95(1)$ is measured when employing a Young double-slit of spacing 20 μm and thus sampling the variation of the harmonic phase on this length-scale. As discussed before, it can be expected that the spatial coherence varies significantly on a length scale of ≥ 50 μm, and thus across the spatial profile of the harmonic beam.

For larger α, and in particular as $\alpha \rightarrow 1$, spatial distortions become much more severe. Due to the significant amount of generated plasma, $\eta_{max} \approx 0.36$, defocusing can take place and generation of higher harmonics becomes less efficient in the centre of the beam. In particular, when the laser focus is placed at the exit of the gas cell the harmonic beam splits into two parts. It is well known that defocusing effects can lead to an oscillating intensity at specific points in time and space of the laser beam and form two packets that move away from each other [136]. However, the formation of the centres occurs only along the former minor ellipse axis and not in a ring structure. Also, this phenomenon should be more prominent when the laser focus is placed inside the gas cell rather than at the exit due to the longer propagation length. We therefore attribute this complex spatial pattern to peculiarities of the gas flow around the exit plane of the gas cell and possibly off-axis phase-matching [22]. When placed at the exit of the gas cell, the highest harmonic order is the 29th which is detected in the centre. Off-centre, the power spectrum exhibits harmonic orders up to the 31st. However, when the laser focus is placed deep inside the gas cell, the off-centre spectral power distribution exhibits more intense higher harmonic orders as well as the highest harmonic order. In all cases significant red-shifting as well as blue-shifting of the harmonic orders occurs across the beam. It is also interesting to note that the off-centre spectra from the two different perimeters resemble each other but are much different from the spectral power distribution measured in the centre of the harmonic beam. Despite the significantly poorer beam quality a fringe visibility of $\nu \approx 0.95(1)$ is measured for almost all points. Only for sample point 3 and when the laser focus is placed at the exit of the gas cell a somehow smaller fringe visibility of $\nu \approx 0.92(1)$ is detected.

5.1.4.4 Conclusion

By properly adjusting the macroscopic phase-matching parameters, in particular the effective interaction length and the aperture diameter, harmonic emission of effectively one to four intense orders around ~ 30 nm with a high degree of spatial coherence and a good spatial profile can be achieved. The procedure of in-situ spectral characterization across the spatial profile of the harmonic beam by applying the maximum entropy method to the interference pattern from a Young double-slit pair is essential to control the generation process and to tailor the harmonic emission in the spectral domain according to the experimental requirements. High spatial quality and high intensity of the harmonic beam are achieved for small aperture diameters and when the laser focus is placed close to the exit plane of the gas cell. In that case spectral characterization across the harmonic beam reveals that the spectral range and the relative weighting of the harmonic orders are distributed homogeneously across the harmonic beam. For larger aperture diameters, when ionization-induced defocusing is the main mechanism for high-intensity pulse propagation, a non-uniform spectral distribution of harmonic emission across the harmonic beam is observed. In particular, for a virtually unapertured laser beam the spectral distribution across the harmonic beam varies significantly and the highest order as well as the most intense harmonic order is found far off the centre of the harmonic beam. In all cases and for all sample points of spectral characterization across the spatial profile of the harmonic beam, a very good fringe visibility close to unity is determined when employing a Young double-slit with slit-to-slit spacing of 20 μm. This indicates that almose perfect spatial coherence of the (spatially restricted) harmonic beam can be assumed when employing this source for coherent diffractive imaging of samples of size ≤ 20 μm.

5.2 Variation of the focal point position and the gas cell pressure (argon and helium)

In the following, femtosecond-laser-based generation of a few phase-matched high-order harmonics in a helium and argon semi-infinite gas cell are discussed. The experimental conditions are kept constant for this experiment. In particular, this applies to the length of the gas cell, the focal length lens and the laser output. Only the nonlinear medium of the gas cell is changed, and the intensity of the emission is scanned by varying the position of the laser focus inside the gas cell. The phase-matching parameters are adjusted for an output optimized for maximum flux from the gas cell. By varying the effective interaction length the effects of the coherence length related to plasma formation and the Gouy phase shift on the output can be observed. The atomic scattering factors for photoabsorption, the effective propagation lengths and the energy conversion efficiencies are deduced for harmonic generation in helium (77th to 95th orders) and argon (21st to 27th orders) for comparison. This work is reported in [4].

5.2.1 Introduction

In most of the work presented in this dissertation the focus is on the phase-matched emission of just a few harmonic orders around ~ 30 nm in an argon gas cell [3, 2] where the absorption coefficient varies significantly with wavelength. It is shown that high-harmonic generation by a freely propagating fundamental laser beam in a gas cell has the same benefits of homogeneous phase matching as in hollow-core fibres at low gas pressures [24]. Because a much higher gas pressure can be applied in a gas cell the optimal interaction length needs to be studied in more detail in order to balance the harmonic generation process with the re-absorption [23, 21, 25]. In a helium gas cell, high-order harmonics with much shorter wavelengths can be achieved and the optimal gas pressure is typically very high. Under these conditions, the harmonic emission has a significantly shorter coherence length and the variation of the absorption coefficient is very different to that in an argon gas cell. In this experiment the generation of the 77th (H77) to 95th (H95) harmonic orders in a helium semi-infinite gas cell with energy conversion efficiency one-fifth of that achieved in an argon gas cell, but with much shorter wavelength, is reported. The coherence lengths which are related to plasma formation and the Gouy phase shift, the relative position of the laser foci in the gas cell and the effective interaction lengths between the fundamental laser and the harmonic field, and the generated photon flux are determined and discussed. Effectively, the harmonic beam is confined to 4 to 6 intense harmonic orders around ~ 9.5 nm. Thus, this source is a potential source for time-resolved spectroscopy, such as femtosecond photoelectron spectroscopy, in the extreme-ultraviolet and soft x-ray region [10], and for multiple wavelength coherent diffractive imaging with high spatial resolution [6], where few harmonic orders of short wavelength or a dominant photon energy are required and any optics in the harmonic beam path, such as reflection gratings, is undesirable.

5.2.2 Experimental conditions

The laser system is described in section 5.1.2. A calibrated aperture is applied to the laser beam before it is focused into a 260 mm-long helium (argon) gas cell of pressure 810 Torr (58 Torr) by a lens of focal length 400 mm. The in-vacuo e^{-2}-radius of the focused intensity distribution of the laser beam, when truncated to a diameter of 8.25 mm (6.25 mm) for helium (argon), is $w_{0,He} = 33\ \mu$m ($w_{0,Ar} = 43\ \mu$m) as shown in figure 5.1.1, and the in-vacuo Rayleigh range is $z_{0,He} = 11.3$ mm ($z_{0,Ar} = 6.6$ mm) as shown in figure 5.1.2 [129]. The pressure, aperture diameter, energy of the laser pulses, position of the laser focus relative to the exit of the gas cell, and chirping of the laser pulses are optimized in an iterative procedure for maximum flux of all available harmonics. For the helium (argon) gas cell a silver or zirconium (aluminium) metal filter is applied to separate the harmonics from the fundamental laser beam. The charge-coupled device detector chip is illuminated directly and positioned 0.94 m from the exit of the gas cell. Optionally, the grazing incidence spectrometer (Setpoint GIMS#4) can be inserted into the beam path. The spectrally-resolved far-field beam profile can then be detected along the height of the exit slit of the spectrometer. Alternatively, in-situ spectral analysis can be performed by applying the maximum entropy method to the interference pattern of a Young double-slit pair illuminated with the emission of the harmonic source [8].

5.2.3 Phase-matched emission in the argon gas cell

5.2.3.1 Harmonic intensity of the argon gas cell as a function of the gas cell pressure

The intensity of the qth harmonic order in the presence of absorption is given by [24, 23]

$$I_q \propto N_a^2 A_q^2 \frac{1 + exp\left(-2\alpha l_{eff}\right) - 2exp\left(-\alpha l_{eff}\right) cos\left(\Delta k l_{eff}\right)}{\alpha^2 + \Delta k^2}, \tag{5.2.1}$$

where N_a is the atom density, A_q is the atomic response for the qth harmonic order, α is the absorption coefficient, l_{eff} is the effective interaction length between the fundamental laser field and the nonlinear medium, and Δk is the phase mismatch between the fundamental and harmonic field. For $\alpha \approx 0$, $I_q \propto sinc^2\left(\Delta k l_{eff}\right)$ where $sinc(x) = sin(x)/x$. If the atomic response is constant or varies only slightly over a propagation length that corresponds to the coherence length and the phases between the fundamental and harmonic field are matched, then the harmonic intensity scales as

$$I_q \propto N_a^2, \text{ or } I_q \propto p^2, \tag{5.2.2}$$

where p is the pressure of the generating gaseous medium.

Figure 5.2.1 shows the intensity dependence on the pressure in the argon gas cell. The settings for the pressure, aperture diameter, energy of the laser pulses, position of the laser focus inside the gas cell and chirping of the laser pulses are optimized in an iterative procedure for maximum flux and, except the pressure, kept constant. The optimized value for the pressure is found to be $p_{Ar} = 58$ Torr. For $p_{Ar} < 58$ Torr the intensity $I_{\Delta q} \propto N_{a,Ar}^2 \propto p_{Ar}^2$ increases quadratically with pressure (fitted red line) and thus indicates that the harmonic emission is phase-matched for the spectral band Δq, which consists of several harmonic orders as shown in figure 5.2.2. For $p_{Ar} \gg 58$ Torr the variation of harmonic emission intensity is dominated by re-absorption [23, 21, 25] of the generating gas and an exponential decay curve can be fitted (green line). The effective interaction length $l_{eff} \approx 7.2$ mm between the fundamental laser field and the nonlinear medium can be extracted from the exponential decay constant [152]

$$C_{Ar,p} = 2 l_{eff} r_0 \langle\lambda\rangle_{Ar} \langle f_2\rangle_{Ar} / (k_B T) \approx 0.059(4), \tag{5.2.3}$$

where r_0 is the classical electron radius, $\langle\lambda\rangle_{Ar} \approx 30$ nm is the average wavelength of the spectral power distribution (see figure 5.2.2), k_B is the Boltzmann constant, T is the temperature, and the (imaginary part of the) atomic scattering factor for photoabsorption $\langle f_2 \rangle_{Ar}$ is extracted from figure 5.2.3.

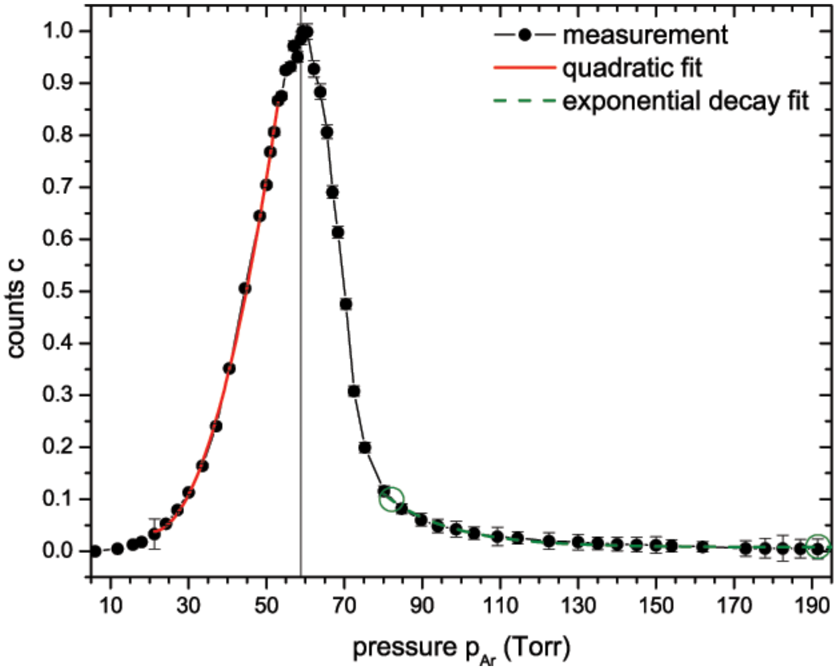

Figure 5.2.1: Harmonic intensity versus pressure in the argon gas cell. The red solid line indicates a quadratic fit for phase-matched harmonic emission, and the green dashed line indicates a fit of an exponential decay curve.

5.2.3.2 Spectral characteristics of the argon gas cell as a function of the laser focus position

In parallel with the measurement of the harmonic intensity, the spectrum of the multiple-order harmonic beam has been analyzed as a function of the pressure in the gas cell. In this measurement the focal point position is constantly $z = 0$ mm (see figure 5.2.3). The composition of the harmonic power spectrum differs significantly depending on the chosen pressure as displayed in figure 5.2.2.

Generally, the highest (lowest) harmonic order increases (decreases) with larger values of the pressure. This behaviour is associated with the fact that the absorption characteristic of the generating medium itself varies significantly with the wavelength.

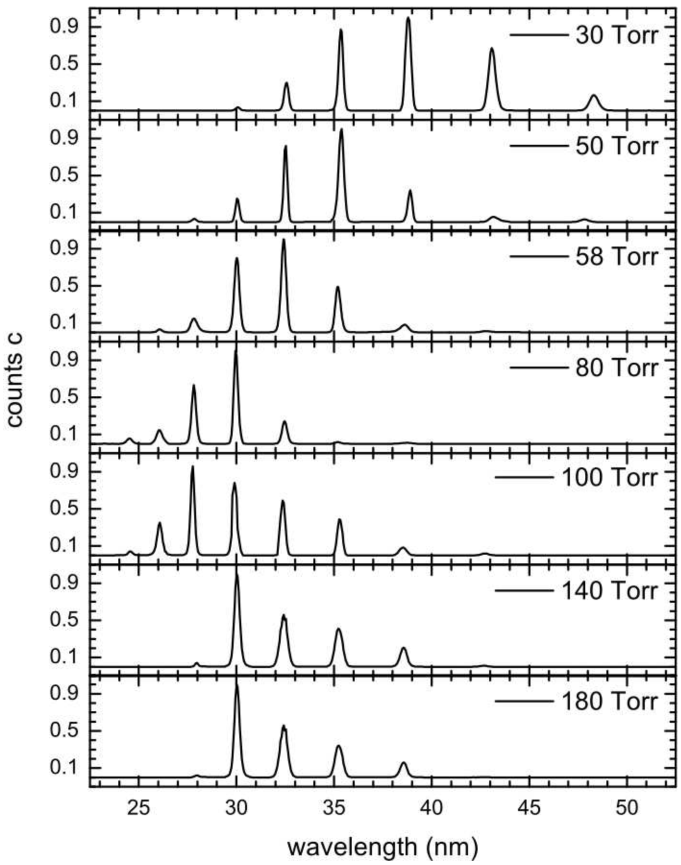

Figure 5.2.2: Spectral composition of the multiple-order harmonic beam in argon for different values of the pressure in the gas cell.

The transmission is maximum for wavelengths between 24 and 25 nm and quickly drops off between 25 and 30 nm [152]. Also, larger values of pressure appear to optimize the phase-matching conditions for higher harmonic orders and allow a larger number of atoms $\propto N_a$ to contribute to the coherent build-up of a higher harmonic order. The role of different phase-matching conditions is clearly displayed in the spectral composition of the harmonics within the particular harmonic band. Not only does the number of harmonic orders depend on the pressure, but also their spectral weighting changes with increased pressure. Also, for $p_{Ar} \geq 100$ Torr the highest harmonic order now decreases, most likely due to a plasma-induced phase-mismatch. Interestingly, the lowest harmonic order increases as well. For these harmonic orders the phase-matching conditions must be ideal, which thus over-compensate the strong absorption characteristic of the generating medium itself for harmonic orders ≥ 30 nm.

5.2.3.3 Harmonic intensity of the argon gas cell as a function of the laser focus position

The dependence of the harmonic intensity on the position of the laser focus is shown in figure 5.2.3. The x-axis is calibrated such that the global intensity maximum is at $z = 0$ mm. The laser focus is close to the exit plane and deeper inside the gas cell for larger values of z. The harmonic intensity scales quadratically with increasing values of z over a propagation length of ~ 7 mm (fitted solid red line) and thus indicates phase-matched harmonic emission (see equation (5.2.2)). This value agrees very well with the value $l_{eff,Ar} = 7.2$ mm extracted from the exponential decay constant $C_{Ar,p}$ (see figure 5.2.1 and equation (5.2.3)) and is also comparable to the Rayleigh range $z_{0,Ar} = 6.6$ mm from the truncated and focused Gaussian laser beam. Thus, when the laser focus is properly positioned inside the gas cell the high-harmonic generation is phase-matched over the whole Rayleigh range of the laser focus.

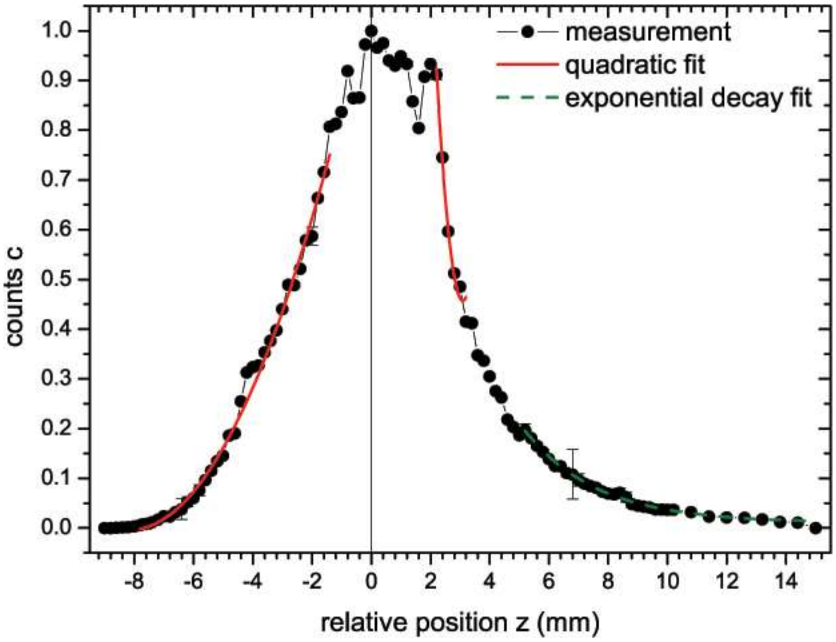

Figure 5.2.3: Harmonic intensity versus laser focus position in the argon gas cell. The red solid line indicates a quadratic fit for phase-matched harmonic emission, and the green dashed line indicates a fit of an exponential decay curve.

5.2.3.4 The role of the Gouy-phase-related and plasma-related coherence lengths

The Gouy phase-related coherence length is given by (see section 2.5.1.1)

$$l_{c,Gouy} = \frac{\pi\left(z_0 + \frac{z^2}{z_0}\right)}{q}, \tag{5.2.4}$$

where z_0 is the Rayleigh range of the focused apertured Gaussian laser beam. At the focus $l_{c,Gouy}(0) = \pi z_{0,Ar}/q$ ranges from ~ 0.7 to 1.2 mm for $H31$ to $H19$ as displayed in figure 5.2.4. Here the experimentally measured value $l_{eff,Ar} = 7.2$ mm has been chosen for $z_{0,Ar}$. The optimized position $z = 0$ mm is associated with an harmonic power spectrum that consists of predominantly three harmonic orders: 23rd, 25th and 27th (see figure 5.2.7). These harmonic orders are linked to a Gouy-phase-related coherence length of ~ 7 mm when harmonic generation occurs ~ 18 to 19 mm far off the focal centre point.

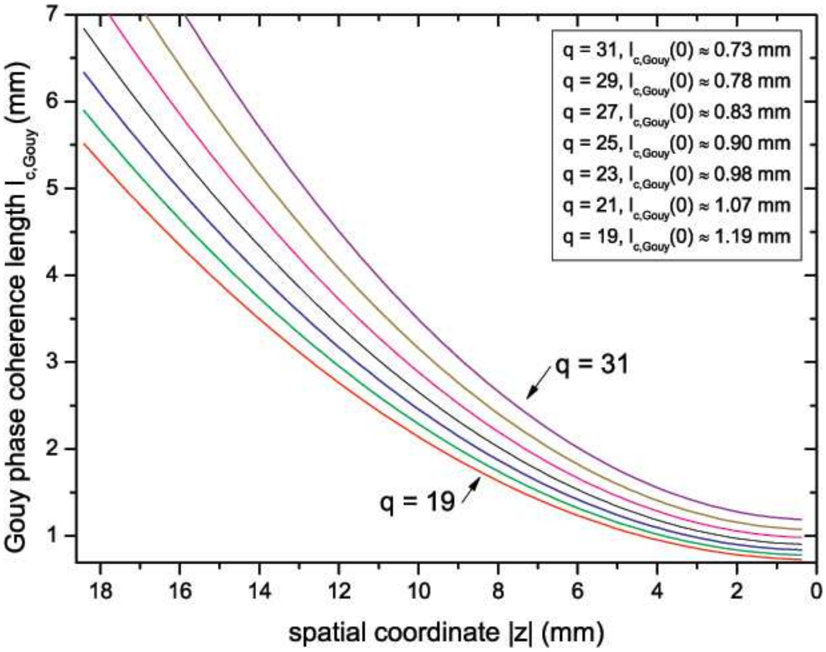

Figure 5.2.4: The Gouy phase-related coherence lengths for the harmonics $H31$ to $H19$ in argon.

Calculating the minimum intensity to generate the qth harmonic order according to the semi-classical cutoff and employing the Ammosov-Delone-Krainov model [74] to determine the level of ionization η_q of argon at the end of the laser pulse (see figure 5.2.5) allows the value of the plasma-related coherence length (see section 2.5.1.2)

$$l_{c,plasma} = \frac{4\pi^2 m_e}{q\lambda_0 e^2 \mu_0 \eta_q p} \tag{5.2.5}$$

to be established and to be compared with $l_{c,Gouy}$, where $p = 58$ Torr is the pressure of the argon gas cell. For $H31$ to $H19$ $l_{c,plasma}$ ranges from ~ 1.2 to 1343 mm (see figure 5.2.6). Thus, when the laser focus is properly positioned inside the gas cell the Gouy phase shift can be exploited in order to phase-match the harmonics $H31$ to $H19$ over a propagation length of $l_{eff,Ar} \approx 7.2$ mm.

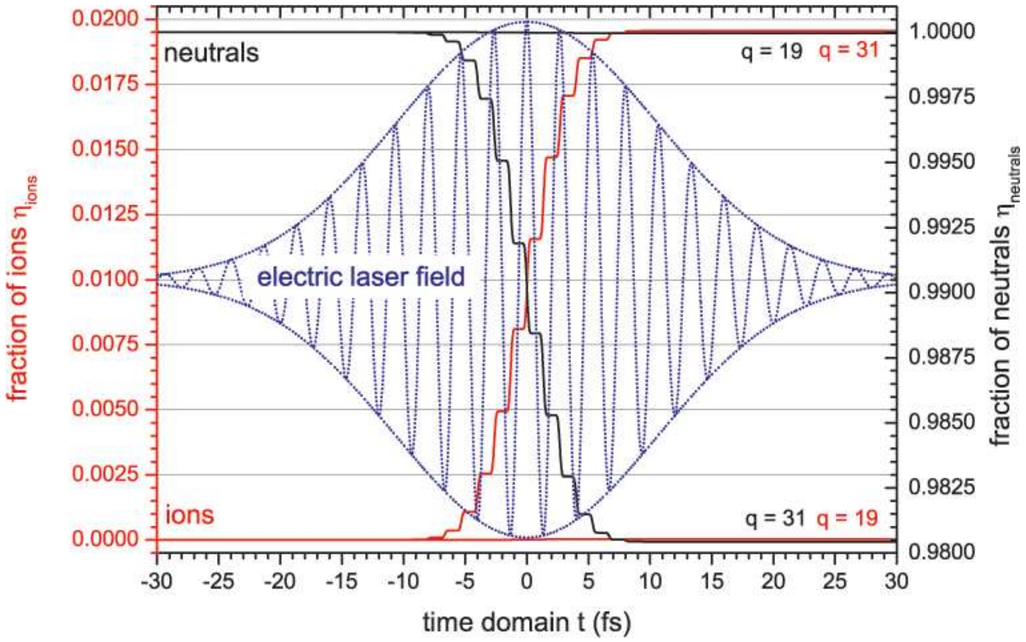

Figure 5.2.5: Calculation of the fraction of ions η_{ions} and neutrals $\eta_{neutrals}$ for the harmonics $H31$ to $H19$ in argon.

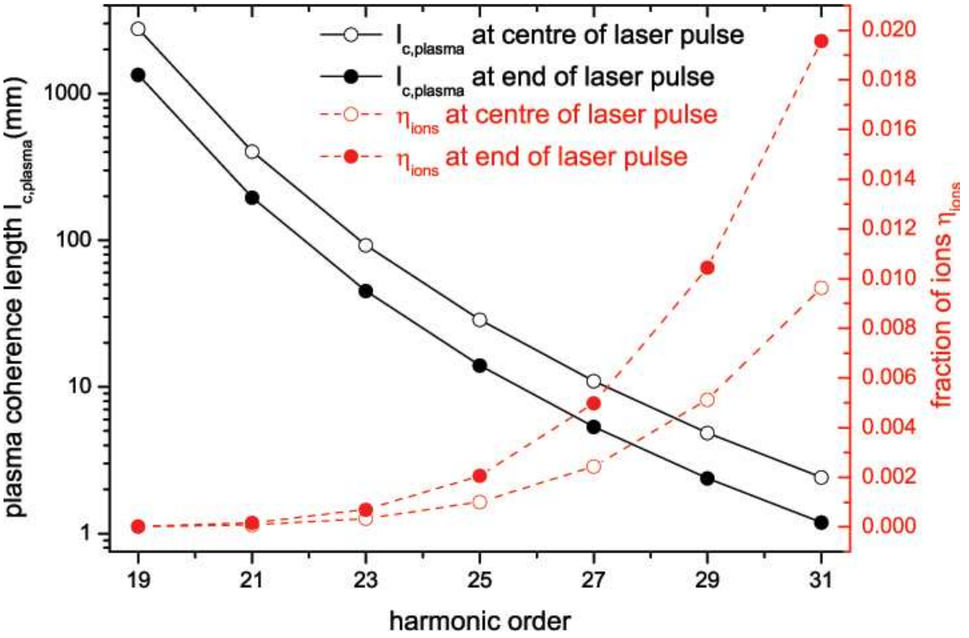

Figure 5.2.6: The plasma-related coherence lengths for the harmonics $H31$ to $H19$ in argon.

5.2.3.5 Spectral characteristics of the argon gas cell as a function of the laser focus position

In parallel with the measurement of the harmonic intensity, the spectrum of the multiple-order harmonic beam has been analyzed as a function of the position of the laser focus inside the gas cell. The composition of the harmonic power spectrum depends significantly on the focal point position as displayed in figure 5.2.7. In this figure the values for z are associated with the x-axis calibration of figure 5.2.3, where the global intensity maximum is at $z = 0$ mm. For the position of maximum flux, the laser focus is close to the exit plane and deeper inside the gas cell for larger values of z.

Generally, lower harmonic orders are emitted when the laser focus is placed close to exit plane or even outside of the gas cell ($z = -7$ to 0 mm), whereas higher harmonic orders are emitted when the laser focus is placed inside the gas cell ($z = 0$ to

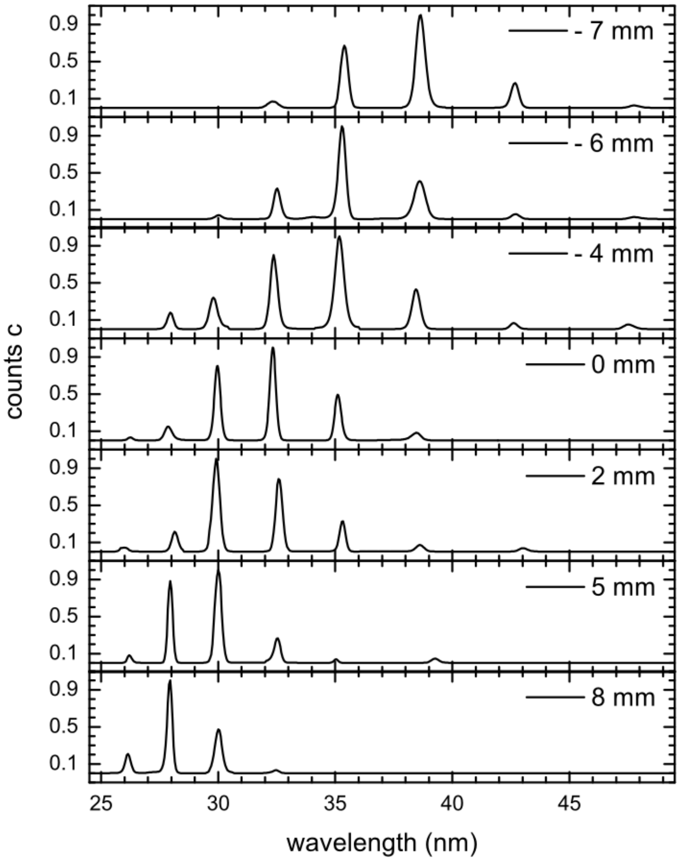

Figure 5.2.7: Spectral composition of the multiple-order harmonic beam in argon for different values of z (see figure 5.2.3).

8 mm). When moving the focal point position, the spectral composition changes not only in the number of harmonic orders, but also in the spectral weighting within that particular spectral band. This behaviour cannot be explained simply by absorption of the lower harmonic orders of the generating medium itself when the laser focus is placed deep inside the gas cell. Clearly, different focal point positions are associated with different phase-matching conditions, which in turn favour particular harmonic orders. The spectrum of the harmonic beam for $z = -7$ mm consists of the 25th to 17th orders. For larger values of z the maximum detected harmonic order increases and reaches a maximum - 31st order - when the laser focus is placed at the position $z = 0$ mm for maximum flux. The detected smallest harmonic order increases as well. For larger values of z the maximum detected order remains the 31st order, whereas the smallest detected harmonic order becomes the order that is the maximum detected

order for $z = -7$ mm - the 25th harmonic order. The detected smallest harmonic order is shifted towards smaller wavelengths for an increasing value of z as the absorption characteristic of the generating medium itself varies significantly with wavelength. The transmission is maximum for wavelengths between 24 and 25 nm and quickly drops off between 25 and 30 nm [152]. The reason the maximum detected harmonic order increases for $z = -7$ to 0 mm is because of the overlap of the laser focus position with the generating gas itself. As the laser focus is only shifted longitudinally inside the gas cell, the 3D-distribution of the focal intensity can be assumed to be a constant within that moving framework. However, for very small values of z the laser focus is positioned outside of the gas cell. The pressure of argon quickly drops outside of the gas cell so that higher harmonic orders cannot be generated.

5.2.3.6 The photoabsorption atomic scattering factor of the argon gas cell

When the laser focus is placed deeper inside the gas cell, re-absorption [23, 21, 25] by the generating medium dominates and an exponential decay curve can be fitted (dashed green line in figure 5.2.3). An average value of the (imaginary part of the) atomic scattering factor for photoabsorption $\langle f_2 \rangle_{Ar} = 1.4$ can be extracted from the decay constant [152]

$$C_{Ar,z} = 2p_{Ar} r_0 \langle \lambda \rangle_{Ar} \langle f_2 \rangle_{Ar} / (k_B T) \approx 0.409(8), \tag{5.2.6}$$

where $p_{Ar} = 58$ Torr, $\langle \lambda \rangle_{Ar} = 30$ nm is the average wavelength of the spectral power distribution of the harmonics $H31$ to $H21$ (see figure 5.2.7). The value for $\langle f_2 \rangle_{Ar}$ compares reasonably well with the average literature value $\sum f_q w_q = 1.1$ [152], where f_q is the atomic scattering factor of the qth harmonic order with centre wavelength λ_q of spectral weight w_q (see figure 5.2.7). For $z = 0$ mm a total of $\approx 5 \times 10^{10}$ generated harmonic photons per second is calculated (see equation (3.3.1)), corresponding to an energy conversion efficiency of $\epsilon_{Ar} \approx 5 \times 10^{-7}$.

We note that comparison with peer experimental work is difficult as the conversion efficiency strongly depends on the experimental conditions, in particular on the driving laser system as well as the chosen interaction geometry (e.g., compare [153] with [21]). Record conversion efficiencies have been reported for particular harmonic orders and under particular conditions [23, 154]. Furthermore, some literature refers to the harmonic intensity, in particular when optics is involved for focusing of the harmonic beam, rather than the raw number of generated photons. Comparison can be hampered even further when the photon count refers to an extraction area of the harmonic beam that has not been specified properly. However, for harmonic orders around 30 nm generated in argon similar conversion efficiencies, around 10^{-7} to 10^{-6}, can be found [21].

5.2.4 Phase-matched emission in the helium gas cell

5.2.4.1 Harmonic intensity of the helium gas cell as a function of the laser focus position

Comparison of the dependence of the high-harmonic generation intensity on the position of the laser focus in the argon gas cell with the helium gas cell can be made by means of figure 5.2.8 with the same experimental procedure. The x-axis calibration is consistent with figure 5.2.3, but comparing the settings of the translation stage for the focusing lens reveals that the laser focus is $\Delta = 2.6$ mm deeper inside the gas cell. When varying the position of the laser focus, a coherence length-induced oscillating intensity can be observed with the global and local maxima separated by $\Delta z_{He} = 900$ μm. This value is consistent with the propagation length over which phase matching can be observed (see equation (5.2.2)) and the intensity scales quadratically with z (fitted solid red line in figure 5.2.8).

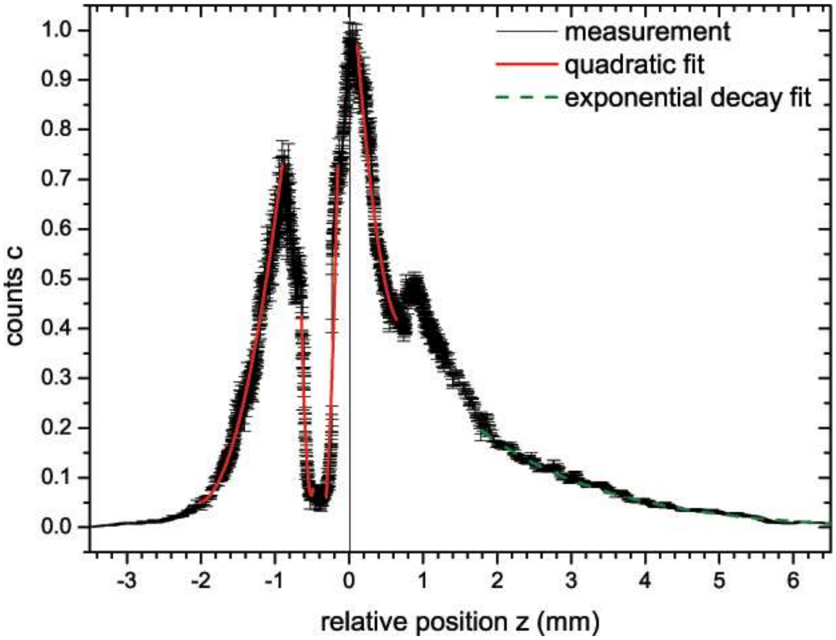

Figure 5.2.8: The harmonic intensity versus the laser focus position in the helium gas cell. The red solid line indicates a quadratic fit for phase-matched harmonic emission, and the green dashed line indicates a fit of an exponential decay curve.

5.2.4.2 The role of the Gouy-phase-related and plasma-related coherence lengths

At the focus the Gouy-phase-related coherence length $l_{c,Gouy}(0) = \pi z_{0,He}/q$ (see section 2.5.1.2) ranges from ~ 366 to 461 μm for $H97$ to $H77$ as displayed in figure 5.2.9. However, when taking into account that the effective propagation length in argon is $l_{eff,Ar} = 7.2$ mm (see equation (5.2.3)) and that the laser focus is $\Delta = 2.6$ mm deeper inside the gas cell when filled with helium, $l_{c,Gouy}(z = l_{eff,Ar} + \Delta \approx 1 \text{ cm}) \approx 0.9$ mm, which is comparable with Δz_{He}.

Calculating the minimum intensity to generate the qth harmonic order according to the semi-classical cutoff and employing the Ammosov-Delone-Krainov model [74] to determine the level of ionization η_q of helium at the end of the laser pulse (see figure 5.2.10) allows the value of the plasma-related coherence length (see section 2.5.1.1) to be established and to be compared with $l_{c,Gouy}(z \approx 1 \text{ cm})$, where m_e

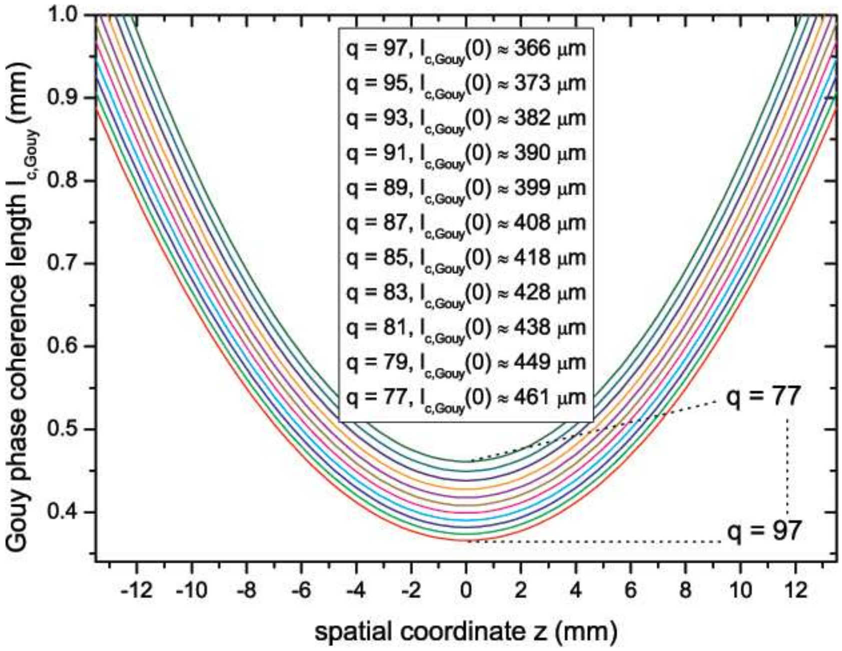

Figure 5.2.9: The Gouy phase-related coherence lengths for the harmonics $H97$ to $H77$ in helium.

and e are the electron mass and charge, λ_0 is the centre wavelength of the fundamental laser field, μ_0 is the magnetic constant and p is the pressure of the gas cell. For $H77$ to $H97$, $l_{c,plasma}$ ranges from ~ 538 to 66 μm (see figure 5.2.11) and is significantly shorter than Δz_{He}. Thus, when the laser focus is properly positioned inside the gas cell the Gouy phase shift can be exploited in order to phase-match the harmonics $H77$ to $H97$ over a propagation length of $l_{eff,He} \approx 0.9$ mm.

5.2.4.3 The photoabsorption atomic scattering factor

When the laser focus is placed deeper inside the gas cell, harmonic emission is dominated by re-absorption [23, 21, 25] by the generating gas and an exponential decay curve can be fitted (dashed green line in figure 5.2.8). An average value of the (imaginary part of the) atomic scattering factor for photoabsorption $\langle f_2 \rangle_{He} \approx 0.39$ can be extracted from the decay constant [152]

$$C_{He,z} = 2pr_0\langle\lambda\rangle_{He}\langle f_2\rangle_{He}/(k_BT) \approx 0.556(8), \tag{5.2.7}$$

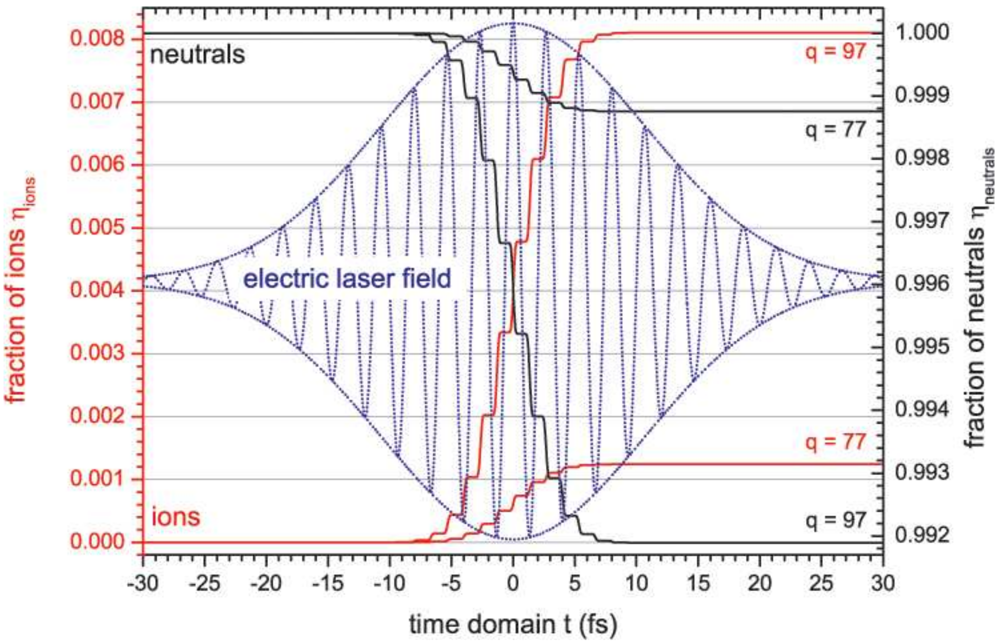

Figure 5.2.10: Calculation of the fraction of ions η_{ions} and neutrals $\eta_{neutrals}$ for the harmonics $H97$ to $H77$ in helium.

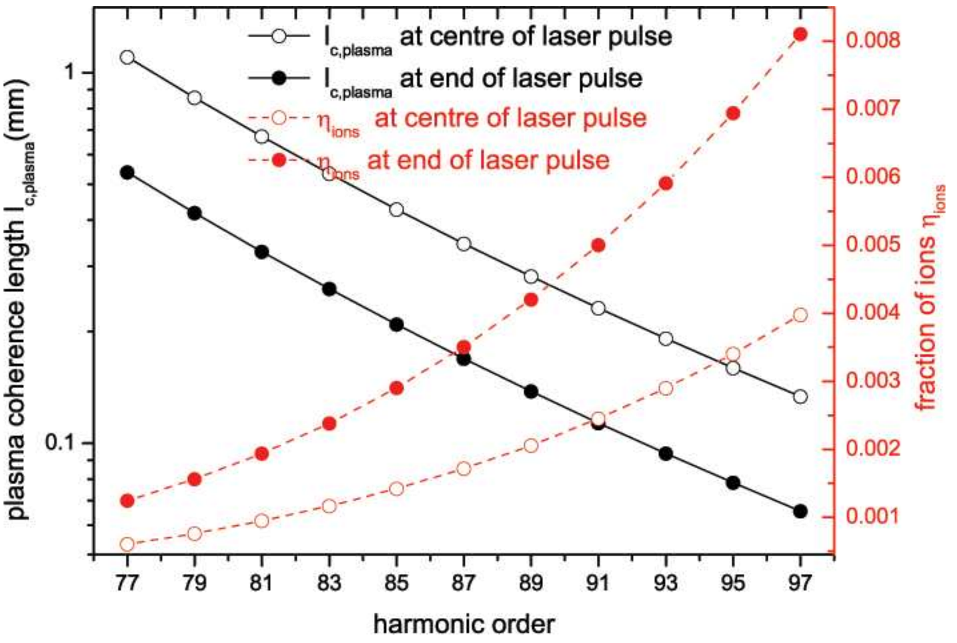

Figure 5.2.11: The plasma-related coherence lengths for the harmonics $H97$ to $H77$ in helium.

where $p_{He} = 810$ Torr, $\langle\lambda\rangle_{He} \approx 9.5$ nm is the average wavelength of the spectral power distribution of the harmonics $H77$ to $H95$. This value for $\langle f_2\rangle_{He}$ compares well with the average literature value $\sum f_q w_q = 0.38$ [152]. The exponential decay exhibits modulations with period of order ≤ 538 μm which can be attributed to the process of intrinsic plasma formation. For $z = 0$ mm a total of $\approx 5 \times 10^9$ generated harmonic photons per second is calculated (see equation (3.3.1)), which is associated with an energy conversion efficiency of $\epsilon_{He} \approx 10^{-7}$ and is to be compared with $\epsilon_{Ar} \approx 5 \times 10^{-7}$ for the argon gas cell (for a brief discussion about the comparison of values given for generated harmonic flux in literature please see section 5.2.3.6).

5.2.5 Conclusion

The generation of just a few coherent modes $H77$ to $H95$ in a helium semi-infinite gas cell with an energy conversion efficiency of one-fifth of that in an argon semi-infinite gas cell has been achieved. Macroscopic phase matching by exploiting the Gouy phase shift is achieved when the laser focus is properly placed inside the gas cell and deeper than in the case of the argon gas cell. Given the reasonably efficient generation of effectively 4 to 6 intense harmonic orders around ~ 9.5 nm, this helium-based high-harmonic generation source is a potential source for multiple-wavelength coherent diffractive imaging at a much higher resolution than previously achieved [6]. So far, image reconstruction of a non-periodic object with a resolution of < 100 nm using multiple harmonic orders of the argon gas cell has been achieved. As $\langle\lambda\rangle_{He} \approx 9.5$ nm and $\langle\lambda\rangle_{Ar} \approx 30$ nm, a significantly higher resolution of the reconstruction can be expected.

5.3 Degree of spatial coherence

In the following, the degree of spatial coherence is determined using different pairs of Young double-slits as explained in section 4.2.2. The fringe visibility of the different pairs of Young double-slits is tested for several experimental conditions, that is, for any variation of the parameters for macroscopic phase-matching.

5.3.1 Introduction

As explained in section 4.2.2 the average degree of spatial coherence is given by

$$\langle|\gamma_{12}|\rangle \approx \nu = \frac{I_{T,max} - I_{T,min}}{I_{T,max} + I_{T,min}}, \tag{5.3.1}$$

where ν is the fringe visibility (see equation (5.1.4)) and $I_{T,max(min)}$ is the intensity of the centre (first minimum) of the interferogram as depicted in figure 5.3.1. Great care is taken so that both of the Young double-slits are illuminated equally. Also, the harmonic orders can be assumed to have the same, or at least a very similar, degree of spatial coherence. Thus, to a very good approximation, the measured average degree of spatial coherence varies only negligibly when adjusting the macroscopic phase-matching parameters which strongly influence the number of effective harmonic orders and their relative weighting in the power spectrum. Therefore, the degree of spatial coherence is given by an average value of all of the effective orders in the harmonic beam and is directly determined by the fringe visibility of the measured interference pattern. .

5.3.2 Experimental conditions

The laser system is described in section 5.1.2. A calibrated aperture is applied to the laser beam before it is focused into a 400 mm-long argon gas cell, or a 260 mm-long helium or argon gas cell of different pressures, by a lens of focal length 500 or 400 mm. In general, the pressure, aperture diameter, energy of the laser pulses, position of the laser focus relative to the exit of the gas cell, and chirping of the laser pulses are optimized in an iterative procedure for maximum flux of all available harmonics. For the helium (argon) gas cell a silver or zirconium (aluminium) metal filter is used to separate the harmonics from the fundamental laser beam. The harmonic emission

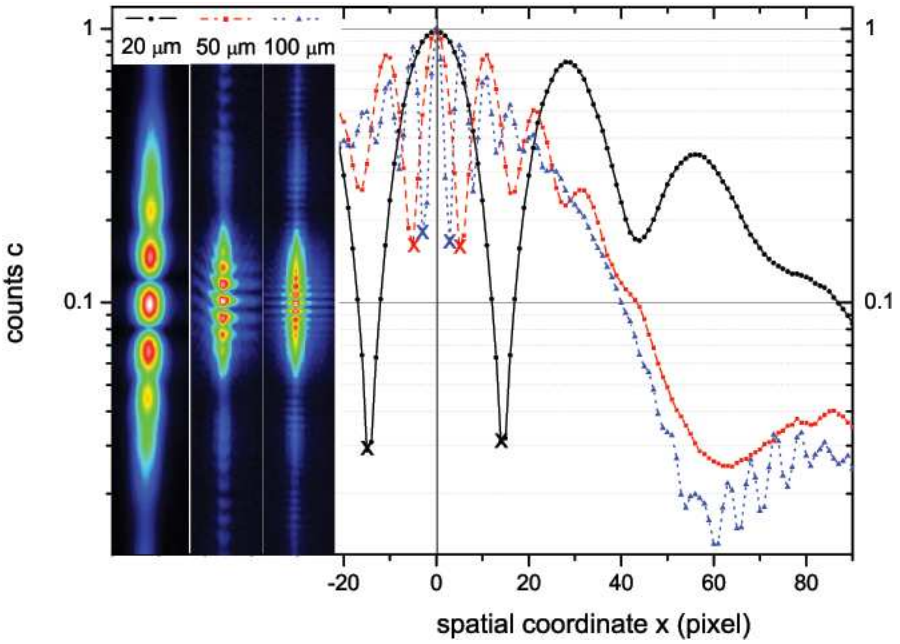

Figure 5.3.1: Cross-sections of the interference pattern for the 20, 50 and 100 μm spaced Young double-slits in the argon gas cell. The insets show contour plots of the interference pattern.

illuminates the Young double-slit pairs $S1$, $S2$ and $S3$, with a slit spacing of 20, 50 and 100 μm, respectively (table 4.1). The interferogram is detected directly by a charge-coupled device detector chip positioned 0.94 m from the exit of the gas cell. In-situ spectral analysis is performed by applying the maximum entropy method to the interference pattern of a Young double-slit pair illuminated with the emission of the harmonic source [8].

5.3.3 Results

The fringe visibility is determined for several experimental conditions, that is, for any variation of the parameters for macroscopic phase-matching. In fact, the fringe visibility is not affected, or only negligibly affected, by using different focal length lenses (400 and 500 mm), applying different pressures to the gas cell, using different aperture diameters and changing the energy of the laser pulses, the position of the laser focus relative to the exit of the gas cell, and chirping of the laser pulses. Therefore, the following measurement, which is based on the experimental conditions described in section 5.2 is representative of all the mentioned cases.

Figure 5.3.2 shows the degree of spatial coherence, or the fringe visibility, as a function of the spacing of the Young double-slits of an unapertured harmonic beam and an harmonic beam that is spatially filtered by a 100 μm-diameter-pinhole. For argon reliable values are achieved in all cases. However, due to technical limitions, for helium a reliable value of the degree of spatial coherence is only achieved for the Young double-slit pair $S1$ with slit spacing 20 μm. For argon a fringe visibility of $\sim$ 0.95 is measured for both the spatially filtered and unapertured beam when the Young double-slit pair $S1$ of spacing 20 μm is used. For the case of a spatially filtered harmonic beam, to a good approximation the fringe visibility decreases linearly to a value of $\sim$ 0.70 for the 100 μm spaced Young double-slit pair $S3$. Almost the same value is achieved for the unapertured harmonic beam. However, the value of the fringe visibility for the 50 μm spaced Young slits ($S2$) is considerably smaller compared to the spatially filtered beam. It is not clear why the spatial filter increases the degree of spatial coherence for the 50 μm spaced Young slits. For helium a fringe visibility of $\sim$ 0.80 for the Young double-slit pair of spacing 20 μm is measured. This value decreases rapidly for slit pairs of larger spacing. However, due to technical limitations, these values cannot be regarded as reliable; that is, the resolution of the interference pattern from the Young double-slits of larger spacing on the detector was insufficient due to the chosen distance between the Young double-slits and the detector and the pixel size of the detector. Therefore, for helium, the measurement of the degree of spatial coherence is limited to the slit pair $S1$.

In section 5.1.4 the degree of spatial coherence is measured across the spatial profile of the harmonic emission from an argon gas cell. Different aperture diameters are

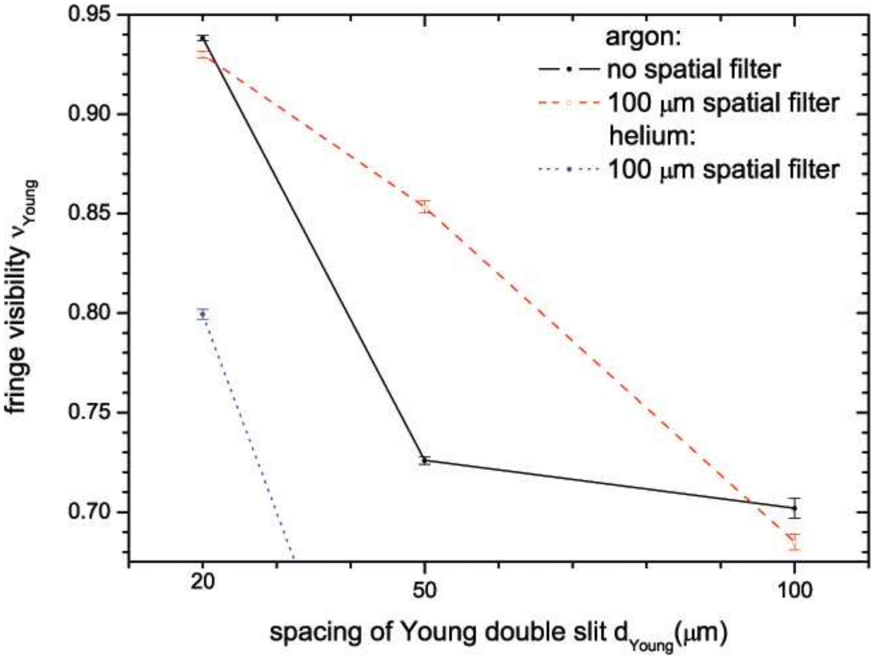

Figure 5.3.2: Degree of spatial coherence/fringe visibility as a function of the spacing of the Young double-slits with and without a spatial filter.

applied to the fundamental laser beam and different effective interaction lengths are chosen. In all cases and for all sample points across the spatial profile of the harmonic beam, almost perfect spatial coherence with a Young slit spacing of 20 μm is measured, indicating a spatial coherence length significantly larger than 20 μm.

5.3.4 Conclusion

For the argon gas cell a very high degree of spatial coherence is determined $\gamma_{12} > 0.71$. In particular, almost perfect spatial coherence with a Young slit spacing of 20 μm is measured. This indicates a spatial coherence length that is significantly larger than 20 μm. This result is important for the experiments on multiple-harmonic order coherent diffractive imaging [6] based on the argon gas cell that are presented in this work. As all samples investigated are < 20 μm, a perfect degree of spatial coherence can be assumed and incorporated in the algorithms for reconstruction of the samples from the diffractive images. Given the reasonably efficient generation of harmonic emission in helium with respect to the argon gas cell, the helium-based high-harmonic generation source is also a potential source for multiple-wavelength coherent diffractive imaging, but at a much better resolution than previously achieved [6] due to the smaller average wavelength of the harmonic orders around ~ 9.5 nm. Even for this source a reasonably high degree of spatial coherence, $\gamma_{12} \approx 0.80$, with the 20 μm-spaced Young slit spacing is measured. This too indicates that the diffractive images generated over the size of the samples discussed in this work are based on an harmonic electric field that exhibits a spatial coherence length reasonably close to 20 μm. Therefore the helium-based high-harmonic generation source is in fact a good source for multiple-wavelength coherent diffractive imaging.

5.4 Coherent diffractive imaging based on multiple-order harmonic emission

In the following, experimental work on coherent diffractive imaging is presented. Different samples are chosen, such as binary regular and irregular samples as well as a non-binary regular sample; here, binary refers to either opaque or fully transmissive for the harmonic emission, whereas the term non-binary refers to a sample in which the refractive index depends strongly on the wavelength of the harmonic beam. Regular refers to an array of pinholes of the same size and geometry, and irregular refers to an arbitrarily-shaped structure. All experiments are based on the harmonic emission generated in a semi-infinite argon gas cell. Rather than discriminating against all wavelengths but one, all effectively available harmonic orders are used for coherent diffractive imaging. The technique of coherent diffractive imaging based on multiple-order harmonic emission is explained in detail in section 4.3. In particular, this section features information about the preparation of the samples, acquisition of very high-dynamic range diffraction images using a beam stop, stitching of these images, and the algorithm for reconstruction of the object from the stitched image. Details about the experimental setup are given in section 3.3 in general, but in particular in section 3.3.3. This work has been published in [6, 9, 7].

5.4.1 Introduction

High harmonic generation sources naturally produce a laser-like beam that consists of multiple longitudinal coherent modes. In fact, the ratio $\Delta\lambda/\lambda$ can be as large as 1. However, traditional coherent diffractive imaging, which is based on error reduction or a hybrid input-ouput algorithm [44, 45], requires $\Delta\lambda/\lambda \leq 1$. Only then can the diffraction pattern be considered to be the Fourier transform of the object. Thus, usually coherent diffractive imaging is performed using one single harmonic order or one single wavelength of the harmonic spectrum. Discrimination of the wavelengths is achieved by means of optical elements such as narrow-bandwidth multilayer mirrors or a monochromator. Unless curved mirrors are used and the harmonic beam is focused onto the sample, this approach involves a significant loss of harmonic intensity due to the discrimination process itself and due to the intrinsic inefficiences of the optical elements. The brightness of harmonic sources is one of the major challenges of the field, and is several orders of magnitude lower than that of large installations such as synchrotrons or x-ray free-electron lasers. Thus, it is desirable to utilize as much harmonic flux as possible. Therefore, a new approach is pursued which involves acquisition of diffraction patterns based on multiple harmonic orders and reconstruction of the object by means of an algorithm that comprises a modified Gerchberg-Saxton iteration procedure and reconstruction refinement by means of an application of the maximum entropy method [6, 9].

In order to achieve a high resolution of the reconstruction of the object from the coherent diffractive images, diffractive images of high dynamic range need to be taken. Only then can diffractive features be captured at high angles, where the high-resolution information resides. Depending on the desired resolution of the reconstruction, speckles at high-angles need to be detected. The dynamic range of such a diffractive image can be 10^9 to 10^{10} or larger, where the term dynamic range refers to the intensity of the speckles measured as counts by a detector such as a charge-coupled device. The natural dynamic range of such a charged-coupled detector, usually 10^5 to 10^6, is not sufficient to cover this range. It is possible to mount the device on a precision x/y-stage and move the detector to the area of interest. Another approach is to use a beam stop that is placed over the intense speckles in the centre of the detector. Thus, a much longer exposure time can be chosen and speckles up to the edges of the detector can be recorded while avoiding saturation of any other pixels. Mounting such a beam stop on a wire can result in a contribution of the wires to the recorded diffraction pattern. Thus, a different approach is chosen. Here, two beam stops on a vertical and horizontal support are used to acquire two images so that, when combined with the intense centre speckles, a diffraction pattern of high dynamic range is achieved without any contribution from horizontal or vertical supporting material. A detailed discussion can be found in section 4.3.

5.4.2 Experimental conditions

The laser system is described in section 5.1.2. A calibrated aperture is applied to the laser beam before it is focused into a 260 mm-long argon gas cell of pressure 58 Torr by a lens of focal length 400 mm. The pressure, aperture diameter, energy of the laser pulses, position of the laser focus relative to the exit of the gas cell, and chirping of the laser pulses are optimized in an iterative procedure for maximum flux of all available harmonics. For the argon gas cell a silver or aluminium metal filter is inserted to separate the harmonics from the fundamental laser beam. The charge-coupled device detector chip (see section 3.3.4.1) is illuminated directly and positioned 0.94 m from the exit of the gas cell. Optionally, the grazing incidence spectrometer (Setpoint GIMS#4) can be inserted into the beam path. The spectrally-resolved far-field beam profile can then be detected along the height of the exit slit of the spectrometer. In-situ spectral analysis is performed by applying the maximum entropy method to the interference pattern of a Young double-slit pair illuminated with the emission of the harmonic source [8]. This in-situ spectral analysis allows the spectral power distribution of the harmonic source to be precisely tailored according to the experimental requirements, e.g., it allows the harmonic spectrum to be optimized with respect to the wavelength-dependent refractive index of the sample. By properly adjusting the macroscopic phase-matching parameters, in particular the effective interaction length and the aperture diameter, the harmonic emission can be confined to effectively one to four intense orders around ~ 30 nm with a high degree of spatial coherence and a good spatial profile [3, 2, 5, 4].

In order to obtain a high-quality reconstruction from the diffraction pattern of the illuminated objects, some experimental parameters, such as the distance between the sample and the detector, the sample size, the quality of the harmonic emission and the nature of the wavefield leaving the sample, need to be considered. In order to record a far-field diffraction pattern and thus satisfy the Fraunhofer criterion for plane wave illumination, the sample needs to be placed at a distance $z \gg d^2/\lambda_c \approx 12.4$ mm from the detector, where $d = \{10\ \mu\text{m}, 20\ \mu\text{m}\}$ is the dimension of the used samples and $\lambda_c \approx 32.2$ nm is the centre wavelength of the harmonic power spectrum. In all cases, the samples were placed at a distance $z = \{40\ \mu\text{m}, 60\ \mu\text{m}\}$ from the detector. Thus, for all cases the oversampling ratio is given by $OR = z\lambda_c/(dp) \geq 4.93$ so that the phase can be recovered easily from the diffractive images. Here $p = 13\ \mu$m is the size of the pixel of the detector. The fundamental limit of the resolution, the pixel size of the reconstructed image, is then given by $76 \text{ nm} \leq r_{recon} = ORd/N = z\lambda_c/(pN) \leq 114$ nm, where $N = 1300$ is the number of pixels of the detector chip in the x- and y-direction.

5.4.3 Two-dimensional array periodic samples

5.4.3.1 The periodic carbon film sample

The carbon film sample (2SPI Quantifoil R2/1) is a non-binary sample. The refractive index changes significantly over the spectral range of the harmonic beam. Thus, the diffracted spectrum will be altered after transmission through the carbon film. The reconstruction of the thickness function $T(\mathbf{r})$ therefore requires the input of the optical properties of carbon [152]. The perforated carbon film is of thickess $\sim$ 40 nm and features an array of 2 μm-diameter pinholes spaced from each other by 3 μm. Detailed information about the preparation of this sample can be found in section 4.3.6. This work has been published in [6, 9].

The diffraction data of this particular sample is acquired without the beam stop by the acquisition of one image containing the intense low-angle diffraction features and another image containing the weak high-angle diffraction speckles. Here the low-angle diffraction speckles in the centre of the charged-coupled detector are acquired with an exposure time of 1.2 s, and the high-angle speckles with an exposure time of 78 s. In the latter case, the centre of the image is highly overexposed and the detector was saturated. Each image consists of several frames for averaging and for statistical purposes. Both images are then normalized to each other and combined by image stitching (see section 4.3.4) so as to retain the high-angle scattering from the long-exposure data with the non-saturated low-angle diffraction data from the data of short-exposure time. The stitched diffraction pattern is shown in figure 5.4.1. The spectral composition of the harmonic beam used for illumination of the carbon film sample is shown in figure 5.4.2. The most intense harmonic order, the 25th, contains approximately 1/4th of the harmonic energy of the complete power spectrum. An efficient monochromator system, such as wavelength-selective multilayer mirrors, will have an efficiency of around 25 % [34]. Thus, employing the whole effectively harmonic

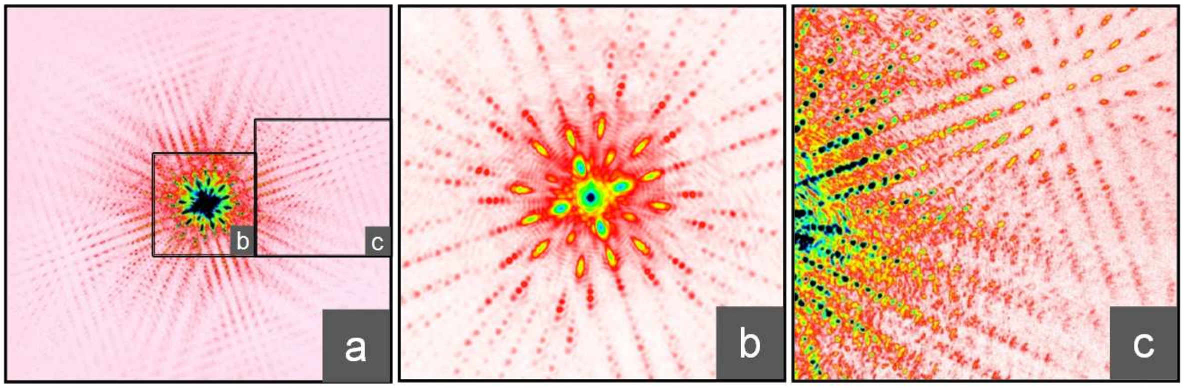

Figure 5.4.1: Diffraction pattern of the carbon film sample (a); zoom into centre (b); zoom into high-angle area (c).

spectrum from ~ 26 to 38 nm will have led to a reduction of the acquisition time by a factor of 16. Nevertheless, the differences in the experimental arrangement between the present work and other reports [34] make a precise comparison of the relative exposure

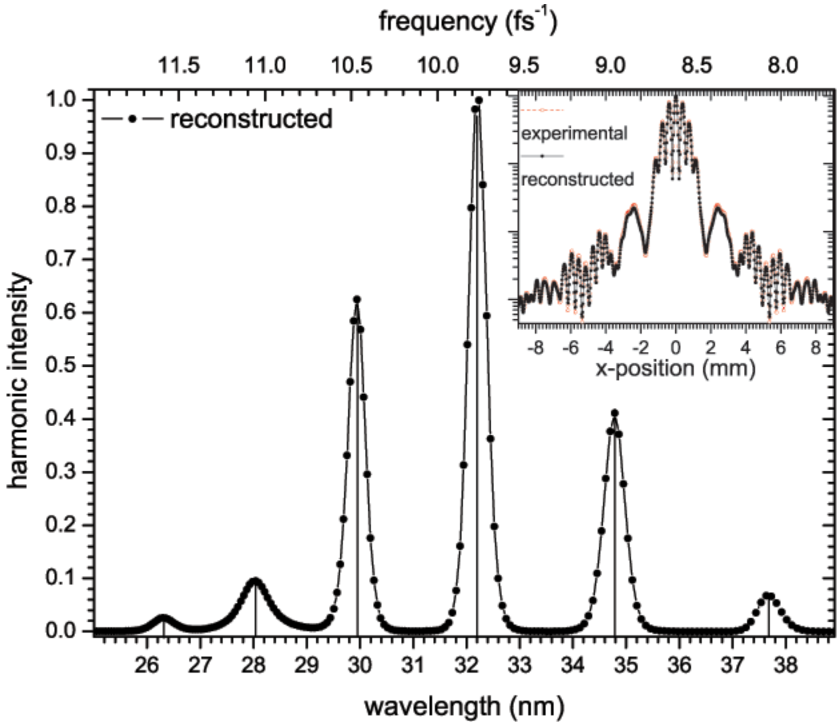

Figure 5.4.2: Spectral composition of the harmonic beam used for coherent diffractive imaging of the carbon film sample. The inset shows the excellent overlap of the experimental and reconstructed cross-section of the interference pattern from the Young double-slit (see section 4.2.3).

times difficult. The sample contains only a small number of periods within its finite extent defined by the 20 μm-diameter of the sandwiched pinhole. But the diffraction pattern has a strong qualitative resemblance to the diffraction pattern that would be produced by a larger periodic sample. However, closer inspection of the diffraction pattern reveals some important differences. There is significant diffraction between the diffraction speckles, and the speckles exhibit some structure. Moreover, the individual diffraction peaks themselves contain a series of peaks produced by each of the harmonic orders within the harmonic power spectrum (see picture c) of figure 5.4.1). Thus, the diffraction pattern is an incoherent superposition of the diffraction pattern produced by each of the harmonic orders.

A scanning electron microscope image of the carbon film sample is shown in picture a) of figure 5.4.3. The reconstruction, based on the modified Gerchberg-Saxton iteration (see section 4.2.3.1), is displayed in picture b), where the white dotted circle indicates the support that is used for the reconstruction. Due to the high level of noise, a maximum-entropy-method-based refinement (see section 4.3.5.2) is applied to this reconstruction as shown in picture c). This refinement produces a smoother image, but some of the details that could be recovered in the reconstruction are lost. This is an indication that the algorithm overestimates the level of noise in the reconstructed image and thus probably underfits the data. In picture c) it can be seen that each of the pinholes exhibits a faint cross-like structure that probably has the same or a related origin. It can be seen that the otherwise circular reconstruction is obscured by a polymer layer at the top. Due to the manufacturing process this polymer layer of thickness ≤ 20 nm remained on the carbon film. The polymer layer is completely opaque to the electrons, as seen in the scanning electron microscopy image a), but partially transparent to the harmonic beam due to the greater penetration depth. Thus, the individual pinholes can be seen through the polymer in the reconstructed images b) and c). The carbon film is not completely opaque to the incident light and so the diffracted spectrum is altered by transmission of the harmonic light through the foil. It is apparent that the pinhole array extends further in the image of the reconstruction compared to the scanning electron microscope image and that the edge of the sandwiched 20 μm-diameter pinhole is much sharper. This feature can be attributed to the greater penetration of the extreme-ultraviolet radiation and the greater depth of field. The reconstruction algorithm directly returns a value for the average sample thickness of the carbon foil of 37(2) nm, which is consistent with the thickness of $\sim$ 40 nm stated by the manufacturer. In order to determine the resolution, a sigmoid is fitted to the edge distribution of the individual pinholes in the reconstructed image. A value of 165(5) nm is obtained for the full width at half maximum. This value is consistent with the estimated value $\Delta = 0.94\lambda_c/NA \approx 151$ nm based on the Sparrow criterion (see [6]), where $NA \approx 0.2$ is given by the sine of the vertex angle of the largest cone of meridional rays that can enter the 26.8 mm×26.8 mm charge-coupled device detector chip of pixel size $p = 13$ μm (see section 3.3.4.1), from which the sample is placed at a distance of 6 cm, and $\lambda_c = 32.2$ nm. The fundamental limit of the resolution, the pixel size of the reconstructed image, is given by $r_{recon} = z\lambda_c/(pN) \approx 114$ nm. We note that similar research carried out by other groups has yielded in reconstructed images of resolutions around 100 nm [33, 155] (see sections 5.4.3.2 and 5.4.4).

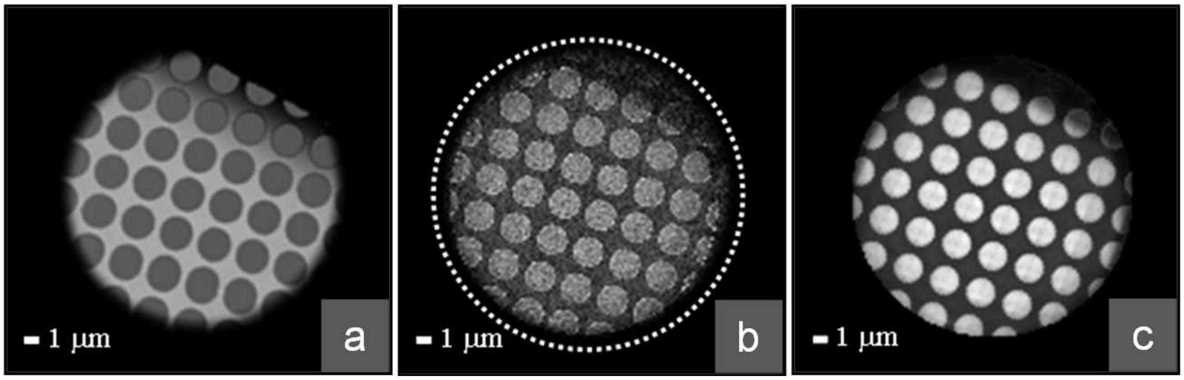

Figure 5.4.3: Scanning electron microscopy image of the carbon film sample (a); reconstruction before (b) and after (c) the maximum entropy method-based refinement.

5.4.3.2 A periodic Si_3N_4 substrate sample

The Si_3N_4 substrate sample is a binary sample that is micromachined into a thin (≥ 100 nm) gold layer on a Si_3N_4 substrate. Except for the featured structures, this sample is opaque to the harmonic emission. The binary regular sample exhibits an array of 2 μm-diameter pinholes spaced by 3 μm arranged in the domain of a 20 μm-diameter circle. Thus, this sample is similar to the carbon film sample from section 5.4.3.1 or 4.3.6.1. However, this sample does not require a pinhole to restrict the illumination to a particular area, it is either transmissive or opague and does not have any polymer film on its surface. A scanning electron microscope image of this sample is shown in picture a) of figure 5.4.5. Compared to the carbon film sample, this sample did not require any sample preparation and could be readily installed on the sample holder. This work has been published in [7].

The diffraction data set of the binary regular sample is characterized by the acquisition of one image containing the intense low-angle diffraction features and two images containing the weak high-angle diffraction speckles by employment of the horizontal and vertical beam stops. The low-angle diffraction speckles in the centre of the charged-coupled detector are acquired with an exposure time of 1 s, and the high-angle speckles with an exposure time of 135 s. Each image consists of several frames for averaging and statistical purposes. All three images are then normalized to each other and combined by image stitching (see section 4.3.4) in order to retain both the high-angle scattering data (with long exposure time) and low-angle diffraction (with short-exposure time). The stitched diffraction pattern is shown in figure 5.4.4.

A scanning electron microscope image of the carbon film sample is shown in picture a) of figure 5.4.5. The reconstruction, based on the modified Gerchberg-Saxton iteration (see section 4.2.3.1) and refinement by the application of the maximum-entropy-method (see section 4.3.5.2) is displayed in picture b). Clearly, the algorithm

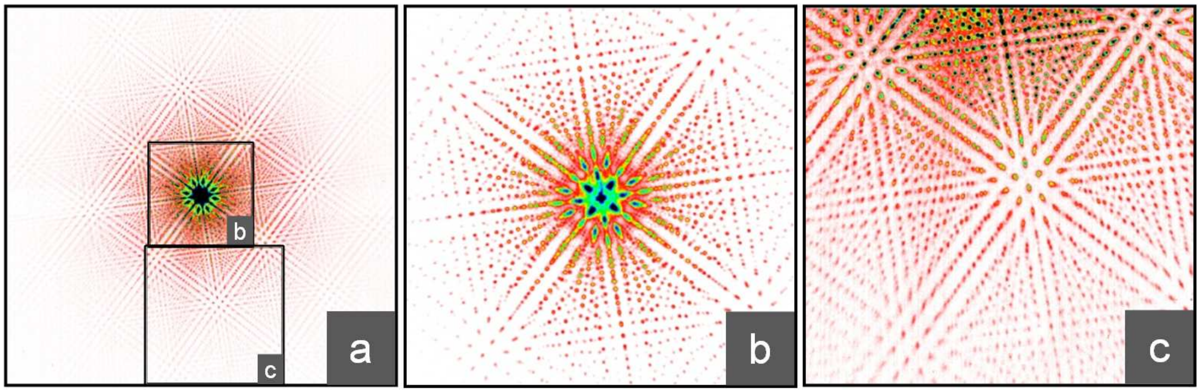

Figure 5.4.4: Diffraction pattern of the binary regular sample (a); zoom into centre (b); zoom into high-angle area (c).

can recover the pinholes from the diffraction pattern. However, the algorithm also fits a non-zero intensity inside these holes and even fits very-weak-intensity pinholes at the edges of the circle that hosts the array of pinholes. In order to determine the resolution, a sigmoid is fitted to the edge distribution of the individual pinholes in the reconstructed image. A value of 100 nm is obtained for the full width at half maximum. This value is consistent with the estimated value $\Delta = 0.94\lambda_c/NA \approx 100$ nm based on the Sparrow criterion, where $NA \approx 0.29$ is given by the sine of the vertex angle of the largest cone of meridional rays that can enter the 26.8 mm×26.8 mm charge-coupled device detector chip of pixel size $p = 13$ μm (see section 3.3.4.1), from which the sample is placed at a distance of 4 cm, and $\lambda_c = 32.2$ nm. The

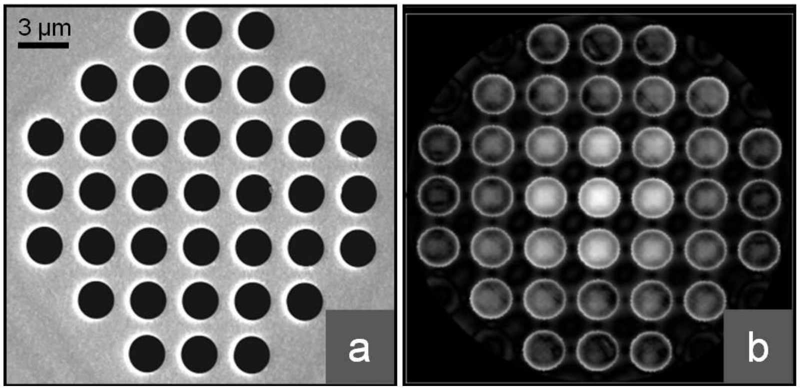

Figure 5.4.5: Scanning electron microscopy image of the binary regular sample (a); reconstruction after the maximum entropy method-based refinement (b).

resolution achieved in this experiment is comparable to the resolution of reconstructed images of similar research on coherent diffractive imaging by well-established and well-experienced experimental groups, in particular [33, 155] (see sections 5.4.3.1 and 5.4.4). We note that the fundamental limit of the resolution, the pixel size of the reconstructed image, is given by $r_{recon} = z\lambda_c/(pN) \approx 76$ nm.

5.4.4 An aperiodic Si_3N_4 substrate sample

The aperiodic Si_3N_4 substrate sample is a binary sample that is micromachined into a thin (≥ 100 nm) gold layer on a Si_3N_4 substrate. Except for the featured structures, this sample is opaque for the harmonic emission. This binary irregular sample features an array of size 10 μm × 10 μm and rectangular pinholes of different lengths and widths. A scanning electron microscope image of this sample is shown in picture a) of figure 5.4.7. Compared to the carbon film sample, this sample did not require any sample preparation and could be readily installed on the sample holder. This work has been published in [7].

The diffraction data set of this binary irregular sample is characterized by the acquisition of one image containing the intense low-angle diffraction features and two images containing the weak high-angle diffraction speckles by employment of the horizontal and vertical beam stops. The low-angle diffraction speckles in the centre of the charged-coupled detector are acquired with an exposure time of 3 s, and the high-angle speckles with an exposure time of 300 s. Each image consists of several frames for averaging and statistical purposes. All three images are then normalized to each other and combined by image stitching (see section 4.3.4) in order to retain both the high-angle scattering data (with long exposure time) and the low-angle diffraction data (with short exposure time). The stitched diffraction pattern is shown in figure 5.4.6.

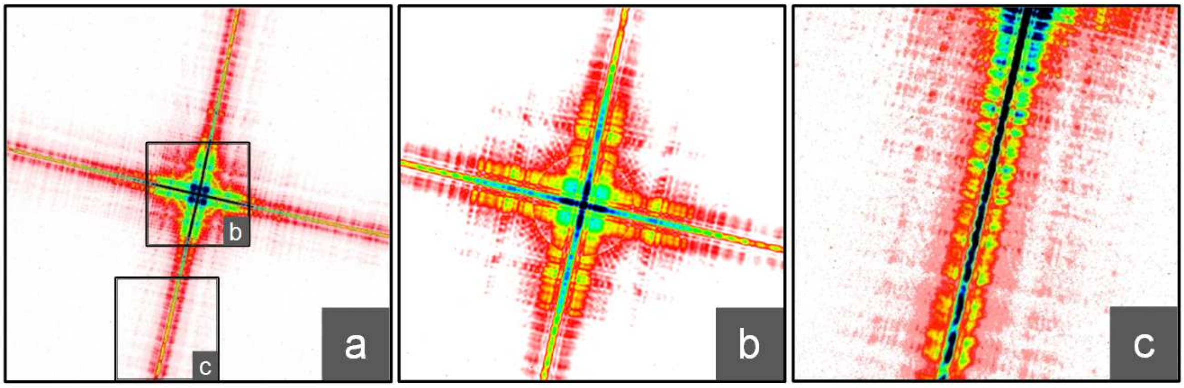

Figure 5.4.6: Diffraction pattern of the binary irregular sample (a); zoom into centre (b); zoom into high-angle area (c).

A scanning electron microscope image of the carbon film sample is shown in picture a) of figure 5.4.7. The reconstruction, based on the modified Gerchberg-Saxton iteration (see section 4.2.3.1) and refinement by the application of the maximum-entropy-method (see section 4.3.5.2) is displayed in picture b). Clearly, the algorithm can recover the rectangular pinholes from the diffraction pattern. Moreover, as indicated by the white circle in pictures a) and b), the algorithm even recovers a contamination particle on the edge of one of the pinholes. It is apparent that each of the pinholes exhibits faint cross-like structures that probably have the same or a related origin. A similar effect is observed in the reconstruction of the carbon film sample in picture c) of figure 5.4.3. In order to determine the resolution, a sigmoid is fitted to the edge distribution of the individual pinholes in the reconstructed image.

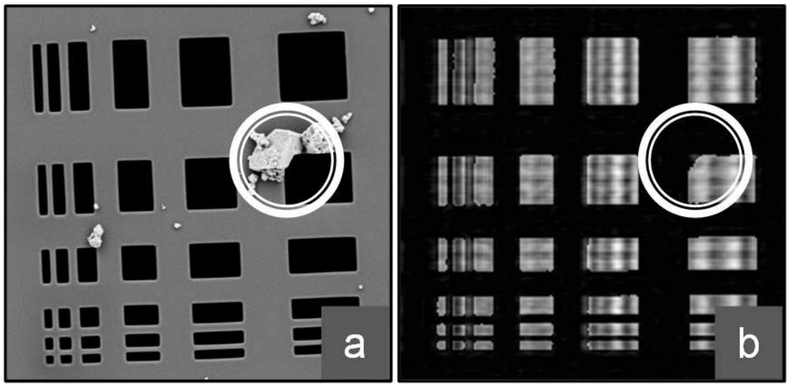

Figure 5.4.7: Scanning electron microscopy image of the binary irregular sample (a); reconstruction after the maximum entropy method-based refinement (b).

Again, a value of 100 nm is obtained for the full width at half maximum. This value is consistent with the estimated value $\Delta = 0.94\lambda_c/NA \approx 100$ nm based on the Sparrow criterion, where $NA \approx 0.29$ is given by the sine of the vertex angle of the largest cone of meridional rays that can enter the 26.8 mm×26.8 mm charge-coupled device detector chip of pixel size $p = 13$ μm (see section 3.3.4.1), from which the sample is placed at a distance of 4 cm, and $\lambda_c = 32.2$ nm. As mentioned in section 5.4.4, the resolution achieved in this experiment is comparable to the resolution achieved by by well-established and well-experienced experimental groups doing similar research on coherent diffractive imaging [33, 155]. Again, the fundamental limit of the resolution, the pixel size of the reconstructed image, is given by $r_{recon} = z\lambda_c/(pN) \approx 76$ nm.

5.4.5 Conclusions

A new approach to coherent diffractive imaging is the illumination of a sample with high harmonic emission consisting of several harmonic orders. A new algorithm is used to compute the diffraction pattern produced by this experimental setup. This algorithm is a modified version of the conventional coherent diffractive imaging algorithm and includes the spectrum optimization (gradient descent method) iterative procedure inside the main reconstruction iterative process, and furthermore the image quality could be improved significantly by applying the maximum entropy method. The presented results demonstrate that this approach is successful in reconstructing the object from experimentally collected data. In particular, the employment of a horizontal and a vertical beam stop allows the achievement of very high dynamic range coherent diffractive images comprising low-angle and high-angle diffraction speckles with no information from any supporting material of the beam stops.

The results are relevant to coherent diffractive imaging of homogeneous objects, and is directly applicable to many cases of practical interest. In particular, binary, non-binary, regular and irregular samples have been successfully imaged. However, in a first step, this approach can be extended to include the analysis of objects consisting of several known materials, and in a second step, it can be applied to non-homogeneous objects comprised of unknown materials. In general, the approach of multiple-harmonic-order coherent diffractive imaging eliminates the need for an illuminating wavefield that exhibits perfect spatial and temporal coherence and allows diffraction images to be processed that are a superposition of different diffraction images associated with each harmonic order of the multiple-harmonic order high-harmonic generation source. The possibility of using non-monochromatic sources will extend the applicability of coherent diffractive imaging experiments to better enable the usage of high-harmonic generation sources. However, while only diffraction data produced using a high-harmonic generation source is considered explicitly here, the formalism can be readily adapted to any short-wavelength polychromatic source in which there is a high degree of spatial coherence at each sampled wavelength but poor temporal coherence across the sampled spectrum. This novel approach may also, consequentially, be adapted and applied to the multi-mode x-ray free-electron laser sources currently under development. The current activity in the development of multi-mode x-ray free-electron laser sources with high spatial resolution suggests that this approach may find direct application in proposals for imaging single molecules with atomic resolution using short pulse coherent diffractive imaging. The relaxation of the requirement that the illuminating source be strictly monochromatic in diffractive imaging technologies may well prove to be valuable in the future design and analysis of materials and biomolecules.

Chapter 6

Future Directions

The generation of just a few coherent modes in a helium semi-infinite gas cell can be performed with an energy conversion efficiency of one-fifth of that achieved in the argon semi-infinite gas cell, i.e., $\epsilon_{He} = 10^{-7}$ [4]. Given this reasonably efficient generation of effectively 4 to 6 intense harmonic orders around $\langle\lambda\rangle_{He} \approx 9.5$ nm, the helium-based high-harmonic generation source is a potential source for multiple-wavelength coherent diffractive imaging at a much higher resolution than previously achieved [6, 9]. So far, image reconstruction of a non-periodic object with a resolution of < 100 nm using multiple harmonic orders from an argon gas cell has been achieved. As $\langle\lambda\rangle_{He} \approx 9.5$ nm and $\langle\lambda\rangle_{Ar} \approx 30$ nm [2, 3, 5], a significantly higher resolution of the reconstruction can be expected. This work could be performed without any adjustments to the experimental setup or to the algorithm developed for the multiple-wavelength coherent diffractive imaging.

The multiple-order harmonic emission can also be employed to develop imaging schemes [8, 9] for non-homogeneous objects by slightly varying the laser frequency in order to obtain overlapping diffraction images and by using various exotic polymers as an absorbing sample, such as polyacetylene polymers (pure carbon), fluoro-polymers, polymers with sulphonate side groups and polymers doped with very heavy elements. Furthermore, the multiple-order harmonic emission can facilitate studies of birefringence/dichroism by analyzing the polarization properties of the polymers in the presence of stress/strain and external electric fields. This work could be performed without any major adjustments to the high-harmonic generation apparatus or the femtosecond laser system.

The high-harmonic generation apparatus can reliably deliver highly coherent phase-matched extreme-ultraviolet radiation around $\langle\lambda\rangle_{Ar} \approx 30$ nm based on an argon gas cell setup [2, 3, 5] and around $\langle\lambda\rangle_{He} \approx 9.5$ nm based on an helium gas cell setup [4]. Extending the harmonic emission of this source into the water-window is one of the major goals of this group and is currently under exploration. Here, the flux has to be sufficient for biophysical applications in general and coherent diffractive imaging in particular. This work requires the existing experimental setup (see chapter 3) to be upgraded. Employing an electrical discharge gas cell or an additional laser beam prior to triggering the high-harmonic generation process, the first approach may allow the creation of a plasma and thus the generation of high harmonics in the soft x-ray region. Because of the higher nonlinear susceptibility of ionic media, high-harmonic radiation in the extreme-ultraviolet and soft x-ray region can be generated more efficiently. When employing an additional laser beam to generate a preformed plasma and using a train of laser pulses, the laser system has to be able to provide pulses of sufficient energy. The high-power femtosecond laser system consists of a highly stable femtosecond titanium:sapphire oscillator and two amplification stages (see chapter 3.1). The second amplification stage has recently been updated with a second pump laser and is now able to generate pulses of energy 13 mJ. Furthermore, an optical parametric amplifier is currently being set up that will allow the laser radiation to be frequency down-converted from ~ 800 nm to ~ 1.6 μm. This allows a second approach to extend the high-harmonic generation into the water-window due to the fact that the electrons can acquire a larger maximum kinetic energy during the generation process. The ponderomotive potential is proportional to the square of the centre wavelength of the laser light, $U_{pond} \propto I\lambda^2$ (equation (2.3.8) in chapter 2.3.2.2), and the harmonic cutoff is given by $E_{cutoff} = I_p + 3.17U_{pond}$ (equation (2.3.5) in chapter 2.3.2.2), where I_p is the ionization potential of the nonlinear medium.

Once the high-harmonic generation apparatus is able to deliver a reasonable flux of harmonic emission in the water-window region, it may allow us to pursue the major goal of the ARC Centre of Excellence for Coherent X-Ray Science, that is, the non-crystallographic structural determination of membrane proteins (see chapter 1). The short-pulse, short-wavelength bright and coherent light may then allow the direct observation of the structures and reaction dynamics of isolated molecules, and thus a study of biological systems such as membrane proteins. These proteins mediate the activity of pharmaceuticals in human medical therapies. Their structures, however, are still mostly unknown as they are largely inaccessible to conventional crystallographical techniques due to their reluctance to form crystalline specimens. A breakthrough in this area could revolutionize rational drug design through the insight gained into the function of membrane proteins. Furthermore, fundamental issues in the use of this type of light source, including the nature of the interaction between intense coherent x-rays and electronic matter and the management of radiation damage throughout the interaction, the efficiency of diffraction processes in these highly coupled light-matter systems, and the design of algorithms to extract structural information from diffraction data are also under exploration.

We also intend to continue our work on quasi-phase-matching, in particular on a new kind of excimer-laser micromachined, modulated waveguide for corrugation-induced, first-order quasi-phase-matching as presented in section A.4.2. The technique of employing laser micromachining of the inside of the waveguide is be superior to the established technique of precision glass blowing and modulation by means of applying a high pressure inside the waveguide and area-confined heating.

Appendix A

Supplementary information

A.1 The 'Strong Field Approximation'

The strong field approximation to the time-dependent Schrödinger equation is the quantum-mechanical counterpart of the 'Simple Man's Model' (see section 2.3.2). When extended to allow for rescattering (see [76] and section 2.3.2.2) and atom-specific electron-atom scattering potentials, the predictions of this model provide good qualitative and quantitative agreement with ab initio calculations. Compared to the numerical integration of the time-dependent Schrödinger equation, it allows both a physical understanding and an analytical description with much less computational effort. The 'Strong Field Approximation' is based on the following assumptions: (1) only the ground state exists and the bound states are neglected, which implies that the ionization potential I_p is larger than the photon energy, (2) the depletion of the ground state can be neglected, which allows only a weak field, and (3) the electron can be treated like a free particle in the laser electric field once it leaves the parent ion, which is valid for a Keldysh parameter $\gamma < 1$. These approximations are valid in the tunneling regime as elaborated in section 2.4.4. A complete derivation and discussion of the main output of this model is provided in a number of publications [67, 75, 88].

A.2 Chromatic aberrations

In general, the refractive index n of a particular material depends on the wavelength λ of the electromagnetic radiation passing through the material. Thus a lens has a focal length that depends on the wavelength of the radiation. The diffracted transverse and longitudinal cross-section of the focused laser pulse depends on the wavelength, too. As the bandwidth of an ultrashort laser pulse is broadband, chromatic aberration leads to the distribution of laser pulse energy over a larger longitudinal and transverse cross-section of the focused pulse and thus can modify the interaction volume of the focused pulse and the nonlinear target medium significantly. All calculations are in-vacuo and to be understood as estimations based on a plane-wave and homogeneous illumination. A more precise estimation of the transverse and longitudinal focal volume can be found in section 5.1.3, 5.1.4 and 5.2 and is based on a laser beam that is Gaussian in its spatial domain and truncated radially by a variable-diameter aperture [129]. Effects due to propagation in the nonlinear medium are not considered.

A.2.1 Aberrated transverse and longitudinal cross-section of the focused pulse

To consider the change in focal length with wavelength,

$$\frac{d\left(\frac{1}{f}\right)}{d\lambda} = -\frac{1}{f^2}\frac{df}{d\lambda} \tag{A.2.1}$$

needs to be calculated, where f is the wavelength-dependent focal length of the lens given by

$$\frac{1}{f(\lambda)} = (n(\lambda) - 1)\left(\frac{1}{R_1} - \frac{1}{R_2}\right), \tag{A.2.2}$$

where R_1 and R_2 are the front and back surface radii of the curvature of the lens. With equations (A.2.2) and $df/d\lambda \approx \Delta f/\Delta\lambda$ it follows that

$$\Delta f \approx -0.441 \frac{f\lambda^2}{(n-1)\, c\tau_p} \frac{dn}{d\lambda}, \tag{A.2.3}$$

where $\Delta\lambda \approx 0.441\lambda^2/(c\tau_p)$ is the bandwidth of a pulse that is Gaussian in its temporal domain with pulse duration τ_p and c is the speed of light. To calculate the chromatic aberration at the diffraction limit of the transverse cross-section of the focused laser spot, $dd_{dfr}/d\lambda \approx \Delta d_{dfr}/\Delta\lambda$ has to be calculated, where $d_{dfr} = 4/\pi \cdot f\lambda/d_p$ is the diffraction limit of the focused incident laser beam of diameter d_p. Thus, the uncertainty of the transverse cross-section of the diffraction-limited focused laser beam is given by

$$\Delta d_{dfr} \approx 0.441 \frac{d_{dfr}\lambda}{c\tau_p}. \tag{A.2.4}$$

A.2.2 Transverse and longitudinal cross-sectional abberations for an experimental pulse

In the following a focal length of $f = 0.4$ m, $(n-1) \approx 0.453$ and $\lambda \cdot dn/d\lambda \approx -0.016$ are assumed for a fused silica lens. We let the $\lambda = 805$ nm laser pulse have a duration of $\tau_p = 30$ fs and a diameter of $d_p = 12$ mm after the amplification process. Divergence is neglected. Using equation (A.2.3) it can be estimated that $\Delta f \approx 558$ μm. Diffraction levels the transverse cross-section of the focused spot to a limit of $d_{dfr} \approx 34$ μm. Therefore the Rayleigh length is given by $z_R = \pi d_{dfr}^2/\lambda \approx 4.5$ mm. For the aberration of the diffraction limit of the focused laser beam diameter equation (A.2.4) is used to estimate $\Delta d_{dfr} \approx 1.3$ μm. This value is much smaller than the diffraction limit of the focused beam itself, $d_{dfr} \approx 34$ μm. Thus, $\Delta f/z_R \approx 0.12$ and $\Delta d_{dfr}/d_{dfr} \approx 0.04$ are small, but cannot be neglected. Note that Δf and Δd_{dfr} depend on the first power of the inverse of the pulse length τ_p. Therefore, for the same experimental conditions, chromatic aberrations are more severe for few-cycle laser pulses than for many-cycle laser pulses and must be considered when planning experiments that are highly sensitive to spatio-temporal distortions.

A.2.3 Distortion effects due to group delay

A lens is determined by the material and the radii of the front and back surface curvature. Assuming a radially symmetric lens, its thickness differs radially and so does the group delay. Therefore the different spatial parts of the pulse arrive at different times at the focus, with the latest pulse arrival time on-axis. As the group velocity is smaller than the phase velocity, the pulse fronts of the emerging pulse will not be flat. In fact the pulse fronts will become distorted and lag the phase fronts, with the largest effect on-axis. In general the radially varying group delay leads to spatial pulse lengthening and focal distortions.

A.2.3.1 Radially varying group delay

The temporal difference between the pulse and phase front varies radially and is given by

$$\begin{aligned} \Delta t(r) &= \left(\frac{1}{v_\phi} - \frac{1}{v_g}\right) L(r) && \text{(A.2.5)} \\ &= \frac{\lambda}{c}\frac{dn}{d\lambda}\left(\frac{r_0^2 - r^2}{2}\right)\left(\frac{1}{R_1} - \frac{1}{R_2}\right), && \text{(A.2.6)} \end{aligned}$$

where $L(r) = \left(\left(r_0^2 - r^2\right)/2\right)\left(1/R_1 - 1/R_2\right)$ is the radially varying thickness of the lens. R_1 and R_2 are the front and back-surface radii of curvature of the lens and r_0 is the maximum radius of the lens. Here the phase velocity is given by $v_p = c/n$ and the group velocity is given by $v_g = c/n \cdot 1/\left(1 - \lambda/n \cdot dn/d\lambda\right)$. The influence of the chromaticity of the lens can be elucidated when using equation (A.2.2) and combining it with equation (A.2.6). The temporal difference can be rewritten as

$$\Delta t(r) = \frac{\lambda}{c}\left(\frac{r_0^2 - r^2}{2}\right)\frac{d}{d\lambda}\left(\frac{1}{f}\right). \tag{A.2.7}$$

Using equation (A.2.2) and comparing the difference in group delay at the radial position of the lens corresponding to the beam diameter $r = d_p/2$ and at the radial position corresponding to the optical axis $r = 0$ one obtains

$$\begin{aligned} \Delta t_g &= \Delta t_g(r_0) - \Delta t_g(0) && \text{(A.2.8)} \\ &= \frac{-\lambda}{(n-1)\,f(\lambda)c}\frac{dn}{d\lambda}\frac{d_p^2}{8}. && \text{(A.2.9)} \end{aligned}$$

Note that the phase delays are equal and cancel out. Also, equation (A.2.9) is a function of wavelength as chromatic aberration of the focal length of the lens occurs.

A.2.3.2 Radially temporal delays for an experimental pulse

In the following a focal length of $f = 0.5$ m, $(n - 1) \approx 0.453$ and $\lambda \cdot dn/d\lambda \approx -0.016$ are assumed for a radially symmetric, fused silica lens. We let the $\lambda = 805$ nm laser pulse have a duration of $\tau_p = 30$ fs and a diameter of $d_p = 12$ mm after the amplification process. Divergence is neglected. Using equation (A.2.9) it can be estimated that $\Delta t_g \approx$ 5.3 fs. $\Delta t_g/\tau_p \approx 0.18$, and thus pulse lengthening cannot be neglected. Therefore, for the same experimental conditions, temporal distortions due to radially varying group delay are more severe for few-cycle laser pulses than for many-cycle laser pulses and must be considered when planning experiments that are highly sensitive to spatio-temporal distortions.

A.2.4 Achromaticity and group velocity dispersion

Chromatic aberration as described by equation (A.2.1) and radially varying pulse delay as described by equation (A.2.9) can lead to severe spatio-temporal effects depending on the experimental parameters of the driver pulse and the focusing geometry and can be the reason for serious focal distortions. Nevertheless, both effects are based on the chromaticity of the focusing means and can be canceled, i.e., by means of an achromatic lens for which $d\left(1/f\right)/d\lambda = 0$. When combining two lenses the focal length is given by

$$\frac{1}{f} = (n_1 - 1)\left(\frac{1}{R_{11}} - \frac{1}{R_{12}}\right) + (n_2 - 1)\left(\frac{1}{R_{21}} - \frac{1}{R_{22}}\right). \tag{A.2.10}$$

By carefully choosing the first lens with refractive index n_1 and radii of curvature R_{11} and R_{12} of the front and back surface curvature and the second lens with refractive index n_2 and radii of curvature R_{21} and R_{22} of the front and back surface curvature, a lens can be created that is achromatic to first order. Thus chromatic aberration and the effects of radially varying group delay can be avoided or minimized, a necessary requirement for keeping few-cycle laser pulses short at their focus.

A.2.5 Minimizing focus distortions

Radially varying group delay is the reason for spatial chirp of the driver pulse with maximum chirp on axis, whereas group delay dispersion is the reason the pulse also becomes chirped temporally. The magnitude of the chirp depends on the radial position where maximum chirp occurs on-axis. While chromatic aberration and radially varying group delay can be minimized or eliminated using an achromatic lens, we note that using a Fresnel lens, which has no group velocity component in the delay, to avoid group delay dispersion cannot solve the problem. This is due to the fact that in that case the pulse fronts lead the phase fronts. Using an achromatic lens and pre-compensating for average group delay dispersion can hardly be done exactly. Moreover some pulses have a bandwidth that can hardly be supported by a lens. When using a curved mirror in Cassegrain design, on-axis problems occur as the beam centre is blocked. Off-axis astigmatism is a problem. The use of an off-axis paraboloid is hampered due to the fact that it is difficult to manufacture and align such an paraboloid.

A.3 Quasi-phase-matching

The first proposal of phase-corrective techniques was made by Armstrong et al. in 1962 [156], later termed quasi-phase-matching. Quasi-phase-matching does not try to eliminate or minimize the phase mismatch between a pump and a signal beam totally. Instead, it aims to correct the phase mismatch periodically. Here a period corresponds to two times the coherence length, which is defined as the length of the optical path where the phase difference between the pump and signal beam accumulates to π, corresponding to half an optical cycle. In this case destructive interference would occur and back-convert the harmonic radiation into the fundamental field. The approach to eliminate high-harmonic generation in out-of-phase zones is known as quasi-phase-matching. Several approaches have been suggested [157, 98]: first, modulating the gas density is able to counteract geometric phase mismatches, but cannot eliminate or counteract index phase-mismatches and intrinsic intensity phase-mismatches. Moreover this approach involves significant experimental challenges. Second, relatively weak counter-propagating light can seriously disrupt phase-matching at a microscopic level. Multiple counter-propagating light pulses can be made to collide with the main generating pulse throughout the laser focus. The timing and duration of these counter-propagating pulses can be chosen appropriately to frustrate harmonic production in regions with undesirable phase. The emission from the remaining regions then constructively interferes. A third approach for quasi-phase-matching is difference-frequency-mixing, and a fourth approach angular tuning of crossing beams. Nevertheless, the highly nonlinear nature of high-harmonic generation allows the high-harmonic generation spectrum to be easily modulated by periodically modulating the intensity of the driving pulse. High-harmonic generation can be turned off when the phase slip between the pump and signal beam accumulates an odd multiple integer of π and can be turned on again when the phase slip is an even multiple integer of π thus preventing destructive interference. Therefore the harmonic radiation can add constructively with the harmonic radiation generated down-stream in the waveguide.

High-harmonic generation will be quasi-phase-matched when the geometric waveguide modulation of its diameter matches the period of the phase-mismatch between the pump and signal, which is twice the coherence length. In fact, very high-order nonlinear processes where very small phase changes can dramatically change the output allow quasi-phase-matching to work. Harmonics near the cut-off that require high laser intensity for the generation can thus easily be turned on or off by the modulation.

A.3.1 Required modulation for quasi-phase-matching

The procedure to calculate the required modulation of the corrugated waveguide that aims for quasi-phase-matching of a particular harmonic order is given as follows: first, the Ammosov-Delone-Krainov model [74] or quantum calculations are used to determine how much of the generating medium will be ionized at a high intensity of the driver pulse. Second, the phase-mismatch $\Delta k = k_q - k_{laser}$ is calculated which depends on the wavelength of the driver pulse, the harmonic order, the waveguide radius, the ionization fraction, the gas pressure and the number density and the refraction of the neutral gas. At high ionization levels the phase-mismatch can be approximated by the contributions of the plasma. Third, the calculated phase-mismatch can be compensated by the modulated waveguide since this leads to modulation of the nonlinear coefficient. It turns out that a maximum power output can be achieved for a particular modulation period and a particular quasi-phase-matching process order (which is not the harmonic order). Even if the phase-mismatch cannot be compensated by a first order quasi-phase-matching process, which would lead to a maximum enhancement of the harmonic yield, it can be compensated by a higher-order quasi-phase-matching process, which allows at least a somewhat lower enhancement in harmonic output.

A.3.2 Experimental quasi-phase-matching

Experimentally quasi-phase-matching can be achieved by a variety of different techniques.

Modulated and straight guided-beam geometries: the straight waveguide geometry offers the possibility of phase-matching and thus enhanced harmonic power output. At low ionization levels the negative contribution of the waveguide to the total waveguide k-vector can compensate positive contributions of the medium. Note that the sign of the plasma and the waveguide contributions are both negative. Thus this scheme does not work when the ionization level is above a certain level. This limits the possibility to achieve output of very high harmonics since these require high intensities. The choice of an alternative nonlinear medium with a higher ionization energy is limited due to the fact that these media usually have a smaller cross-section of the nonlinear susceptibility and thus provide only small harmonic power output. Moreover, comparing the output of a modulated and straight waveguide of the same geometry clearly indicates that the output is not limited by the cutoff rule for long driver pulses but by ionization-induced phase-mismatch. A modulated waveguide can enhance the conversion efficiency and the maximum order of harmonic output and theoretically work even for fully ionized gases. It allows the use of gases with high conversion efficiency for high harmonic power output that have medium ionization energies, such as neon, and thus could not be used for the straight waveguide geometry. The modulations of the waveguide introduce a modulated electric field inside the hollow guiding medium. The spectrum and the phase of the harmonic radiation depend strongly on the intensity of the driver pulse. Thus the waveguide introduces amplitude and phase modulations of the vacuum-ultraviolet or extreme-ultraviolet radiation and allows interference between the already generated radiation and radiation emerging from out-of-phase areas to be avoided. Thus, the generation of radiation from out-of-phase areas can be suppressed by reducing the intensity below the threshold required for high harmonic generation.

Non-stationary spatial waveguide modes: launching a non-stationary spatial mode in a hollow waveguide is another technique that allows quasi-phase matching. This can be achieved by mismatching the coupling of the driver pulse with the waveguide. A smaller-than-necessary diameter of the laser beam will lead to oscillations of the beam profile and may lead to a spontaneous quasi-phase matched regime of harmonic emission.

Counter-propagating light: using counter-propagating light also is a quasi-phase matching technique [158, 159]. It can be used to eliminate the harmonic radiation in out-of-phase zones. The harmonic output significantly depends on the temporal shape of the counter-propagating pulse.

Modulating the nonlinear medium: an intuitive quasi-phase matching approach is to modulate the nonlinear medium itself [157]. This technique can eliminate geometric phase mismatches, which are mainly due to the Gouy phase.

Nonlinear non-adiabatic self-phase-matching: another technique is non-adiabatic phase matching by self-phase-matched high harmonic generation [87]. Note that this quasi-phase-matching approach is based on the single-cycle regime and works only for plateau-harmonics.

A.4 Alternative interaction geometries

The interaction section (see section 3.3.1) is designed in such a way that another interaction geometry can be quickly incorporated. Alternative geometries, such as a gas get, a finite gas cell, or even a guided-beam geometry, are shown in figure A.4.1.

A.4.1 Finite gas cell

An example of a finite gas cell is shown in picture a) of figure 3.3.3. This gas cell was designed as a metallic cube (< 1 cm) with two thin metal foils in the entry and exit

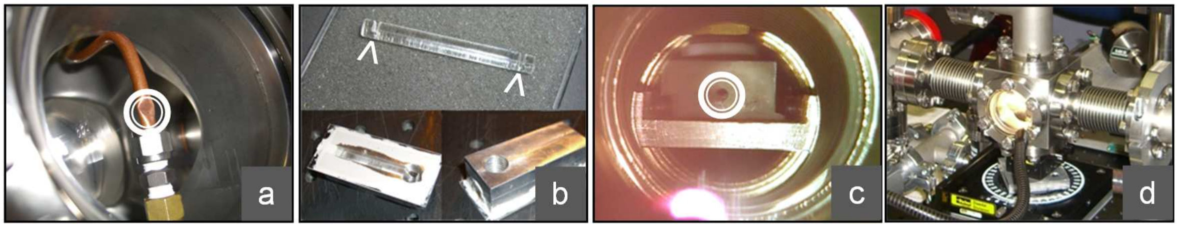

Figure A.4.1: Alternative interaction geometries: a) finite gas cell, b) straight hollow glass capillary and its mount for the guided-beam geometry, c) mounted glass capillary and entry for the focused laser beam, d) flexibly installed interaction section.

plane. Another example of a finite gas cell design is shown in picture a) of figure A.4.1. Here, the gas cell was realized by squeezing copper tubing in such a way that the wall-to-wall distance, corresponding to the length of the gas cell, was $\sim 100\ \mu$m. In both cases, the gas nozzles were created in-situ by femtosecond laser ablation. The main disadvantages of these designs are as follows: first, due to the small-scale geometry the pressure inside the gas cell cannot be determined directly by means of a commercial pressure gauge. Second, the entry and the exit gas nozzle lead to twice the gas ballast. Third, the entry gas nozzle is subject to continuous femtosecond laser ablation due to instabilities of the beam pointing of the high-power femtosecond laser system. Often the gas cell needs daily replacement in order to keep the gas ballast low. Furthermore, the entry gas nozzle, which continuously increases in size during operation, is detrimental for a region of constant pressure inside the gas cell and does not allow significant flow peculiarities to be excluded. Fourth, the second design does not allow the processes going on inside the gas cell to be monitored visually. Therefore the finite gas cell design was used for early work only. It was later replaced by the semi-infinite gas cell design which turned out to be a more effective means to realize a high-harmonic source of reasonable flux for coherent diffractive imaging.

A.4.2 Guided-beam geometry

Straight waveguide: an example of a straight waveguide, featuring the guided-beam geometry, is shown in the top of picture b) of figure A.4.1. The glass capillary is 5 cm long, and its inner diameter is 150 μm. Two ~ 1 mm-thick gaps are cut into the glass capillary 5 mm from its ends (marked by white arrows in the picture). Thus, the 4-cm-long centre part could be flooded with gas at a constant pressure. The gaps extend only until the inner diameter. Therefore, when glued into a metal block (left bottom part of the picture), no alignment of the three segments is necessary. This metal block provides a feed-through to supply the capillary with gas (right bottom part of the picture) and is mounted inside the interaction geometry. In picture c) the entry part (marked by the white circle) for the focused laser beam can be seen. Flexible tubing connects the metal block to the gas reservoir. The metal block was mounted between the glass window at the beginning of the interaction section and the vacuum gate at its end by flexible bellows (picture d)). A combination of x/y-translation stages, a rotation stage and a tilt stage allows the glass capillary to be aligned with respect to the optical axis of the apparatus and the laser beam. Due to the small-scale geometry the pressure inside the waveguide cannot be determined directly by a commercial pressure gauge. Instead, the backing pressure can be measured. The input port as well as the output port of the glass capillary and proper coupling of the laser beam can be monitored by means of optical elements and charge-coupled device cameras and, in particular, by means of the viewport of the second differential pumping stage with the magnetically coupled silver mirror (part f)) in figure 3.3.1.

Corrugated waveguide: harmonic generation of the waveguide design as described above was successful. However, its main purpose was to prepare the interaction section for a new kind of modulated waveguide for corrugation-induced, first-order quasi-phase-matching (see section A.3). The concept of this corrugated waveguide will be presented below. However, it has to be noted that, although possible, this waveguide has not been realized experimentally. Instead, the semi-infinite gas cell was employed to provide a harmonic source of reasonable flux for coherent diffractive imaging. First, the time-dependent Schrödinger equation for the response of an appropriate atomic, molecular or ionic nonlinear medium and the propagation equations was employed to calculate the necessary electric field of the fundamental laser beam that would lead to a maximum output of a particular harmonic order or a small-bandwidth range of harmonic orders at or around the desired wavelength of ~ 4.2 nm, which corresponds to the water-window. This designer electric field would be a superposition of multiple optical modes that are eigenmodes of the combination of the corrugated waveguide and the nonlinear medium. Second, the designer electric field, which is optimized as described above, would be generated through propagation of the laser electric field inside the corrugated waveguide. Its propagation would not be characterized by the focusing geometry of the chosen optical elements, but rather through the designed geometrical characteristics of the corrugated waveguide and the physical characteristics of the nonlinear medium. Propagation equations would be employed to calculate the necessary designer corrugation that generates this particular designer electric field. Third, the waveguide of the designer corrugation pattern can be manufactured by laser micromachining. The designer corrugation pattern would be imprinted onto a suitable surface (e.g., a particular polymer). The surface would then be treated with coating that is highly reflective at ~ 800 nm (e.g., like the protected silver mirrors or a chirped-multi-layer dielectric coating). The corrugation and the coating then allow the generation and propagation of the designer electric field inside the waveguide. Two of these optical-quality surfaces would be machined and glued together. It is possible to fix possible gaps due to imperfect glueing by means of a flow of colloidal metal (the material corresponds to the chosen metal coating, e.g., colloidal silver) through the waveguide.

The technique of employing laser micromachining of the inside of the waveguide is superior to that of precision glass blowing and modulation by means of applying a high pressure inside the waveguide and area-confined heating. The technique described here allows a precision designer corrugation pattern to be manufactured that is not limited by the size of the modulation period, the amplitude of the corrugation, or the corrugation pattern in general. Also, rather than using a lossy glass surface for the propagation of the designer electric field a highly reflective coating can be chosen. In the context of experimentally realizing this approach a test surface has been manufactured (MiniFAB (AUST) Pty Ltd, Victoria 3179, Australia) as shown in picture a) of figure A.4.2. The test surface is manufactured from a polymer by excimer-laser micromachining. It features a sinusoidally-shaped corrugation pattern (see picture b)) of period 100 μm (see section A.3.1) and amplitude 10 μm. This surface is coated with a 300 nm-thick layer of gold. Characterization of the surface by atomic force microscopy (see picture c)) allowed the determination of the roughness (rms) of this surface as 5 nm (see picture b)), which corresponds to optical quality of the surface.

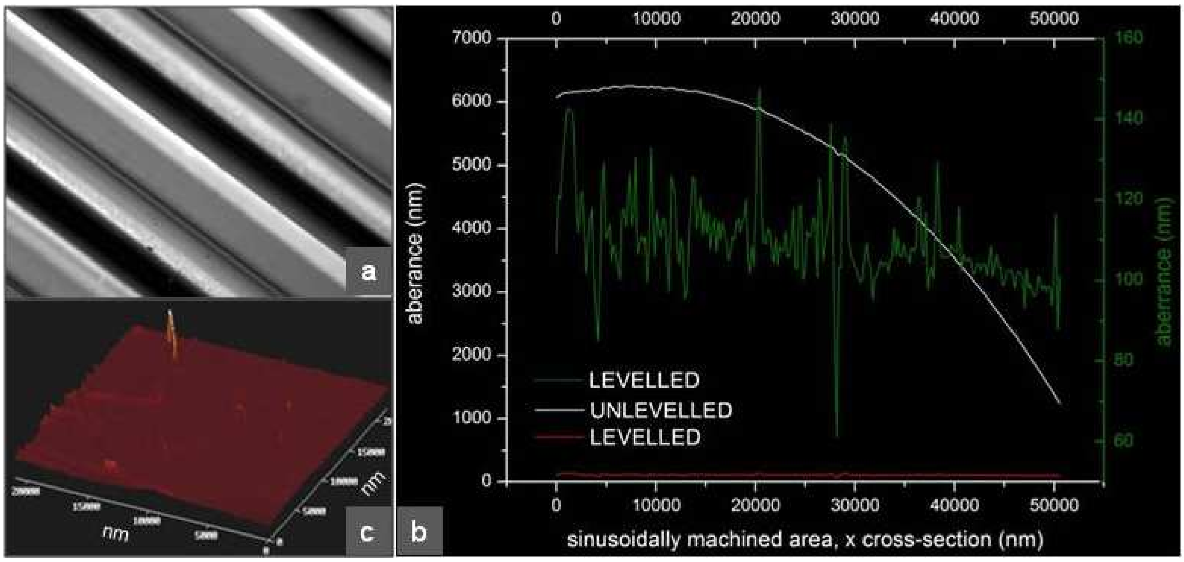

Figure A.4.2: A carefully chosen corrugated waveguide can induce multi-mode quasi-phase-matching: a) excimer-laser micromachined sinusoidally shaped polymer surface, b) to c) characterization by atomic force microscopy.

A.5 Detection and characterization hardware

A.5.1 Detector

Table A.1 gives details of the controller gain of the camera system depending on the chosen readout port, and figure A.5.1 displays the quantum efficiency of the camera system depending on the wavelength of the detected radiation.

readout port	1 (low)	2 (medium)	3 (high)
low noise	4 electrons/count	2 electrons/count	1 electron/count
high capacity	16 electrons/count	8 electrons/count	4 electrons/count

Table A.1: Controller gain of the camera system used for the experimental work.

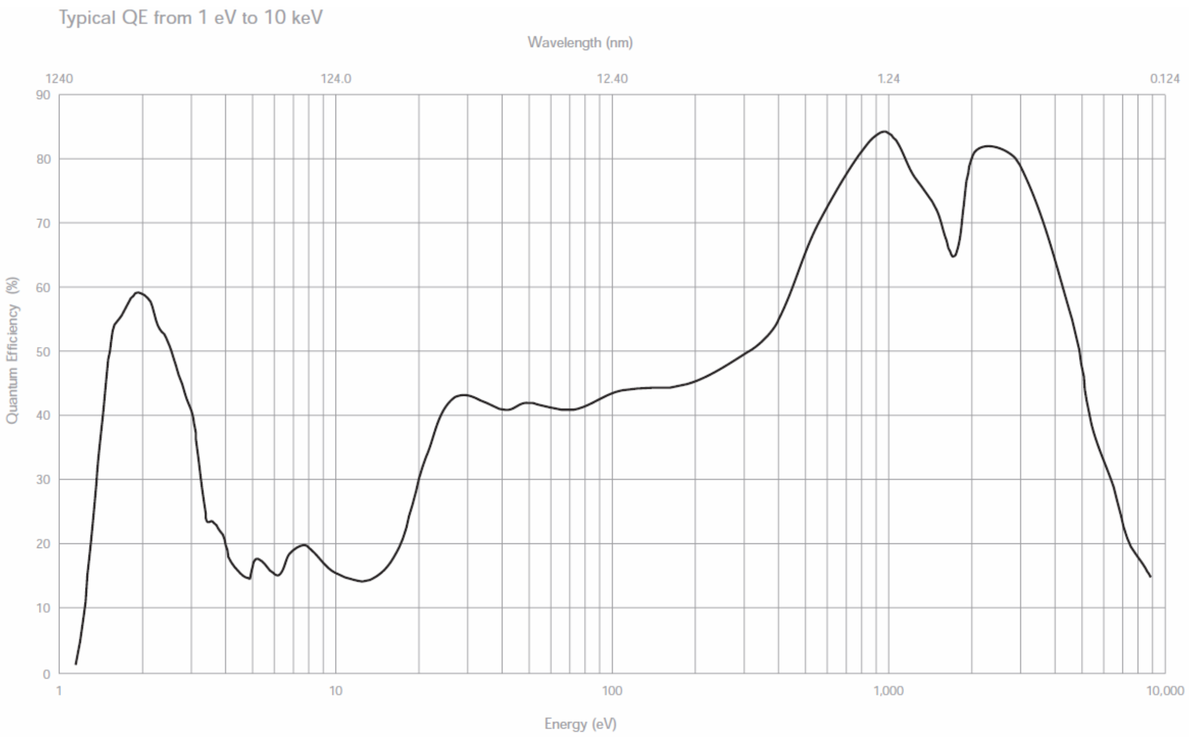

Figure A.5.1: Quantum efficiency of the camera system used for the experimental work.

A.5.2 Spectrometer

Table A.2 provides details about the gratings of the spectrometer.

grating (grooves/mm)	$\Delta\lambda$ (nm)	D ($\AA$/mm)	$\delta\lambda$ ($\AA$)
1200	4.4 – 10.6	7.3 – 9.1	0.5
600	8.9 – 21.3	14.6 – 18.2	1.0
300	17.7 – 42.5	29.2 – 36.4	2.0
150	35.4 – 85.0	58.4 – 72.8	4.0

Table A.2: Parameters of the gratings: wavelength range $\Delta\lambda$, dispersion D at the exit slit plane (focal plane), and spectral resolution $\delta\lambda$ at the entrance slit width of 15 μm.

A.6 Software interface and automation of the experimental setup

A.6.1 Software interface to WinView

The charge-coupled device detector chip comes in a camera whose controller can be programmed by means of the software WinView (Princeton Instruments), referred to as WinView. This software is necessary for programming the parameters for data acquisition and also allows the collection, storage and processing of data acquired by the charge-coupled device detector chip. However, as the software only provides basic processing functionality, WinView is only used for data acquisition purposes. For extraction of the harmonic intensity from the data images, the resulting data files are processed by means of software written in the programming suite LabView (National Instruments), referred to as LabView. This allows customized data read-out and processing on-the-fly while WinView is in data acquisition mode. This section is of technical nature. However, its precise description is important to understand how the different software modules fit together in order to establish an experimental setup that can be computer-controlled and that can take measurements in an automatic mode.

In the following the mechanism is explained that allows a software interface to WinView via LabView-based software to be established. WinView is linked to LabView by means of defining an ActiveX object of the class *WINX32Lib.IDocWindows2*. This object allows LabView to track any activity of WinView and is referenced (so-called automation refnum) to ActiveX functions. Therefore the method *GetActive* of the class *IDocWindows2* is invoked on this object. The output is directed to two invoke nodes of the methods *GetROI* (1) and *GetDocument* (2) of the class *IDocWindow*. (1) The output of the method *GetROI* is passed on to an invoke node of method *Get* of the class *IROIRect*. Several different parameters (top, left, bottom, right) allow extraction of the dimension and position of the region of interest that contains the desired intensity information. (2) The output of the method *GetDocument* is the input for invoke nodes configured for the two methods *GetParam* (2a) and *GetFrame* (2b) of the class *IDocFile*. (2a) Several input parameters are chosen to extract any necessary and available information by means of the method *GetParam*: *DM_XDIM* and *DM_YDIM*: the dimensions of the active image; *DM_FILENAME* and *DM_FILEDATE*: the file name and date for automated storage of the processed data; *DM_NUMFRAMES*: the number of frames of the active image. (2b) The output of the invoke node configured for the method *GetFrame* of the class *IDocFile* contains the data of the image. This data can be extracted and processed by means of information about the number of frames and the region of interest.

When processing the data the general experimental scheme for measurements is as follows: (1) Any number of arbitrary initial frames can be taken to avoid possible timing problems with a particular hardware component. (2) A series of signal frames can be taken. These frames contain information about the harmonic as well as possible stray fundamental light and readout noise of the charge-coupled device detector chip and controller. A series can be taken for statistical purposes. (3) Any number of arbitrary break frames can be captured to avoid possible timing problems with a particular hardware component. (4) A series of background frames may be taken. These frames contain only stray fundamental light and the readout noise of the charge-coupled device detector chip and the controller. A series can taken for extraction of statistical information. (5) Any number of cycles containing break, signal, break, and background frames can be taken while changing experimental parameters. (6) Any number of arbitrary final frames can be acquired in order to avoid possible timing problems with a particular hardware component. The data is extracted and processed to average values and associated values of the standard deviation of the measurement while WinView is in acquisition mode and displaying the active image. The data can be processed in any way by adjusting the routines of the LabView-based program used for calculations. This scheme is highly flexible and can be extended by further LabView-based software modules for automated and synchronized control of any hardware components, such as linear stepper motors (e.g., to control the position of the laser focus inside the gas cell) or rotation stepper motors (e.g., to control the rotation mount of the spectrometer, or the quarter-waveplate for acquisition of background images).

A.6.2 Automated control over experimental hardware

The need for automation of the experimental setup requires appropriate synchronization of any hardware, which needs to be controlled, with the data acquisition software WinView. In combination with the previously described ActiveX-based software interface to WinView for automated extraction of information from acquired images, a very flexible and efficient scheme has been established and changes or extensions of the existing experimental hardware can be quickly incorporated in order to conduct computer-based automated measurements of the experimental setup.

A schematic representation of the method for synchronization of the software

WinView with any necessary or desired experimental hardware is displayed in figure A.6.1. The software WinView is linked to the controller of the camera for the charge-coupled device detector chip by one of the computer's input/output ports. Thus, the parameters oft the experimental acquisition setup can be sent to the controller, and the data acquired by the controller can be sent to WinView in return. It is important to note that, once the acquisition process has been started, the computer only serves as a data-receiving station. The controller for the charge-coupled device detector chip is now the crucial element for data acquisition and appropriate timing. The input/output interface of the controller is linked to a mechanical shutter for the fundamental laser beam. Thus, the exposure time of the acquisition process can be controlled, that is, the time that the nonlinear medium is exposed to the fundamental laser beam for high-harmonic generation. The input/output interface of the controller is also linked to an input/output interface box which communicates with the input/output ports of the computer. Therefore, before, during or after an image or frame is being acquired, procedures and methods of a LabView-based program can be invoked, which monitor the computer's input/output interface. These procedures and methods can access the computer's input/output interface as well as the input/output box in return and thus control any external hardware components.

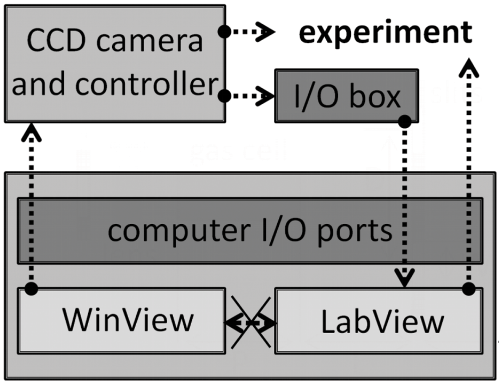

Figure A.6.1: Schematic representation of the method for synchronization of the software WinView with any experimental hardware via LabView-based software.

The scheme of computer-controlled experimental hardware, its synchronization with the data acquisition software WinView and the ActiveX-based interface to WinView for on-the-fly data readout and processing is very flexible and efficient, and allows changes or extensions to the existing experimental hardware to be quickly incorporated. In particular, the opportunity of synchronization with the controller-based procedure of data acquisition is needed for the following applications:

Acquisition of the spectrum: the harmonic power spectrum is recorded by precision rotation of the diffraction grating inside the grazing-incidence spectrometer (Setpoint GIMS#4). The grating holder is linked to a micrometer screw. This micrometer screw is coupled to a rotation stepper motor that is controlled by the aforementioned scheme. The LabView-based software module allows the user to define a start and an end position for the micrometer screw, the step size and the number of frames that are used for statistical purposes.

Acquisition of the background images: the acquired images contain information from both the harmonic and fundamental light and will also incorporate read-out noise from the charge-coupled device detector chip and the controller. In order to exclude any information except from the harmonic emission, a number of background images can be taken. One option is the evacuation of the gas cell. It can be shown that this only leads to an insignificant perturbation of the repeatability of the harmonic source. However, the process of repressurization and stabilization of the gas cell occurs on a long time scale (> 1 min). Another option of acquiring background images is to transform the linear polarization of the fundamental laser beam into circular polarization, which suppresses any harmonic generation. Experimentally this approach is realized by means of a quarter-waveplate and is a reliable and very fast experimental means. Therefore the quarter-waveplate is placed on a precision rotation mount which is operated by a precision stepper motor. This stepper motor can be controlled by means of the aforementioned scheme. Here the background frames are taken on-the-fly after the signal frames for exactly the same experimental settings. Repeating the whole experiment for acquisition of the background frames is detrimental due to issues related to experimental instabilities or poor repeatability and the highly nonlinear nature of high-harmonic generation and its sensitivity towards experimental changes. The LabView-based software module allows the user to define any number of signal, break and background images and incorporates the rotation of the quarter-waveplate automatically during the process of data acquisition and the desired changes of the experimental changes.

Control over linear stepper motors for precise positioning of the laser focus inside the gas cell: the focusing lens is mounted on a precision $x/y/z$-stage. This stage is driven by linear stepper motors which are controlled by the aforementioned scheme. The LabView-based software module allows one to define a start and an end position for the linear stepper motors, the step size and the number of frames that are used for statistical purposes.

Control over a set of $x/y/z$-translation stages for precise positioning of a sample that is subject to coherent diffractive imaging: the stages are driven by linear stepper motors which are controlled by the aforementioned scheme. Therefore, a LabView-based software module allows one to address motors individually with respect to their speed and acceleration and relative and absolute movement.

Depending on the settings of the parameters for data acquisition, which is conducted independently from the computer by the controller of the charge-coupled device detector chip, a very short processing time per frame ($\sim$ 10 ms) can result. As processing of the trigger signal for the shutter and the adequate software routines can take a somewhat longer time, the software can work in a so-called delay mode, where invoking the software methods can be linked to the previous trigger pulse rather than to the current one. In that case the option of initial frames of the general scheme of measurement, as explained before, becomes important. Generally, the developed software methods and procedures in combination with the established opportunity of the data acquisition software synchronized access over the experimental hardware allows one to quickly, reliably and automatically conduct automation of any desired experimentally scheme.

A.7 Employment of a quarter-waveplate for elliptical polarization

The required background images can be obtained either by acquiring reference images with an evacuated high-harmonic interaction geometry, or by rotation of the linear polarization of the fundamental laser beam. Compared to the process of repressurizing the interaction section with the nonlinear medium, the process of employing a quarter-waveplate for rotation of the polarization occurs on a much faster time scale. The quarter-waveplate is a broadband 0th-order-waveplate centred at 800 nm.

A.7.1 Harmonic intensity as a function of ellipticity

The twostep model [66, 65, 67] predicts that high-harmonic generation is suppressed when the nonlinear medium is driven by laser light that is elliptically polarized. For laser light of linear polarization, some of the classical electron trajectories pass the nucleus periodically, and thus allow the electron to radiatively recombine with the parent ion. However, for elliptic polarization there are no such trajectories. But high-harmonic generation is not suppressed, but rather greatly reduced: that is due to the finite extent of the electronic wave packet and quantum diffusion effects [75]. As the harmonic conversion efficiency decreases rapidly with an increase of the ellipticity of the laser beam, a quarter-waveplate can be employed to circularly polarize the laser beam and thus allow the acquisition of background images, which only contain fundamental laser light and the readout noise of the charge-coupled device chip and the detector controller. The term ellipticity is defined as the ratio of the minor axis to the major axis components of the electric field, for a fixed laser intensity. It is important to note that effects such as phase-matching and propagation in the nonlinear medium show relatively weak dependence on the ellipticity of the fundamental laser beam [160].

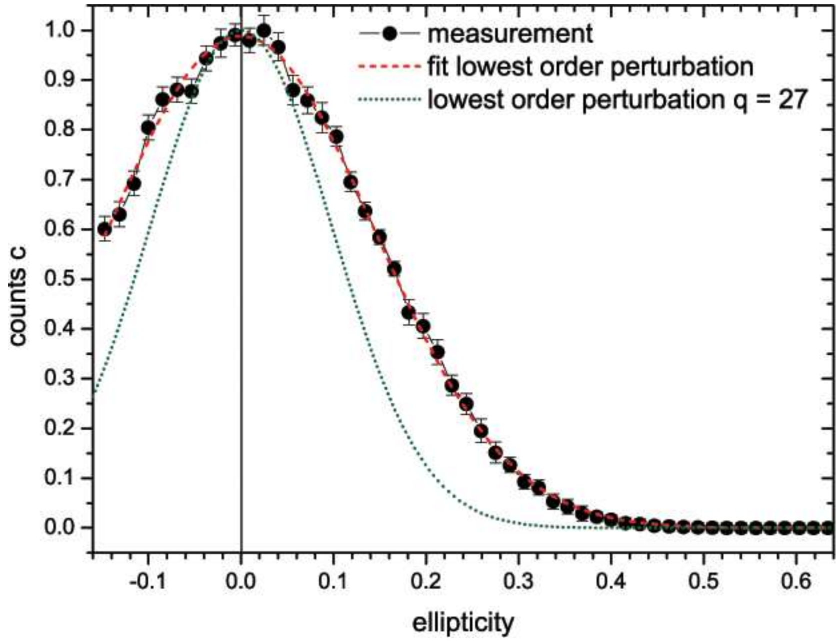

Figure A.7.1: Harmonic intensity as a function of ellipticity.

Figure A.7.1 shows the harmonic intensity as a function of ellipticity ϵ for an harmonic beam generated in argon gas that consists of some harmonic orders centred around $\sim$ 30 nm, corresponding to the 27th harmonic order. The intensity $I = I(q) \approx -8.22 \times 10^{13} + 8.03 \times 10^{12} q$ that is necessary for the generation of the 27th harmonic order has been calculated by means of the 2-step model. Here the Keldysh or tunneling parameter is given by $\gamma = (I_P/(2U_P))^{1/2} \approx 0.98 < 1$, with I_P being the ionization potential of argon and $U_P[\mathrm{eV}] = 9.33 \times 10^{-14} I[\mathrm{W/cm^2}]\lambda^2[\mu\mathrm{m}^2]$ being the ponderomotive potential. $\gamma = 1$ is the threshold between the multiphoton regime ($\gamma > 1$) and the tunneling regime ($\gamma < 1$). For the low-intensity regime $\gamma > 1$, and thus for this case, the lowest-order perturbation theory can predict the effect of ϵ on the harmonic intensity [161]

$$I_q \propto \left(\frac{1-\epsilon^2}{1-\epsilon^2}\right)^{q-1} . \tag{A.7.1}$$

Employing a fit of equation (A.7.1) (red short-dashed curve) to the experimental data (black dots) in figure A.7.1 yields the value $q_{fit} = 13$, which is considerably smaller than $\langle q \rangle = 27$. Plotting equation (A.7.1) with $q = 27$ (green short-dotted curve) underestimates the measured data. So, although $\gamma \approx 1$, the lowest-order perturbation theory can not be employed in this case. In general, the effect of ϵ on I_q strongly depends on the experimental parameters, in particular the focused laser intensity and the species of gas (atomic or molecular). Simulation of the relative single-atom harmonic response as a function of the laser ellipticity is described in [75].

A.7.2 Reliability and repeatability of the harmonic emission

Employing the quarter-waveplate as a means of background acquisition requires the knowledge about its effect on the harmonic beam with respect to the spatial profile and the spectral composition. Although a broadband 0th-order-waveplate is used for the experiments and always remains in the beam path, it has the potential to lead to an increased reliability and repeatability of the characteristics of the harmonic emission. Thus, for the experimental work presented in this dissertation, it is of particular interest to achieve the same spatial profile and the same spectral composition when the quarter-waveplate is rotated back and forth.

Figure A.7.2 displays the harmonic beam in its spatial domain. Measurements are taken for the quarter-waveplate at the position of linear polarization and circular polarization, and for positions in between. Each position is tested several times. In all cases the spatial profile of the harmonic beam is recorded over ~ 10 to 100 laser shots. Thus, each measurement incorporates shot-to-shot instabilities of the fundamental laser beam. These single measurements are normalized and compared with each other, leading to a mean value (left picture) of the spatial profile of the harmonic beam and its standard deviation (right picture). The experimental settings for the harmonic beam are as described in the experimental conditions of the section on page 143. The standard deviation across the averaged spatial profile of the harmonic beam for several settings of the quarter-waveplate is very small < 3.4 %. This indicates a very good realiability and repeatability of the harmonic beam across the spatial profile for different and repeated back-and-forth settings of the quarter-waveplate.

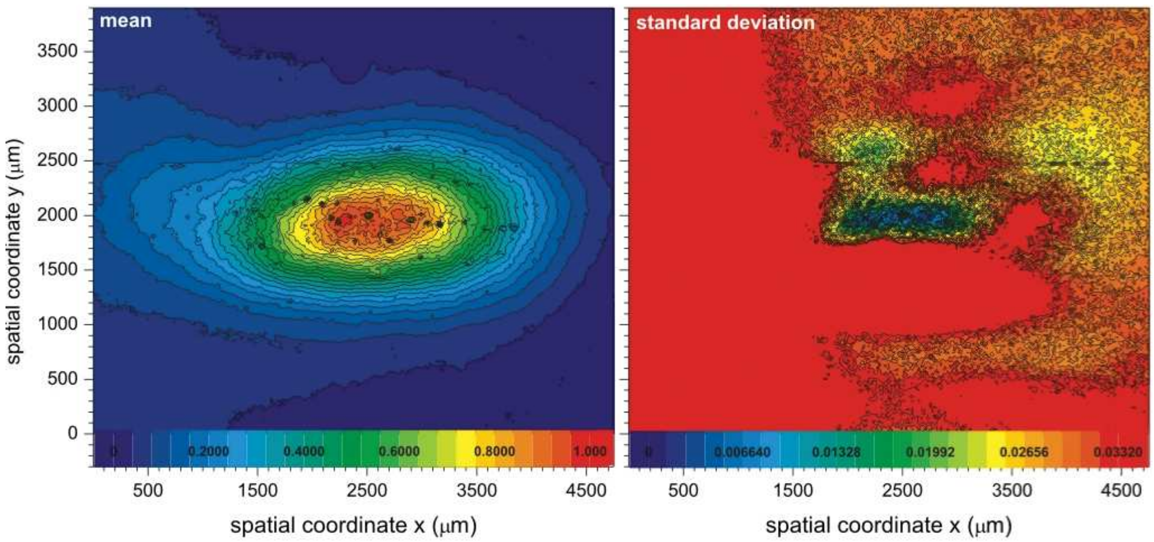

Figure A.7.2: Averaged profile (left picture) of the harmonic beam and associated standard deviation (right picture) for different settings of the quarter-waveplate.

Figure A.7.3 displays the harmonic beam in its spectral domain. The spectrum is extracted by applying the maximum entropy method to the interference pattern emerging from a Young double-slit illuminated with the harmonic emission as explained in section 4.2.3. The very good reliability and repeatability of the harmonic emission in the spatial domain implies that the same applies to the interference pattern and thus to the spectral composition of the harmonic emission. Measurements are taken for the quarter-waveplate at the position for linear polarization and circular polarization, and for positions between. Each position is tested several times. In all cases the spectral composition of the harmonic beam is recorded over ∼ 10 to 100 laser shots. Thus, each measurement incorporates shot-to-shot instabilities of the fundamental laser beam. These single measurements are normalized and compared with each other, leading to a mean value of the spectral profile of the harmonic beam and its standard deviation. The experimental settings for the harmonic beam are as described in the experimental conditions of section 5.2. The standard deviation across the averaged spectrum of the harmonic beam for several settings of the quarter-waveplate is reasonably small. For the peak of the dominant harmonic orders - 23rd to 27th - it ranges from ∼ 2 to 10 %. The averaged intensity of the spectral range between the harmonic orders is characterized by a standard deviation < 0.1 %. This indicates a reasonably good realiability and repeatability of the spectral characteristics of the harmonic beam for different and repeated back-and-forth settings of the quarter-waveplate.

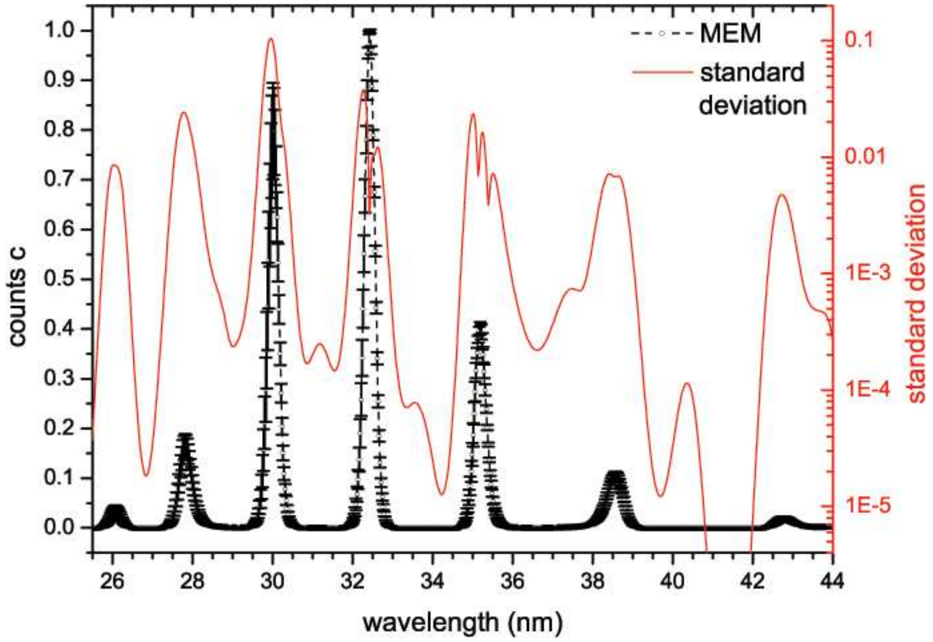

Figure A.7.3: The averaged spectrum (black dashed curve) of the harmonic beam obtained by the maximum entropy method and associated standard deviation (red solid curve) for different settings of the quarter-waveplate.

Bibliography

[1] B. R. Benware, C. D. Macchietto, C. H. Moreno, and J. J. Rocca. Demonstration of a high average power tabletop soft x-ray laser. *Phys. Rev. Lett.*, **81**:5804–5807, 1998.

[2] L. Van Dao, S. Teichmann, and P. Hannaford. Phase-matching for generation of few high order harmonics in a semi-infinite gas cell. *Phys. Lett. A*, **372**:5254–5257, 2008.

[3] L. Van Dao, S. Teichmann, J. A. Davis, and P. Hannaford. Generation of high flux, highly coherent extreme ultraviolet radiation in a gas cell. *J. Appl. Phys.*, **104**:023105, 2008.

[4] S. Teichmann, P. Hannaford, and L. Van Dao. Phase-matched emission of few high-harmonic orders from a helium gas cell. *Appl. Phys. Lett.*, **94**:171111, 2009.

[5] S. Teichmann, P. Hannaford, and L. Van Dao. Spectral characteristics across the spatial profile of a high-harmonic beam. *J. Phys. D: Appl. Phys.*, **42**:135108, 2009.

[6] B. Chen, R. A. Dilanian, S. Teichmann, B. Abbey, A. G. Peele, G. J. Williams, P. Hannaford, L. Van Dao, H. M. Quiney, and K. A. Nugent. Multiple wavelength diffractive imaging. *Phys. Rev. A*, **79**:023809, 2009.

[7] B. Chen, R. A. Dilanian, S. Teichmann, L. V. Dao, H. Quiney, G. Williams, A. Peele, E. Balaur, C. Tran, and K. A. Nugent. High resolution multiple wavelength diffractive imaging. *In preparation*, **x**:y, 2009.

[8] R. A. Dilanian, B. Chen, S. Teichmann, L. Van Dao, H. M. Quiney, and K. A. Nugent. High-harmonic-generation spectrum reconstruction from Young's double-slits interference pattern using the maximum entropy method. *Opt. Lett.*, **33**:2341–2343, 2008.

[9] R. A. Dilanian, B. Chen, G. J. Williams, H. M. Quiney, K. A. Nugent, S. Teichmann, P.Hannaford, L. V. Dao, and A. G. Peele. Diffractive imaging using a polychromatic high-harmonic generation soft-x-ray source. *J. Appl. Phys.*, **106**:023110, 2009.

[10] M. Bauer. Femtosecond ultraviolet photoelectron spectroscopy of ultra-fast surface processes. *J. Phys. D: Appl. Phys.*, **38**:R253–R267, 2005.

[11] Ch. Spielmann, N. H. Burnett, S. Sartania, R. Koppitsch, M. Schnürer, C. Kan, M. Lenzner, P. Wobrauschek, and F. Krausz. Generation of coherent x-rays in the water window using 5-femtosecond laser pulses. *Science*, **278**:661–664, 1997.

[12] E. A. Gibson, A. Paul, N. Wagner, R. Tobey, D. Gaudiosi, S. Backus, I. P. Christov, A. Aquila, E. M. Gullikson, D. T. Attwood, M. M. Murnane, and H. C. Kapteyn. Coherent soft x-ray generation in the water window with quasi-phase matching. *Science*, **302**:95–98, 2003.

[13] E. J. Takahashi, T. Kanai, K. L. Ishikawa, Y. Nabekawa, and K. Midorikawa. Coherent water window x ray by phase-matched high-order harmonic generation in neutral media. *Phys. Rev. Lett.*, **101**:253901, 2008.

[14] A. Rundquist, C. G. Durfee III, Z. Chang, C. Herne, S. Backus, M. M. Murnane, H. C. Kapteyn . Phase-matched generation of coherent soft x-rays. *Science*, **280**:1412–1415, 1998.

[15] S. Marchesini, H. N. Chapman, S. P. Hau-Riege, R. A. London, A. Szoke, H. He, M. R. Howells, H. Padmore, R. Rosen, J. C. H. Spence, and U. Weierstall. Coherent x-ray diffractive imaging; applications and limitations. *Opt. Expr.*, **11**:2344–2350, 2003.

[16] H.C. Kapteyn, M. M. Murnane, and I. P. Christov. Extreme nonlinear optics: Coherent x rays from lasers. *Phys. Today*, **58**:39–44, 2005.

[17] C. Figueira de Morisson Faria, P. Salières, P. Villain, and M. Lewenstein. Controlling high-harmonic generation and above-threshold ionization with an attosecond-pulse train. *Phys. Rev. A*, **74**:053416, 2006.

[18] A. McPherson, G. Gibson, H. Jara, U. Johann, T. S. Luk, I. A. McIntyre, K. Boyer, and C. K. Rhodes. Studies of multiphoton production of vacuum-ultraviolet radiation in the rare gases. *J. Opt. Soc. Am. B*, **4**:595–601, 1987.

[19] Z. Chang, A. Rundquist, H. Wang, M. M. Murnane, and H. C. Kapteyn. Generation of coherent soft x rays at 2.7 nm using high harmonics. *Phys. Rev. Lett.*, **79**:2967–2970, 1997.

[20] J. Seres, E. Seres, A. J. Verhoef, G. Tempea, C. Streli, P. Wobrauschek, V. Yakovlev, A. Scrinzi, C. Spielmann, and F. Krausz. Laser technology: Source of coherent kiloelectronvolt x-rays. *Nature (London)*, **433**:596, 2005.

[21] M. Schnürer, Z. Cheng, M. Hentschel, G. Tempea, P. Kálmán, T. Brabec, and F. Krausz. Absorption-limited generation of coherent ultrashort soft-x-ray pulses. *Phys. Rev. Lett.*, **83**:722–725, 1999.

[22] P. Salières, A. L'Huillier, and M. Lewenstein. Coherence control of high-order harmonics. *Phys. Rev. Lett.*, **74**:3776–3779, 1995.

[23] E. Constant, D. Garzella, P. Breger, E. Mével, Ch. Dorrer, C. Le Blanc, F. Salin, and P. Agostini. Optimizing high harmonic generation in absorbing gases: Model and experiment. *Phys. Rev. Lett.*, **82**:1668–1671, 1999.

[24] C. G. Durfee III, A. R. Rundquist, S. Backus, C. Herne, M. M. Murnane, and H. C. Kapteyn. Phase matching of high-order harmonics in hollow waveguides. *Phys. Rev. Lett.*, **83**:2187–2190, 1999.

[25] S. Kazamias, D. Douillet, F. Weihe, C. Valentin, A. Rousse, S. Sebban, G. Grillon, F. Augé, D. Hulin, and Ph. Balcou. Global optimization of high harmonic generation. *Phys. Rev. Lett.*, **90**:193901, 2003.

[26] M. Berglund, L. Rymell, M. Peuker, T. Wilhein, and H. M. Hertz. Compact water-window transmission x-ray microscopy. *J. Microsc.*, **197**:268–273, 2000.

[27] P. Sprangle, A. Ting, E. Esarey, and A. Fisher. Tunable, short pulse hard x-rays from a compact laser synchrotron source. *J. Appl. Phys.*, **72**:5032, 1992.

[28] R. A. Bartels, A. Paul, H. Green, H. C. Kapteyn, M. M. Murnane, S. Backus, I. P. Christov, Y. Liu, D. Attwood, and C. Jacobsen. Generation of spatially coherent light at extreme ultraviolet wavelengths. *Science*, **297**:376–378, 2002.

[29] J. Kirz, C. Jacobsen, M. Howells. Soft x-ray microscopes and their biological applications. *Q. Rev. Biophys.*, **28(1)**:33–130, 1995.

[30] G. J. Williams, H. M. Quiney, A. G. Peele, and K. A. Nugent. Coherent diffractive imaging and partial coherence. *Phys. Rev. B*, **75**:104102, 2007.

[31] J. C. H. Spence, U. Weierstall, and M. Howells. Coherence and sampling requirements for diffractive imaging. *Ultramicroscopy*, **101(2-4)**:149–152, 2004.

[32] S. P. Hau-Riege. Effect of the coherence properties of self-amplified-spontaneous-emission x-ray free electron lasers on single-particle diffractive imaging. *Opt. Expr.*, **16(4)**:2840–2844, 2008.

[33] R. L. Sandberg, C. Song, P. W. Wachulak, D. A. Raymondson, A. Paul, B. Amirbekian, E. Lee, A. E. Sakdinawat, C. La-O-Vorakiat, M. C. Marconi, C. S. Menoni, M. M. Murnane, J. J. Rocca, H. C. Kapteyn, and J. Miao. High numerical aperture tabletop soft x-ray diffraction microscopy with 70-nm resolution. *Proc. Natl. Acad. Sci. U.S.A*, **105**:24–27, 2008.

[34] R. L. Sandberg, A. Paul, D. A. Raymondson, S. Hädrich, D. M. Gaudiosi, J. Holtsnider, R. I. Tobey, O. Cohen, M. M. Murnane, H. C. Kapteyn, C. Song, J. Miao, Y. Liu, and F. Salmassi. Diffractive imaging using tabletop coherent high-harmonic soft-x-ray beams. *Phys. Rev. Lett.*, **99**:098103, 2007.

[35] D. Shapiro, P. Thibault, T. Beetz, V. Elser, M. Howells, C. Jacobsen, J. Kirz, E. Lima, H. Miao, A. M. Neiman, and D. Sayre. Biological imaging by soft x-ray diffraction microscopy. *Proc. Natl. Acad. Sci. U.S.A*, **102**:15343–15346, 2005.

[36] J. Miao, P. Charalambous, J. Kirz, and D. Sayre. Extending the methodology of x-ray crystallography to allow imaging of micrometre-sized non-crystalline specimens. *Nature (London)*, **400**:342–344, 1999.

[37] L. W. Whitehead, G. J. Williams, H. M. Quiney, and K. A. Nugent. Fresnel diffractive imaging: Experimental study of coherence and curvature. *Phys. Rev. B*, **77**:104112, 2008.

[38] M. A. Pfeifer, G. J. Williams, I. A. Vartanyants, R. Harder, and I. K. Robinson. Three-dimensional mapping of a deformation field inside a nanocrystal. *Nature (London)*, **442**:63–66, 2006.

[39] S. Marchesini, H. He, H. N. Chapman, S. P. Hau-Riege, A. Noy, M. R. Howells, U. Weierstall, and J. C. H. Spence. X-ray image reconstruction from a diffraction pattern alone. *Phys. Rev. B*, **68**:140101, 2003.

[40] I. K. Robinson, I. A. Vartanyants, G. J. Williams, M. A. Pfeifer, and J. A. Pitney. Reconstruction of the shapes of gold nanocrystals using coherent x-ray diffraction. *Phys. Rev. Lett.*, **87**:195505, 2001.

[41] J. Miao, T. Ishikawa, B. Johnson, E. H. Anderson, B. Lai, and K. O. Hodgson. High resolution 3D x-ray diffraction microscopy. *Phys. Rev. Lett.*, **89**:088303, 2002.

[42] G. J. Williams, H. M. Quiney, B. B. Dhal, C. Q. Tran, K. A. Nugent, A. G. Peele, D. Paterson, and M. D. de Jonge. Fresnel coherent diffractive imaging. *Phys. Rev. Lett.*, **97**:025506, 2006.

[43] C. G. Schroer, P. Boye, J. M. Feldkamp, J. Patommel, A. Schropp, A. Schwab, S. Stephan, M. Burghammer, S. Schöder, and C. Riekel. Coherent x-ray diffraction imaging with nanofocused illumination. *Phys. Rev. Lett.*, **101**:090801, 2008.

[44] J. R. Fienup. Phase retrieval algorithms: a comparison. *Appl. Opt.*, **21**:2758–2769, 1982.

[45] J. R. Fienup. Reconstruction of an object from the modulus of its Fourier transform. *Opt. Lett.*, **3**:27–29, 1978.

[46] R. A. Bartels, A. Paul, M. M. Murnane, H. C. Kapteyn, S. Backus, Y. Liu, and D. T. Attwood. Absolute determination of the wavelength and spectrum of an extreme-ultraviolet beam by a Young's double-slit measurement. *Opt. Lett.*, **27**:707–709, 2002.

[47] R. W. Gerchberg, and W. O. Saxton. A practical algorithm for the determination of phase from image and diffraction plane pictures. *Optik*, **35**:237–246, 1972.

[48] W. F. Schlotter, R. Rick, K. Chen, A. Scherz, J. Stöhr, J. Lüning, S. Eisebitt, Ch. Günther, and W. Eberhardt. Multiple reference fourier transform holography with soft x rays. *Appl. Phys. Lett.*, **89**:163112, 2006.

[49] S. Marchesini, S. Boutet, A. E. Sakdinawat, M. J. Bogan, S. Bajt, A. Barty, H. N. Chapman, M. Frank, S. P. Hau-Riege, A. Szöke, C. Cui, D. A. Shapiro, M. R. Howells, J. C. H. Spence, J. W. Shaevitz, J. Y. Lee, J. Hajdu, and M. M. Seibert. Massively parallel x-ray holography. *Nature Photonics*, **2**:560–563, 2008.

[50] J. Larsson, E. Mevel, R. Zerne, A. L'Huillier, C.-G. Wahlström, and S. Svanberg. Two-colour time-resolved spectroscopy of helium using high-order harmonics. *J. Phys. B: At. Mol. Opt. Phys.*, **28**:L53–L58, 1995.

[51] M. Gisselbrecht, D. Descamps, C. Lyngå, A. L'Huillier, C.-G. Wahlström, and M. Meyer. Absolute photoionization cross sections of excited He states in the near-threshold region. *Phys. Rev. Lett.*, **82**:4607–4610, 1999.

[52] O. Bjórneholm, I. Hjelte, T. Kihlgren, G. Öhrwall, S. Sundin, and S. Svensson. Femtosecond pump-probe photoelectron spectroscopy of predissociative Rydberg states in acetylene. *J. Chem. Phys.*, **112**:8038–8042, 2000.

[53] M. Bauer, C. Lei, K. Read, R. Tobey, J. Gland, M. M. Murnane, and H. C. Kapteyn. Direct observation of surface chemistry using ultrafast soft-x-ray pulses. *Phys. Rev. Lett.*, **87**:025501, 2001.

[54] L. Nugent-Glandorf, M. Scheer, D. A. Samuels, A. M. Mulhisen, E. R. Grant, X. Yang, V. M. Bierbaum, and S. R. Leone. Ultrafast time-resolved soft x-ray photoelectron spectroscopy of dissociating Br_2. *Phys. Rev. Lett.*, **87**:193002, 2001.

[55] R. Haight, and D. R. Peale. Antibonding state on the Ge(111):As surface: Spectroscopy and dynamics. *Phys. Rev. Lett.*, **70**:3979–3982, 1993.

[56] F. Quéré, S. Guizard, Ph. Martin, G. Petite, H. Merdji, B. Carré, J.-F. Hergott, and L. Le Déroff. Hot-electron relaxation in quartz using high-order harmonics. *Phys. Rev. B*, **61**:9883–9886, 2000.

[57] T. Sekikawa, T. Ohno, Y. Nabekawa, and S. Watanabe. Auger-free luminescence excited by high-order harmonics of a femtosecond Ti:sapphire laser. *J. Lumin.*, **87–89**:827–829, 2000.

[58] W. Theobald, R. Háßner, C. Wülker, and R. Sauerbrey. Temporally resolved measurement of electron densities ($> 10^{23}$ cm^{-3}) with high harmonics. *Phys. Rev. Lett.*, **77**:298–301, 1996.

[59] D. Descamps, C. Lyngå, J. Norin, A. L'Huillier, C.-G. Wahlström, J.-F. Hergott, H. Merdji, P. Salières, M. Bellini, and T. W. Hänsch. Extreme ultraviolet interferometry measurements with high-order harmonics. *Opt. Lett.*, **25**:135–137, 2000.

[60] P. Salières, L. Le Déroff, T. Auguste, P. Monot, P. d'Oliveira, D. Campo, J.-F. Hergott, H. Merdji, and B. Carré. Frequency-domain interferometry in the XUV with high-order harmonics. *Phys. Rev. Lett.*, **83**:5483–5486, 1999.

[61] D. Attwood. *Soft x-rays and extreme ultraviolet radiation.* Cambridge University Press, New York, first edition, 1999.

[62] P. A. Franken, A. E. Hill, C. W. Peters, and G. Weinreich. Generation of optical harmonics. *Phys. Rev. Lett.*, **7**:118–119, 1961.

[63] P. Jaegle. *Coherent sources of XUV radiation.* Springer, Berlin, first edition, 2006.

[64] A. L'Huillier. Atoms in strong laser fields. *Europhys. News*, **33**:205–207, 2002.

[65] P. B. Corkum. Plasma perspective on strong field multiphoton ionization. *Phys. Rev. Lett.*, **71**:1994–1997, 1993.

[66] J. L. Krause, K. J. Schafer, and K. C. Kulander. High-order harmonic generation from atoms and ions in the high intensity regime. *Phys. Rev. Lett.*, **68**:3535–3538, 1992.

[67] M. Lewenstein, Ph. Balcou, M. Yu. Ivanov, A. L'Huillier, and P. B. Corkum. Theory of high-harmonic generation by low-frequency laser fields. *Phys. Rev. A*, **49**:2117–2132, 1994.

[68] W. Becker, S. Long, and J. K. McIver. Modeling harmonic generation by a zero-range potential. *Phys. Rev. A*, **50**:1540–1560, 1994.

[69] A. L'Huillier, K. J. Schafer, and K. C. Kulander. Higher-order harmonic generation in xenon at 1064 nm: The role of phase matching. *Phys. Rev. Lett.*, **66**:2200–2203, 1991.

[70] A. L'Huillier, K. J. Schafer, and K. C. Kulander. Theoretical aspects of intense field harmonic generation. *J. Phys. B: At. Mol. Opt. Phys.*, **24**:3315–3341, 1991.

[71] K. J. Schafer, B. Yang, L. F. DiMauro, and K. C. Kulander. Above threshold ionization beyond the high harmonic cutoff. *Phys. Rev. Lett.*, **70**:1599–1602, 1993.

[72] S. J. Smith, and P. L. Knight. *Multiphoton Processes (Cambridge Studies in Modern Optics)*. Cambridge University Press, New York, May 27, 1988 edition, 1988.

[73] P. B. Corkum, N. H. Burnett, and F. Brunel. Above-threshold ionization in the long-wavelength limit. *Phys. Rev. Lett.*, **62**:1259–1262, 1989.

[74] M.V. Ammosov and N.B. Delone, and V.P. Krainov. Tunnel ionization of complex atoms and of atomic ions in an alternating electromagnetic field. *Sov. Phys. JETP*, **64**:1191–1194, 1986.

[75] P. Antoine, A. L'Huillier, M. Lewenstein, P. Salières, and B. Carré. Theory of high-order harmonic generation by an elliptically polarized laser field. *Phys. Rev. A*, **53**:1425–1445, 1996.

[76] M. Protopapas, D. G. Lappas, C. H. Keitel, and P. L. Knight. Recollisions, bremsstrahlung, and attosecond pulses from intense laser fields. *Phys. Rev. A*, **53**:R2933–R2936, 1996.

[77] S. Augst, D. Strickland, D. D. Meyerhofer, S. L. Chin, and J. H. Eberly. Tunneling ionization of noble gases in a high-intensity laser field. *Phys. Rev. Lett.*, **63**:2212–2215, 1989.

[78] P. Moreno, L. Plaja, V. Malyshev, and L. Roso. Influence of barrier suppression in high-order harmonic generation. *Phys. Rev. A*, **51**:4746–4753, 1995.

[79] C. Kan, N. H. Burnett, C. E. Capjack, and R. Rankin. Coherent XUV generation from gases ionized by several cycle optical pulses. *Phys. Rev. Lett.*, **79**:2971–2974, 1997.

[80] I. P. Christov, M. M. Murnane, and H. C. Kapteyn. High-harmonic generation of attosecond pulses in the “single-cycle”regime. *Phys. Rev. Lett.*, **78**:1251–1254, 1997.

[81] J. Zhou, J. Peatross, M. M. Murnane, H. C. Kapteyn, and I. P. Christov. Enhanced high-harmonic generation using 25 fs laser pulses. *Phys. Rev. Lett.*, **76**:752–755, 1996.

[82] T. F. Gallagher. Above-threshold ionization in low-frequency limit. *Phys. Rev. Lett.*, **61**:2304–2307, 1988.

[83] Anne L’Huillier, M. Lewenstein, P. Salières, and Ph. Balcou. High-order harmonic-generation cutoff. *Phys. Rev. A*, **48**:R3433–R3436, 1993.

[84] P. Lan, P. Lu, W. Cao, X. Wang, and G. Yang. Phase-locked high-order-harmonic and sub-100-as pulse generation from stretched molecules. *Phys. Rev. A*, **74**:063411, 2006.

[85] P. Antoine, A. L’Huillier, and M. Lewenstein. Attosecond pulse trains using high-order harmonics. *Phys. Rev. Lett.*, **77**:1234–1237, 1996.

[86] X.-M. Tong, and S.-I Chu. Probing the spectral and temporal structures of high-order harmonic generation in intense laser pulses. *Phys. Rev. A.*, **61**:021802, 2000.

[87] G. Tempea, M. Geissler, M. Schnürer, and T. Brabec. Self-phase-matched high harmonic generation. *Phys. Rev. Lett.*, **84**:4329–4332, 2000.

[88] M. Lewenstein, P. Salières, and A. L’Huillier. Phase of the atomic polarization in high-order harmonic generation. *Phys. Rev. A*, **52**:4747–4754, 1995.

[89] S. Kazamias, F. Weihe, D. Douillet, C. Valentin, T. Planchon, S. Sebban, G. Grillon, F. Augé, D. Hulin, and Ph. Balcou. High order harmonic generation optimization with an apertured laser beam. *Eur. Phys. J. D*, **21**:353–359, 2002.

[90] C. Altucci, T. Starczewski, E. Mevel, C.-G. Wahlström, B. Carré, and A. L'Huillier. Influence of atomic density in high-order harmonic generation. *J. Opt. Soc. Am. B*, **13**:148–156, 1996.

[91] P. W. Miloni, and J. H. Eberly. *Lasers.* John Wiley & Sons, Inc., New York, Wiley Series in Pure and Applied Optics edition, 1988.

[92] J. Peatross, M. V. Fedorov, and K. C. Kulander. Intensity-dependent phase-matching effects in harmonic generation. *J. Opt. Soc. Am. B*, **12**:863–870, 1995.

[93] J. Peatross, and D. D. Meyerhofer. Intensity-dependent atomic-phase effects in high-order harmonic generation. *Phys. Rev. A*, **52**:3976–3987, 1995.

[94] U. Heitmann, M. Kótteritzsch, S. Heitz, and A. Hese. Efficient generation of tunable VUV laser radiation below 205 nm by SFM in BBO. *Appl. Phys. B*, **55**:419–423, 1992.

[95] A. Paul, R. A. Bartels, R. Tobey, H. Green, S. Weiman, I. P. Christov, M. M. Murnane, H. C. Kapteyn, and S. Backus. Quasi-phase-matched generation of coherent extreme-ultraviolet light. *Nature (London)*, **421**:51–54, 2003.

[96] C. G. Durfee III, S. Backus, M. M. Murnane, and H. C. Kapteyn. Ultrabroadband phase-matched optical parametric generation in the ultraviolet by use of guided waves. *Opt. Lett.*, **22**:1565–1567, 1997.

[97] E. A. J. Marcatili, and R. A. Schmelzer. Hollow metallic and dieletric waveguides for long distance optical transmission and lasers. *Bell. Syst. Tech. J.*, **43**:1783–1809, 1964.

[98] A. Paul, E. A. Gibson, X. Zhang, A. Lytle, T. Popmintchev, X. Zhou, M. M. Murnane, I. P. Christov, and H. C. Kapteyn. Phase-matching techniques for coherent soft x-ray generation. *IEEE J. Quantum Electron.*, **42**:14–26, 2006.

[99] A. N. Naumov, A. M. Zheltikov, A. B. Fedotov, D. A. Sidorov-Biryukov, A. P. Tarasevitch, P. Zhou, and D. von der Linde. Ionization and absorption effects

in high-order harmonic generation in gas-filled hollow fibers. *Laser Part. Beams*, **19**:75–79, 2001.

[100] A. R. Libertun, X. Zhang, A. Paul, E. Gagnon, T. Popmintchev, S. Backus, M. M. Murnane, and H. C. Kapteyn . Design of fully spatially coherent extreme-ultraviolet light sources. *Appl. Phys. Lett.*, **84**:3903–3905, 2004.

[101] D. Homoelle, A. L. Gaeta. Nonlinear propagation dynamics of an ultrashort pulse in a hollow waveguide. *Opt. Lett.*, **25**:761–763, 2000.

[102] C. Courtois, A. Couairon, B. Cros, J. R. Marquès, and G. Matthieussent. Propagation of intense ultrashort laser pulses in a plasma filled capillary tube: Simulations and experiments. *Phys. Plasmas*, **8**:3445–3456, 2001.

[103] C. Jacobsen. Soft x-ray microscopy. *Trends in Cell Biology*, **9**:44–47, 1999.

[104] S. M. Hurtley, and L. Helmuth. The future looks bright ... *Science*, **300**:75, 2003.

[105] C. A. Larabell, and M. A. Le Gros. X-ray tomography generates 3-D reconstructions of the yeast, saccharomyces cerevisiae, at 60-nm resolution. *Molecular Biology of the Cell*, **15**:957–962, 2004.

[106] S. Eisebitt, J. Lüning, W. F. Schlotter, M. Lörgen, O. Hellwig, W. Eberhardt, and J. Stöhr. Lensless imaging of magnetic nanostructures by x-ray spectro-holography. *Nature (London)*, **432**:885–888, 2004.

[107] P. Fischer, D.-H. Kim, W. Chao, J. A. Liddle, E. H. Anderson, and D. T. Attwood. Soft x-ray microscopy of nanomagnetism. *Materials Today*, **9(1-2)**:26–33, 2006.

[108] D. Sayre, J. Kirz, R. Feder, D. M. Kim, and E. Spiller. Transmission microscopy of unmodified biological materials. Comparative radiation dosages with electrons and ultrasoft x-ray photons. *Ultramicroscopy*, **2**:337–349, 1977.

[109] W. Chao, B. D. Harteneck, J. A. Liddle, E. H. Anderson, and D. T. Attwood. Soft x-ray microscopy at a spatial resolution better than 15 nm. *Nature (London)*, **435**:1210–1213, 2005.

[110] J. E. Trebes, S. B. Brown, E. M. Campbell, D. L. Matthews, D. G. Nilson, G. F. Stone, and D. A. Whelan. Demonstration of x-ray holography with an x-ray laser. *Science*, **238**:517–519, 1987.

[111] I. McNulty, J. Kirz, C. Jacobsen, E. H. Anderson, M. R. Howells, and D. P. Kern. High-resolution imaging by Fourier transform x-ray holography. *Science*, **256**:1009–1012, 1992.

[112] J. W. Goodman. *Introduction to Fourier Optics.* Roberts and Company Publishers, Greenwood Village, third edition, 2004.

[113] H. N. Chapman, A. Barty, M. J. Bogan, S. Boutet, M. Frank, S. P. Hau-Riege, S. Marchesini, B. W. Woods, S. Bajt, W. H. Benner, R. A. London, E. Plönjes, M. Kuhlmann, R. Treusch, S. Düsterer, T. Tschentscher, J. R. Schneider, E. Spiller, T. Móller, C. Bostedt, M. Hoener, D. A. Shapiro, K. O. Hodgson, D. van der Spoel, F. Burmeister, M. Bergh, C. Caleman, G. Huldt, M. M. Seibert, F. R. N. C. Maia, R. W. Lee, A. Szóke, N. Timneanu, and Janos Hajdu. Femtosecond diffractive imaging with a soft-x-ray free-electron laser. *Nature Physics*, **2**:839–843, 2006.

[114] H. N. Chapman, A. Barty, S. Marchesini, A. Noy, S. P. Hau-Riege, C. Cui, M. R. Howells, R. Rosen, H. He, J. C. H. Spence, U. Weierstall, T. Beetz, C. Jacobsen, and D. Shapiro. High-resolution ab initio three-dimensional x-ray diffraction microscopy. *J. Opt. Soc. Am. A*, **23**:1179–1200, 2006.

[115] J. Miao and D. Sayre. On possible extensions of x-ray crystallography through diffraction-pattern oversampling. *Acta Cryst. A*, **56**:596–605, 2000.

[116] D. Sayre. Some implications of a theorem due to Shannon. *Act. Cyrst.*, **5(6)**:843, 1952.

[117] J. Miao, T. Ishikawa, E. H. Anderson, K. O. Hodgsen. Phase retrieval of diffraction patterns from noncrystalline samples using the oversampling method. *Phys. Rev. B*, **67**:174104, 2003.

[118] J. Miao, H. N. Chapman, J. Kirz, D. Sayre, and K. O. Hodgson. Taking x-ray diffraction to the limit: Macromolecular structures from femtosecond x-ray pulses and diffraction microscopy of cells with synchrotron radiation. *Ann. Rev. Biophys. Biomol. Struc.*, **33**:157–176, 2004.

[119] R. Szipocs, K. Ferencz, Ch. Spielmann, and F. Krausz. Chirped multilayer coatings for broadband dispersion control in femtosecond lasers. *Opt. Lett.*, **19**:201–203, 1994.

[120] A. Stingl, M. Lenzner, Ch. Spielmann, F. Krausz, and R. Szipöcs. Sub-10-fs mirror-dispersion-controlled Ti:sapphire laser. *Opt. Lett.*, **20**:602–604, 1995.

[121] M. Pessot, P. Maine, and G. Mourou. 1000 times expansion/compression of optical pulses for chirped pulse amplification. *Opt. Commun.*, **62**:419–421, 1987.

[122] E. Treacy. Optical pulse compression with diffraction gratings. *IEEE J. Quantum Electron.*, **5**:454–458, 1969.

[123] O. Martinez. 3000 times grating compressor with positive group velocity dispersion: Application to fiber compensation in $1.3 - 1.6$ μm region. *IEEE J. Quantum Electron.*, **23**:59–64, 1987.

[124] CVI Melles Griot. Optical Coatings, Metallic Coatings. *CVI Melles Griot BV, CVI Laser, LLC (USA)*, **Internet**:http://www.mellesgriot.com, http://www.mellesgriot.com/products/optics/oc_5_1.htm.

[125] Y. Li, and E. Wolf. Three-dimensional intensity distribution near the focus in systems of different Fresnel numbers. *J. Opt. Soc. Am. A*, **1**:801–808, 1984.

[126] R. G. Wenzel. Effect of the aperture-lens separation on the focal shift in large-fnumber systems. *J. Opt. Soc. Am. A*, **4**:340–345, 1987.

[127] C. J. R. Sheppard, and P. Török. Dependence of Fresnel number on aperture stop position. *J. Opt. Soc. Am. A*, **15**:3016–3019, 1998.

[128] M. Martínez-Corral, L. Muñoz-Escrivá, A. Pons, and M. T. Caballero. An experiment to study the structure of the focal volume in apertured focusing systems. *Eur. J. Phys.*, **22**:361–369, 2001.

[129] Z. L. Horváth, and Z. Bor. Focusing of truncated Gaussian beams. *Opt. Commun.*, **222**:51–68, 2003.

[130] V. V. Korobkin, and A. J. Alcock. Self-focusing effects associated with laser-induced air breakdown. *Phys. Rev. Lett.*, **21**:1433–1436, 1968.

[131] V. I. Bespalov, and V. I. Talanov. Filamentary structure of light beams in nonlinear liquids. *JETP Lett.*, **3**:471–476, 1966.

[132] J. K. Koga, N. Naumova, M. Kando, L. N. Tsintsadze, N. Nakajima, S. V. Bulanov, H. Dewa, H. Kotaki, and T. Tajima. Fixed blueshift of high intensity short pulse lasers propagating in gas chambers. *Phys. Plasmas*, **7**:5223–5231, 2000.

[133] J. Peatross, J. R. Miller, K. R. Smith, S. E. Rhynard, and B. W. Pratt . Phase matching of high-order harmonic generation in helium- and neon-filled gas cells. *J. Mod. Opt.*, **51**:2675–2683, 2004.

[134] Y. Tamaki, Y. Nagata, M. Obara, and K. Midorikawa. Phase-matched high-order-harmonic generation in a gas-filled hollow fiber. *Phys. Rev. A*, **59**:4041–4044, 1999.

[135] Y. Tamaki, J. Itatani, Y. Nagata, M. Obara, and K. Midorikawa. Highly efficient, phase-matched high-harmonic generation by a self-guided laser beam. *Phys. Rev. Lett.*, **82**:1422–1425, 1999.

[136] F. Osman, R. Castillo, and H. Hora. Focusing and defocusing of the nonlinear paraxial equation at laser-plasma interaction. *Laser Part. Beams*, **18**:73–79, 2000.

[137] W. M. Wood, G. Focht, and M. C. Downer. Tight focusing and blue shifting of millijoule femtosecond pulses from a conical axicon amplifier. *Opt. Lett.*, **13**:984–986, 1988.

[138] J. J. Macklin, J. D. Kmetec, and C. L. Gordon, III. High-order harmonic generation using intense femtosecond pulse. *Phys. Rev. Lett.*, **70**:766–769, 1993.

[139] C.-G. Wahlström, J. Larsson, A. Persson, T. Starczewski, S. Svanberg, P. Salières, Ph. Balcou, and Anne L'Huillier. High-order harmonic generation in rare gases with an intense short-pulse laser. *Phys. Rev. A*, **48**:4709–4720, 1993.

[140] X. Zhang, A. R. Libertun, A. Paul, E. Gagnon, S. Backus, I. P. Christov, M. M. Murnane, H. C. Kapteyn, R. A. Bartels, Y. Liu, and D. T. Attwood. Highly coherent light at 13 nm generated by use of quasi-phase-matched high-harmonic generation. *Opt. Lett.*, **29**:1357–1359, 2004.

[141] Y. Liu, Y. Wang, M. A. Larotonda, B. M. Luther, J. J. Rocca, and D. T. Attwood. Spatial coherence measurements of a 13.2 nm transient nickel-like cadmium soft x-ray laser pumped at grazing incidence. *Opt. Expr.*, **14**:12872–12879, 2006.

[142] J. W. Goodman. *Statistical Optics*. John Wiley & Sons, Inc., New York, Wiley Classics Library Edition edition, 2000.

[143] E. Wolf, and A. J. Devaney. On a relationship between spectral properties and spatial coherence properties of light. *Opt. Lett.*, **6**:168–170, 1981.

[144] D. D. Marcenac, and J. E. Carroll. Maximum-entropy optical spectrum analyzer. *Opt. Lett.*, **20**:1074–1076, 1995.

[145] F. Izumi, and R. A. Dilanian. Structure refinement based on the maximum-entropy method from powder diffraction data. *Recent. Res. Dev. Phys.*, **3**:699–726, 2002.

[146] M. Born, and E. Wolf. *Principles of Optics: Electromagnetic Theory of Propagation, Interference and Diffraction of Light*. Cambridge University Press, New York, seventh edition, 1999.

[147] S. F. Gull, and G. J. Daniell. Image reconstruction from incomplete and noisy data. *Nature (London)*, **272**:686–690, 1978.

[148] E. Fill. Focusing limits of ultrashort laser pulses: Analytical theory. *J. Opt. Soc. Am. B*, **11**:2241–2245, 1994.

[149] T. Ditmire, E. T. Gumbrell, R. A. Smith, J. W. G. Tisch, D. D. Meyerhofer, and M. H. R. Hutchinson. Spatial coherence measurement of soft x-ray radiation produced by high order harmonic generation. *Phys. Rev. Lett.*, **77**:4756–4759, 1996.

[150] T. Ditmire, J. W. G. Tisch, E. T. Gumbrell, R. A. Smith, D. D. Meyerhofer, and M. H. R. Hutchinson. Spatial coherence of short wavelength high-order harmonics. *Appl. Phys. B*, **65**:313–328, 1997.

[151] L. Le Déroff, P. Salières, B. Carré, D. Joyeux, and D. Phalippou. Measurement of the degree of spatial coherence of high-order harmonics using a Fresnel-mirror interferometer. *Phys. Rev. A*, **61**:043802, 2000.

[152] Center for X-Ray Optics. X-ray interactions with matter. *Lawrence Berkeley National Laboratory (USA)*, **Internet**:http://www–cxro.lbl.gov/, http://henke.lbl.gov/optical_constants.

[153] K. Midorikawa, Y. Tamaki, J. Itatani, Y. Nagata, and M. Obara. Phase-matched high-order harmonic generation by guided intensefemtosecond pulses. *IEEE J. Quantum Electron.*, **5**:1475–1485, 1999.

[154] I J. Kim, C. Min Kim, H. Taek Kim, G. Hwang Lee, Y. Soo Lee, J. Yun Park, D. Jaeyun Cho, and C. Hee Nam. Highly efficient high-harmonic generation in an orthogonally polarized two-color laser field. *Phys. Rev. Lett.*, **94**:243901, 2005.

[155] R. L. Sandberg, D. A. Raymondson, W. F. Schlotter,K. Raines, C. La-O-Vorakiat, A. Paul, M. M. Murnane, H. C. Kapteyn, and J. Miao. Near diffraction limited coherent diffractive imaging with tabletop soft x-ray sources. *J. Phys.: Conf. Ser.*, **186**:012058, 2009.

[156] J. A. Armstrong, N. Bloembergen, J. Ducuing, and P. S. Pershan. Interactions between light waves in a nonlinear dielectric. *Phys. Rev.*, **127**:1918–1939, 1962.

[157] P. L. Shkolnikov, A. Lago, and A. E. Kaplan. Optimal quasi-phase-matching for high-order harmonic generation in gases and plasma. *Phys. Rev. A*, **50**:R4461–R4464, 1994.

[158] J. Peatross, S. Voronov, and I. Prokopovich. Selective zoning of high harmonic emission using counter-propagating light. *Opt. Expr.*, **1**:114–125, 1997.

[159] X. Zhang, A. L. Lytle, T. Popmintchev, X. Zhou, H. C. Kapteyn, M. M. Murnane, and O. Cohen. Quasi-phase-matching and quantum-path control of high-harmonic generation using counterpropagating light. *Nature Phys.*, **3**:270–275, 2007.

[160] A. Flettner, J. König, M. B. Mason, T. Pfeifer, U. Weichsmann, R. Düren, and G. Gerber. Ellipticity dependence of atomic and molecular high harmonic generation. *Eur. Phys. J. D*, **21**:115–119, 2002.

[161] K. S. Budil, P. Salières, A. L'Huillier, T. Ditmire, and M. D. Perry. Influence of ellipticity on harmonic generation. *Phys. Rev. A*, **48**:R3437–R3440, 1993.